

# Design and Analysis of Telescope Receiver Systems for Future Far-Infrared Missions

Presented by  
**Adam Byrne, B.Sc.**

A thesis submitted for the degree of  
**Master of Science**



Department of Experimental Physics  
Maynooth University  
Maynooth  
Co. Kildare  
Ireland

**October 2017**

**Head of Department**  
Prof. J. Anthony Murphy

**Research Supervisor**  
Dr. Neil Trappe

# Table of Contents

<b>Abstract</b>	<b>v</b>
<b>Acknowledgements</b>	<b>vi</b>
<b>Chapter 1: Background and Research Overview</b>	<b>1</b>
1.1 Introduction . . . . .	1
1.2 Introduction to Submillimetre Astronomy . . . . .	1
1.3 Applications of the Submillimetre Region . . . . .	2
1.4 Technology . . . . .	5
1.5 Modelling Optical Systems . . . . .	10
1.6 The Big Bang and Cosmic Microwave Background . . . . .	11
1.6.1 The Big Bang Theory . . . . .	11
1.6.2 Theory of Cosmic Inflation . . . . .	13
1.6.3 Temperature Anisotropies of the CMB . . . . .	14
1.6.4 Polarisation of the CMB . . . . .	15
1.7 Historical Observations of the CMB . . . . .	19
1.8 CMB Satellite Missions . . . . .	20
1.8.1 <i>COBE</i> . . . . .	21
1.8.2 <i>WMAP</i> . . . . .	22
1.8.3 <i>Planck</i> . . . . .	23
1.8.4 <i>CORE</i> . . . . .	25
1.9 Thesis Outline . . . . .	26
<b>Chapter 2: Theory</b>	<b>29</b>
2.1 Introduction . . . . .	29
2.2 Quasioptical Systems and Gaussian Beam Mode Analysis . . . . .	30
2.2.1 The Paraxial Wave Equation . . . . .	30
2.2.2 Gaussian Distribution and Parameters . . . . .	32
2.2.3 One Dimensional Fundamental Gaussian Beam Mode . . . . .	34
2.2.4 Two Dimensional Fundamental Gaussian Beam Mode . . . . .	35
2.2.5 Gaussian Beam Coupling . . . . .	37
2.3 Physical Optics and Physical Theory of Diffraction . . . . .	39
2.4 GRASP Overview . . . . .	40
2.4.1 Geometrical Objects . . . . .	41
2.4.2 Surface and Rim Definitions . . . . .	42
2.4.3 Coordinate Systems . . . . .	43

2.4.4	Electrical Objects . . . . .	48
2.4.5	Feeds . . . . .	48
2.4.6	Field Storage . . . . .	50
2.4.7	PO Analysis Objects . . . . .	51
2.4.8	Commands . . . . .	53
2.5	Zemax OpticStudio and Mirror Optimisation . . . . .	55
2.5.1	Overview of OpticStudio . . . . .	55
2.5.2	Optimisation . . . . .	58
2.6	CAD and Meshing Techniques . . . . .	63
2.7	Summary . . . . .	66
<b>Chapter 3: Analysis of Beams</b>		<b>68</b>
3.1	Introduction . . . . .	68
3.2	VNA Measurements with New Waveguide Probes . . . . .	68
3.2.1	Theory . . . . .	69
3.2.2	Measurements . . . . .	71
3.2.3	Results . . . . .	72
3.3	Investigation of Patch Antennae . . . . .	75
3.3.1	Theory . . . . .	76
3.3.2	Implementation in CST . . . . .	77
3.3.3	Verification of Centre Frequency Equation . . . . .	78
3.4	Ray Matrix Analysis . . . . .	79
3.4.1	Element Matrices . . . . .	81
3.4.2	Example: Verifying LLAMA Beam Parameters . . . . .	82
3.5	Gaussian Beam Calculations . . . . .	84
3.5.1	Gaussian Fitting . . . . .	84
3.5.2	Example: Fitting to a Predefined Gaussian Function . . . . .	85
3.5.3	Example: Fitting to a GRASP Gaussian Beam . . . . .	87
3.6	Useful Beam Parameters . . . . .	87
3.6.1	Gaussicity . . . . .	87
3.6.2	Ellipticity . . . . .	88
3.7	Optimisation of ALMA Receiver . . . . .	89
3.7.1	Construction in GRASP . . . . .	89
3.7.2	Analysis using GRASP . . . . .	92
3.8	Conclusions . . . . .	97
<b>Chapter 4: Meshing</b>		<b>100</b>
4.1	Introduction . . . . .	100

4.2	FreeCAD and Meshing . . . . .	101
4.3	Creating Meshes using CAD Files . . . . .	105
4.4	Formatting Mesh Data with Notepad++ . . . . .	108
4.5	Importing Mirror Surfaces into GRASP . . . . .	111
4.6	Comparison of Mesh Types . . . . .	113
4.6.1	Conclusions . . . . .	115
<b>Chapter 5: LLAMA Optical Analysis</b>		<b>118</b>
5.1	Background . . . . .	118
5.2	GRASP Implementation . . . . .	120
5.3	GRASP Analysis . . . . .	122
5.4	Results of the Physical Optics Analysis . . . . .	125
5.4.1	Band 5 Results (163 - 211 GHz) . . . . .	126
5.4.2	Band 5 Plots . . . . .	127
5.4.3	Band 5 Results and Discussion . . . . .	131
5.4.4	Band 6 Results (211 - 275 GHz) . . . . .	131
5.4.5	Band 6 Plots . . . . .	132
5.4.6	Band 6 Results and Discussion . . . . .	136
5.4.7	Band 9 Results (602 - 720 GHz) . . . . .	136
5.4.8	Band 9 Plots . . . . .	137
5.4.9	Band 9 Results and Discussion . . . . .	141
5.5	Mirror Verification and CAD Exportation . . . . .	141
5.5.1	Elliptical Mirror . . . . .	142
5.5.2	Hyperbolic Mirror . . . . .	143
5.5.3	Irregular XY Grid Mirrors . . . . .	144
5.5.4	Verification of Standard Mirror Geometries . . . . .	145
5.5.5	Comparison of CAD Mirrors with Conic Mirror Surfaces . . . . .	152
5.5.6	Exporting the Mirrors in CAD Format . . . . .	159
5.6	Conclusions . . . . .	161
<b>Chapter 6: CORE Analysis</b>		<b>164</b>
6.1	Introduction . . . . .	164
6.2	Information on the CORE Mission . . . . .	164
6.2.1	Focal Plane . . . . .	166
6.3	Offset Gregorian Design . . . . .	167
6.3.1	Implementation in GRASP . . . . .	167
6.3.2	Physical Optics Analysis . . . . .	171
6.3.3	Depth of Field Analysis . . . . .	172

6.3.4	Evolution of Beam along Local Z-Axis . . . . .	173
6.4	Offset Dragonian Design . . . . .	175
6.4.1	Implementation in GRASP . . . . .	175
6.4.2	Positioning and Orienting Feeds and Grids . . . . .	176
6.4.3	Physical Optics Analysis . . . . .	178
6.5	Comparison of Designs . . . . .	179
6.5.1	Design . . . . .	179
6.5.2	Focal Plane . . . . .	179
6.5.3	Conclusion . . . . .	181
6.6	<i>CORE</i> Finalised Design . . . . .	181
6.6.1	Meshing the New Design . . . . .	182
6.6.2	Implementing <i>CORE</i> in GRASP . . . . .	186
6.6.3	Modelling Information . . . . .	187
6.6.4	Positioning Feeds on the Focal Plane . . . . .	188
6.6.5	Orienting Feeds on Focal Plane . . . . .	189
6.6.6	Verification of Feed Positioning . . . . .	196
6.6.7	Setting up Detector Grids . . . . .	197
6.7	PO Analysis of the <i>CORE</i> Design . . . . .	198
6.7.1	Analysis at CMB Frequencies . . . . .	198
6.7.2	145 GHz <i>CORE</i> Beam Contour Plots . . . . .	201
6.7.3	145 GHz <i>CORE</i> Beam Log Plots . . . . .	210
6.7.4	Conclusions on 145 GHz Analysis . . . . .	213
6.7.5	Analysis across the Focal Plane . . . . .	213
6.7.6	Multi-Frequency <i>CORE</i> Beam Contour Plots . . . . .	215
6.7.7	Multi-Frequency <i>CORE</i> Beam Log Plots . . . . .	233
6.7.8	Conclusions . . . . .	239
6.8	Importing Telescope Components . . . . .	240
6.8.1	Creating Viable GRASP Meshes . . . . .	241
6.8.2	New Mesh File Formatting . . . . .	243
6.8.3	GRASP Multi-Face Scatterers . . . . .	246
6.8.4	New Coordinate System Integration . . . . .	249
<b>Chapter 7: Future Work</b>		<b>253</b>
7.1	<i>CORE</i> . . . . .	253
7.2	LLAMA . . . . .	254
7.3	Meshing . . . . .	255

<b>Bibliography</b>	<b>256</b>
---------------------	------------

# Abstract

The main topic of this thesis is the design and analysis of the **Cosmic OR**igins Explorer (*CORE*) telescope, a proposed mission for the ESA M5 mission call. Its focus was the study of the Cosmic Microwave Background (CMB), particularly its polarisation. An ambitious space mission, it would endeavour to detect elusive primordial B-modes. B-modes are considered the key piece of evidence for inflation theory and require extraordinary sensitivity to detect. *CORE* would house up to 2100 detectors on its large, super-cooled focal plane; granting the high sensitivity and wide field of view (FOV) required for CMB study but leads to challenging optical design. Maynooth's role was to examine telescope designs capable of delivering diffraction-limited quality field of view over this 50 cm focal plane area. Two telescope designs (Offset Gregorian and Offset Dragonian) were analysed. The import and export of the mirrors with correct surface definition and orientation form a central part of this work. Physical optics analysis program GRASP was used to simulate beams on the sky from various focal plane positions to verify the positioning of different frequency detectors over the focal plane. This work would form a part of the *CORE* proposal.

In addition, analysis was carried out on the receiver of the Large Latin American Millimetre Array (LLAMA) telescope, currently under construction in Argentina. Based on existing Atacama Large Millimetre/submillimetre Array (ALMA) telescope designs, LLAMA is an independent instrument that will be able to study a large array of astronomical phenomenon at millimetre wavelengths. Eventually it plans to form the first South American Very Long Baseline Interferometer (VLBI) array alongside ALMA and the Atacama Pathfinder Experiment (APEX). The Department of Experimental Physics was asked to perform analysis using three frequency bands on the Nasmyth B receiver of the telescope and the author was given the task.

# Acknowledgements

Before we get down to business, there are a number of people that I have to thank.

First and foremost, I want to thank my postgraduate supervisor Dr. Neil Trappe. I am continually astounded by your boundless enthusiasm and your endless patience. Whether it was heaps of thesis corrections, posters, talks, funding applications, beam plots or anything else; you never failed to find time no matter how busy you were to answer my questions and help me through the problems I encountered. Lord knows I was never the best student but throughout my postgraduate I can recall no arguments, no shouting, not even a heated discussion. In fact, it was quite the opposite. Thank you so very much.

I owe a special thanks to Dr. Darragh McCarthy, who helped me immensely with my early work on *CORE*. He was always generous with his time when he had far more important things to do that help me with my many inane questions on everything Offset Gregorian related. He even agreed to sit in on one my tutorial sessions, a fate I would not wish on my worst foe. Thank you.

I also want to acknowledge all of the help that I have received from the staff of the Experimental Physics Department during my years in Maynooth. My thanks to Prof. J. Anthony Murphy for allowing me the use of department facilities and for the immensely helpful terahertz lectures. I want to offer my thanks to Dr. Cr  idhe O’Sullivan, Dr. Marcin L. Gradziel, Dr. Frank Mulligan, Dr. Peter van der Burgt, Dr. Michael Cawley and Dr. Emma Whelan for their lectures in my undergraduate days and their assistance during my masters. I also must thank Mr. Derek Gleeson for help with travel, Ms. Gr  ainne Roche for, well, *everything*, Mr. John Kelly for the IT support (and the second monitor!), Mr. Pat Seery and Mr. David Watson for their brilliant technical course, Ms. Marie Galligan and Dr. Niall McKeith for organising and helping us in the First Year Labs and Dr.

Ian McAuley, for reminding me to switch on the lights in the office.

To my fellow postgrads, your help and reassurances steadied me during my *many* moments of doubt. Eimante, Joe, Sharon, Julianne, Donnacha, Steve, David, Rory, James, Eoin, Aisling, Michael and Melissa; thank you all for the uncountable hours of joy and friendship you have given me. I owe a special thanks to those who shared an office with me. To George and Mark, thank you for the amazing conversations which ranged from D&D to religion to the Roman Empire. It has been a true pleasure to work with you both. And Benraad, you plucky little radiator.

To Mum and Dad, I would not be here if the two of you hadn't been the supreme parents you are. Your support and advice kept me going through thick and thin. To Zoë and Matthew, the best siblings I could ask for. And to Rosie, I never expected to undertake a postgraduate at the same time as my aunt but I'm glad it worked out that way. You were a unique source of empathy during my masters. I wish you the best in your remaining time as a Ph.D. student and hope that you continue showing the youth how it's done.

Sam, Fabrizio, James and Sean; you all helped to keep me afloat; not just now either.

# Chapter 1

## Background/Research Overview

### 1.1 Introduction

The main theme of this thesis is the design and analysis of far infrared optical receivers. The purpose of this chapter is to establish the background science which drives the science requirements to develop a next generation CMB satellite, which sets challenging technical requirements. An overview of submillimetre astronomy, the CMB, the history of its observation and associated receiver technology is also presented. In addition the technology and software used in the field of far infrared and terahertz optics modelling is described. The chapter will conclude with an outline of the content of this thesis, including the authors specific contribution to the various topics presented.

### 1.2 Introduction to Submillimetre Astronomy

Submillimetre astronomy is a term that encompasses astronomy performed in the range of  $10^9$  Hz to  $10^{12}$  Hz with corresponding wavelengths of 300 mm - 0.3 mm.

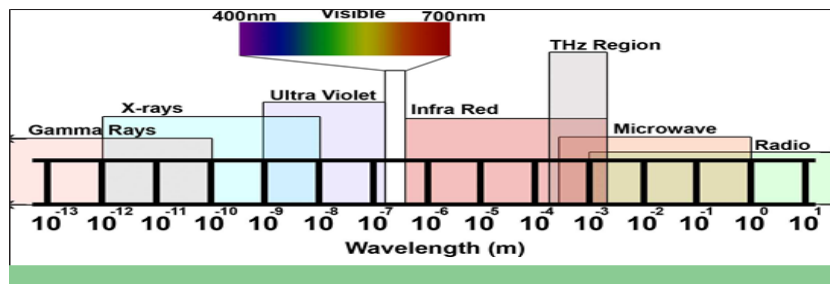


Figure 1.1: The Far-Infrared, Terahertz and Microwave regions of the EM spectrum from Sciencetech-inc.com (2017).

This frequency range (visible in Figure 1.1) is sometimes referred to as the “Terahertz Gap”, referencing the relatively low utilisation of this frequency band, due to the limited availability of cheap and efficient sources and detectors. Existing sources of optical and radio emissions cannot be re-purposed easily to work in this band. Instead, sources to generate terahertz radiation are highly specialised and expensive. Detection technology at one time was limited to bolometers (detectors that measure small changes in temperature associated with photon impact), but new iterations such as Transition Edge Sensor (TES) bolometers and Kinetic Inductance Detectors (KIDs) offer the opportunity (in the future) for test beds to be cheaper and more robust to implement. The specific technology utilised for astronomical purposes will be discussed in **Section 1.4**. Analysis software that relies on ray tracing and geometric optics (staples of optical wavelength analysis) is fast and relatively simple to implement but results from these methods are not always accurate in submillimetre systems, primarily due to diffraction limited propagation. Conversely, software using physical optics techniques (commonly associated with radio wavelength analysis) are accurate and reliable, but suffer from long simulation times which may be anywhere from multiple hours to multiple days for volumetrically large receivers. As a result, multiple programs are often used in conjunction with one another to alleviate the issues that the other techniques possess. An example of ray tracing software is Zemax OpticStudio by Zemax (1990), while GRASP (Generalised Reflector Antenna Software Package) by TICRA (1976) is a commercial physical optics package. Both programs will be discussed extensively throughout this thesis.

### 1.3 Applications of the Submillimetre Region

Despite the lack of widespread utilisation of technology in the submillimetre region due to the aforementioned reasons, many potential benefits could be realised in developing cheaper and more portable terahertz sources and detectors.

Imaging in the terahertz region has potential both for the security and medical sectors. The radiation in the terahertz region is non-ionising and can therefore be used safely for non-invasive imaging techniques. Dry cloth and fabric are transparent in the terahertz region. As a result, there is the ability to image wounds without removing a patient's bandages. Arnone et al. (1999) have performed scans of teeth in the terahertz spectrum using Terahertz Pulse Imaging, measuring enamel thickness and revealing cavities hidden within. Figure 1.3 shows an example of a scan of tooth. Terahertz Pulse Imaging has also been identified by Fitzgerald et al. (2002) as having applications in dermatology, specifically imaging of burn wounds without contact with the affected area as would be required using ultrasound. Metal detectors and x-ray scanners are able to pick up metallic knives and firearms. However, unless they are constructed of very dense ceramic, ceramic blades and modern polymer-framed handguns are very difficult to detect with these traditional methods. Ceramics are highly reflective in the terahertz band. This allows them to be easily spotted even when obscured or hidden within other objects (see Figure 1.2). Federici et al. (2005) discuss the benefits of THz scanning vs. millimetre-wave scanning. They state that the resolution of THz scanners is inherently sharper than conventional scanners due to the shorter wavelength. In addition, many explosive, chemical and biological agents have characteristic transmission/reflection spectra in the THz band, potentially allowing for spectral fingerprinting of these elements should they be concealed.



Figure 1.2: Terahertz scan reveals hidden knife. Credit: UVA Terahertz Lab

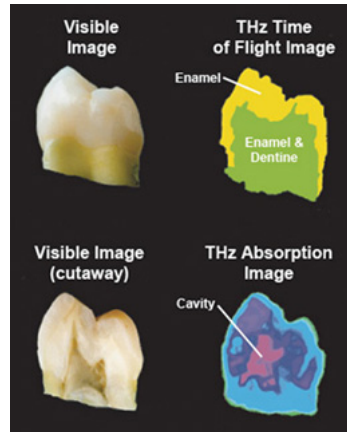


Figure 1.3: Image of a tooth revealing cavity within. Credit: paultownsend.co.uk (2013).

The application of terahertz imaging is not just limited to terrestrial concerns. Walker (2016) mentions several Interstellar Medium (ISM) features that emit in the terahertz band. One of the most important emitters of terahertz radiation is water. Many transitions in the  $\text{H}_2\text{O}$  molecule are in the terahertz region. Active star forming regions can be identified by emission lines from  $^{12}\text{CO}$ . Figure 1.4 demonstrates a slow reveal of these regions at higher frequencies.

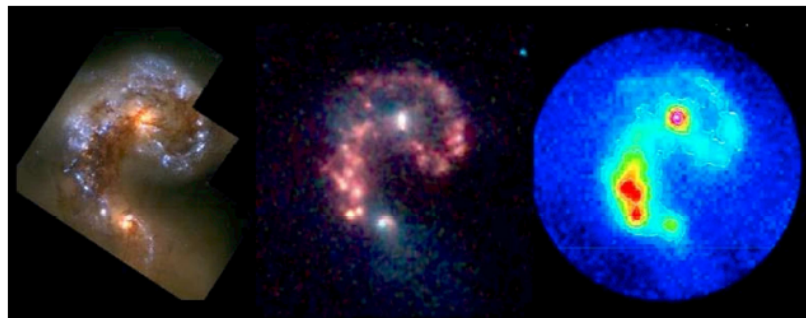


Figure 1.4: Comparison of galaxy showing the star-forming regions being uncovered at longer wavelengths. Credit: <http://astro.cornell.edu/~spifiweb/Motivation.html>

This thesis will feature the CMB heavily. Measurements of this relic radiation peak at frequencies around 100 GHz, which is just below the terahertz band. However, the radiation from the CMB must first travel through the galaxy before it can reach our telescopes and satellites. The Sunyaev-Zeldovich effect refers to

the Compton scattering of CMB photons by energetic electrons in heated gas in galaxy clusters. The effect causes the CMB to become distorted. Emissions from dust in the ISM is also an issue as the CMB radiation can have its polarisation altered by dust grains as well as foreground contamination. In order to retrieve the unaffected signal from the CMB this “foreground” must be subtracted. Therefore higher frequency channels (up to 600 GHz) are required to remove the influence of the galaxy and the dust. Take, for example, the case of apparent primordial gravitational wave detection by *BICEP2* as described by Ade et al. (2014a). The authors claimed to have detected B-mode signals from the CMB at a tensor to scalar ratio of 0.2. Flauger et al. (2014) and many others expressed scepticism that this result could be attributed wholly to primordial gravitational waves. Later study of the region by *Planck* suggested that the result could be attributed to polarised emission from galactic dust. After further *BICEP2-Planck* collaboration, the detection was eventually attributed to this source, as reported by Cowen (2015).

## 1.4 Technology

Detector technology in the terahertz band can be broken into two types: coherent and incoherent. Here coherence means the ability to measure the phase of a received signal, often referred to as a single-mode system.

Walker (2016) reports that coherent detector technology in the terahertz band is based on lower frequency coherent detection systems utilised all over the world for radio, television and wireless networking. One type of coherent detector is the heterodyne receiver (layout shown in Figure 1.5). The principle of any heterodyne receiver is to take a high frequency signal and translate it to a lower frequency. This makes the signal easier to amplify and process. A local oscillator signal (LO), which is much stronger than the astronomical signal, is mixed in with the

astronomical signal using a mixer device. The new intermediate frequency (IF) signal is then amplified and passes on to further processing.

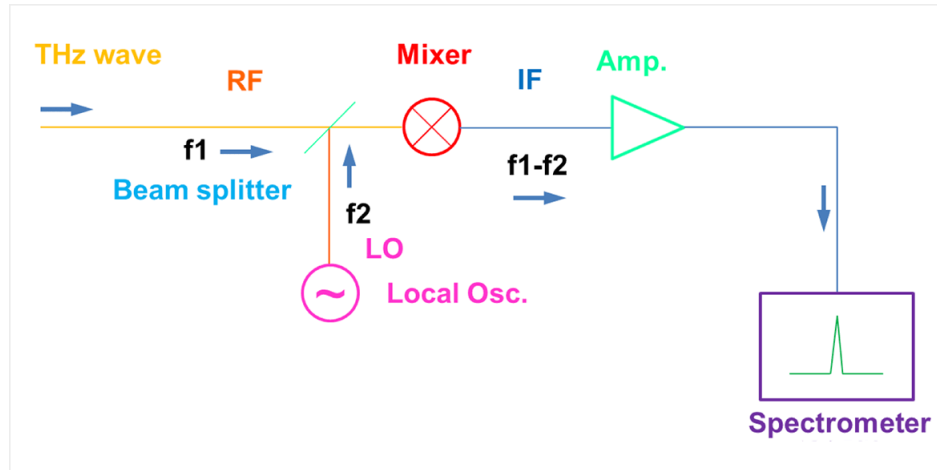


Figure 1.5: Layout of a heterodyne receiver. Credit: [http://aer.nict.go.jp/en/people/res\\_irimajiri.html](http://aer.nict.go.jp/en/people/res_irimajiri.html)

Our research group hosts a Vector Network Analyser (VNA). A VNA is a form of network analyser which has the capability to measure both amplitude and phase properties of a signal. This is done by measurement of S-parameters for reflection and transmission. The Department of Experimental Physics possesses a VNA with W-Band (75 - 110 GHz) capability.

There are numerous examples of incoherent detection devices. Three examples will be discussed below. The first example of incoherent detector technology in the sub-millimetre astronomy regime is the bolometer. This device works on the principle of detection via heating of a material which has a temperature dependent electrical resistance. The absorbing element of the bolometer, typically metallic or made of semiconductor material, is connected to a thermal reservoir. Any photon incident on the absorber raises its temperature above that of the thermal reservoir. Thus a detection is made. Usually these devices are kept at cryogenic temperatures to increase their sensitivity and makes these detection systems expensive and specialised. A crucial aspect of any detector technology

is its noise equivalent power (NEP), a measure of the signal power that a detector can distinguish. Taking data from Byrd (2010), silicon bolometers for the far infrared can achieve an NEP  $\approx 1 \times 10^{-13} \text{ W}/\sqrt{\text{Hz}}$  at 4.2 K to an NEP  $\approx 2.4 \times 10^{-16} \text{ W}/\sqrt{\text{Hz}}$  at 0.3 K.

The second example of incoherent detectors are pyroelectric detectors. Byrd (2010) and Liu and Long (1978) provide descriptions of these devices. They share a principle of operation with bolometers; detection of radiation via heating. Ferroelectric material (such as Lithium Tantalate,  $\text{LiTaO}_3$ ) exhibits an electrical response as a result of temperature change. This surface charge is also spontaneously polarised. If electrodes are attached to one face (or opposite edges) of the material, this response will be seen as an electrical signal. As these devices are based on the pyroelectric effect, an AC (time-varying) signal is required for detection. To balance out this drawback, pyroelectric detectors are able to work at a range of temperatures, as long as temperature of the detector changes it will function. According to Byrd (2010), these detectors have an NEP  $\approx 1 \times 10^{-9} \text{ W}/\sqrt{\text{Hz}}$ .

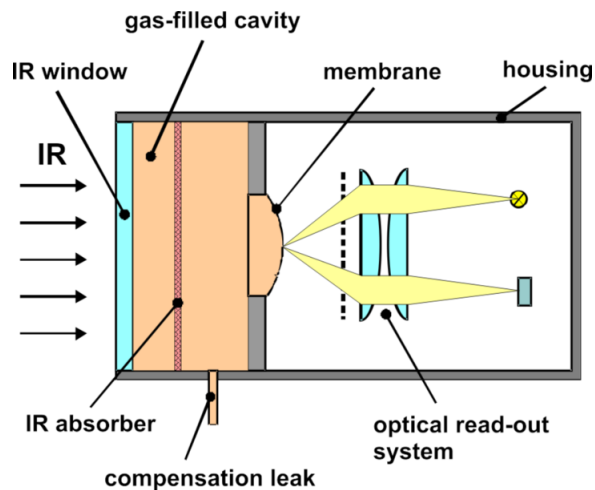


Figure 1.6: Structure of a Goly Cell. Credit: By Ehab Ebeid CC BY 3.0, <https://commons.wikimedia.org/w/index.php?curid=24140065>.

Also, there are Goly Cells (shown above in Figure 1.6). From Lee (2009) and Byrd (2010), Goly Cells are opto-acoustic detectors covering a broad radiation

spectrum that includes the terahertz band. Incident radiation passes through the window of the cell to a gas-filled enclosure behind. The radiation is absorbed by a film in the enclosure, heating up the gas (usually Xenon). As the gas heats, the increase in pressure deforms a mirror at the rear of the enclosure. There is an LED behind the gas cavity whose light is focused onto this mirror. The light reflects off the deformable mirror and is absorbed by a photodiode. Thus a change in the shape of the mirror caused by incident radiation is sensed by the readout system. As with the above pyroelectric detectors, Golay cells can operate at room temperature. They are very sensitive detectors, having an NEP  $\approx 1 \times 10^{-10} - 1 \times 10^{-9} W/\sqrt{Hz}$  according to Lee (2009). However, the materials used in constructing these devices must be very insulating so that as much radiation as possible is taken in by the absorbing film. They are also sensitive to mechanical vibrations, an important factor to be considered in laboratory optical benches.

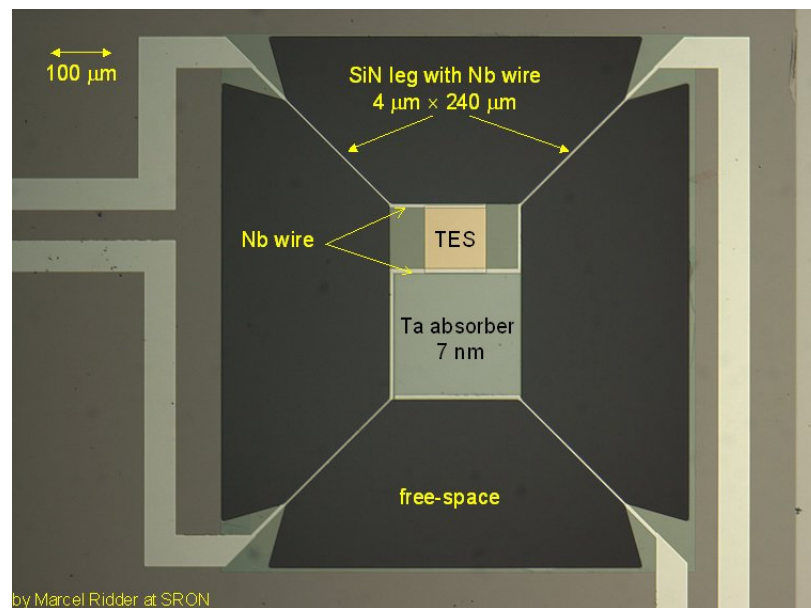


Figure 1.7: Diagram of a TES Bolometer. Credit: SRON

Two new detector technologies are set to become the sub-millimetre detector of choice for future astronomical receivers where high sensitivity is required. The first of these is the TES bolometer (see Figure 1.7). These detectors possess

very high sensitivities. Kuo et al. (2008) provides an overview of these detectors. When a photon is absorbed by a TES, it changes the resistance of that pixel. SRON Netherlands Institute for Space Research report on their website (sron.nl (2017)) that they have tested TES devices that have an NEP that is as low as  $2 \times 10^{-19} \text{ W}/\sqrt{\text{Hz}}$ . The advantage of using TES bolometers is that they can be multiplexed, leading to larger arrays with larger numbers of pixels than previously available. Readouts are achieved using superconducting quantum interference devices (SQUIDS). However, as they are superconducting devices they must be cryogenically cooled to sub-Kelvin temperatures in order to function. The *Simons Array* (currently *POLARBEAR*, with additional antennae under construction), *BICEP2* and *QUBIC* utilise TES bolometers to carry out experiments to study the polarisation of the CMB.

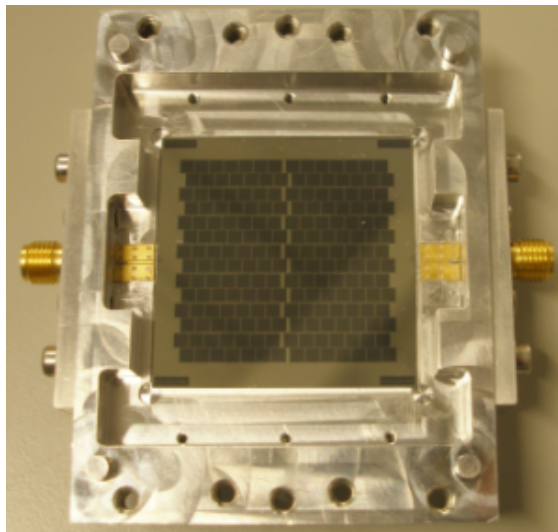


Figure 1.8: Prototype KID device. Credit: Cardiff University School of Physics and Astronomy.

The second promising technology is the Kinetic Inductance Detector. One example is shown in Figure 1.8. These detectors function on the basis of splitting a pair of electrons which are bound together (known also as Cooper pairs). The detector material experiences a change in inductance if a photon is absorbed. Like with the TES bolometers above, KIDS must be kept at cryogenic temperatures to

function. They are easier to multiplex than TES devices as they require a single readout line for one array. Additionally, they can be grouped into large arrays and printed in laboratories. The NEP of a KID has been theorised to be as low as  $2 \times 10^{-20} \text{ W}/\sqrt{\text{Hz}}$  by Baryshev et al. (2011).

## 1.5 Modelling Optical Systems

The modelling of optical systems is carried out in different ways for the sub-millimetre regime. One approach is to use ray tracing software, such as Zemax OpticStudio. Geometrical optics is the basis for ray-tracing. This method benefits from a very quick simulation time due to its simplicity. However, the approach is not necessarily the most representative of receivers where diffraction can dominate the optical behaviour of propagation. These programs would most likely be used in preliminary optical design.

A more accurate technique is that based on physical optics. This is the approach favoured by those working the radio wavelengths as it is very accurate. However, the accuracy comes at a cost in simulation time. Physical optics software must work out the current induced on the surfaces of the reflectors under investigation. This process is computationally intensive, especially if the surfaces are large in terms of wavelength, as is the case for terahertz astronomical receivers.

LLAMA is a receiver whose analysis will be featured later in this thesis. It is a Vertex class 12 m telescope that is under construction in the Puna region of Argentina. It will initially work as a single receiver but further dishes will be added in future. It will connect with ALMA and APEX to create a VLBI. It will study a wide range of objects, including the Sun, astrophysical jets, star-forming regions, ISM and active galactic nuclei (AGN). It will eventually work alongside

ALMA, and so will use ALMA-equivalent optics and ALMA-equivalent frequency bands. Maynooth's contribution to this project was to establish the Nasmyth B receiver system and perform preliminary physical optics analysis of this system.

## 1.6 The Big Bang and Cosmic Microwave Background

### 1.6.1 The Big Bang Theory

The Big Bang Theory is the prevailing theory that explains the existence of the Universe. The theory of an expanding Universe was first proposed by physicist Georges Lemaître in 1927. The paper, Lemaître (1931), uses an expanding Universe model to account for the redshifts of extragalactic nebulae. This was followed by an essay in 1931, *L'hypothèse de l'atome primitif*, as reported by Giovannini (2004). Here he proposed that an expanding Universe could be traced back to a primeval atom with the mass of the Universe, better known today as an initial gravitational singularity. Historically, there was contention at the time between the Big Bang Theory and the Steady State Theory, the latter stating that the Universe was immutable and unchanging. Many physicists expressed doubt that the Universe could even have a beginning, and that if it did then one day it might also have an end. This contention was dealt a death blow two years later by Edwin Hubble and his study of galactic redshifts. Hubble concluded that the redshifting of the light from distant galaxies he observed must be due to the fact that they were moving apart from one another. This was strong evidence for an expanding Universe. From Carroll and Ostlie (2014), physicist George Gamow would refine Lemaître's idea with his theory of Big Bang nucleosynthesis and calculations of cosmic abundances. His associates Ralph Alpher and Robert Herman would predict the CMB, remnant radiation left over from the beginning of the Universe, as part of the expanding Universe theory. Finally, the theory would

get its name from Fred Hoyle, a steady state universe advocate who derisively referred to this expanding universe theory as “this Big Bang idea”.

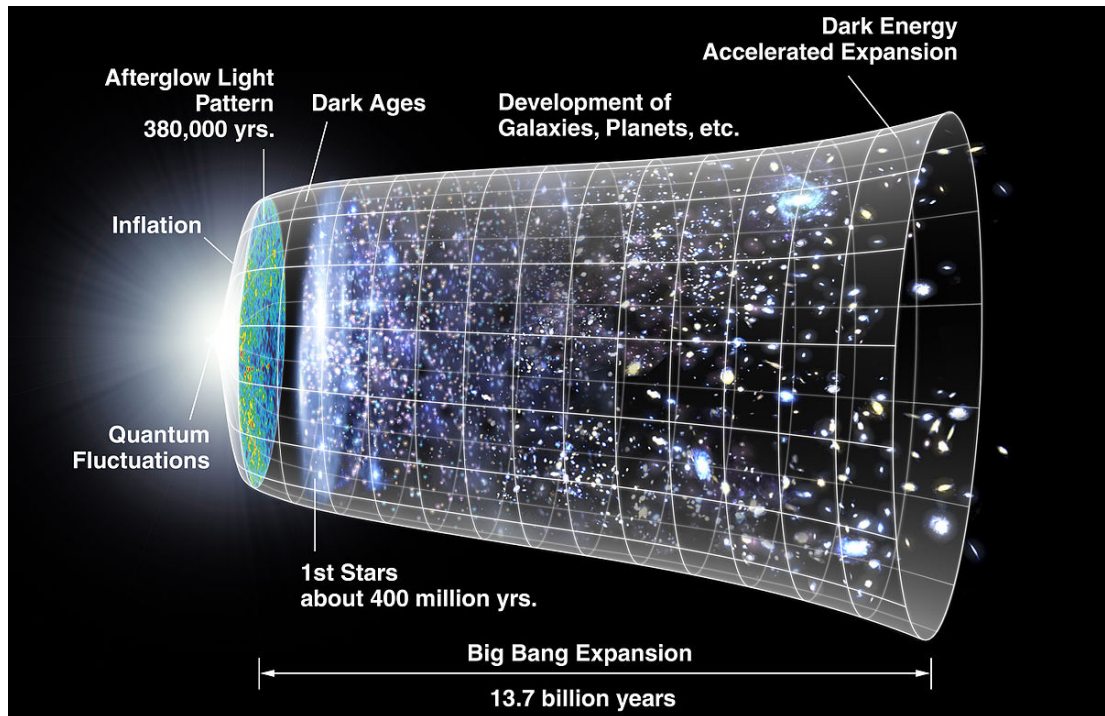


Figure 1.9: Timeline of the history of the Universe. Credit: NASA

Figure 1.9 shows a timeline of the Universe, highlighting major events in its history. According to the Big Bang theory, all matter was once compressed into a point-like region of space known as a singularity. For reasons still to be determined, this singularity expanded, causing space to expand outwards. This early stage of the Universe (10 s - 380'000 yrs) was unimaginably hot and dense. Photons produced at this time would have been absorbed immediately by nearby atoms. In this way, matter and radiation were said to be “coupled”. As a consequence of this the Universe would have been opaque, as no photon could escape the maelstrom. As the Universe continued to expand it would cool and become less dense. Eventually it would reach a point where the mean free path of photons could increase as reaction rates decreased. This allowed photons to escape and travel without absorption or excessive scattering. This point in time is known as the “Surface of Last Scattering”. Matter and radiation were now “decoupled”

and those photons that were able to move freely can be seen today as the CMB.

### 1.6.2 Theory of Cosmic Inflation

The theory of cosmic inflation is an addendum to the Big Bang Theory. Set out in Linde (1984), it attempts to explain several discrepancies that developed in the Big Bang Theory, namely the lack of magnetic monopoles and the Horizon and Flatness problems. Alan Guth, who was studying the monopole issue, proposed the theory in 1979. While working on this problem he found that, under general relativity, a false vacuum should generate an expansion of space. This inflationary period should have left its mark in the CMB.

The Horizon Problem describes the fact that the Universe appears to be homogeneous and isotropic, even for causally disconnected regions. This should only be the case if there was some mechanism that set the initial conditions of the Universe to be the same everywhere. The Flatness Problem describes the fact that density of matter in the Universe is enough for the large-scale geometry of the Universe to flat, as opposed to spherical or hyperboloidal. From Guth (1981), this requires the total density parameter of our Universe,  $\Omega_0$ , to be close and have remained close to the critical density parameter of 1 for the geometry to have remained unchanged.  $\Omega_0$  is made up of  $\Omega_m + \Omega_\Lambda$ , the density of matter and energy respectively. The *Planck* survey data from Ade and the *Planck* collaboration (2015) sets these value to be  $0.6911 \pm 0.0062$  and  $0.3089 \pm 0.0062$ . This gives a total density parameter of 1. The issue that forms the core of the flatness problem is known as a fine-tuning problem: there is a limited range of values for critical density of the Universe that allow the Universe to be flat.

Cosmic Inflation purports to solve these problems. From Guth (1981), the flatness of the Universe is addressed in a similar manner to the apparent flatness of the Earth. The volume of the entire Universe may be so much greater than

that of the observed Universe that the apparent flatness may just be an effect of this. The homogeneity of the observable Universe can be explained with the rapid expansion of the Universe. The size of the Universe increased by a factor of  $10^{26}$ , from the size of a proton to the size of a grapefruit. This occurred in a time span of less than a trillionth of a second. Such a rapid expansion meant that all regions of our observable Universe were causally connected. The small inhomogeneities that are present are explained through quantum fluctuations present in the early Universe being blown up to immense scales.

### 1.6.3 Temperature Anisotropies of the CMB

The CMB is composed of the remnant light of the Big Bang. The photons that comprise this background, once white-hot and highly energetic, have cooled as they travelled in the intervening years. Today their temperature is the temperature of empty space ( $\approx 2.7$  K), a thermal energy which corresponds to the microwave region of the electromagnetic spectrum. These photons hold a wealth of information about the earliest times of the Universe, much the same way the spectrum of a distant star holds information on its progenitor.

The earliest theories involving the CMB also included a prediction that temperature anisotropies should be visible in the CMB itself. These microscopic temperature differences would correspond to different regional densities present in the Universe before inflation. After inflation, the distances between those regions would become exaggerated, leading to areas of matter separated by empty voids. This describes the current matter distribution in the Universe, namely filaments of galaxies surrounded by depleted intergalactic space. Figure 1.10 shows the map of anisotropies as measured by *Planck*.

The anisotropies are bipolar, corresponding to a higher or lower temperature. Fixsen (2009) states this temperature difference to be  $\pm 0.00057$  K based on a

review of *WMAP* data. These tiny fluctuations in temperature represent different densities present at the surface of last scattering. The colder regions are likely more dense than the warmer regions. These densities can be seen as the seed regions where the galaxies that we have today would form.

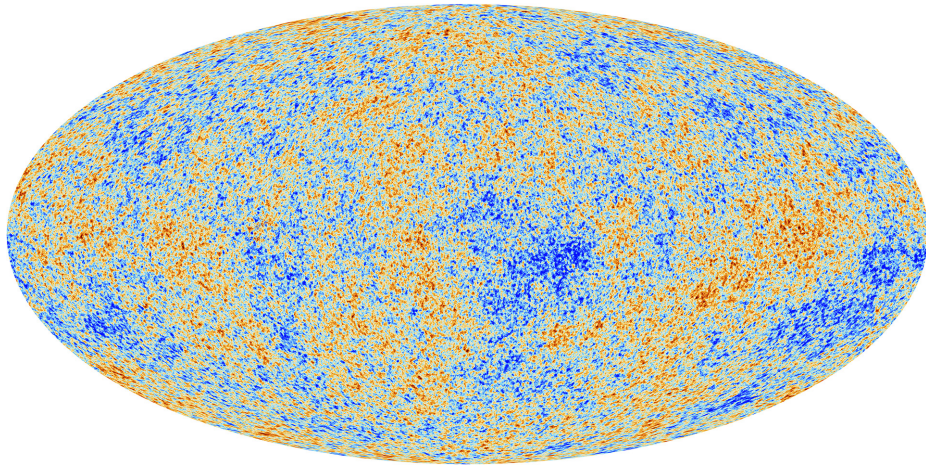


Figure 1.10: Map of CMB temperature anisotropies. Credit: [www.cosmos.esa.int/web/planck/picture-gallery](http://www.cosmos.esa.int/web/planck/picture-gallery)

#### 1.6.4 Polarisation of the CMB

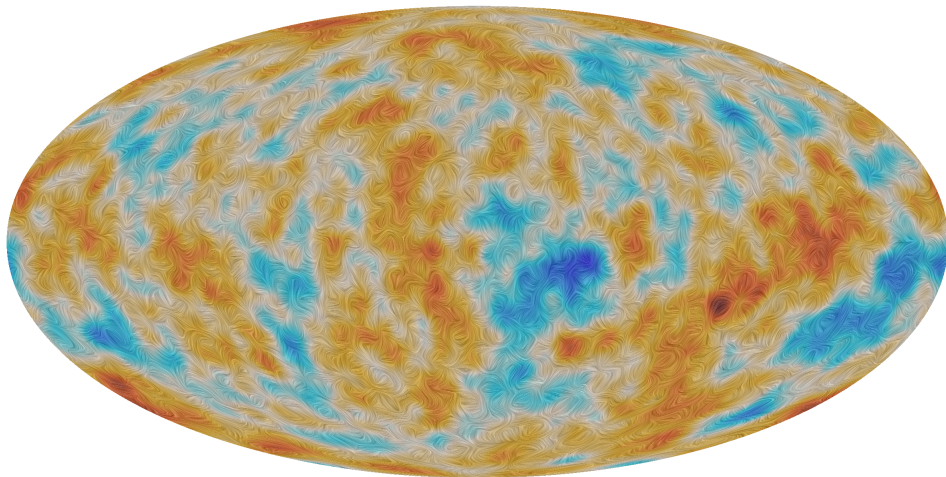


Figure 1.11: Polarisation map from *Planck*. Credit: [www.cosmos.esa.int/web/planck/picture-gallery](http://www.cosmos.esa.int/web/planck/picture-gallery)

According to Samtleben et al. (2007), interest in the CMB is now shifting to the study of the patterns of polarisation. The different sources of the CMB

temperature anisotropies give different polarisation patterns. Figure 1.11 shows the polarisation map measured by *Planck*. Each perturbation generates a unique polarisation pattern. A paper by Hu and White (1997) provides a breakdown of each type of perturbation:

- **Scalar:** These perturbations arise from gravitational instability at last scattering. These fluctuations are the only ones that can create structure through gravitational instability, namely regions of lower density (hot effective temperature) and greater density (cold effective temperature). The polarisation associated with this type of perturbation is E-mode and is generated by Thomson scattering of quadrupole radiation. The quadrupole occurs thanks to the compression of cold regions by hotter regions.
- **Vector:** These perturbations represent vortical motions of the matter of the early Universe. Here the velocity field  $\mathbf{v}$  obeys  $\nabla \cdot \mathbf{v} = 0$  and  $\nabla \times \mathbf{v} \neq 0$ . There are no density perturbations associated with these perturbations as the expansion of the Universe would dampen the vorticity. However, the temperature fluctuations do not decay. Bulk motion of the velocity field produces a dipole pattern radiation field via Doppler shifting of the velocity field itself. However, a quadrupole pattern is produced between the two velocity extremes. The polarisation field is generated using Thomson scattering in the same fashion as mentioned above. This perturbation generates primarily B-mode polarisation.
- **Tensor:** These perturbations are due to gravitational waves. As space is stretched by the gravitational waves a perturbation is set up in the plane of the wave. The stretching of space by this method is quadrupolar. There are no temperature fluctuations associated with this type of perturbation. This perturbation generates comparable amounts of E and B modes.

E-mode and B-mode polarisations are curl-free and divergence-free respectively.

Figure 1.12 illustrates the difference between the two modes.

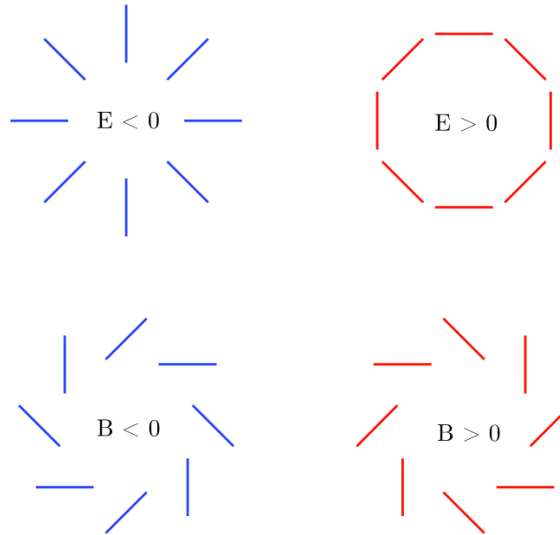


Figure 1.12: Diagram demonstrating E and B mode polarisation. Credit: <https://astrobit.es/2013/07/24/lensing-b-modes-in-the-cosmic-microwave-background-polarization/>

E-mode polarisation emerges from Thomson scattering in a heterogeneous plasma.

This mode is by far the dominant form of polarisation found in CMB radiation.

Figure 1.13 shows the mechanism by which E-mode polarisation arises.

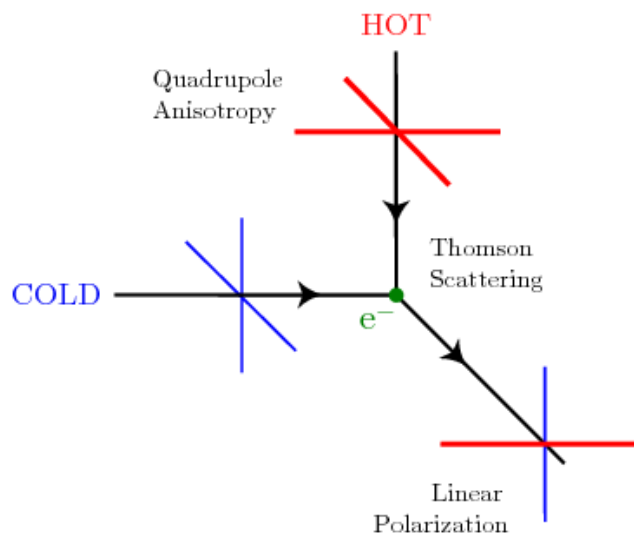


Figure 1.13: Thomson scattering leading to E-mode polarisation. Credit: <http://inspirehep.net/record/827549/plots>

B-mode polarisation is far weaker than E-mode polarisation (see Figure 1.14 for a comparison). In addition to the perturbations mentioned above, B-mode polarisation can arise due to the effect of gravitational lensing by nearby galaxies on E-mode photons. This mode is also produced by as-yet-undetected primordial gravitational waves, which are theorised to be present during the time of cosmic inflation. This type of B-mode polarisation cannot be produced by scalar perturbations. As a result, detection of these primordial B-modes is often referred to as the “Smoking Gun” of Inflation Theory (Baumann et al. (2009) provide such a reference).

As these primordial B-mode photons are in the overwhelming minority in terms of overall CMB radiation, detection is incredibly difficult and would require exquisite sensitivity to detect.

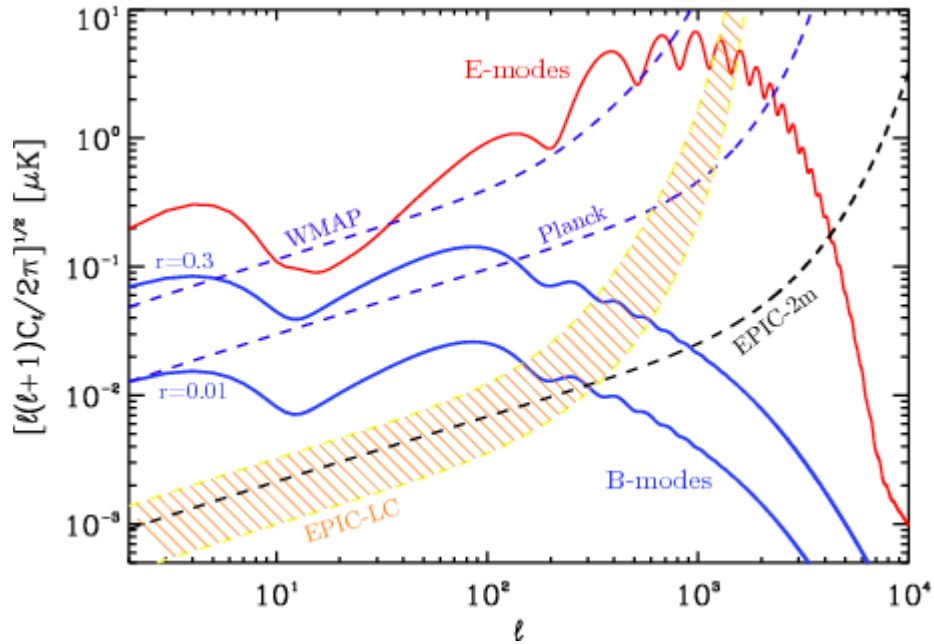


Figure 1.14: Level of primordial B-modes in comparison to E-modes. Credit: <http://inspirehep.net/record/803379/plots>

Ground based CMB observations have been proven successful in the past, but this type of sensitivity can only be realistically achieved by satellite missions. As stated before by Yang et al. (2011) the attenuation of far infrared signals

by Earth's atmosphere would limit the accuracy of detection of faint B-mode signals. Additionally, ground-based observatories cannot produce full-sky maps of the CMB nor cover the large range of frequencies required to remove foreground contamination.

## 1.7 Historical Observations of the CMB

The initial observation of CMB radiation was carried out by Arno Penzias and Robert Wilson in 1964. According to Carroll and Ostlie (2014), they had been working to re-purpose a Bell Laboratories horn antenna in New Jersey (shown in Figure 1.15). Initially developed as a prototype in the fledgling field of satellite communication, Wilson (an astronomer) thought that it would have interesting properties for radio astronomy.

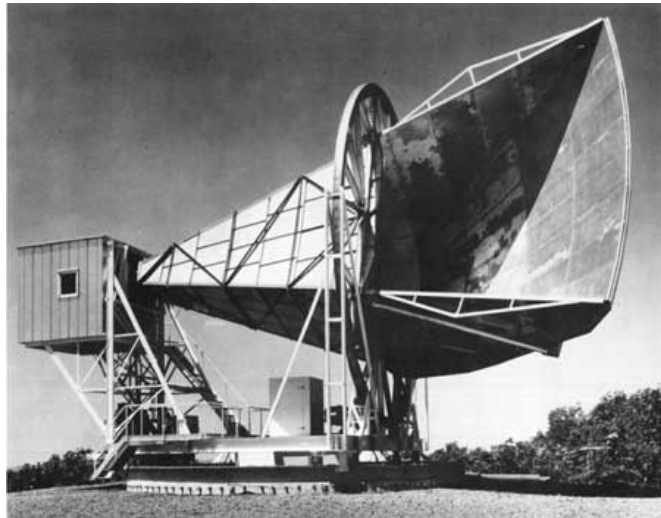


Figure 1.15: The Holmdel Horn Antenna where the CMB was first detected. Credit: <http://www.cv.nrao.edu/course/astr534/RadioTelescopes.html>

The two were constructing a device known as a Dicke Radiometer. Developed by Robert Dicke of nearby Princeton University, they frequently ran into problems when testing their device. Specifically, they always seemed to encounter a 4.2 K antenna temperature. Measures which were taken to reduce this noise failed. Eventually they would realise that this noise was not noise at all, but rather a hiss

of radiation emanating from all points in space. They were aware of theoretical predictions of such a background radiation. They confirmed their on consultation with the research group in Princeton, with Robert Dicke famously saying “Boys, we’ve been scooped”.

Future ground-based observations of the CMB would refine and lower the temperature from Penzias and Wilson’s finding. While ground-based observations continue today, with notable experiments being *POLARBEAR*, *QUIET*, *BICEP2* and soon *QUBIC*, satellite-based missions are far better suited to study the CMB in detail. Ground-based missions are hampered by the Earth’s atmosphere in a number of ways. Atmospheric absorption via water vapour limits the number of frequency bands that can be viewed from Earth. Yang et al. (2011) performed a study of attenuation of radiation from 0.2 - 2 THz, performed at sea level for a number of different weather conditions. The general trend was towards increased attenuation at higher frequencies, with attenuation in general rising in humid weather and falling in winter. To get around this particular issue, instruments are deployed in high altitude or extremely cold environments. Even so, the polarisation sensitivity will be lower than that achievable via satellite. Ground instruments are also not able to produce full sky maps, being limited by sky overhead. Finally, these instruments require heavy cooling to reduce random electrical noise within the detectors and increase the instruments sensitivity. For *BICEP2*, Ade et al. (2014b) state that the focal plane tiles were cooled to 250 mK, despite an atmosphere (and hence aperture) temperature of 230 K. While cryogenic cooling is still required for satellite missions, the average temperature of the satellite will be the average temperature of the space around it.

## 1.8 CMB Satellite Missions

As stated in the previous section, only satellite missions can realistically achieve the sensitivity, frequency and sky coverage required for the detection of primordial

B-Modes. There is a rich heritage of CMB satellite missions.

### 1.8.1 *COBE*

The Cosmic Background Explorer (*COBE*) was a CMB satellite mission launched on November 18<sup>th</sup> 1989. An illustration of the satellite can be see in Figure 1.16. The purpose of the mission was to map the emissions of the CMB over the whole sky and measure the temperature anisotropies contained within. Of the three instruments on-board the satellite, the Differential Microwave Radiometer (DMR) was responsible for measuring the anisotropy. According to a paper by Smoot et al. (1992) the instrument operated at three frequencies: 31.5, 53 and 90 GHz. These frequencies were chosen as they corresponded to maximal CMB emissions with minimum emissions from foreground galactic sources. The DMR was composed of three receivers spaced  $120^\circ$  apart on the aperture. Each radiometer was made up of a pair of horn antennas. These antennas had an angular resolution of  $7^\circ$  on the sky. For reference, the angular size of the moon is  $0.5^\circ$  on the sky.



Figure 1.16: *COBE*. Credit: <https://map.gsfc.nasa.gov/media/081000/>

The data from *COBE* was used to produce the first full sky map of the temperature anisotropies of the CMB. *COBE* also holds the distinction of providing the evidence which confirmed the Big Bang theory of the origin of the Universe. The CMB map produced by *COBE* is displayed in Figure 1.17:

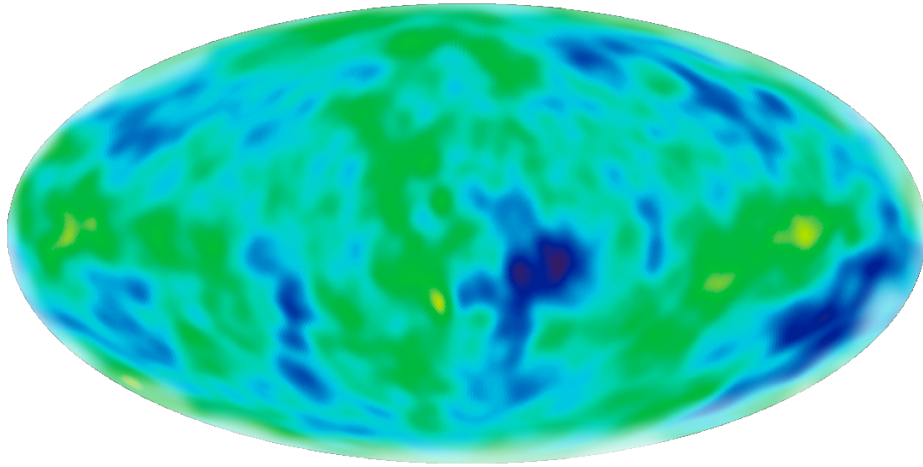


Figure 1.17: *COBE* map of anisotropies. Credit: <https://wmap.gsfc.nasa.gov/media/030653/index.html>

## 1.8.2 *WMAP*

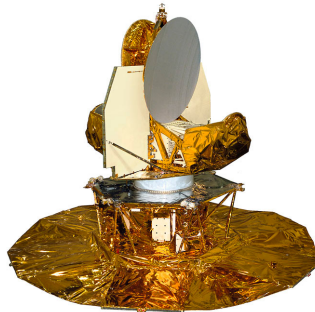


Figure 1.18: *WMAP*. Credit: <https://map.gsfc.nasa.gov/media/990389/index.html>

The Wilkinson Microwave Anisotropy Probe (*WMAP*) was designed with many goals in mind. Figure 1.18 displays the *WMAP* satellite. One of them was to measure the temperature anisotropies discovered by *COBE* to a much higher precision. *WMAP* built on the success of *COBE* in that it not only measured the temperature anisotropies to a higher precision but also attempted to measure the polarisation of the CMB at large angular scales as well. It was launched on 30<sup>th</sup> June 2001. The map of anisotropies it produced is shown below in Figure 1.19:

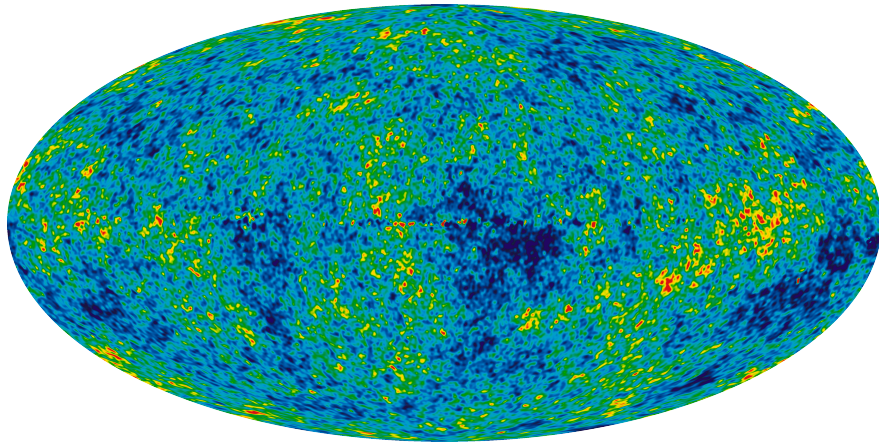


Figure 1.19: *WMAP* anisotropies. Credit: <https://map.gsfc.nasa.gov/media/101080/index.html>

*WMAP*'s optics consist of two back-to-back Offset Gregorian reflectors. An array of corrugated feeds are coupled to each reflector. *WMAP* carried 20 differential radiometers that covered 5 different frequency bands ranging from 20 to 106 GHz. The angular resolution of *WMAP* was significantly higher than that achieved by *COBE*, NASA (2010) reporting a range from  $0.93^\circ$  at 22 GHz to  $< 0.23^\circ$  at 90 GHz. The map of temperature anisotropies *WMAP* produced contained much more information on the structure of the early Universe.

### 1.8.3 *Planck*



Figure 1.20: *Planck*. Credit: <http://planck.caltech.edu/spacecraft.html>

*Planck* was an ESA satellite launched in 2009. The satellite can be seen in Figure 1.20 above. The aim of the mission was to measure the fluctuations of the CMB to an accuracy set by fundamental astrophysical limits. In this sense, it builds upon the legacy of *COBE* and *WMAP*. However, *Planck* also had a prerogative to provide evidence which would test the theory of inflation. This would require a study of the polarisation of the CMB more accurate than *WMAP* and an attempt to detect primordial gravitational waves via primordial B-modes, which Page et al. (2007) report *WMAP* did not achieve. Its map of anisotropies can be seen in Figure 1.21.

*Planck* carried two instruments on board: The Low Frequency Instrument (LFI) and the High Frequency Instrument (HFI). These provide a frequency coverage of 27 GHz to 1 THz. *Planck* was designed to measure the CMB with more angular resolution and sensitivity than before. The wider range of signals accepted by *Planck* allows it to cancel out foreground sources from the galaxy. HFI has a resolution of 9.2 arcminutes at 100GHz that reduces to 5 arcminutes at the higher frequencies  $> 217$  GHz. Despite this, ESA (2015) explain that *Planck* was unable to conclusively provide evidence for primordial gravitational waves.

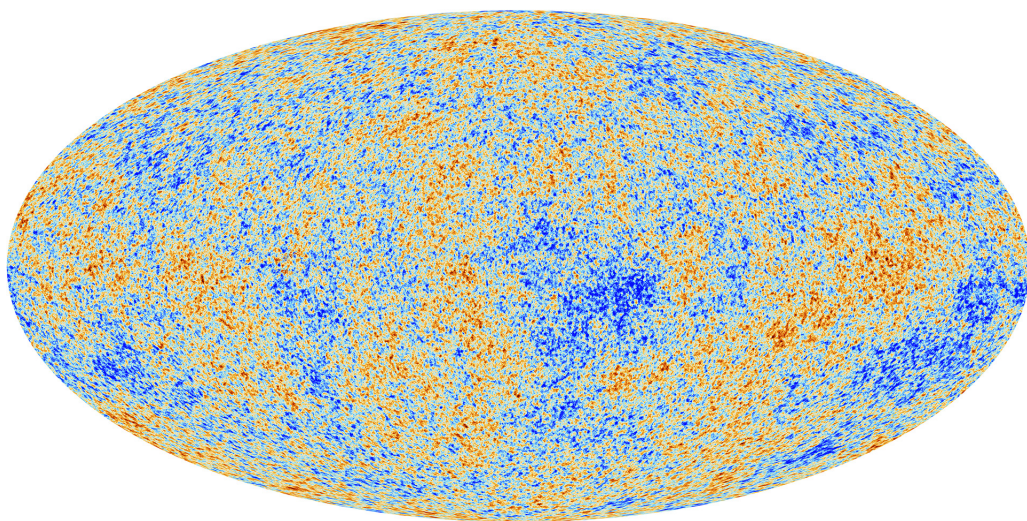


Figure 1.21: *Planck* map of anisotropies. Credit: <https://www.cosmos.esa.int/web/planck/picture-gallery>

### 1.8.4 *CORE*

*CORE* is a proposed next generation satellite mission whose goal is to achieve unparalleled sensitivity to the primordial B-mode signal of the CMB with the aim of providing evidence for cosmic inflation. *CORE* was submitted in late 2016 as part of the Cosmic Vision M5 medium-class mission call by ESA. It was planned to utilise a 1.2 m telescope coupled to an unprecedented large focal plane filled with sensitive detectors. This will allow for a diffraction limited field-of-view of  $11^\circ$  on the sky. The focal plane itself will be packed with the latest in detector technology (and as many as 2100 detectors). This should allow *CORE* to have a polarisation sensitivity of less than  $2.5 \mu\text{K}$ , which is 20 times that of the *Planck* satellite. The satellite is developed from previous proposals *BPOL*, *PRISM* and *COrE*. The optical design and analysis of *CORE* will form a significant part of this thesis. The model of *CORE* is shown in Figure 1.22.

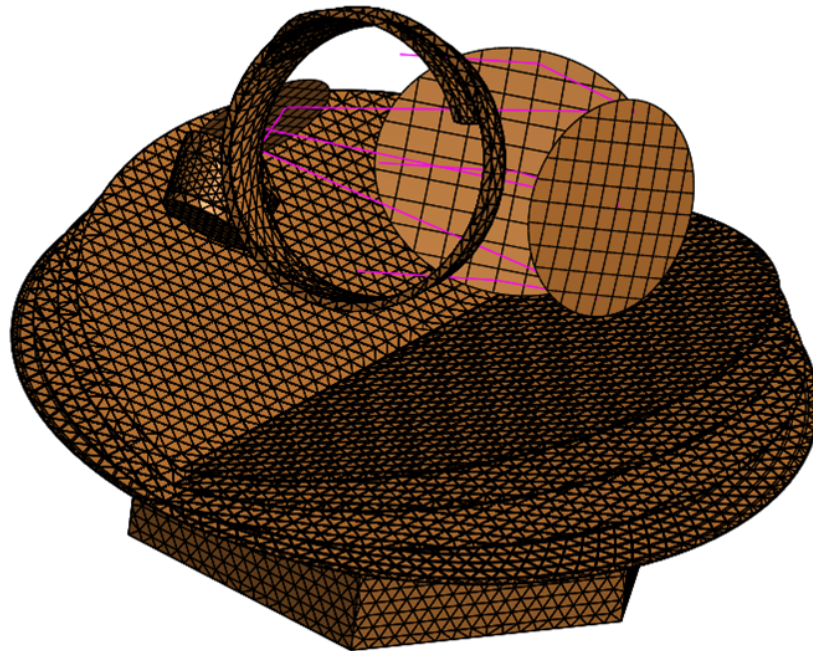


Figure 1.22: The final design of the *CORE* telescope in GRASP.

## 1.9 Thesis Outline

The format of this thesis will now be set out, chapter-by-chapter, with a brief overview of the contents of these chapters (including the author's contribution where appropriate).

### Chapter 2

This chapter will begin by covering the theory of Gaussian Beam Mode analysis, a core concept of this work. The analysis software packages GRASP and Zemax OpticStudio will be explored in greater detail. CAD modelling and meshing techniques will be covered as part of this chapter, given their prevalence in **Chapter 5** and **Chapter 6**.

### Chapter 3

This chapter will provide an overview of associated theory and background of calculations used in this thesis, mainly beam coupling calculations, Gaussicity and beam ellipticity evaluation. These parameters will appear in resulting chapters to analyse optical properties of receivers developed by the author. Measurements with the VNA to characterise new waveguide probes will also be presented.

### Chapter 4

The fourth chapter will contain an outline of the meshing process used in the CAD software FreeCAD, which was subsequently used to define the optical surface of a mirror in physical optics analysis. The investigation of meshing methods and the impact of each mesh type on the optical performance of mirror surfaces was vital to the work carried out on several telescopes and receivers. A comparative study will be presented comparing the different meshing methods possible and associated accuracy. Following on from this, another study will investigate the

effect of the density of a mesh on simulation time and beam prediction accuracy. This is important as the mirrors of *CORE* were optimised in CODE V (a commercial ray tracing package) and exported as a CAD model. The surfaces were non-standard and so preserving the correct profile as the surfaces were exported and imported between packages is extremely important. A deep understanding of how the surface of a mirror is defined is needed before mirrors are imported into GRASP for analysis, where fidelity of a surface definition is paramount.

## Chapter 5

The modelling and analysis of the LLAMA receiver will be discussed in this chapter. The design and verification of the receiver was the responsibility of the author. The background, aims and design of LLAMA will be explained. Next, the process of designing and implementing the mirrors of the receiver will be outlined. The method of physical optics analysis will be described and the results shown for ALMA Bands 5, 6 and 9. Finally, the procedure of exporting the mirrors for manufacture will be outlined, given that the mirrors designed by the author were manufactured for the LLAMA project.

## Chapter 6

This chapter will cover the full breath of work which was done modelling and verifying the different designs of optics for *CORE*. Two initial telescope designs for *CORE* were tested for their suitability for the mission. The preliminary results from both designs are discussed. The final proposed design for *CORE* is then presented and analysed. The process of transferring the design from a CAD format to one readable by GRASP is described. Once successfully represented in GRASP, tests using Gaussian source fields were carried out to determine the quality of the beams produced over the full area of the focal plane, propagated to the sky for a variety of frequencies and focal plane locations. Finally, the

process of importing complex geometries will be shown as the baffle and other shielding elements are imported into the design. The author was responsible for verifying the *CORE* optics in GRASP and analysing the optical performance with software developed to analyse the quality of beams produced by the telescope. All the import/export procedures between the optics package GRASP and FreeCAD ensuring correct surface definitions were developed and implemented successfully by the author.

## Chapter 7

The final chapter of this thesis will conclude with a discussion of how the work presented could be expanded and associated recommendations of the author.

# Chapter 2

## Theory

### 2.1 Introduction

This chapter will outline for the analytical techniques and software used throughout this thesis. The field of quasioptical modelling utilises methods like physical and geometric optics, physical theory of diffraction and Gaussian Beam Mode analysis. Gaussian Beam Mode analysis is a method which allows beams of radiation (which have a quasi-Gaussian distribution in their power pattern) to be modelled accurately and efficiently. This analysis technique will be introduced in the following section, with subsequent analysis techniques following on from it. The background mathematical aspects of the various analysis methods will be discussed in **Chapter 3**.

CAD will be used in later chapters as an accepted method of transferring models of telescopes between both computer programs and research groups. This necessitates a grounding in the subject.

Finally, the reader must also be familiarised with the software and tools used to carry out the work, lest they be cast adrift in a sea of acronyms and abbreviations. To remedy this, an overview of the analysis programmes will be provided through the chapter where appropriate.

## 2.2 Quasioptical Systems and Gaussian Beam Mode Analysis

Quasioptics refers to an optics field of study where beams of radiation are well collimated but of a similar size to optical components (lenses, mirrors and apertures) used. The comparable size of beam and component means that diffraction effects become a significant factor to consider. The range of wavelengths where this occurs covers the microwave to sub-millimetre frequencies and is of particular interest to this thesis.

### 2.2.1 The Paraxial Wave Equation

Gaussian beams differ from those encountered in geometrical optics as they do not originate from a point source and they do contain a transverse wave component. From Goldsmith (1998), these beams are assumed to be highly collimated, which is to say that they are very directional and do have the previously mentioned transverse component. In addition, a Gaussian beam has a power distribution that is dependent on propagation distance (i.e. its position); the only form of electromagnetic wave that is not relevant would be the plane wave. Taking this all into consideration, a paraxial wave equation can be formed to express the propagation of a Gaussian beam. Goldsmith (1998) explains that a component of an electromagnetic wave propagating in a uniform medium satisfies the Helmholtz equation:

$$(\nabla^2 + k^2)\psi = 0 \tag{2.1}$$

where  $\psi$  is any electric  $\mathbf{E}$  or  $\mathbf{H}$  magnetic component,  $k$  is the wave number which is equal to  $2\pi/\lambda$  and  $\nabla^2$  is the Laplacian. Setting the axis of propagation to be the  $z$ -axis, any component of either  $\mathbf{E}$  or  $\mathbf{H}$  can be described in Cartesian terms

as:

$$\psi(x, y, z) = u(x, y, z)e^{-jkz} \quad (2.2)$$

where  $u$  is a complex scalar function that describes the non-planar part of the beam. Equation 2.2 can be described in Cartesian terms as:

$$\frac{\partial^2 \psi}{\partial x^2} + \frac{\partial^2 \psi}{\partial y^2} + \frac{\partial^2 \psi}{\partial z^2} + k^2 \psi = 0 \quad (2.3)$$

According to Goldsmith (1998), Equation 2.2 can be substituted into Equation 2.3 to produce what is known as the *reduced wave equation*:

$$\frac{\partial^2 u}{\partial x^2} + \frac{\partial^2 u}{\partial y^2} + \frac{\partial^2 u}{\partial z^2} - 2jk \frac{\partial u}{\partial z} = 0 \quad (2.4)$$

The paraxial approximation assumes that:

- The on-axis variation of the beam will be small compared to the variation perpendicular to the axis of propagation
- The variation of the amplitude  $u$  along the propagation axis will be small over a distance comparable to one wavelength

The first point implies that  $\frac{\partial^2 u}{\partial z^2} \ll \frac{\partial^2 u}{\partial x^2}, \frac{\partial^2 u}{\partial y^2}$  and the latter point implies that  $\frac{\partial^2 u}{\partial z^2} \ll \frac{\partial u}{\partial z}$ . Goldsmith (1998) then mentions that the final second order derivative can be excluded, leaving the paraxial wave equation:

$$\frac{\partial^2 u}{\partial x^2} + \frac{\partial^2 u}{\partial y^2} - 2jk \frac{\partial u}{\partial z} = 0 \quad (2.5)$$

Gaussian beam modes form solutions to the paraxial wave equation and are the basis of quasioptical system design.

## 2.2.2 Gaussian Distribution and Parameters

A Gaussian beam is one whose profile can be described using a Gaussian function:

$$f(r) = \exp\left[-\left(\frac{r}{\omega_0}\right)^2\right] \quad (2.6)$$

Goldsmith (1998) mentions that Equation 2.6 above describes a Gaussian function in one dimension. Here  $r$  refers to distance from the transverse axis of the beam.  $\omega_0$  refers to the size of the beam waist, the narrowest part of the beam where the radius of curvature is infinite (i.e. plane).

There are other parameters of the beam required which are contained in the beam parameter  $q$ :

$$\left(\frac{1}{q}\right) = \frac{1}{R} - \frac{j\lambda}{\pi\omega^2} \quad (2.7)$$

$$q = z + \frac{j\pi\omega_0^2}{\lambda} \quad (2.8)$$

Equation 2.7 defines the beam radius  $\omega$  and beam radius of curvature  $R$ , both functions of propagation distance  $z$ .  $\lambda$  is the wavelength of the radiation. The beam parameter  $q$  is a complex value. The first part of the equation contains the real part of  $q$  and the second term contains the complex term. Equation 2.8 defines the propagation distance  $z$  and the beam waist radius  $\omega_0$ . These two equations can be used to obtain the radius of curvature  $R$  and beam radius  $\omega$ :

$$R = z + \frac{1}{z} \left(\frac{\pi\omega_0^2}{\lambda}\right)^2 \quad (2.9)$$

$$\omega = \omega_0 \left[1 + \left(\frac{\lambda z}{\pi\omega_0^2}\right)^2\right]^{0.5} \quad (2.10)$$

The Gaussian beam phase shift,  $\phi_0$ , is the difference between the phase of a Gaussian beam and that of a plane wave of the same frequency. It is also known

as the Gouy phase shift. It can be calculated using Equation 2.11:

$$\phi_0 = \arctan\left(\frac{\lambda z}{Z_R}\right) = \arctan\left(\frac{\lambda z}{\pi\omega_0^2}\right) \quad (2.11)$$

where  $Z_R$  is the Rayleigh distance, the distance from the beam waist where the beam radius is increased by a factor of  $\sqrt{2}$ . This denotes the point of transition between a near-field beam and a far-field beam.

Gaussian beams are used to represent the power contained in a beam of radiation. The beam can be said to have two components in a far-field state: co-polar and cross-polar. The co-polar beam component is the part of the beam that is polarised in the same orientation as the detector and is considered the main component of interest. It is this component that possesses the Gaussian profile. The cross-polar beam component refers to the orthogonal component of the beam. Due to this fact, it is treated as noise in the system and it is therefore desirable that this component be low in power for a linearly polarised detector. Beam power may be presented as normalised logarithmic plots with units of decibels (dB). Normalisation is carried out with respect to the peak power of the co-polar beam, both for co-polar and cross-polar. Assuming that electric and magnetic field components are related to each other as with a plane wave, the total power of the beam is proportional to the square of the electric field integrated over the beam area (assumed to be circular). Normalisation involves setting the value of this integral to 1:

$$\int |E|^2 \cdot 2\pi r dr = 1 \quad (2.12)$$

When evaluated at the beam waist, the integral yields a value of  $\pi\omega_0^2/2$ . The two methods of beam plotting are shown below in Figures 2.1 and 2.2:

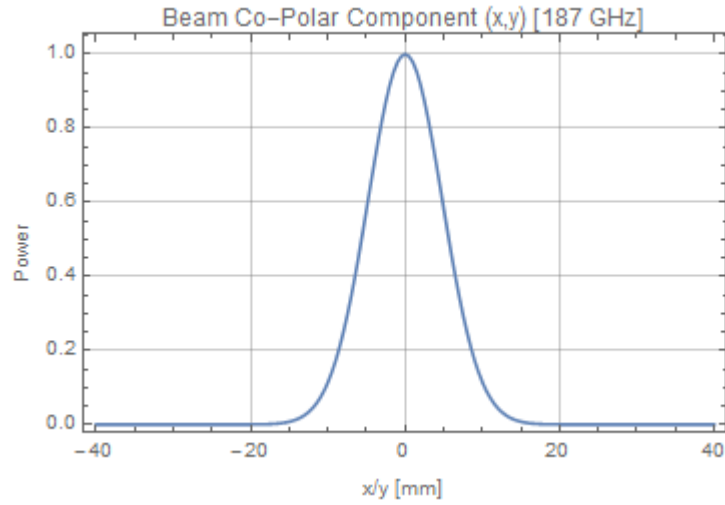


Figure 2.1: Linear plot of the intensity of a Gaussian Beam with  $\omega_0 = 9.6$  mm.

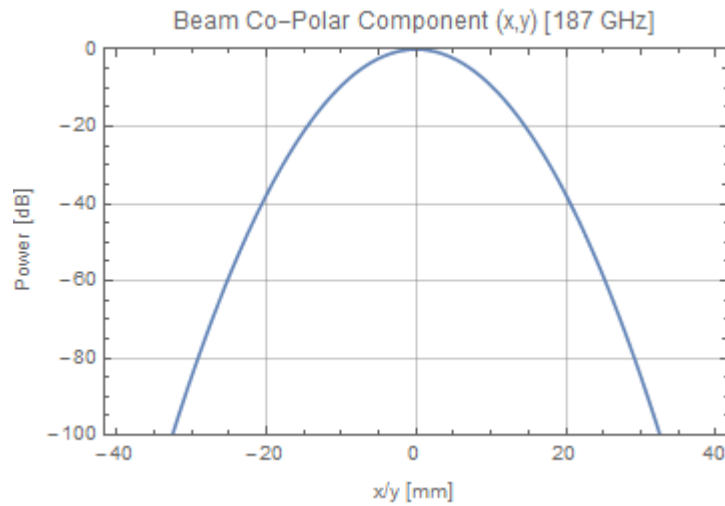


Figure 2.2: Logarithmic plot of the intensity of a Gaussian Beam with  $\omega_0 = 9.6$  mm.

### 2.2.3 One Dimensional Fundamental Gaussian Beam Mode

When considering a beam that has variation in a dimension  $x$  perpendicular to the axis of propagation but but with uniform behaviour in the orthogonal  $y$  direction.

In this case, Equation 2.5 reduces to:

$$\frac{\partial^2 u}{\partial x^2} - 2jk \frac{\partial u}{\partial z} = 0 \quad (2.13)$$

The beam parameter in this case becomes:

$$\left(\frac{1}{q_x}\right) = \frac{1}{R_x} - \frac{j\lambda}{\pi\omega_x^2} \quad (2.14)$$

$$q_x = z + \frac{j\pi\omega_{0x}^2}{\lambda} \quad (2.15)$$

From Goldsmith (1998), the normalised form of the electric field distribution is developed from Equation 2.2:

$$\mathbf{E}(x, z) = \left(\frac{2}{\pi\omega_x^2}\right)^{0.25} \exp\left(-\frac{x^2}{\omega_x^2} - jkz - \frac{j\pi x^2}{\lambda R_x} + \frac{j\phi_{0x}}{2}\right) \quad (2.16)$$

The beam parameters for  $x$  are able to be obtained using the equations below:

$$R_x = z + \frac{1}{z} \left(\frac{\pi\omega_{0x}^2}{\lambda}\right)^2 \quad (2.17)$$

$$\omega_x = \omega_{0x} \left[1 + \left(\frac{\lambda z}{\pi\omega_{0x}^2}\right)^2\right]^{0.5} \quad (2.18)$$

$$\phi_{0x} = \arctan\left(\frac{\lambda z}{\pi\omega_{0x}^2}\right) \quad (2.19)$$

## 2.2.4 Two Dimensional Fundamental Gaussian Beam Mode

Of course to define a meaningful two-dimensional beam we need a two-dimensional description. It is more likely that a beam produced by a telescope or receiver system will be asymmetric, owing to symmetry breaking due to the conic form of the mirrors in one of the orthogonal directions. A more realistic approach should include both orthogonal dimensions in any model. This would allow beam radii  $\omega_x$  and  $\omega_y$  in both  $x$  and  $y$  to be solved independently of each other, which in turn would allow additional parameters of the beam to be analysed, such as its ellipticity (shape relative to a circular beam). **Chapter 3** will cover these methods in more detail than the background presented here.

In two dimensions, the beam parameter  $q$  separates so that the other beam parameters can be treated independently:

$$\left(\frac{1}{q_x}\right) = \frac{1}{R_x} - \frac{j\lambda}{\pi\omega_x^2} \quad (2.20)$$

$$\left(\frac{1}{q_y}\right) = \frac{1}{R_y} - \frac{j\lambda}{\pi\omega_y^2} \quad (2.21)$$

$$q_x = z + \frac{j\pi\omega_{0x}^2}{\lambda} \quad (2.22)$$

$$q_y = z + \frac{j\pi\omega_{0y}^2}{\lambda} \quad (2.23)$$

The electric field distribution is a simple product of the field distributions in  $x$  and  $y$ :

$$\mathbf{E}(x, y, z) = \left(\frac{2}{\pi\omega_x^2\omega_y^2}\right)^{0.5} \exp\left(-\frac{x^2}{\omega_x^2} - \frac{y^2}{\omega_y^2} - \frac{j\pi x^2}{\lambda R_x} - \frac{j\pi y^2}{\lambda R_y} + \frac{j\phi_{0x}}{2} + \frac{j\phi_{0y}}{2}\right) \quad (2.24)$$

The beam parameters for both  $x$  and  $y$  can be retrieved using the equations below:

$$\omega_x = \omega_{0x} \left[1 + \left(\frac{\lambda z}{\pi\omega_{0x}^2}\right)^2\right]^{0.5} \quad (2.25)$$

$$\omega_y = \omega_{0y} \left[1 + \left(\frac{\lambda z}{\pi\omega_{0y}^2}\right)^2\right]^{0.5} \quad (2.26)$$

$$R_x = z + \frac{1}{z} \left(\frac{\pi\omega_{0x}^2}{\lambda}\right)^2 \quad (2.27)$$

$$R_y = z + \frac{1}{z} \left(\frac{\pi\omega_{0y}^2}{\lambda}\right)^2 \quad (2.28)$$

$$\phi_{0x} = \arctan\left(\frac{\lambda z}{\pi\omega_{0x}^2}\right) \quad (2.29)$$

$$\phi_{0y} = \arctan\left(\frac{\lambda z}{\pi\omega_{0y}^2}\right) \quad (2.30)$$

## 2.2.5 Gaussian Beam Coupling

Beam coupling is a method of comparing one beam (usually from an optical system) to one which is idealised or considered to be correct. The first beam will be an electric field distribution from GRASP denoted  $E_b$ . The second beam could be characteristic of an optical component or represent an ideal beam generated under ideal conditions, in this case a Gaussian function. This beam will be denoted  $E_a$ . Beam coupling is used to calculate the shape characteristics of the beam relative to a Gaussian function and any potential mismatch of the two. The power transfer, quality and alignment of an optical system can all be inferred from the coupling. Two beams can be considered imperfectly coupled if either their beam radii, radii of curvature, relative position or propagation axes do not match.

From Goldsmith (1998), the field coupling coefficient between  $E_a$  and  $E_b$  can be expressed as follows:

$$c_{ab} = \int \int E_a^* E_b dA \quad (2.31)$$

$E_a$  and  $E_b$  have been normalised to give unity power. Since power is of interest, the overall phase term can be ignored. This leads to:

$$c_{ab} = \int \int u_a^* u_b dA \quad (2.33)$$

This describes the field over the beam area A. Narrowing to a single dimension  $x$  for evaluation:

$$c_{ab}^{1x} = \int \int u_a^*(x) u_b(x) dx \quad (2.34)$$

With this, two dimensional field coupling can now be performed. The two dimensional field coupling coefficient is the product of two one dimensional field coupling coefficients taken at orthogonal angles:

$$c_{ab}^2 = c_{ab}^{1x} \cdot c_{ab}^{1y} \quad (2.35)$$

The power coupling coefficient can now be derived as the square of the two dimensional field coupling coefficient. This represents the fraction of the power of  $E_a$  present in  $E_b$ :

$$\mathbf{K}_{ab} = \frac{(\int E_a^* E_b)^2 dA}{\int |E_a|^2 dA \int |E_b|^2 dA} \quad (2.36)$$

For offset beams, the power coupling coefficient for two axially aligned beams must first be described:

$$\mathbf{K}_{axial} = \left| \frac{2j\lambda}{\pi\omega_a\omega_b(1/q_a^* - 1/q_b)} \right|^2 \quad (2.37)$$

From Goldsmith (1998), the power coupling coefficient of a two dimensional beam is then:

$$\mathbf{K}_{offset} = \mathbf{K}_{axial} \exp \left[ \frac{-2x_0^2(\omega_{0a}^2 + \omega_{0b}^2)}{(\omega_{0a}^2 + \omega_{0b}^2)^2 + (\lambda\Delta z/\pi)^2} \right] \quad (2.38)$$

where  $\mathbf{K}_{axial}$  is the axial power coupling coefficient,  $x_0$  is the size of the offset between  $E_a$  and  $E_b$ ,  $\omega_{0a}$  and  $\omega_{0b}$  are the beam waists of  $E_a$  and  $E_b$  and  $\Delta z$  is the distance between the two beam waists along the axis of propagation. To express this equation in terms of offset alone, the equation is modified to:

$$\mathbf{K}'_{offset} = \exp \left[ -2 \left( \frac{x_0}{\delta_{offset}} \right)^2 \right] \quad (2.39)$$

where  $\mathbf{K}'_{offset}$  is the power coupling coefficient due to offset alone and  $\delta_{offset}$  is the lateral offset distance that would reduce coupling amplitude by a factor of  $e$ . Its value is determined by:

$$\delta_{offset} = \left[ \frac{(\omega_{0a}^2 + \omega_{0b}^2)^2 + (\lambda\Delta z/\pi)^2}{(\omega_{0a}^2 + \omega_{0b}^2)} \right]^{0.5} \quad (2.40)$$

This can be simplified if the two beam waists from  $E_a$  and  $E_b$  are coincident:

$$\delta_{offset} = (\omega_{0a}^2 + \omega_{0b}^2)^{0.5} \quad (2.41)$$

For tilted beams, the power coupling coefficient is given by Goldsmith (1998):

$$\mathbf{K}'_{tilt} = exp \left[ \frac{-(2\pi^2\theta^2/\lambda^2)(1/\omega_a^2 + 1/\omega_b^2)}{(1/\omega_a^2 + 1/\omega_b^2) + (\pi/\lambda)^2(1/R_b - 1/R_a)^2} \right] \quad (2.42)$$

where  $\theta$  is the angle of tilt in the  $xz$  plane between beams  $E_a$  and  $E_b$ ,  $\omega_a$  and  $\omega_b$  are the beam radii of  $E_a$  and  $E_b$  and  $R_a$  and  $R_b$  are the radius of curvature for  $E_a$  and  $E_b$  at  $\omega_a$  and  $\omega_b$ . As with the offset beams, this equation can be expressed in terms of tilt alone:

$$\mathbf{K}'_{tilt} = exp \left[ -2 \left( \frac{\theta}{\theta_t} \right)^2 \right] \quad (2.43)$$

where  $\theta_t$  is the tilt which would reduce the coupling amplitude by a factor of  $e$  (similar in function to  $\delta_{offset}$ ). Its value is determined by:

$$\theta_t = \frac{\lambda}{\pi} exp \left[ \frac{(1/\omega_a^2 + 1/\omega_b^2) + (\pi/\lambda)^2(1/R_b - 1/R_a)^2}{(1/\omega_a^2 + 1/\omega_b^2)} \right] \quad (2.44)$$

This expression also has a case for the tilt at the co-located beam waists of  $E_a$  and  $E_b$ :

$$\theta_{twaiast} = \frac{\lambda}{\pi} (1/\omega_{0a}^2 + 1/\omega_{0b}^2)^{0.5} \quad (2.45)$$

## 2.3 Physical Optics and Physical Theory of Diffraction

Physical optics (PO) is an approximation whereby an incident electric field induces currents on the surface of a mirror or lens. Those induced currents then inform the electric field that will be transmitted by that mirror or lens. According to Pontoppidan (2015), two assumptions are made in physical optics calculations. The first is that the surface where currents are being induced is assumed to be a perfect conductor. The second is that the current induced on that perfectly conducting surface is assumed to be the same as that which would be induced

on a planar surface which is infinite in extent and tangent to the surface at the point at which the total electric field is calculated. The incident and scattered field are related through the following equation found in Pontoppidan (2015):

$$\mathbf{E}_{PO} = \mathbf{E}_{incident} + \mathbf{E}_{scattered} \quad (2.46)$$

where  $\mathbf{E}_{PO}$  is the total electric field,  $\mathbf{E}_{incident}$  is the field incident on the surface and  $\mathbf{E}_{scattered}$  is the field scattered by that surface.

The Physical Theory of Diffraction (PTD) is required to account for the field at the edge of a surface. Regular PO cannot be used at an edge as the induced currents are assumed to be the same as those for an infinite planar surface. The PTD edge currents are calculated using an approximation based on a perfectly conducting infinite half plane, based on work from Johansen (1996). They can be considered a correction to any existing PO currents. Thus the full scattered field can be obtained via:

$$\mathbf{E}_{scattered} = \mathbf{E}_{PO} + \mathbf{E}_{PTD} \quad (2.47)$$

## 2.4 GRASP Overview

The Generalised Reflector Antenna Software Package (GRASP) is an optical analysis and modelling program developed by Copenhagen-based company TICRA. It can implement Geometrical Optics/Geometrical Theory of Diffraction, Physical Optics/Physical Theory of Diffraction and Method of Moments solutions to analyse an optical system. It is primarily focussed on testing reflector antennae systems but can simulate lenses with additional add-on packages. In GRASP, mirrors are treated as reflector objects with multiple properties that are positioned in a 3D environment. The main parts that will be covered in this chapter will

be geometrical objects (which construct the optical components) and electrical objects (which are used in calculations). PO calculations alone will be discussed as GO, GTD and MoM were not used. Figure 2.3 displays the user interface of GRASP.

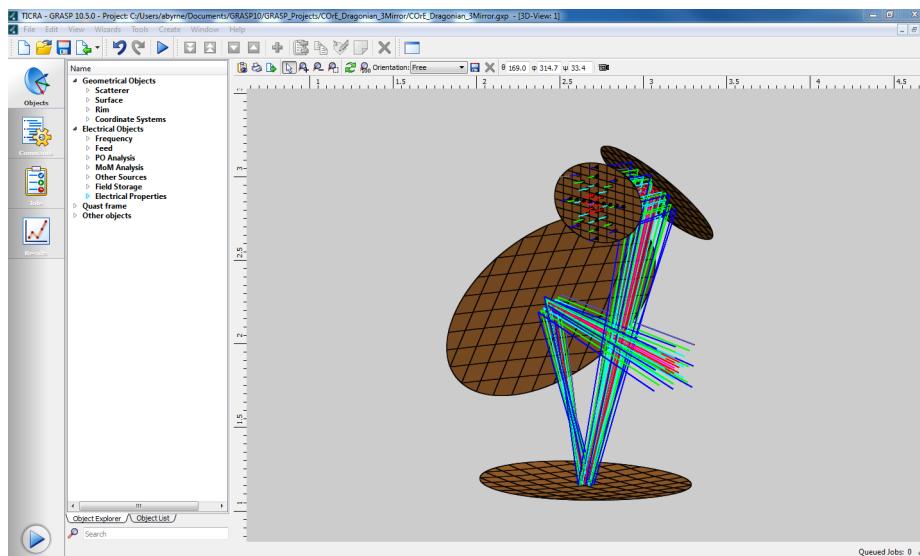


Figure 2.3: The GRASP User Interface. The menu on the far left allows the user to switch between the model, commands and PO results.

## 2.4.1 Geometrical Objects

A reflector object requires many components to function. The process of creating one of these objects will be discussed, hopefully illustrating the different object types in GRASP and their functionality. Reflectors need a minimum of three components to be defined in the GRASP environment: A surface object, a rim object and a coordinate system object. The surface defines the mathematical surface description or profile of the mirror while the rim object defines the area of the finite part of the mirror (surface edges are included for diffraction calculations). Put simply, the surface defines the shape of the mirror and the rim defines the usable part of that surface, much like a cookie cutter or a hole punch. The coordinate system controls how the mirror is placed and oriented in the 3D environment.

## 2.4.2 Surface and Rim Definitions

The user has a large choice of surface object. The three classic conic surfaces (parabola, ellipse and hyperbola) are available for use along with a general precursor class called “Conic Mirror Surface” which can represent all three surfaces.

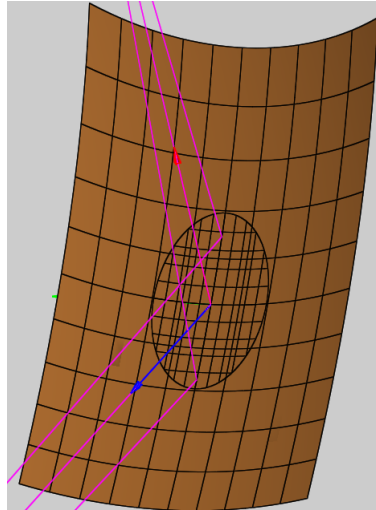


Figure 2.4: A surface in GRASP showing the full defined surface and the mirror area enclosed by the rim.

The parabola class requires two quantities: The focal length of the parabola and the vertex location with respect to the reference coordinate system of the parabola. Ellipsoids and hyperboloids both require a vertex and foci distance, which are the major axis and interfocal distance. The ellipsoid requires an additional quantity: the axis angle. This is the angle which the ellipse will need to be rotated in order for the correct part of the surface to be used. These objects will be discussed in greater detail in **Chapter 5**. In addition to the conic surfaces, there is also a planar surface and other common surface definitions like spherical surfaces and second-order polynomial definitions. A tabulated surface composed of a regular/irregular grid of points can also be used. **Chapter 4** is dedicated to this type of surface as they were crucial to the work undertaken for *CORE* and *LLAMA*.

The rim object can take the form of a 2D shape in broad categorisation, from elliptical and triangular to rectangular. A polynomial definition for the edge can be used. Should the user possess the mirror rim defined in grid form, that can be used as well. Figure 2.4 portrays the surface and rim object together.

### 2.4.3 Coordinate Systems

Coordinate systems are a key component of any reflector system. The placement and orientation of a reflector is determined by its coordinate system object. There is no inherent reference frame in GRASP; the user must instead create their own global coordinate system to serve as a base for the others. The global coordinate system is simply one which lacks a base coordinate system:

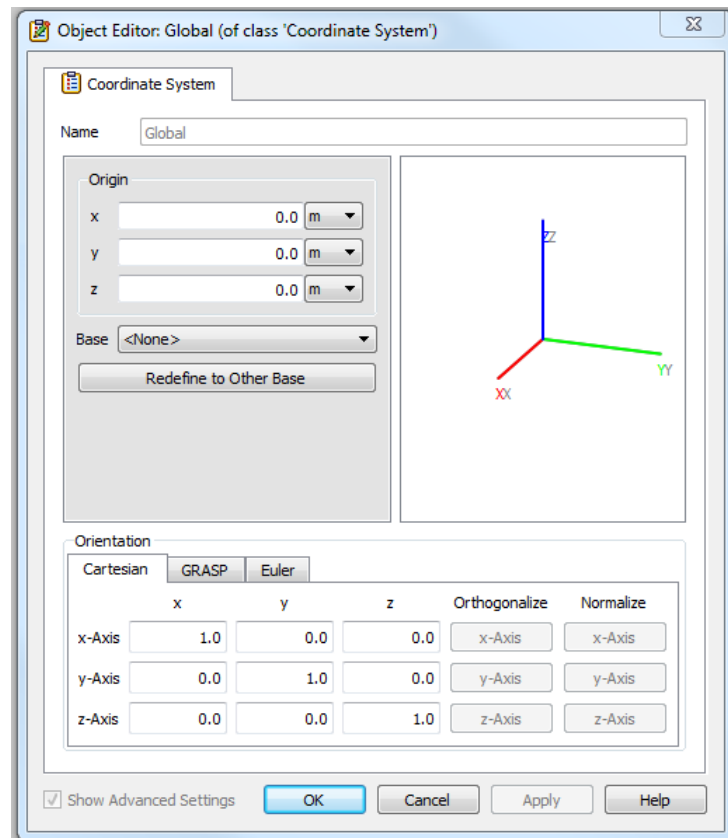


Figure 2.5: A global coordinate system in-editor. A coordinate system with a base of <None> will always be a global coordinate system.

Looking to Figure 2.5, the origin section controls the placement of the coordinate system in reference to its base. The unit for each translation can be adjusted. The base coordinate system can be selected from a drop-down list of existing coordinate systems. The coordinate system can also be translated to a different base coordinate system, adjusting the origin and orientation values to reflect the new base. This will not change the coordinate systems actual location, however. This can be done simply by selecting a new base from the drop-down list.

The placement of the coordinate system occurs before the coordinate system is oriented. There are three available methods by which a coordinate system is oriented: Cartesian, Euler and GRASP.

The screenshot shows a window titled "Orientation" with three tabs: "Cartesian", "GRASP", and "Euler". The "Cartesian" tab is selected. Below the tabs, there are columns for "x", "y", and "z" components, and two columns for "Orthogonalize" and "Normalize" actions. The data is as follows:

	x	y	z	Orthogonalize	Normalize
x-Axis	-0.20421727	-0.88973254	-0.40825399	x-Axis	x-Axis
y-Axis	0.97845091	-0.17253466	-0.11342664	y-Axis	y-Axis
z-Axis	0.030481414	-0.42262016	0.90579417	z-Axis	z-Axis

Figure 2.6: Editor window showing the normalised  $x, y$  and  $z$  components of the  $x, y$  and  $z$  axes of a coordinate system.

Figure 2.6 displays the Cartesian orientation system. Orientation is achieved in this mode via an Euler  $ZY'Z''$  rotation matrix, whose resultant form  $R$  form is:

$$\begin{pmatrix} \cos \theta \cos \phi \cos \psi - \sin \theta \sin \psi & -\cos \psi \sin \theta - \cos \theta \cos \phi \cos \psi & \cos \theta \sin \phi \\ \cos \theta \sin \psi + \cos \phi \cos \psi \sin \theta & \cos \theta \cos \psi - \cos \phi \sin \theta \sin \psi & \sin \theta \sin \phi \\ -\cos \psi \sin \phi & \sin \phi \sin \phi & \cos \phi \end{pmatrix} \quad (2.48)$$

where  $\theta$ ,  $\phi$  and  $\psi$  are the classic elemental Euler rotations of  $\alpha$ ,  $\beta$  and  $\gamma$ . The name “Cartesian” derives from the fact that the components by row of the

rotation matrix form points for the  $x$ ,  $y$  and  $z$  axes of the coordinate system. There are options to orthogonalise one or two axes of a coordinate system when one axis is known; for example, if a user is orienting a coordinate system  $z$  axis using a normalised vector, then the  $x$  and  $y$  axes can be orthogonalised to create a functional coordinate system. An axis of the coordinate system can be also be normalised in GRASP, a quality of life feature that can help when batch-producing coordinate systems that are aligned with vectors.

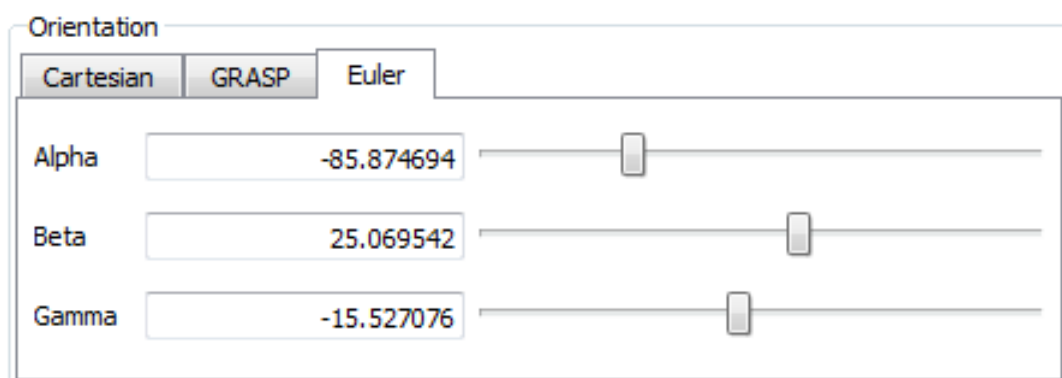


Figure 2.7: A coordinate system in-editor displaying a rotation defined by Euler angles.

Figure 2.7 displays the Euler angles tab. This mode allows the coordinate system to be oriented using classic Euler rotation angles of  $\phi/\alpha$ ,  $\theta/\beta$  and  $\psi/\gamma$ . Any orientation can be achieved using a composition of these three rotations. As mentioned previously, the method of rotation is an Euler  $ZY'Z''$  rotation. First, the system is rotated about the  $z$  axis by  $\phi$ . The new rotated axes are denoted  $x'$ ,  $y'$  and  $z'$ . Next, the system is rotated about the  $y'$  axis by  $\theta$ . The doubly rotated axes are now denoted  $x''$ ,  $y''$  and  $z''$ . Finally, the system is rotated about the new  $z''$  axis by  $\psi$ . Needless to say, this method is tied closely to the previous Cartesian mode. The rotation can be described using Euler rotation matrices:

$$Y = \begin{pmatrix} \cos \theta & 0 & \sin \theta \\ 0 & 1 & 0 \\ \sin \theta & 0 & \cos \theta \end{pmatrix} \quad (2.49)$$

$$Z = \begin{pmatrix} \cos \phi & -\sin \phi & 0 \\ \sin \phi & \cos \phi & 0 \\ 0 & 0 & 1 \end{pmatrix} \quad (2.50)$$

Matrix multiplication is done in the reverse order with respect to the rotations. For GRASP, the resulting matrix will have the form presented in Equation 2.48. The Euler angles can be extracted from this matrix with the following relations:

$$\theta = \arctan(\cos \phi) \quad (2.51)$$

$$\phi = \arctan \left( \frac{\sin \phi \sin \psi}{-\cos \psi \sin \phi} \right) \quad (2.52)$$

$$\psi = \arctan \left( \frac{\sin \phi \sin \psi}{\cos \phi} \right) \quad (2.53)$$

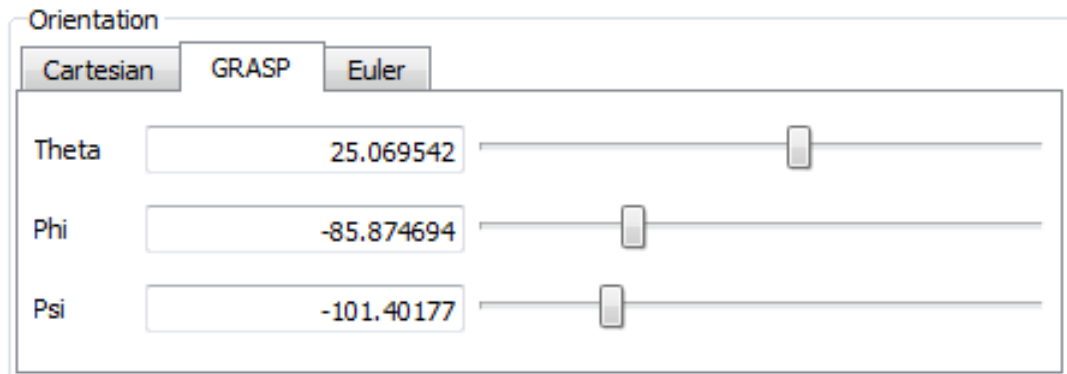


Figure 2.8: A coordinate system in-editor showing a rotation formed via a combination of GRASP angles. There will be value overlap between these angles and the Euler angles.

Figure 2.8 shows the GRASP angle orientation tab. GRASP contains a proprietary rotation which the user can avail of. Unlike the previous modes, this

one preserves the orthogonality of the  $xyz$  unit vectors. The three associated rotations are  $\theta$ ,  $\phi$  and  $\psi$ . First, the  $x$  and  $z$  axes are rotated by  $\theta$  about the  $y$  axis of the coordinate system. The angle  $\phi$  is used to tilt the  $xy$  plane along which the  $x$  and  $z$  axes move. This combination give the partially rotated  $x'y'z'$  coordinate system. To complete the rotation, the system is then rotated about the new  $z'$  axis by  $\psi$ . This rotation is useful when defining the pointing of a feed.  $\theta$  and  $\phi$  determine the direction the feed points and  $\psi$  controls the polarisation direction of the feed. The reader may notice similarities between Figures 2.7 and 2.8. The GRASP angle  $\theta$  is the equivalent of the Euler angle  $\beta$  and the angle  $\phi$  is the equivalent of  $\alpha$ . However, the angles  $\psi$  and  $\gamma$  are not directly related to each other, instead one can translate between the two given  $\gamma = \psi - \phi$  and  $\psi = \gamma + \alpha$ .

With all the components in place, the creation of a reflector object is quite straightforward. Figure 2.9 displays the object editor for a reflector object:

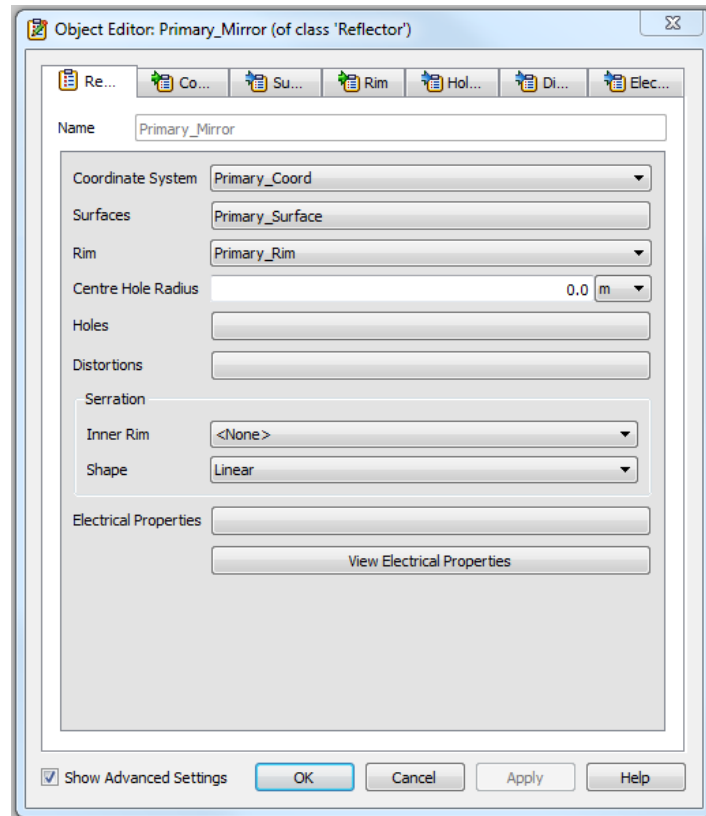


Figure 2.9: Primary Mirror Object Editor. The constituent objects can also be accessed from this window.

The surface, rim and coordinate system are incorporated at the top. There exists the possibility to create a centre hole in the reflector, such as would be required with any on-axis telescope. A file containing surface distortions can be included. Serrated mirrors can be created in this editor given that PO analysis must be altered for these mirror types. Finally, the electrical properties of the reflector can be set. This is necessary for half-silvered mirrors, polarising grids, wire-mesh reflectors and many more. Once the basic criteria have been met for creation, the reflector will be added to the system display over to the right.

#### 2.4.4 Electrical Objects

Electrical objects in GRASP are those concerned with the functioning of PO calculations. There are a number of useful classes under covered by this category, allowing a model to become more complex by customising the electrical properties of reflectors or allowing analysis of mechanical struts. Objects required to use the alternative calculation methods of Geometric Theory of Diffraction (GTD) and Method of Moments (MoM) may be found here. However, all analysis in this thesis was done using PO. The three required components to carry out PO analysis in GRASP are 1) feeds, 2) field storage and 3) PO analysis objects. Like with reflectors, there are objects that must be implemented before these components can be realised.

#### 2.4.5 Feeds

Feeds are sources of radiation that are used as a starting point in PO analysis. In GRASP, these feeds can be planar antennae, horn antennae and Gaussian beam radiation patterns. Discussion will focus on the latter source as neither of the other two were used extensively. Gaussian patterns can be generated using either a beam waist  $\omega_0$  value or a combination of beam radius  $\omega_x$  and radius of curvature  $R_x$ . This method assumes there is no inherent aberration at the source location.

Taper angles can also be used to construct a pattern, but these were not used.

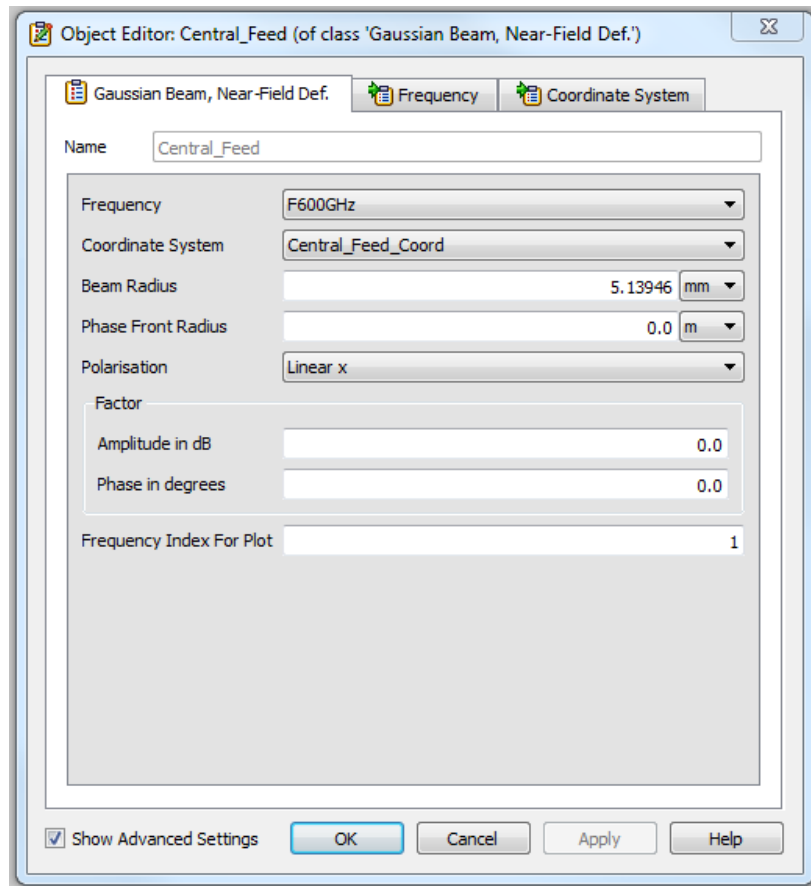


Figure 2.10: Near-Field Definition Gaussian Beam editor. A beam of waist 5.13946 mm will be propagated along the  $z$ -axis of “Central Feed Coord”. The tab selectors at the top of the window allow frequency and coordinate system objects to be accessed from here.

Figure 2.10 shows the editor window for a near-field definition type of feed pattern. The operational frequency is taken in as a separate object, and is simply a list of frequency values in gradations of Hz. Having a phase front radius of 0 m indicates a special case where the beam is originating from a waist location. Beam radius here is the beam waist radius  $\omega_0$  and the radius of curvature  $R$  is infinite (i.e. planar). Non-zero values for this entry will represent a propagating beam with a certain beam radius  $\omega$  and radius of curvature  $R$ . The polarisation be set to Linear X, Linear Y, Right-Hand Circular and Left-Hand Circular. The feed is a physical object in GRASP and must possess a coordinate system. The

axis of propagation is  $z$ -axis by default. Figure 2.11 shows a feed in GRASP.

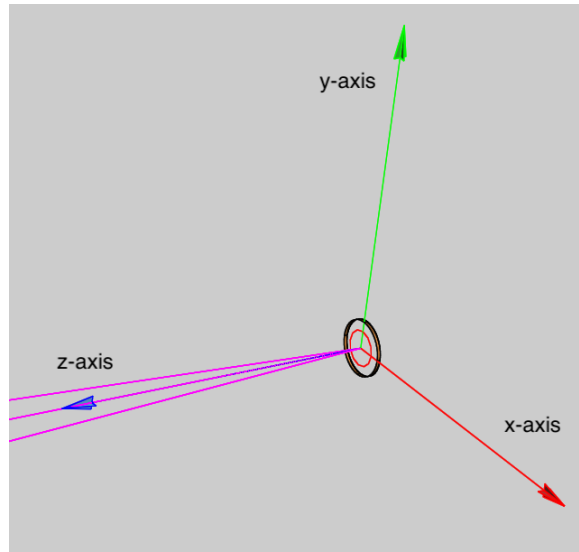


Figure 2.11: A near field Gaussian beam source propagating along the  $z$ -axis of the base coordinate system of the source.

## 2.4.6 Field Storage

Field storage refers to any method which records the power distribution of an incident Gaussian beam. Functionally, they represent a plane where a beam profile is examined. The two field output options that will be discussed are cuts and grids. Cuts are one dimensional field storage objects. They can be planar, circular or cylindrical. As they are 1D objects, they record “cuts” through the incident beam. They require a range in appropriate units for the type of cut: mm for planar, degrees for spherical and both for cylindrical. The sampling is also specified by the user via a set number of points along the range of the cut where the field is evaluated. A range of angles can also be set for a number of cuts in different directions. Grids are two dimensional field storage objects which capture the power of a beam over an spherical surface area projected on a plane. Like cuts, they can be planar, spherical and cylindrical, with units and sampling working the same. These objects can record either the  $\mathbf{E}$  or  $\mathbf{B}$  field components. Both will capture the co-polar and cross-polar beam components. Like with detectors, each

object must specify which type of polarisation it is receptive to. For spherical field storage, the user must choose whether the near or far field beam will be measured. Finally, a file-path must be provided where the recorded data will be stored. Figure 2.12 shows the object editor for spherical grids:

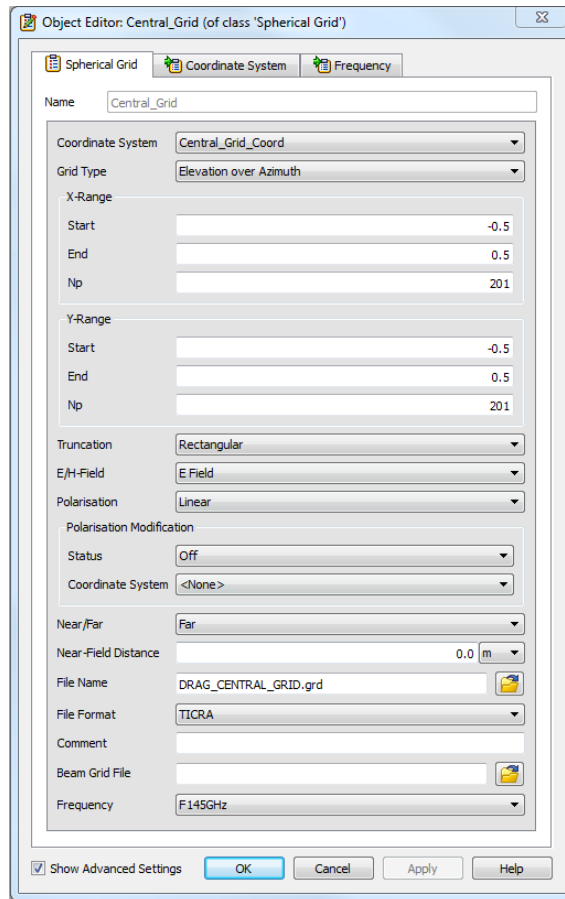


Figure 2.12: The object editor for a spherical grid. This will be the most commonly used field storage object alongside planar grids.

### 2.4.7 PO Analysis Objects

The last component to discuss are PO analysis objects. As the name suggests, these objects are used in GRASP's PO/PTD calculations. They are used to store the currents induced on a reflectors surface (as well as at the edge). The two which will be encountered in this thesis are single and multi-face scatterer PO objects. In essence, the first treats a reflector as a solid object where currents are analysed across the whole face at once. *CORE*'s three mirrors are an example

of reflectors treated as single-face. The second object is used where a reflector is composed of multiple smaller faces. *CORE*'s thermal shielding and baffling are examples of this. While the second method is more advanced and versatile than the former, it pays for this in calculation time and memory requirements. Currents must be evaluated at each face comprising the reflector: the more faces there are, the larger the calculation.

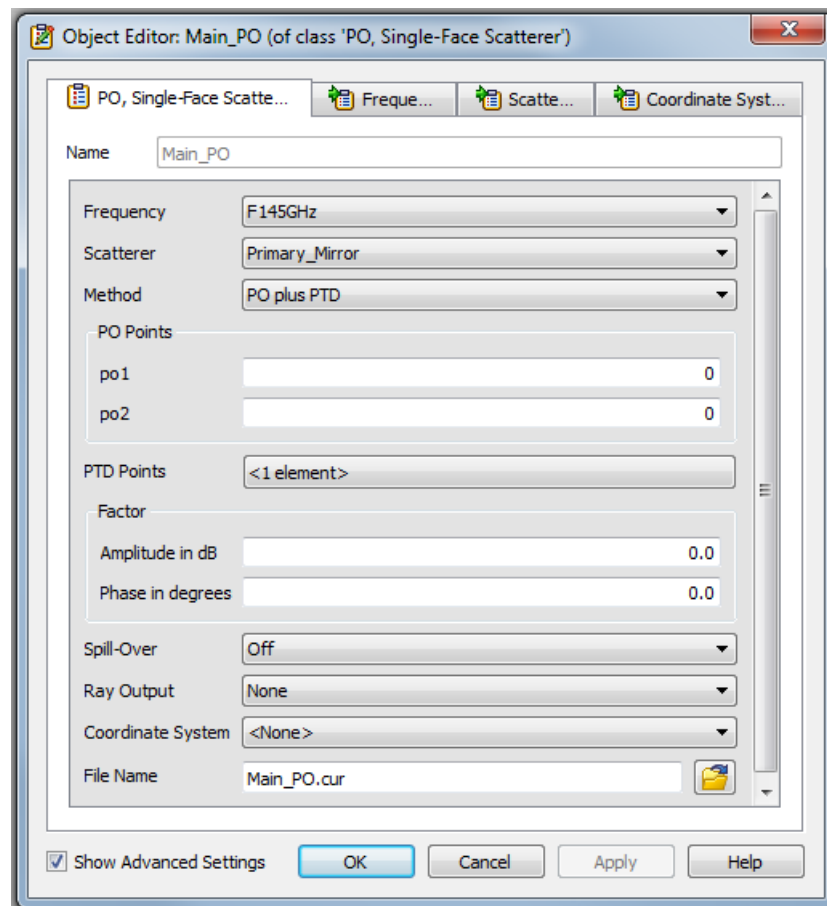


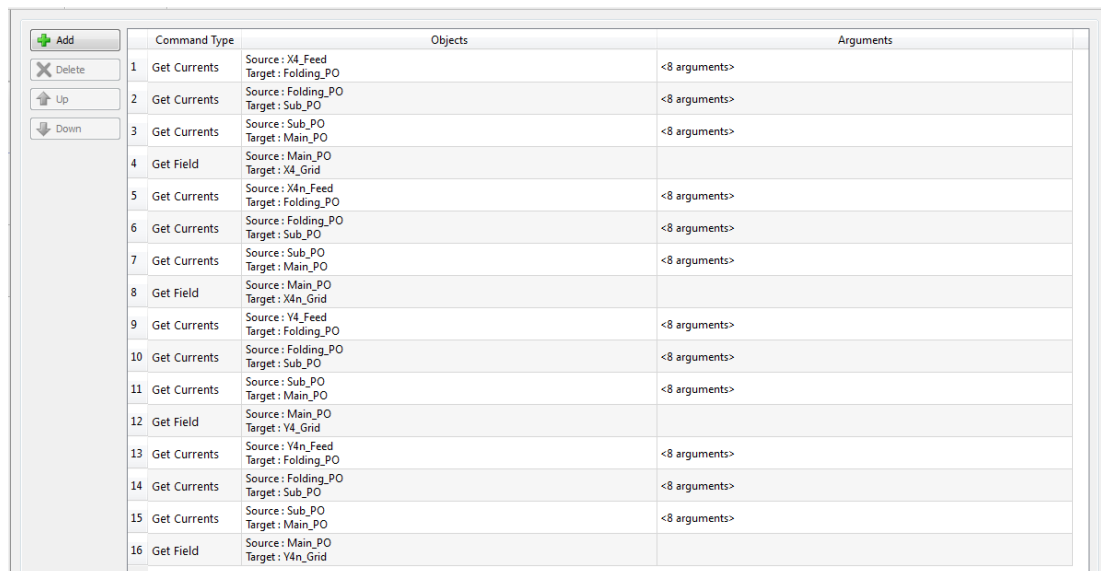
Figure 2.13: The object editor for single-face scatterer PO objects.

Figure 2.13 shows the editor window for single-face scatterer PO objects. PO analysis objects require first and foremost: a reflector. They attach themselves to the specified reflector but can also be positioned with a coordinate system. The method determines whether PO, PTD or PO+PTD will be used in calculations incorporating the object. The number of PO and PTD points can be manually set, or automatically worked out by GRASP by leaving default values in place.

Finally, a frequency must be specified for these objects. As they record currents induced at a reflector, once implemented, PO analysis objects can store these currents for later use.

## 2.4.8 Commands

Once the necessary model is in place, GRASP can carry out calculations via user commands. These commands are managed by the commands window, seen in Figure 2.14.



	Command Type	Objects	Arguments
1	Get Currents	Source: X4_Feed Target: Folding_PO	<8 arguments>
2	Get Currents	Source: Folding_PO Target: Sub_PO	<8 arguments>
3	Get Currents	Source: Sub_PO Target: Main_PO	<8 arguments>
4	Get Field	Source: Main_PO Target: X4_Grid	
5	Get Currents	Source: X4n_Feed Target: Folding_PO	<8 arguments>
6	Get Currents	Source: Folding_PO Target: Sub_PO	<8 arguments>
7	Get Currents	Source: Sub_PO Target: Main_PO	<8 arguments>
8	Get Field	Source: Main_PO Target: X4n_Grid	
9	Get Currents	Source: Y4_Feed Target: Folding_PO	<8 arguments>
10	Get Currents	Source: Folding_PO Target: Sub_PO	<8 arguments>
11	Get Currents	Source: Sub_PO Target: Main_PO	<8 arguments>
12	Get Field	Source: Main_PO Target: Y4_Grid	
13	Get Currents	Source: Y4n_Feed Target: Folding_PO	<8 arguments>
14	Get Currents	Source: Folding_PO Target: Sub_PO	<8 arguments>
15	Get Currents	Source: Sub_PO Target: Main_PO	<8 arguments>
16	Get Field	Source: Main_PO Target: Y4n_Grid	

Figure 2.14: The Commands Window in GRASP. Commands are executed in the order they appear on the list.

The necessary commands to carry out PO analysis are “Get Currents”, which calculates induced currents on a reflector, and “Get Field”, which is used to record the beam with field storage objects. “Get Currents” is a simple command that requires a feed and PO Analysis object. Currents are generated in a chain-like fashion, mirroring the propagation of a real beam through an optical system. The field that is calculated must also converge on the next reflector in the chain. For example, when currents are calculated for *CORE*’s folding mirror via the focal plane feeds, they must converge on the secondary mirror. The field accuracy is

used to select the accuracy of the calculations. The PO integration can be said to be converged when a small increase or decrease in sampling causes a change that is less than the field accuracy. By default this value is -80 dB but calculations presented in this thesis typically used a value of -120 dB.

The “Get Field” command retrieves the currents stored in a PO Analysis object and computes the field by integrating those currents. The target object is a field storage object, which contains the parameters for the field to be calculated. Figure 2.15 shows the final product of a calculation:

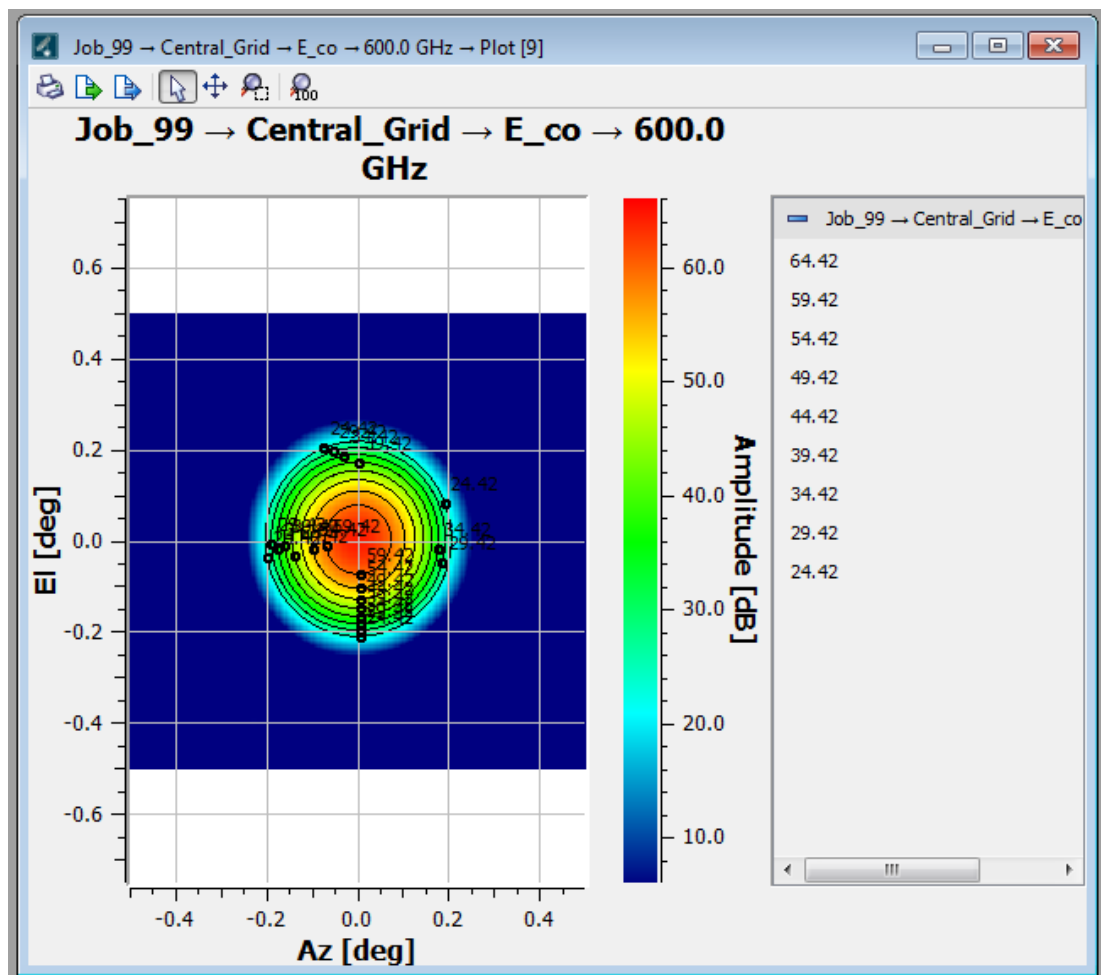


Figure 2.15: Spherical grid output containing a field calculated via PO. Contours have been fitted by GRASP in this file viewer.

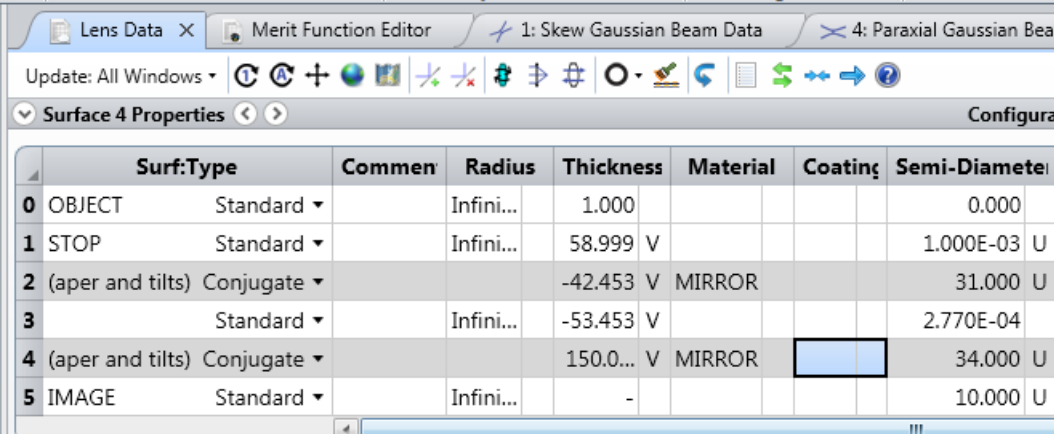
GRASP calculations are always recorded in output files. These files list the internal processes and hidden number-crunching that GRASP runs through when

carrying out a calculation and is essentially a long form version of the screen output shown to the user. Given this fact, they can be a valuable resource should one wish to understand how a calculation is being performed in greater detail.

## 2.5 Zemax OpticStudio and Mirror Optimisation

### 2.5.1 Overview of OpticStudio

Zemax OpticStudio is a ray-tracing and geometrical optics analysis program. It is primarily designed for the testing of lenses, but can also simulate mirrors. OpticStudio can operate in two modes: Sequential Mode and Non-Sequential Mode. The choice of mode determines the type of propagation of rays through an optical system. Sequential mode has rays propagate from optical surface to optical surface from a source down to an output grid. It is capable of paraxial Gaussian beam analysis as well. Surfaces are created using the Lens Data Editor, seen in Figure 2.16:



Surf	Type	Comment	Radius	Thickness	Material	Coating	Semi-Diameter
0	OBJECT	Standard	Infini...	1.000			0.000
1	STOP	Standard	Infini...	58.999 V			1.000E-03 U
2	(aper and tilts)	Conjugate		-42.453 V	MIRROR		31.000 U
3		Standard	Infini...	-53.453 V			2.770E-04
4	(aper and tilts)	Conjugate		150.0... V	MIRROR		34.000 U
5	IMAGE	Standard	Infini...	-			10.000 U

Figure 2.16: The Lens Data Editor of OpticStudio.

Figure 2.16 shows the Lens Data Editor. In this case, rays will propagate from Object 0 through to Object 5 sequentially. Object 0 is always the entrance pupil,

Object 1 is typically the aperture stop and the last surface is the image plane. The surface type attribute determines how the surface will be defined. Radius refers to the radius of curvature of the surface. Thickness is an important attribute. For paraxial lenses, thickness is just the spacing between each lens and optical element. For non-paraxial lenses, thickness defines the distance from the widest part of the lens to the centre of the lens, not the thickness of the lens as might be assumed. Two surfaces are required to define a thick lens; one each to represent the two sides of the lens. For mirrors, thickness is the distance from the previous surface to the point where the centre ray strikes the mirror. Material and coatings can be applied to a surface. OpticStudio has a large built-in catalogue of glass types and coatings for lens design, while MIRROR is a special type of material used to model mirrors by altering the propagation behaviour of the rays. Finally, semi-diameter defines the radius of each object. A 3D plot of the optical system can be created (solid or wireframe) and an example can be seen in Figure 2.17 below:

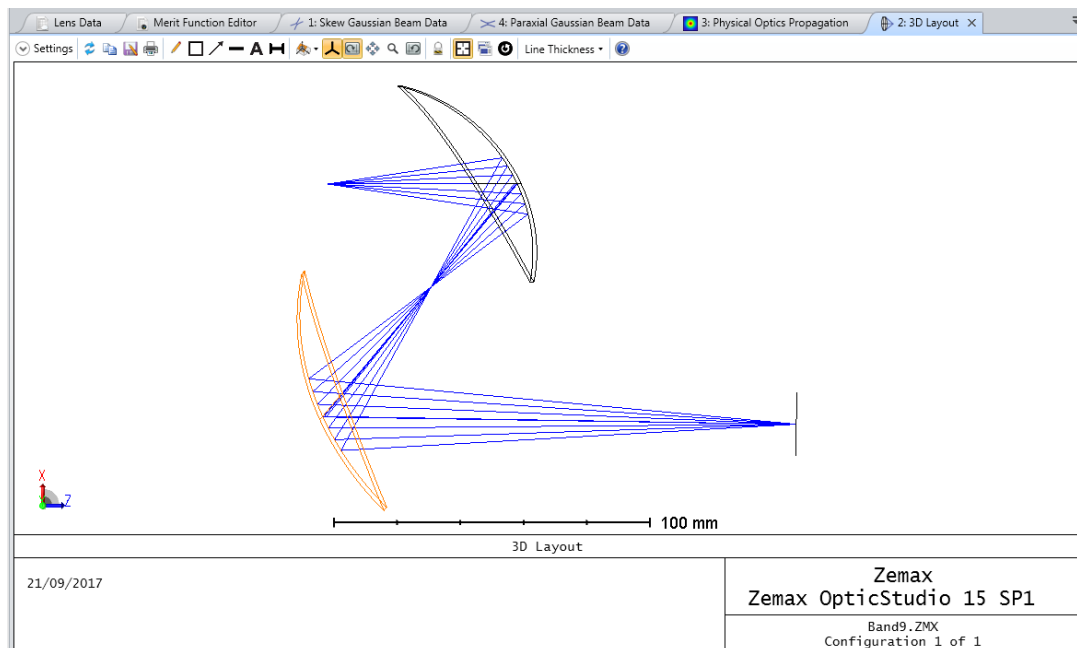


Figure 2.17: A plot of the ALMA Band 9 Receiver in OpticStudio. Both 2D and 3D plots are available.

Non-Sequential Mode has rays propagate from an entrance slit through the optical system, passing through an reflecting off objects as they are encountered, not as they are listed. The Lens Data Editor is now the Non-Sequential Component Editor, seen in Figure 2.18:



Object Type	Comment	Ref Objec	Inside O	X Positor	Y Positor	Z Positor	Tilt About >	Tilt About \	Tilt About z	Material
1 Tab. Faceted Radial	ZONE3.TOB	0	0	-32.000	0.000	-15.000	5.000	0.000	0.000	MIRR...
2 Standard Surface		1	0	0.000	0.000	3.000	0.000	0.000	0.000	MIRR...
3 Source Filament		1	0	0.000	0.000	5.000	0.000	0.000	0.000	-
4 Tab. Faceted Radial	ZONE3.TOB	0	0	0.000	5.000	-15.000	12.000	0.000	0.000	MIRR...
5 Standard Surface		4	0	0.000	0.000	3.000	0.000	0.000	0.000	MIRR...
6 Source Filament		4	0	0.000	0.000	5.000	0.000	0.000	0.000	-
7 Tab. Faceted Radial	ZONE3.TOB	0	0	32.000	0.000	-15.000	5.000	0.000	0.000	MIRR...
8 Standard Surface		7	0	0.000	0.000	3.000	0.000	0.000	0.000	MIRR...
9 Source Filament		7	0	0.000	0.000	5.000	0.000	0.000	0.000	-
10 Detector Rectangle		0	0	0.000	-16.000	50.000	90.000	0.000	0.000	ABSO...
11 Detector Rectangle		0	0	48.000	0.000	50.000	0.000	90.000	0.000	ABSO...
12 Detector Rectangle		0	0	0.000	0.000	100.0...	0.000	0.000	0.000	ABSO...

Figure 2.18: The Non-Sequential Component Editor.

The form of this editor is similar to the previous one. Objects are no longer positioned according to thickness, but rather placed in a 3D Cartesian space. Tilts about the  $xyz$  axes of an object is also possible. Material can be chosen as before. Radius is now used in place of semi-diameter. Object types are different from the lens data editor due to the different nature of each mode. This mode of OpticStudio can only produce solid 3D plots (see Figure 2.19):

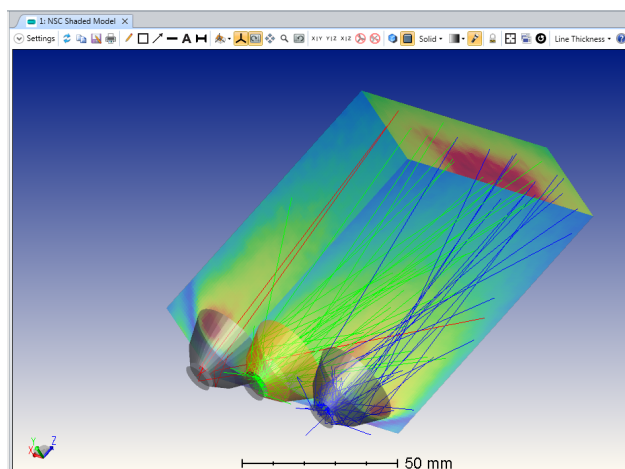


Figure 2.19: A plot of a sample non-sequential illumination system in OpticStudio. Only 3D plots are available in this mode.

Sequential mode is used primarily for the work described in this thesis. Non-sequential mode was only used when CAD files containing mirror objects needed testing. In addition to modelling lenses and mirrors, OpticStudio comes with built-in analysis and tolerancing tools. A large database of articles and examples, The Zemax Knowledgebase ([www.zemax.com/os/resources/learn/knowledgebase](http://www.zemax.com/os/resources/learn/knowledgebase)), complements a well fleshed out user manual. A unique feature of the program are its powerful optimisation tools.

## 2.5.2 Optimisation



Figure 2.20: The optimisation tab in OpticStudio.

The optimisation feature allows various parameters of a lens system (or a mirror system) to be altered in order to achieve some user-defined goal for the system, such as a beam waist at the focal plane of a specific size. It can operate in two modes: Local and Global. Global optimisation uses an algorithm to effectively design a number of optical systems to suit pre-defined specifications. In many ways this can be considered to produce the best possible optimisation to a user's request. That said, its use is not recommended for novice users due to long computation times and the non-interactive nature of this mode. This fact made the global mode unsuitable for our purposes and so it will not be discussed further. Local optimisation works instead by adjusting specific parameters of an existing optical system. The optimisation tab is shown above in Figure 2.20.

The optimiser works by using operands. An operand is a single command used by OpticStudio to perform a calculation or carry out a function. OpticStudio uses these operands to compute a wide range of specific properties, from beam radius

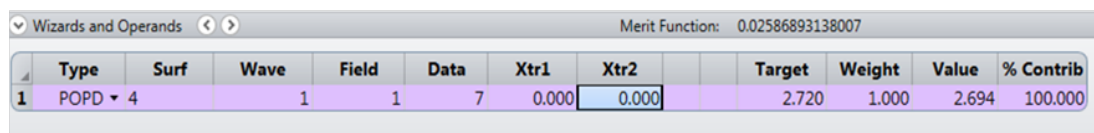
of curvature to surface sag. By adjusting aspects of a mirror system and recomputing parameters (via the operands), OpticStudio can incrementally reconfigure that system to achieve the user's desired goal. OpticStudio can only manipulate properties in the Lens Data Editor that have their solve type set to "Variable". Some operands available for use are listed below with a brief description as to their purpose:

- **POPD**: Physical Optics Propagation Data. Calculates a multitude of different physical optics properties, including Gaussian beam waists, radii of curvature and beam total power.
- **GBPW**: Gaussian Beam Paraxial Waist. Calculates the size of a Gaussian beam waist following a chosen surface.
- **GBPP**: Gaussian Beam Paraxial Position. Calculates the position of a paraxial Gaussian beam waist following a chosen surface.
- **GBPD**: Gaussian Beam Paraxial Divergence. Calculates the divergence of a paraxial Gaussian beam following a chosen surface.
- **GBSW**: Gaussian Beam Skew Waist. Calculates the size of the waist of a skewed Gaussian beam following a chosen surface.
- **GBSP**: Gaussian Beam Skew Position. Calculates the position of a skewed Gaussian beam waist following a chosen surface.
- **OPDX**: Optical Path Difference. Calculates the optical path difference between a chosen wave and the mean OPD.
- **DISG**: Generalised Distortion operand. Calculates wavefront distortion as a percentage.
- **CVGT, CVLT, CVVA**: Constrains curvature of a surface to be greater than, less than or equal to a certain value.

- **EFFL**: Calculates effective focal length of the optical system.
- **EFNO**: Calculates F/# number of a system.

The most relevant operands to the work carried out would be POPD, GBPW and GBPP. The skew operands were also looked into as alternative to the paraxial operands.

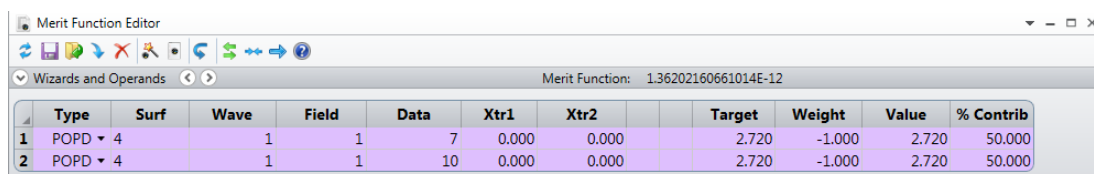
The representation of the user’s goal for a system is known as the Merit Function. Optimisation proceeds based on finding the local or global minimum of that Merit Function. Note that an infeasible design cannot be magically fixed by use of the optimiser; the design must be valid beforehand for the best results. Additionally, the user must have a clear set of quantifiable goals in mind when optimising their design, “a better PSF” simply will not do. The Merit Function is composed of operands, such as those above, chosen by the user. OpticStudio’s Merit Function Editor can be seen below:



The screenshot shows the Merit Function Editor window with the title bar 'Wizards and Operands' and 'Merit Function: 0.02586893138007'. The table below represents the data shown in the window:

	Type	Surf	Wave	Field	Data	Xtr1	Xtr2	Target	Weight	Value	% Contrib
1	POPD ▾ 4		1	1	7	0.000	0.000	2.720	1.000	2.694	100.000

Figure 2.21: Merit Function Editor showing an active operand.



The screenshot shows the Merit Function Editor window with the title bar 'Merit Function Editor' and 'Merit Function: 1.36202160661014E-12'. The table below represents the data shown in the window:

	Type	Surf	Wave	Field	Data	Xtr1	Xtr2	Target	Weight	Value	% Contrib
1	POPD ▾ 4		1	1	7	0.000	0.000	2.720	-1.000	2.720	50.000
2	POPD ▾ 4		1	1	10	0.000	0.000	2.720	-1.000	2.720	50.000

Figure 2.22: Merit Function Editor showing two active operands.

The left-hand columns of both Figures 2.21 and 2.22 are used to configure each operand. The type column holds the user’s choice of operand. The “Surf” column selects which surface will be targeted for optimisation. Wave and Field allow selection of wavelengths which in turn affect some of the values in the

“Value” column. “Data” is used in multi-faceted operands to select which value the operand can compute will be selected for optimisation. Finally, “Xtr1” and “Xtr2” are extra columns which hold ancillary information required by some operands to function.

Turning to the columns on the right of Figures 2.21 and 2.22, the value and target columns contain the current value of the selected operand and the value the user wishes for that operand respectively. The percent contribution column denotes how much of the value of the Merit Function is due to that operand. A large discrepancy between value and target will increase the percent contribution for an operand. Weighting will also increase the percent contribution, but has other important functions as well and so will be discussed in the next paragraph. The value of the Merit Function is given by the Equation 2.54:

$$MF^2 = \frac{\sum W_i (V_i - T_i)^2}{\sum W_i} \quad (2.54)$$

where  $V_i$  is the current value of an operand and  $T_i$  is the target value of that operand.  $W_i$  is the weighting of an operand.

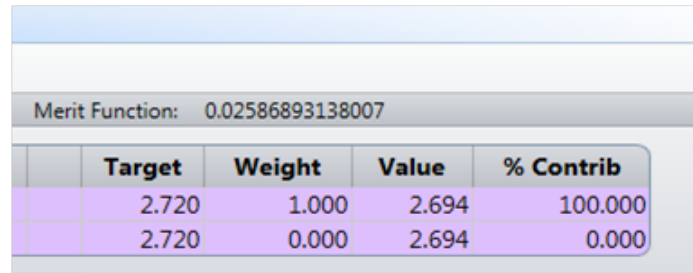
Weighting an operand can have a dramatic effect on the course that an optimisation takes. There are 3 main ways that an operand may be weighted:

- **Weight greater than zero:** The higher an operands weight contribution (represented as a percentage in Figure 2.23), the more the program will try to achieve the desired value for that operand.

Merit Function: 0.02586893138007				
	Target	Weight	Value	% Contrib
	2.720	1.500	2.694	75.000
	2.720	0.500	2.694	25.000

Figure 2.23: Weighting greater than zero.

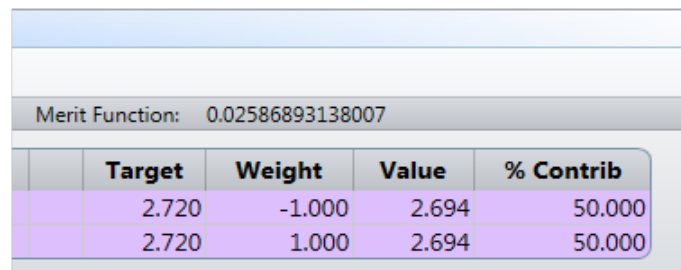
- **Weight equal to zero:** Tells OpticStudio to ignore the operand but still calculate the corresponding value. This can be used to monitor the value of an operand as optimisation occurs. Figure 2.24 shows the editor for this case.



Merit Function: 0.02586893138007				
	Target	Weight	Value	% Contrib
	2.720	1.000	2.694	100.000
	2.720	0.000	2.694	0.000

Figure 2.24: Weighting equal to zero.

- **Weight less than zero:** Tells OpticStudio to treat the operand as a Lagrangian multiplier, essentially forcing OpticStudio to achieve the target value at the expense of other operands. This fact will not be represented in the editor. Figure 2.25 shows the merit function editor for this case.



Merit Function: 0.02586893138007				
	Target	Weight	Value	% Contrib
	2.720	-1.000	2.694	50.000
	2.720	1.000	2.694	50.000

Figure 2.25: Weighting less than zero.

Once the value of the Merit Function has been calculated, an optimisation can finally be undertaken. Once running the optimiser will adjust those operands which have been denoted as “Variable” and then recalculate the value of the Merit Function. This process will loop until a local minimum of the Merit Function is found (i.e. additional adjustments will only lead to an increase in Merit Function value). The user has some control over how the optimisation proceeds, which are accessed from the optimisation window seen in Figure 2.26:

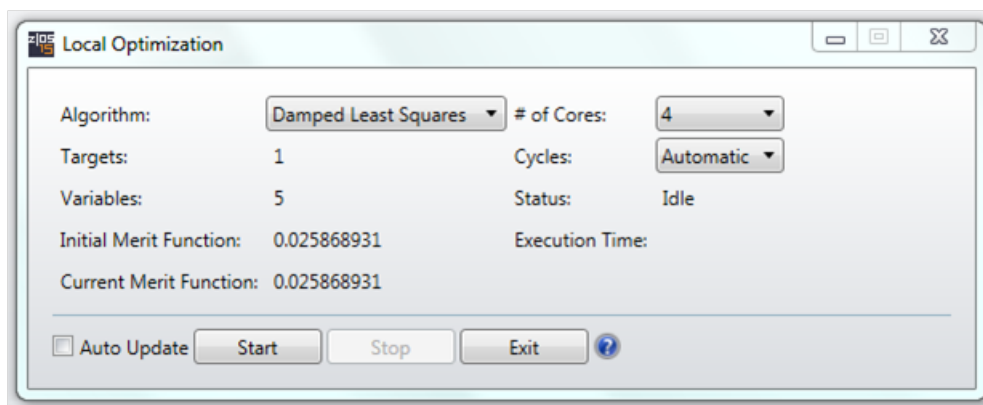


Figure 2.26: UI window launched when starting an optimisation.

The user can first choose which optimisation algorithm they desire: A damped least squares (DLS) or orthogonal descent (OD) algorithm may be used. DLS was used for the optimisations given that it is recommended by Zemax as a capable algorithm for all optical systems. OD is more suited to non-sequential designs. The number of cores used in the computation can be adjusted. The cycles option defaults to automatic, this means that the algorithm will continue until it reaches a point when a reduction in merit function value seems unlikely. The user can override this to perform only 1 optimisation cycle, 5 optimisation cycles or infinite optimisation cycles. The last option is useful to have should the user suspect the algorithm is getting hung up and that a better variant of the system might exist. In any case, the user always has the option to manually stop the optimiser. The starting point for all the optimisations performed by the author was an unedited version of the ALMA Band 9 receiver.

## 2.6 CAD and Meshing Techniques

CAD is, simply, the use of computers to create and analyse a design. CAD software refers to computer programs that are built to carry out this vision. Within such programs, the design may be drafted, modified and measured through graphical representative objects within a two or three dimensional space. Programs

such as these aid engineers by cutting down design times and allowing testing and tolerancing of those designs.

CAD plays an important role in designing optical systems. While OpticStudio and GRASP allow a user to create mirror objects using surfaces and mathematical definitions, mechanical analysis of those objects is not within the scope of those programs. Mechanical structures which are vital to the functioning of such optical systems (support struts, field stops, cowling and shielding) are, in most cases, not the purview of these programs. Despite this, these objects will have an effect on the optical quality of these systems and must therefore be considered in testing. A relevant example would be the thermal shielding and service module of the *CORE* telescope. CAD allowed these components to be imported into GRASP for analysis where otherwise these components would be very difficult to implement, if not impossible. There is also the mundane concern that research collaborators may not use the same analysis software as is used here in Maynooth. In this circumstance, CAD acts as a convenient and trustworthy intermediary form for existing optical models. For example, take an existing mirror system which has been optimised in OpticStudio. No doubt the researcher would want to test the new mirrors to quantify any differences between the two designs. GRASP offers a more robust physical optics analysis regime, so it would be necessary to transfer the optimised mirrors between the two programs. This would be impossible without heavy reformatting of a project file. CAD offers that researcher the ability to transfer the mirrors between the two programs via a process known as meshing.

In CAD terminology, meshing is the process of representing an object through a series of points, fitted to the object and joined together in some fashion to create a group of cells. There are various methods developed to accomplish this. These methods will be discussed in greater detail in **Chapter 4**, which is dedicated to

meshing, while a general overview will be provided here. Two-dimensional meshes were used exclusively by the author, so three-dimensional meshing techniques will not be discussed further. In a broad sense, there exist two types of mesh: regular and irregular. Regular meshes have points fitted to the surface in regular intervals with each cell being well structured and laid out in an ordered fashion. In 2D, the shape of the cells will be of a quadrilateral form. These meshes make better use of computation time and space. There are some complex shapes where these patterns may break down, however. Irregular meshes have no set structure. They are able to represent more complex shapes given that each cell can be of a different area. In 2D, cells take the form of triangles. However, they require more computation time and space as each cell could be connected to others of greatly varying size with no explicit regularity.

Irregular triangular meshes were the type chosen for the work presented in this thesis. The author had no access to CAD programs capable of producing regular meshes. Irregular methods are more popular and tend to be the prevalent forms available in most CAD programs. Additionally, GRASP would accept either mesh type when fabricating mirrors but the ability of irregular meshes to reproduce complex shapes means that they can fit to edges of an object better than the regular meshes. Mirror edges play an important part in PTD calculations. Figures 2.27 and 2.28 show examples of regular and irregular meshes respectively.

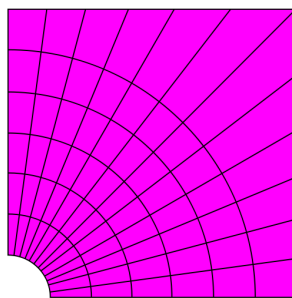


Figure 2.27: A regularly structured mesh. Credit: By Slffea, Mysid - Drawn by Slffea, vectorized by Mysid., CC BY-SA 3.0, <https://commons.wikimedia.org/w/index.php?curid=1367873>

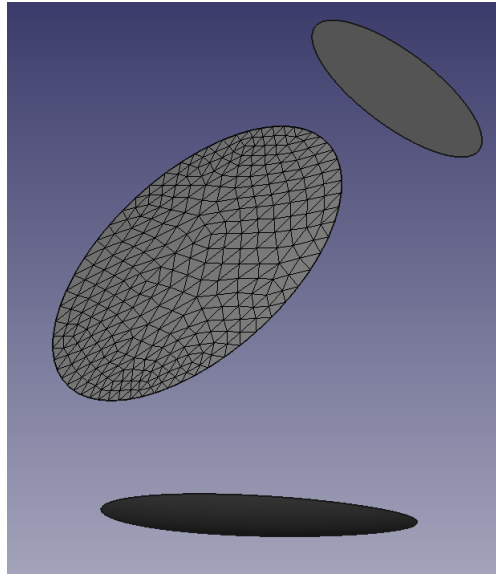


Figure 2.28: An irregularly structured mesh. Object is the primary mirror of the *CORE* telescope.

## 2.7 Summary

The chapter began with an introduction to the fundamentals of quasioptics and Gaussian beams. Beam parameters such as beam radius  $\omega$ , beam waist radius  $\omega_0$ , beam radius of curvature  $R$  and Gouy phase shift  $\phi_0$  were introduced. Co-polar and cross-polar beam components were explained and the process of normalisation for Gaussian beams was set out alongside plotting options for these beams. One and two dimensional beam modes were discussed with equations provided to determine the beam parameters for each mode. Gaussian beam coupling, a method by which fields of radiation may be evaluated was discussed next. This section ended with a brief discussion of PO and PTD and how both are used to determine the full scattered electric field from a surface.

GRASP was covered in detail in this chapter. Geometrical objects were discussed first, beginning with the use of both surfaces and rims to define a reflector. The options available when creating a reflector were also discussed, such as setting the electrical properties of the reflector surface. The different methods of

positioning and orienting objects in GRASP were explained with a focus on the rotational methods one can use. Electrical objects such as feeds, field storage and PO objects were covered in detail with explanation on how to construct each type of object. Lastly, the command system was discussed. Discussion of individual commands was limited which those which computed currents on reflectors and retrieved fields from storage objects, given that these were the most common ones used and necessary for any analysis run.

The creation of optical systems in OpticStudio was discussed. Both sequential and non-sequential modes of propagation were covered, including the function of the lens data editor and non-sequential component editor. The methods of creating optical systems in both modes were also discussed. The optimisation feature of OpticStudio was in detail with a focus on local optimisation. Optimisation operands of use in quasioptics were listed with a brief description supplied for each. The core of any optimisation effort, the merit function, was covered along with the weighting system and its effects.

Finally, the applications of CAD in quasioptics were touched on briefly in this chapter. Meshes of mirrors and other key elements of an optical design allow them to be transferred between analysis programs and CAD environments. The differences between regular and irregular meshes were discussed, including benefits and drawbacks of each type.

# Chapter 3

## Analysis of Beams

### 3.1 Introduction

This chapter follows on from the previous one by discussing the mathematics and calculations involved in later chapters. Fitting routines are a vital tool in optics analysis and will be used frequently to characterise the beams produced by GRASP. The parameters that are to be fitted to a beam (beam radius, offsets etc.) will be explained alongside those which are derived from fitted data (beam ellipticity). Ray matrices are used to model propagation of radiation and Gaussian beam fits are functions used to compute beam parameters. Both can be used in conjunction to model the propagation of a specific Gaussian beam, making them powerful verification and characterising tools for designing optical systems. Additionally, some work undertaken early in the masters will be presented. Waveguide probes of a novel, bespoke design were verified using the Department's VNA. Early investigations into the methods of creating patch antennae in CST Microwave Studio will also be presented. Finally, work done attempting to optimise the mirrors of the ALMA Band 9 receiver using OpticStudio to improve aspects of the design will be discussed.

### 3.2 VNA Measurements with New Waveguide Probes

The VNA is a tool for analysing both the magnitude and phase of electromagnetic radiation. Figure 3.1 shows the ports where the radiation is emitted with the VNA

itself in the background. It emits in the W band (75 - 110 GHz).



Figure 3.1: The VNA ports showing the waveguide probes attached.

### 3.2.1 Theory

The new waveguides were produced by the company SWISSto12. Each waveguide consists of a red plastic exterior which has been fabricated with a 3D printer. The interior and rear portion of the waveguide is plated with gold to aid transmission, like traditional metal waveguide designs. These probes had been designed in Maynooth to have good symmetric beam patterns while having excellent matching to free space impedance (i.e. low  $S_{11}$  return loss) for the probe. Measurements were required to verify their performance. Multiple reflections between the probe apertures were measured at a low level with the optimised designs. The author used this measurement campaign to gain experience in quasioptical measurements in the W band.

There were two types of waveguide probe under test: A stepped circular waveguide probe and a truncated rectangular probe. The former can be seen in Figure 3.2 and the latter in Figure 3.3.



Figure 3.2: The circular waveguide probe.



Figure 3.3: The rectangular waveguide probe.

The expected  $S_{11}$  parameters for the standard waveguide probes and the newer truncated rectangular and stepped circular probes are displayed in Figures 3.4, 3.5 and 3.6:

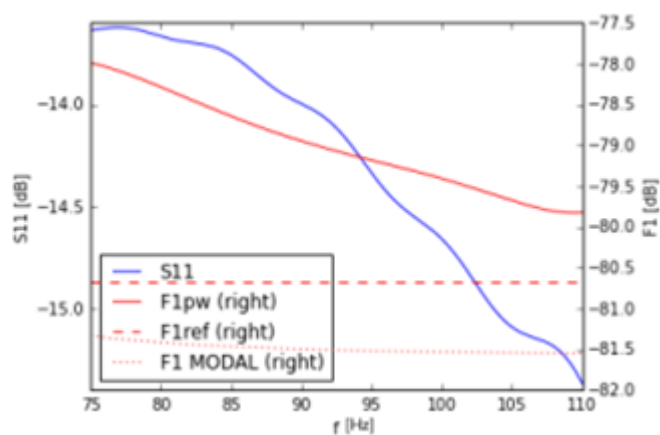
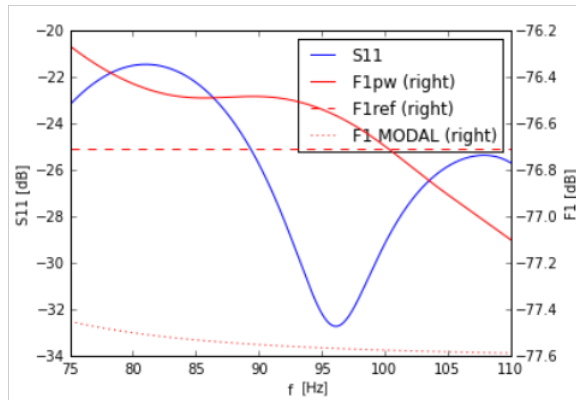
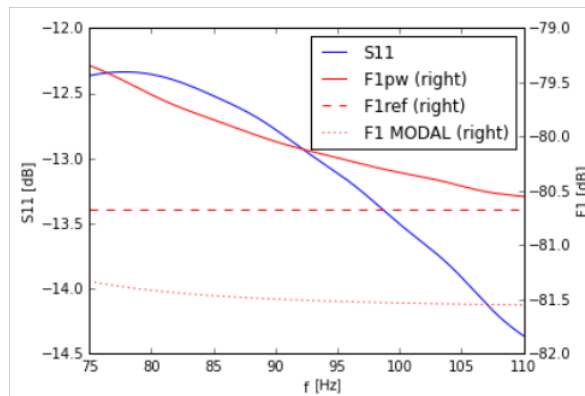


Figure 3.4: Expected  $S_{11}$  of standard probe for 75 - 110 GHz.

Figure 3.5: Expected  $S_{11}$  of rectangular probe for 75 - 110 GHz.Figure 3.6: Expected  $S_{11}$  of circular probe for 75 - 110 GHz.

The above figures are credited to Dr. Marcin Gradziel. Please note that “F1pw” is the coupling of the probe to a plane wave, “F1ref” is the power transmitted through the aperture calculated with CST and “F1 MODAL” is that same power through the aperture calculated with MODAL, which does not include freespace impedance matching.

### 3.2.2 Measurements

Measurements were taken over the course of two weeks in October 2015. The VNA was calibrated using the Through-Offset-Short-Match (TOSM) method. After calibration, the short cables were attached to both port one with long cables on port two. Calibrations were especially important as the VNA was quite susceptible phase drift due to temperature changes.

Measurements began simply by first aligning both ports. Port 1 was placed on a  $z$ -translation stage which would allow the effect of moving the ports away from each other to be investigated, increasing inter-aperture distance to characterise the coupling. The ports were aligned in the  $x$  and  $y$  directions to ensure both were not tilted relative to one another. Port 2 was placed onto an  $x - y$  translation stage which would allow a 2D field profile to be measured using an  $xy$  raster scan over a planar area.

Each measurement consisted of the following routine: Port 2 would move along the  $x - y$  translation stage to build up a grid of amplitude and phase measurements, while Port 1 remained at its home position. Once the grid had been completed, the  $z$ -translation stage would move back by an amount specified by the step size and another planar  $xy$  grid would be measured. This pattern would repeat until the  $z$ -translation stage reached its safe end distance. A review of these measurements is covered in the next section.

### 3.2.3 Results

Measurements were performed with both the circular and rectangular waveguide probes. The results of the measurements taken with the VNA are located below:

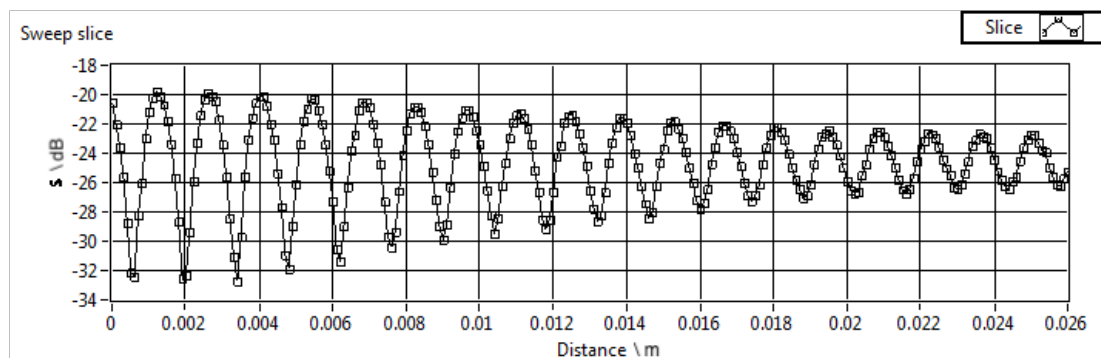


Figure 3.7:  $S_{11}$  parameter of rectangular probe at W band centre frequency 95 GHz. Distance is in metres.

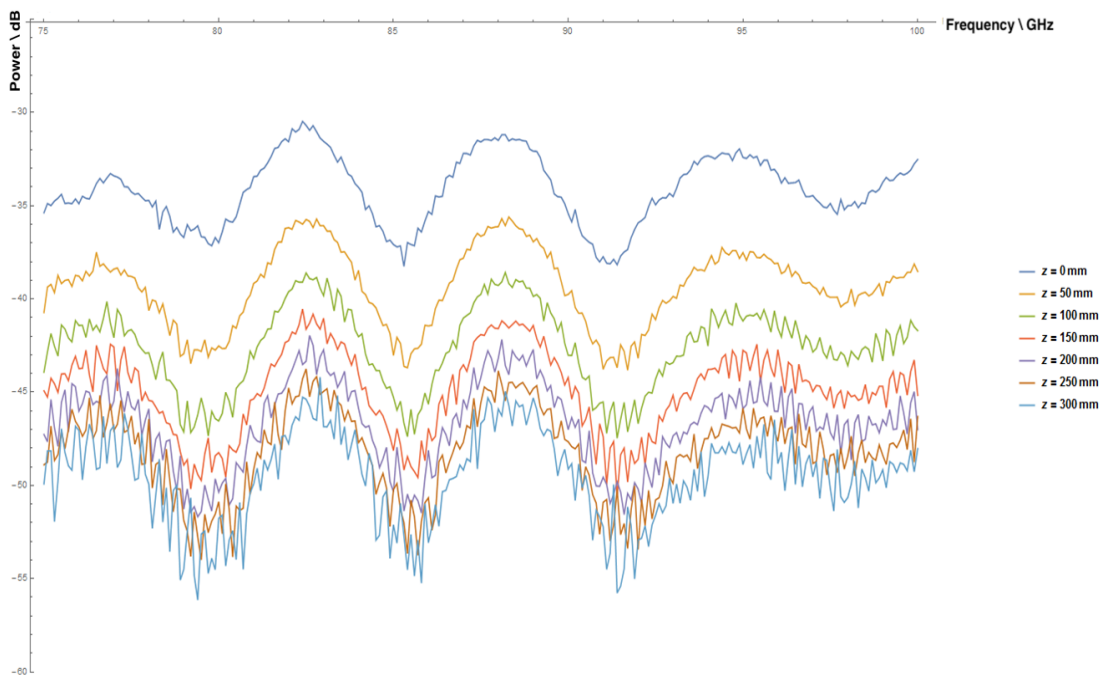


Figure 3.8:  $S_{12}$  plot of the truncated rectangular probe with increasing  $z$  distance over the 75 - 100 GHz range.

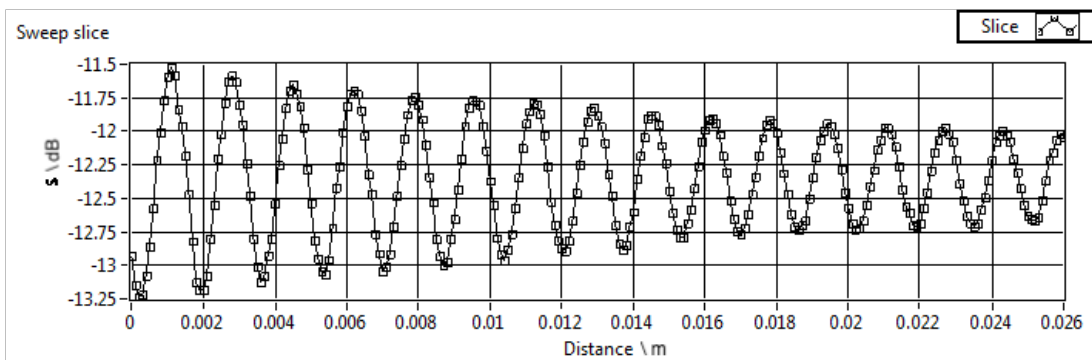


Figure 3.9:  $S_{11}$  parameter of circular probe at W band centre frequency 95 GHz. Distance is again in metres.

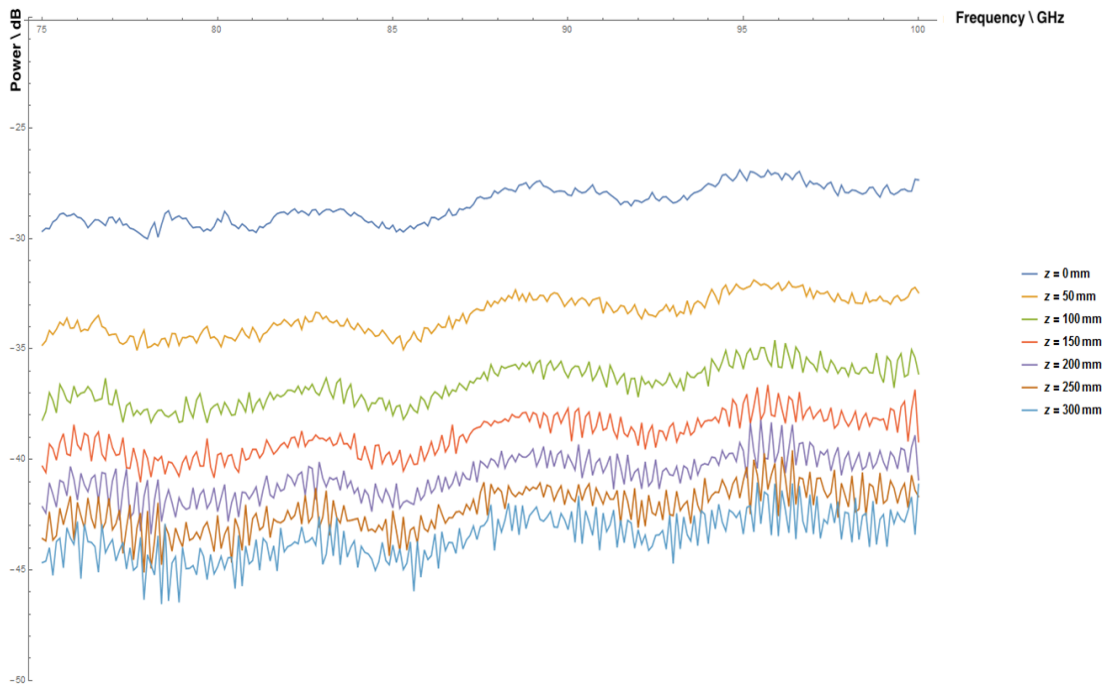


Figure 3.10:  $S_{12}$  plot of stepped circular probe with increasing  $z$  distance over the 75 - 100 GHz range.

The new probes were found to be an improvement over both the current waveguide probes and a naked waveguide and shows a standing wave/multiple reflections between the probes. These standing waves are unavoidable in on-axis systems but the amplitude of these reflections are decreased with the probe designs. In comparison with each other, Figures 3.7 and 3.9 display the  $S_{11}$  parameters for the rectangular and circular probes respectively. The rectangular probe was found to have a lower overall  $S_{11}$  parameter than the circular probe, varying between -20 dB to -32 dB as opposed to -11.5 dB to -13.25 dB for the circular probe. The variation of  $S_{11}$  with distance is more consistent with the circular probe than with the rectangular probe but the rectangular probe will reach a convergent  $S_{11}$  power (equal to “F1ref” from Figure 3.5) faster as a result. This is due to the fact that the amplitude of the standing wave (due to reflection between the probes) will decrease with distance between the probes.

Moving to Figures 3.8 and 3.10, these display the power transmitted between the two ports ( $S_{12}$ ) using the rectangular and circular probes respectively. The

separation was increased from 0 mm to 300 mm to investigate the power loss with distance. Figure 3.8 shows that the rectangular probe displays variation in transmitted power when scanning across the frequency band. The transmitted power drops with increased distance between ports, lowering from -35 dB at 75 GHz when together to -50 dB at a distance of 300 mm. Figure 3.10 displays the transmitted power for the circular probe. In comparison, the transmitted power across the frequency range is more stable than that of the rectangular probe. The power loss for the circular probe is also lessened, dropping from -30 dB at 75 GHz when together to -45 dB when separated by 300 mm. Overall, the higher and more consistent transmitted power of the stepped circular probe makes it more useful in more circumstances than the truncated rectangular probe. The measurements match simulations for both probes and therefore verify the waveguide probe designs.

### 3.3 Investigation of Patch Antennae

An initial study of simple patch antennae was carried out to begin gathering knowledge of antenna designs and also to practice modelling in CST Microwave Studio (created by Dassault Systèmes (2012)). CST (Computer Simulation Technology) is an antenna testing software package. Various types of antennae can be constructed within a CAD-like environment. There is a robust suite of analysis tools that allow the power radiated by an antenna to be characterised, utilising time-domain and frequency-domain calculations. As a result, it is in use frequently in the Experimental Physics Department as a prototyping tool. The two types of antenna studied were patch antennas (also known as microstrip antennas) and log-periodic antennas. However, only the patch antennas will be discussed as they were the only design implemented in CST.

### 3.3.1 Theory

Patch antennas consist of a thin metal strip (usually square, rectangular or circular) known as a patch. The patch is mounted over a larger sheet of metal called a ground plane. Together these two plates form a resonant piece of transmission line with a length approximately half the wavelength of the radiation that the patch is designed to detect. The patch is slightly larger electrically than physically due to the behaviour of radiation at the edges of the patch. The patch should be slightly shorter than necessary for a given frequency to compensate.

This type of antenna is usually constructed on a dielectric substrate like PCB. Drabowitch et al. (1998) provided many of the formulae used in this section. The addition of the ground plane cuts off most of the radiation behind the antenna. The height of the gap between the patch and ground plane is typically smaller than the intended wavelength but should not be smaller than  $\frac{3}{40}$  of the wavelength.

The centre frequency of operation of the patch antenna can be determined using Equation 3.1:

$$f_c = \frac{1}{2L\sqrt{\epsilon_0\epsilon_r\mu_0}} \quad (3.1)$$

where  $L$  is the length of the patch and  $\epsilon_r$  is the relative permittivity of the dielectric substrate.  $L$  is usually half the length of the intended wavelength.

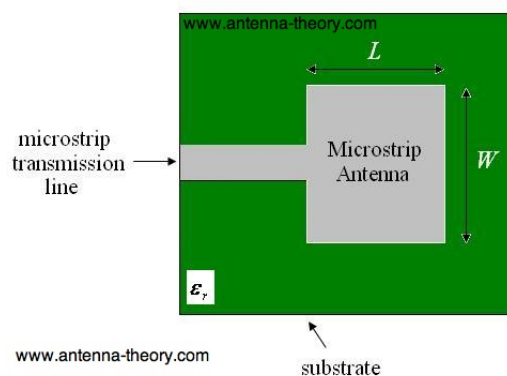


Figure 3.11: Geometry of a patch antenna. (Credit: [www.antenna-theory.com](http://www.antenna-theory.com))

Figures 3.11 and 3.12 display the geometry of a patch antenna. Patch antennas have a small bandwidth. Current and voltage are out of phase in the patch. The voltage is at a minimum at the beginning of the patch and at a maximum at the end of the patch. The fringing of the fields at the edge of the patch leads to emission. The electric field and current both add up in phase at the edge. However, the current is negated by an equal yet opposite current induced in the ground plane. Thus the radiation emitted by a patch antenna is due solely to the voltage. Dielectrics with low  $\epsilon_r$  values cause the fringes to become more bowed, leading to better radiation.

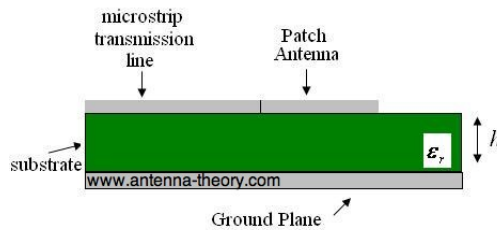


Figure 3.12: Side view of a patch antenna. (Credit: www.antenna-theory.com)

### 3.3.2 Implementation in CST

Patch antennas were implemented in CST Microwave Studio.

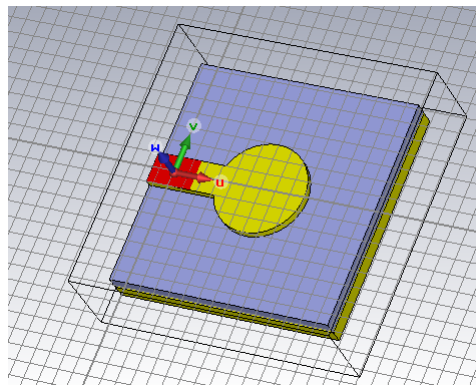


Figure 3.13: Patch antenna in CST. The patch is of length  $\lambda$ . The red area of the patch is the feed where the antenna is excited. In reality a feedline/coaxial cable would be connected at this point.

As can be seen in Figure 3.13, the patch and ground plane (coloured yellow)

were constructed using primitives in CST. Copper was chosen to be the material for both components. The substrate (coloured blue) was set to be vacuum. Ground plane and substrate thickness was 1 cm while patch thickness was 0.5 cm. The red component represents a port, which is where the patch will be excited.

### 3.3.3 Verification of Centre Frequency Equation

As an exercise to judge the correct implementation of the patch antenna, the length of the patch was varied in an attempt to verify that a patch length half the centre wavelength did indeed give the highest directivity.

Three cases were tested, where the size of the patch was varied to be equal to  $2\lambda$ ,  $\lambda$  and  $\lambda/2$ . The farfield patterns for each case were obtained, and these plots describe the directivity of the beam produced by each design at 100 GHz. The results can be seen in Figures 3.14, 3.15 and 3.16:

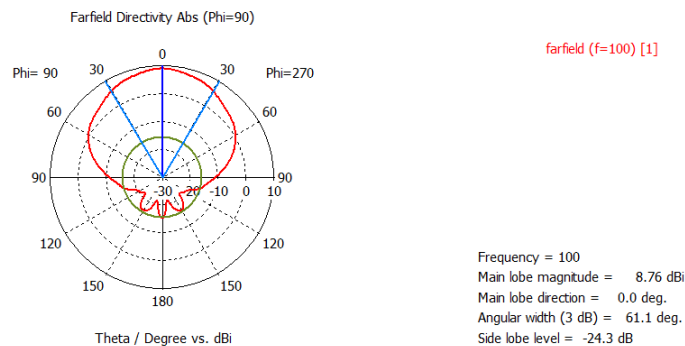


Figure 3.14: Polar plot of the beam from the  $2\lambda$  patch.

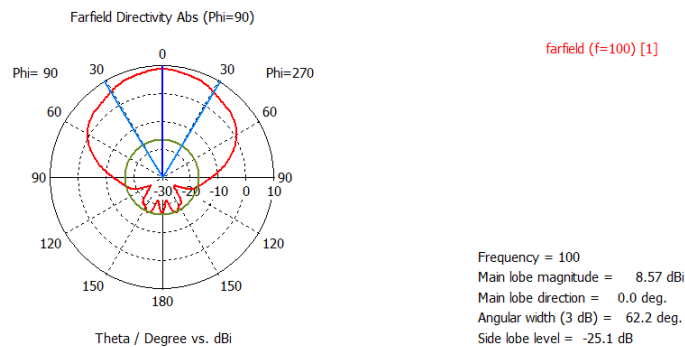
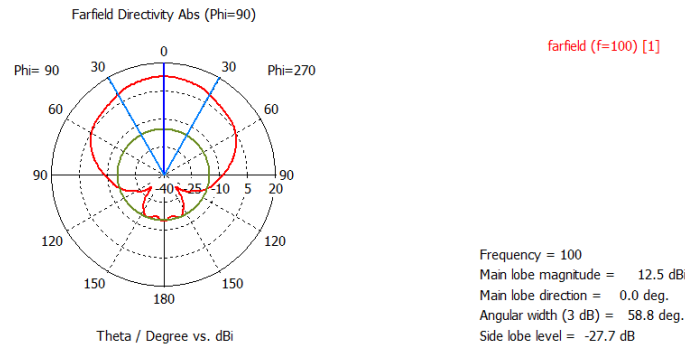


Figure 3.15: Polar plot of the beam from the  $\lambda$  patch.

Figure 3.16: Polar plot of the beam from the  $\lambda/2$  patch.

As can be seen above, the directivity is largest when the patch size is  $\lambda/2$ , though technically it is largest when slightly less than  $\lambda/2$  due to fringe electric fields making the patch seem longer in length. The beams are reasonably collimated for this planar antenna. This simple patch was meant to form part of larger piece of work on antennae but focus soon shifted towards telescope and receiver analysis.

### 3.4 Ray Matrix Analysis

Ray matrix analysis (also known as  $ABCD$  matrix analysis) is a quick and convenient method for rapidly prototyping and testing an optical system. The use of this method in quasioptics arises from its use in geometric optics. By expanding ray matrix analysis to include diffraction, Gaussian beam expansion can be modelled in a paraxial optical system. These two quantities can be updated via application of a linear function on the initial beam parameters. From Goldsmith (1998), the position is defined as  $r$  and the slope as  $r'$ . Then, the linear relationship between input and output beam parameters can be written as:

$$r_{out} = A.r_{in} + B.r'_{in} \quad (3.2)$$

$$r'_{out} = C.r_{in} + D.r'_{in} \quad (3.3)$$

The effect of a system element on ray position and slope can be expressed in matrix form:

$$\begin{pmatrix} r_{out} \\ r'_{out} \end{pmatrix} = \begin{pmatrix} A & B \\ C & D \end{pmatrix} \cdot \begin{pmatrix} r_{in} \\ r'_{in} \end{pmatrix} \quad (3.4)$$

A representative matrix, known as the ray transfer matrix, incorporating all elements of an optical system can be constructed via multiplication of successive element matrices. Some standard forms of element matrices will be shown in the next section. Radius of curvature is given by  $R = r/r'$  in Goldsmith (1998), so Equations 3.2 and 3.3 can be combined to give:

$$R_{out} = \frac{A \cdot R_{in} + B}{C \cdot R_{in} + D} \quad (3.5)$$

The  $ABCD$  law follows on from this extension of geometrical optics. The four parameters  $A$ ,  $B$ ,  $C$  and  $D$  operate here on the complex beam radius of curvature:

$$q_{out} = \frac{A \cdot q_{in} + B}{C \cdot q_{in} + D} \quad (3.6)$$

As mentioned briefly before, the optical system is treated as a paraxial system. The convention is that beams are propagated through the system from left to right, though the systems are reciprocal in nature. Matrix multiplication is ordered backwards, i.e. the last element in the propagation chain is the first in the multiplication chain. The ray transfer matrix is then formed, and can transform the initial beam parameter  $q_{in}$  to form  $q_{out}$ . From  $q_{out}$ , radius of curvature  $R$  and beam radius  $\omega$  can be retrieved via:

$$\omega = \left[ \frac{\lambda}{\pi \text{Im}(-1/q)} \right]^{0.5} \quad (3.7)$$

$$R = \left[ \text{Re} \left( \frac{1}{q} \right) \right]^{-1} \quad (3.8)$$

where  $Re$  stands for the real part of  $q$  and  $Im$  for the complex part of  $q$ .

### 3.4.1 Element Matrices

The simplest form of element matrix is the one that represents propagation over a distance  $L$ . The refractive index of the medium must be uniform along the propagation distance. The ray transfer matrix is given by:

$$\mathbf{M}_{dist} = \begin{pmatrix} 1 & L \\ 0 & 1 \end{pmatrix} \quad (3.9)$$

A curved interface (radius of curvature  $R$ ) between two mediums, one of refractive index  $n_1$  and the other  $n_2$ , has the following ray transfer matrix:

$$\mathbf{M}_{interface} = \begin{pmatrix} 1 & 0 \\ \frac{n_2 - n_1}{n_2 R} & \frac{n_1}{n_2} \end{pmatrix} \quad (3.10)$$

A thin lens of focal length  $f$  has the following ray transfer matrix. Note that, in a paraxial system, a mirror is also approximated by a thin lens:

$$\mathbf{M}_{thin\ lens} = \begin{pmatrix} 1 & 0 \\ -\frac{1}{f} & 1 \end{pmatrix} \quad (3.11)$$

Finally, a thick lens constructed from two curved surfaces  $R_1$  and  $R_2$ , possessing a thickness  $d$  of material with refractive index  $n_2$  surrounded by a material of refractive index  $n_1$  has a ray transfer matrix given by:

$$\mathbf{M}_{thick\ lens} = \begin{pmatrix} 1 + \frac{(n_2 - n_1)d}{n_2 R_1} & \frac{n_1 d}{n_2} \\ \frac{-1}{f} - \frac{(n_2 - n_1)^2 d}{n_1 n_2 R_1 R_2} & 1 + \frac{(n_1 - n_2)d}{n_2 R_2} \end{pmatrix} \quad (3.12)$$

There are many more possible element matrices than these few listed here. Those that are listed here are relevant to the optical systems reported in this thesis.

### 3.4.2 Example: Verifying LLAMA Beam Parameters

Ray matrix analysis was used in the early stages of verifying the LLAMA receiver. Before optical modelling of the receiver was started (see **Chapter 5**), ray matrix analysis was used to confirm the expected beam waists that should be found at the band cartridge with an input beam of the appropriate size. Using the propagation distances and focal lengths supplied in the LLAMA First Light Memo (by Kooi (2016)), a ray transfer matrix was constructed that could then be used to verify the frequency independent nature of the receiver using *ABCD* matrices. The necessary parameters are laid out below in Table 3.1:

<b>LLAMA Parameters</b>	
$z1$ (mm)	1829.0
$z2$ (mm)	3129.5
$z3$ (mm)	1300.0
M3 Focal Length (mm)	1564.75
M4 Focal Length (mm)	1564.75

Table 3.1: LLAMA receiver parameters.

Please note that the correct  $z3$  distance should be 1300.5 mm. The distance of 1300 mm arose from technical drawings from Vertex. The tolerances of the design have yet to be determined. It is reasonable that, given the miscellaneous optical and mechanical uncertainties, the difference will not substantially affect the receiver. As a result, the original model using  $z3 = 1300$  mm was kept in use.

The chain of propagation for this receiver can be broken down into five parts: The beam is propagated a distance  $z1$  from the Cassegrain focus to the first mirror M3. There is a radius of curvature change at M3. The beam is then propagated a distance  $z2$  to M4. There is a radius of curvature change due to M4. Finally, the beam is propagated a distance  $z3$  to the cryostat focus. This chain can be represented as a paraxial system, as evidenced by Figure 3.17 taken from the report by Kooi (2016):

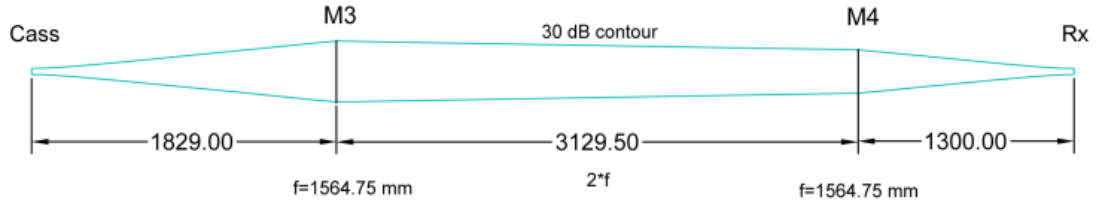


Figure 3.17: The LLAMA receiver described using a thin lens approximation. Credit to Kooi (2016).

The ray transfer matrix can be constructed via:

$$\mathbf{M} = \begin{pmatrix} 1 & 1300 \\ 0 & 1 \end{pmatrix} \cdot \begin{pmatrix} 1 & 0 \\ \frac{-1}{1564.75} & 1 \end{pmatrix} \cdot \begin{pmatrix} 1 & 3129.5 \\ 0 & 1 \end{pmatrix} \cdot \begin{pmatrix} 1 & 0 \\ \frac{-1}{1564.75} & 1 \end{pmatrix} \cdot \begin{pmatrix} 1 & 1829 \\ 0 & 1 \end{pmatrix} \quad (3.13)$$

Multiplication takes place from right to left. The resultant ray transfer matrix was calculated in Mathematica:

$$\mathbf{M} = \begin{pmatrix} -1 & 0.5 \\ -1.0842 \times 10^{-19} & -1 \end{pmatrix} \quad (3.14)$$

The LLAMA receiver was to be tested at three different frequencies: 187 GHz, 243 GHz and 660 GHz. As propagation begins at a beam waist for all three frequencies, the initial radius of curvature was  $\infty$  for all (i.e. planar). Given that the receiver was a Gaussian beam telescope (GBT), the input waist (located at the Cassegrain focus) should match the output waist (located at the focal plane) for each frequency. Table 3.2 contains the values needed to begin analysis.

Initial Parameters			
Frequency (GHz)	$\omega_{0 \text{ input}}$ (mm)	$\omega_{0 \text{ output}}$ (mm)	$R$ (mm)
187	9.60	9.60	$\infty$
243	7.39	7.39	$\infty$
660	2.72	2.72	$\infty$

Table 3.2: Initial parameters used in beam parameter construction.

Input beam parameters were constructed for each frequency using Equation 2.15. The  $ABCD$  values are taken from the ray transfer matrix (3.13) and utilised

in the  $ABCD$  Law (Equation 3.6):

$$q_{out} = \frac{-1 \cdot q_{in} + 0.5}{-1.0842 \times 10^{-19} \cdot q_{in} - 1} \quad (3.15)$$

The radius of curvature and focal plane location beam waist can be extracted from the output beam parameters using Equations 3.7 and 3.8. A comparison of expected values and values returned from Mathematica are set out below in Table 3.3:

Comparison Values				
Frequency (GHz)	$\omega_{0 \text{ expected}}$ (mm)	$\omega_{0 \text{ out}}$ (mm)	$R_{\text{expected}}$ (mm)	$R_{\text{out}}$ (mm)
187	9.60	9.60	$\infty$	-65141.60
243	7.39	7.39	$\infty$	-38521.90
660	2.72	2.72	$\infty$	-5229.89

Table 3.3: Comparison of reported values to  $ABCD$  matrix values.

The waist values match perfectly, showing that the design parameters that would be used to construct the model were correct. The waist values would be further verified using physical optics (see **Chapter 5**). The radius of curvature values were not strictly infinite, but functionally are so large as to indicate that a beam waist had been reached.

## 3.5 Gaussian Beam Calculations

### 3.5.1 Gaussian Fitting

Gaussian fitting refers to the process of fitting an equivalent Gaussian function to a recorded output beam. This allows the critical parameters of that beam to be retrieved from the output field and is key to analysing the beam profile and optical quality after propagating through the optical system.

The process of fitting is straightforward in premise. A model of a Gaussian beam must first be constructed. The model can vary in its complexity, depending

on the user's requirements. The basic form of Gaussian function required is:

$$f(x) = \exp\left[-\frac{x^2}{\omega_{0x}^2}\right]^2 \quad (3.16)$$

This form will fit to a one-dimensional Gaussian beam which is assumed to be at a waist location and the phase radius of curvature is infinite. The beam intensity can also be assessed rather than the phase and amplitude. Once away from a waist position this expression is incomplete as the phase curvature of the beam, which will begin to dominate the coupling, is not accounted for. The only retrievable parameter will be the beam waist radius  $\omega_{0x}$  or beam radius  $\omega_x$ . The beam (waist) radius will have consistent units with the cut or grid which recorded the beam. Spherical cuts and grids can be fitted to with no extra adjustment as the cut or grid is assumed to be a small region on the sky and therefore have negligible curvature, much like the apparent flatness of the Earth's surface. The model can be expanded to easily incorporate spatial offset distance:

$$f(x) = \exp\left[-\frac{(x - x_0)^2}{\omega_{0x}^2}\right]^2 \quad (3.17)$$

where  $x_0$  is the magnitude of the spatial offset, with the same units used by the cut/grid. From this point the model can be expanded out to encompass two-dimensions:

$$f(x, y) = \exp\left[-\frac{(x - x_0)^2}{\omega_{0x}^2} + \frac{(y - y_0)^2}{\omega_{0y}^2}\right]^2 \quad (3.18)$$

### 3.5.2 Example: Fitting to a Predefined Gaussian Function

Before any fitting algorithm can be used, it must first be tested. The code for the fitting algorithm was written in Wolfram Mathematica and utilised the *Non-linearModelFit* function. A model and a set of data must be provided to this function. The model used was the same as is shown in Equation 3.17. The set

of data was simulated to be one where critical beam parameters were known in advance. This way, the fitting algorithm could be debugged until it returned the correct results.

The simulated set of data was created by evaluating a standard form two-dimensional Gaussian function. The function used was:

$$f(x, y) = \exp\left[-\frac{(x - 0.2)^2}{1.5^2} + \frac{(y - 0.3)^2}{2.5^2}\right]^2 \quad (3.19)$$

The fitting code begins by normalising the data set to unity power. This data set is then flattened to one dimension. A grid of points with the same sampling as the data set must be created. This will represent the locations (in  $x$  and  $y$ ) throughout the grid which were sampled ( $\Delta x$  and  $\Delta y$ ). The two datasets are then joined to produce an analysis set that has a size equal to the total number of sampling points, and each element in the set contains a distance in  $x$ , in  $y$  and a magnitude in  $z$ .

Once the analysis dataset has been produced, both it and the model function are submitted as arguments to the Non-Linear Model Fit function. The function will then compute the variable parameters of the model such that the analysis dataset may be reproduced. The fitted values may be retrieved and plotted alongside the analysis dataset for comparison. The fitted variable parameters may be accessed through the “Parameter Table” option. The results for the pre-generated Gaussian data set are given in Table 3.4:

<b>Fitted Model Values (100 GHz)</b>	
<b>Parameter</b>	<b>Value</b>
X Beam Waist (mm)	1.5
Y Beam Waist (mm)	2.5
X Offset (mm)	0.2
Y Offset (mm)	0.3

Table 3.4: Parameters returned from the fitting code for the predefined Gaussian function.

### 3.5.3 Example: Fitting to a GRASP Gaussian Beam

Correctly fitting to a predefined function is acceptable to test the functioning of an algorithm. However, correctly fitting to actual, verifiable data from an independent source would show that the algorithm is indeed working as intended. Given that many of the fitted fields shown later in **Chapter 6** had no other source with which to verify beam waist radii or offset values, it was imperative that the algorithm return fit values that matched those used in GRASP. To this end, a test pattern was created in GRASP to test the fitting program.

The pattern was created using a near-field beam definition object in GRASP. The beam waist was set to 10 mm and the frequency to 100 GHz. A planar output grid was placed at the feed itself so as to obtain a direct reading at the beam waist. The grid size was set to 100 mm by 100 mm. This is quite large given the waist but having a sizeable flat portion in the dataset can help with the stability of the fitting. The process of fitting happens exactly as described in the previous section when using actual data. Table 3.5 contains the returned values:

<b>Fitted Model Values (100 GHz)</b>	
<b>Parameter</b>	<b>Value</b>
Expected Waist (mm)	10
X Beam Waist (mm)	10
Y Beam Waist (mm)	10
X Offset (mm)	0.0
Y Offset (mm)	0.0

Table 3.5: Parameters returned from the fitting code for the GRASP feed.

## 3.6 Useful Beam Parameters

### 3.6.1 Gaussicity

Gaussicity is a term used in beam coupling. It is defined by Johansson (1995) as the maximum achievable power coupling of a recorded output field and a

linearly polarised Gaussian beam. It is usually expressed as either a decimal or a percentage in reference to the equivalent Gaussian beam. It can be calculated using the normalised overlap integral of output field and the equivalent beam:

$$\eta_{Gaussicity} = \frac{\iint E_{Gauss} E_{out}^* dx dy}{\iint E_{Gauss} E_{Gauss}^* dx dy \iint E_{out} E_{out}^* dx dy} \quad (3.20)$$

Perfect coupling between output field and equivalent beam is indicated by a Gaussicity of 100%. The Gaussicity of a beam is a convenient way to express the power being transferred through an optical system. A high Gaussicity indicates that a telescope or receiver is doing a good job of redirecting and manipulating beams of radiation. Meanwhile, a low Gaussicity indicates optical aberration or that power has leaked from the co-polar beam component or has been rotated to an angle that does not suit the detector polarisation, resulting in increased cross-polar levels.

### 3.6.2 Ellipticity

Ellipticity (also known as flattening or oblateness) is a term used to describe the deviation away from a standard circle. It has a simple definition, seen below:

$$e = 1 - \frac{b}{a} \quad (3.21)$$

where  $a$  and  $b$  are the major and minor axis length of an ellipsoid. It is not to be confused with eccentricity, given that they are each the inverse of the other. A perfect circle will have an ellipticity  $e = 0$ . This quantity is useful in the analysis of Gaussian beams. The shape of a beam will be affected by optical elements in a receiver as it propagates through those elements, potentially becoming heavily distorted in the process. Ellipticity therefore serves as a measure of beam symmetry. It is a practical way to establish the quality of a beam produced by an optical system, given that it has an inherent comparative aspect

that the simple quotation of beam radii lacks. If a stated goal of a telescope is to produce well collimated beams of radiation suitable for further analysis (as is the case with *CORE* and *LLAMA*), then ellipticity is a useful standard measurement to gauge this. An ellipticity of less than 5% (i.e not greater than 0.05) is usually an acceptable limit for CMB calibration.

## 3.7 Optimisation of ALMA Receiver

This section will discuss the optimisations carried out the ALMA Band 9 receiver. This would build on the design laid out by Whale (2010) and compare figures against those recorded in Candotti (2007). A Gaussian beam telescope is an optical set-up designed to be wavelength-independent. This makes it a useful tool in broadband instruments, as optimum coupling is achieved over a bandwidth.

### 3.7.1 Construction in GRASP

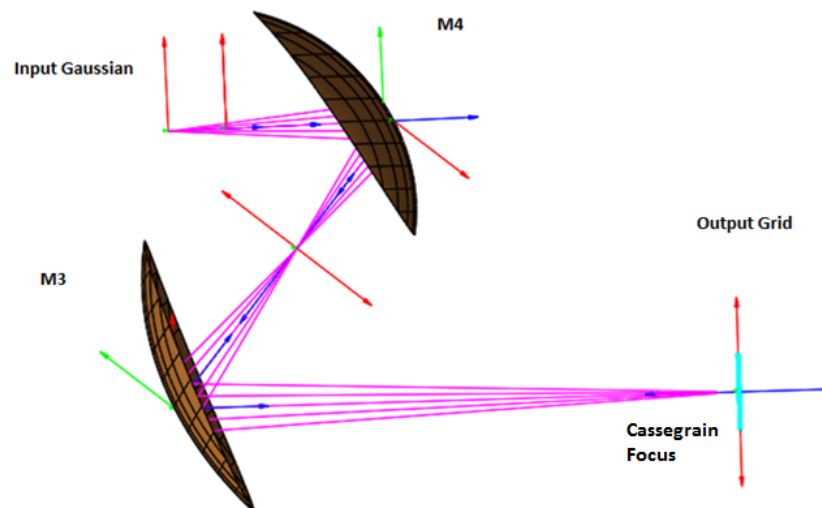


Figure 3.18: ALMA Band 9 receiver modelled in GRASP. The associated optical elements have been labelled. Detector horn is located at the input Gaussian location

Before any optimisations could be performed, the design first had to be implemented in GRASP. The telescope consisted of two elliptical mirrors focussing light onto a subreflector some distance away after coming to a focus at the Cassegrain focal plane. A Mathematica file was written to calculate the parameters of both mirrors, named “M4” and “M3”. The resulting GRASP model can be seen in Figure 3.18 while the parameters are recorded in Table 3.6:

Mirror Parameters		
Mirror	M4	M3
Semi-Major Axis (mm)	51.2262	101.727
Semi-Minor Axis (mm)	45.7407	80.8404
Interfocal Distance (mm)	46.1261	123.501
Focal Length (mm)	24.8618	39.4093
Radius of Curvature (mm)	40.8427	64.2425
Eccentricity	0.4502	0.6070
Conic Constant	-0.2027	-0.3685

Table 3.6: M3 and M4 parameter data used to construct the mirrors in GRASP.

A plane detection grid was placed 150 mm away from M3 (see Figure 3.18). The grid size was 20 mm in  $x$  by 20 mm in  $y$ . The field at this position was simulated and the data passed to Mathematica for analysis via Gaussian fitting at 661 GHz. The results are shown in Figures 3.19, 3.20 and Table 3.7:

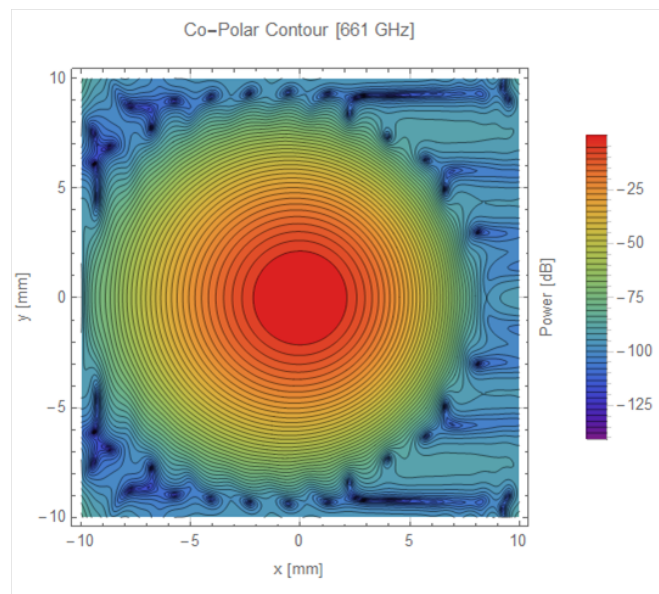


Figure 3.19: Co-Polar beam component at 661 GHz.

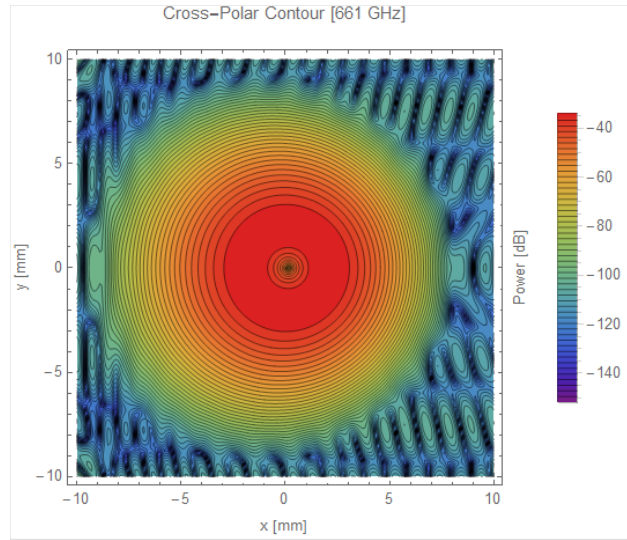


Figure 3.20: Cross-Polar beam component at 661 GHz.

Gaussian Beam Parameters	
Property	Value
<b>X Offset (mm)</b>	0.0017
<b>Y Offset (mm)</b>	0.054
<b>Z Offset (mm)</b>	-1.078
<b>X tilt (°)</b>	0
<b>Y tilt (°)</b>	0.05
$\omega_{0x}$ (mm)	2.715
$\omega_{0y}$ (mm)	2.715
<b>Gaussianity (%)</b>	99.9201
<b>Ellipticity</b>	0.0007

Table 3.7: Gaussian fitting data.

Note that the Z Offset is in relation to the beam waist location. These results are in agreement with those set out in the original design from Whale (2010).

Five optimised systems were created using a combination of the above operands in Zemax OpticStudio. The main goal of every optimisation was the constraint of the output beam waist radius to 2.72 mm. The variable parameters for each optimisation were the distances between the mirrors, the receiver aperture and the cryostat window (Figure 2.16 shows these parameters with a “V” beside them). Each optimisation was saved as its own Zemax project file. The list below discusses the operands used for each optimisation.

- **Opt1:** POPD was used to constrain  $\omega_{0x}$  after M3 to 2.72 mm
- **Opt2:** POPD was used to constrain  $\omega_{0x}$  and  $\omega_{0y}$  after M3 to 2.72 mm
- **Opt3:** GBPW, GBPP were used to constrain  $\omega_{0x}$  after M3 to 2.72 mm and location to 150 mm after M3
- **Opt4:** GBSW, GBSP were used to constrain  $\omega_{0x}$  after M3 to 2.72 mm and location to 150 mm after M3
- **Opt5:** OPDX, the default optimisation carried out by manipulating optical path length difference for different incoming rays

The mirror surfaces were now ready to be transferred back into GRASP where physical optics analysis could be performed on each optimised system. However, only Opt1, Opt2 and Opt5 were transferred. The other optimisations had either distorted the mirrors too severely or had altered the system layout too greatly to be considered further. Opt1 was an optimisation carried out with the goal of constraining the beam waist at the output grid in the  $x$ -dimension only to the expected value of 2.72 mm. Opt2 was intended to constrain both  $x$  and  $y$  beam waists to 2.72 mm. Opt5 is the default OpticStudio optimisation based on manipulation of optical path length difference for different offset rays.

### 3.7.2 Analysis using GRASP

The optimised surfaces were reintroduced into GRASP via a tabulated surface. OpticStudio provides surface sag tables (i.e.  $z$  as a function of  $x$  and  $y$ ) for each surface in the Lens Data Editor. These tables can be used to transfer mirror surfaces to GRASP with little reformatting of files or CAD meshes required.

Physical optics analysis was performed on each optimised system for comparison with the unoptimised system. The mirrors were introduced into the existing

ALMA Band 9 model. The parameters of the model could be adjusted to recreate the all the changes that OpticStudio had made to individual optimised systems. The same planar detection grid was used for the optimised systems as had been used for the unoptimised system. The grid size was 20 mm in  $x$  by 20 mm in  $y$ . The analysis frequency was again 661 GHz. The same source was used with no changes. The results of this were analysed using Gaussian beam fitting in Mathematica. The results can be seen in Table 3.8:

Gaussian Beam Parameters				
Optimisation	Gaussicity (%)	$\omega_{0x}$ (mm)	$\omega_{0y}$ (mm)	Ellipticity
Unopt	99.92	2.715	2.715	0.0007
Opt1	99.93	2.73	2.73	0.0001
Opt2	99.88	3.19	3.26	0.023
Opt5	99.96	2.21	2.21	0.001

Table 3.8: Gaussian fitting data for the three optimisations. The unoptimised system is included for comparison.

The co-polar and cross-polar contour plots for the three optimisations are presented in Figures 3.21 - 3.26:

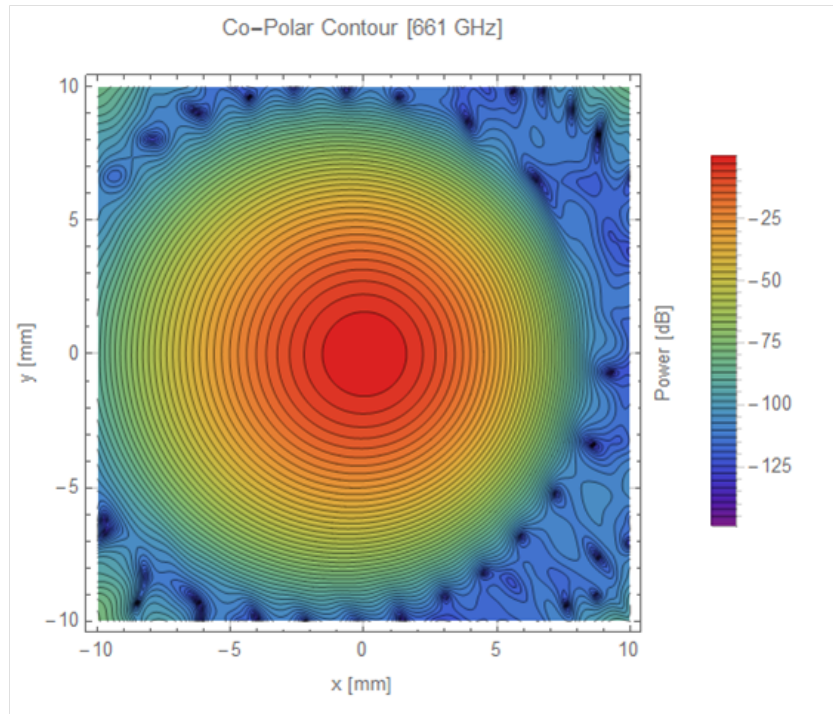


Figure 3.21: Co-Polar Beam Component from the first optimisation at 661 GHz.

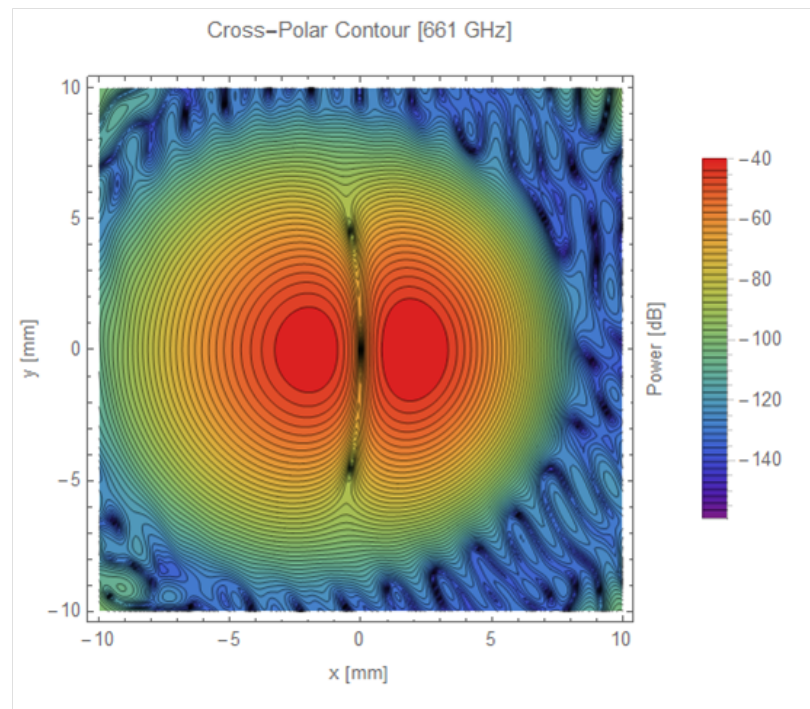


Figure 3.22: Cross-Polar Beam Component from the first optimisation at 661 GHz.

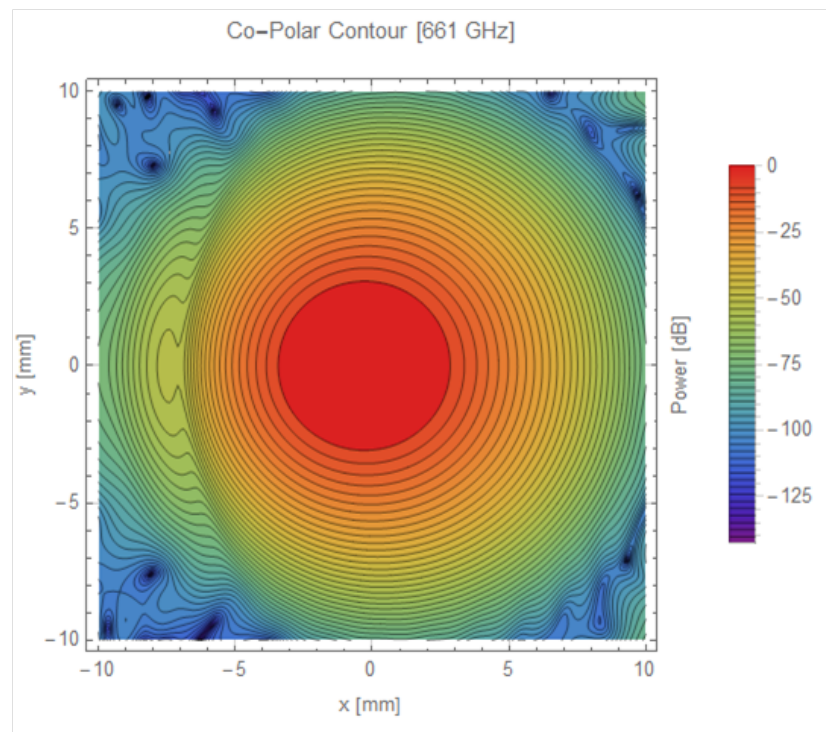


Figure 3.23: Co-Polar Beam Component from the second optimisation at 661 GHz.

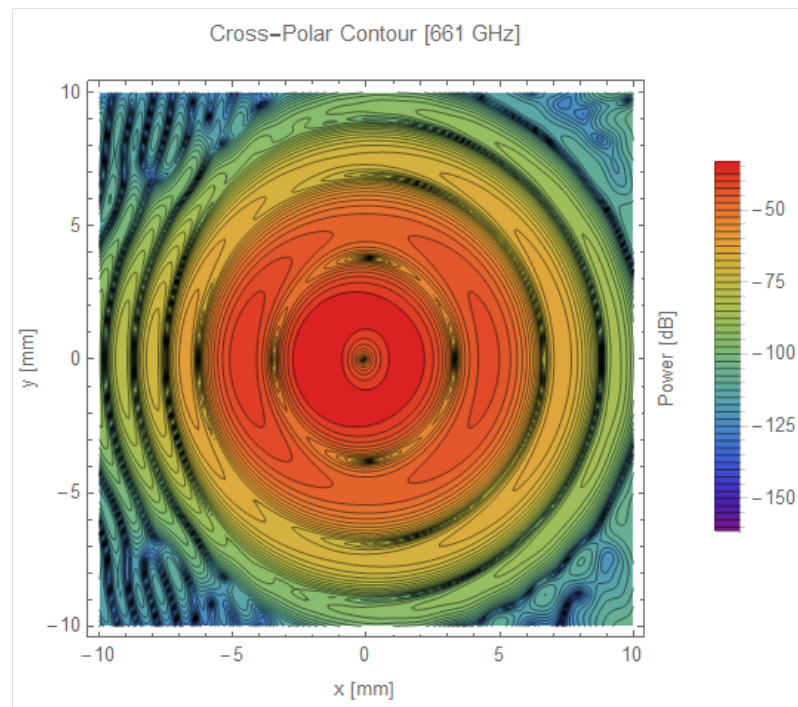


Figure 3.24: Cross-Polar Beam Component from the second optimisation at 661 GHz.

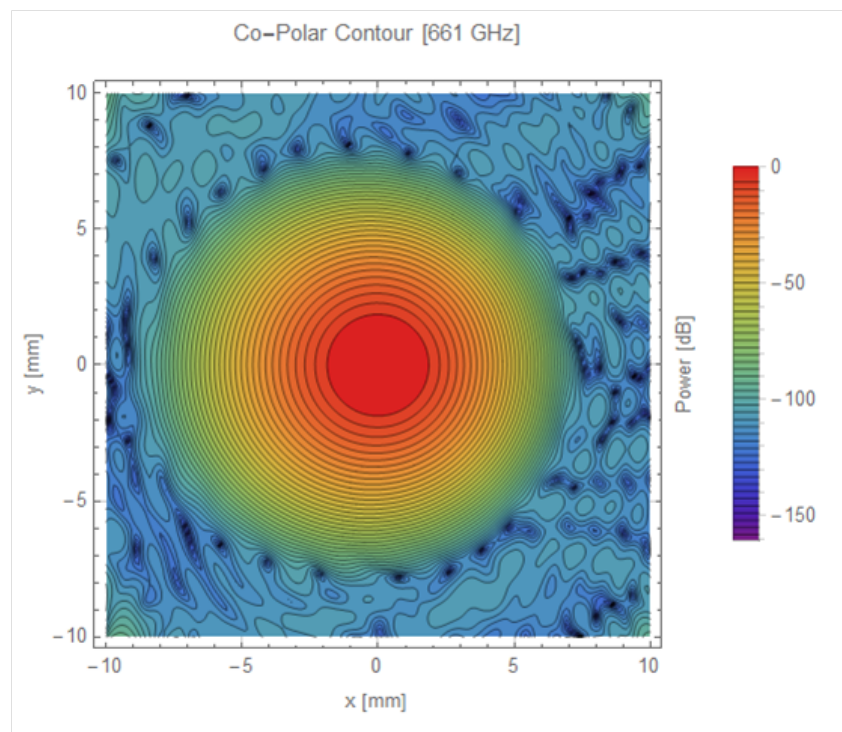


Figure 3.25: Co-Polar Beam Component from the seventh optimisation at 661 GHz.

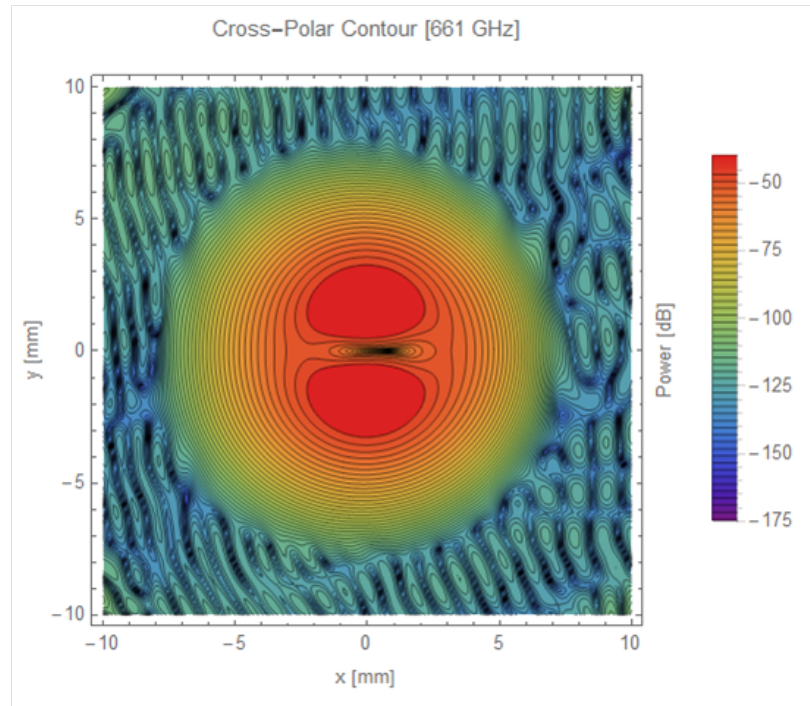


Figure 3.26: Cross-Polar Beam Component from the seventh optimisation at 661 GHz.

Looking at the three chosen optimisations, it is clear that Opt1 and Opt5 have been the most effective. Opt2 has diverged from its goal quite significantly. Opt1 constrained  $\omega_{0x}$  and not  $\omega_{0y}$ , while Opt2 tried to constrain both. The optimiser may have had difficulty in constraining the beam waist size in two dimensions and may have stopped prematurely. Changing the weighting may have helped by giving the optimiser a clearly favoured parameter. The simplest explanation for the discrepancy is simply a misunderstanding on the author's part. Looking to Opt5, the default optimisation has improved Gaussicity over the unoptimised receiver. The beam waist values have been reduced substantially, which is understandable given that the optimisation was not constraining waist size. Opt1 has increased the beam waist sizes to slightly larger than the size specified. The Gaussicity has increased by a modest 0.01%, while the beam ellipticity has decreased by 0.0006. Opt1 can therefore be considered a success, having somewhat achieved the specified goal while reducing aberration and beam distortion in the process. The other two optimisations are infeasible with the existing ALMA Band 9 receiver design.

This work in understanding the optimisation routines in OpticStudio has shown that they could be used as an optimising tool for quasioptical receivers. The ALMA Band 9 receiver has already been designed to operate well at the design frequency band, and so had limited scope for further optimisation.

### 3.8 Conclusions

Results from a series of measurements using new waveguide probes were featured. The probes have been designed to produce more beams than the standard waveguide probes in use in the Department. The measurements taken did not include old probes, however, as the goal of the measurements were to characterise the new probes, ensuring their performance matched simulations (see Figures 3.5 and 3.6). In essence, by matching their expected performance they would outclass the standard waveguide probes. As stated previously, the rectangular probes reach a convergent  $S_{11}$  parameter faster than the circular probes, but the circular probes exhibit a more consistent  $S_{12}$  parameter with both increasing distance between heads and increasing frequency.

A simple verification of the centre frequency equation for patch antenna was shown. Three patch lengths were implemented and tested. Looking to Figures 3.14, 3.15 and 3.16 it can be seen that the patch length that produced both the highest main lobe power of 12.5 dBi and the lowest sidelobe level of -27.7 dB was the patch length of  $\lambda/2$ . In addition, the angular beam width is narrower than for the other two lengths, being  $58.8^\circ$  as opposed to  $62.2^\circ$  and  $61.1^\circ$  for  $\lambda$  and  $2\lambda$  respectively.

The beam parameters of the LLAMA receiver were verified using  $ABCD$  matrix analysis. This was the first step in the LLAMA analysis and is simply a recreation of values provided to the Department. The values used in constructing the ray

transfer matrix (Equation 3.13) were taken from the LLAMA memo by Kooi (2016). For the three frequencies (187, 243 and 660 GHz) the beam waist radii at the output plane generated by the ray matrices matched those supplied in the memo. For a beam waist, the radius of curvature of a beam should be  $\infty$ . The values presented in Table 3.3 are not  $\infty$ , but in practical terms they are so large as to be functionally  $\infty$ .

Two examples of Gaussian beam fitting were provided in this chapter. In the first case, a Gaussian function dataset was generated using Equation 3.19. The fitted values are shown in Table 3.4. In this simple case the fitted values match those in Equation 3.19, demonstrating that the algorithm is capable of correctly fitting a Gaussian to a predefined data set generated by Mathematica. In the second case, Gaussian fitting was performed on a dataset generated by GRASP. Table 3.5 contains the values returned by the fit as well as the original beam waist radius of the feed used in GRASP. Again, the waist radius values in  $x$  and  $y$  match the waist radius of the feed and the beam is not offset in either  $x$  or  $y$ .

Five optimisations were presented in this chapter. Of those, three were selected for implementation in GRASP. Opt3 and Opt4 were discounted due to the fact that the beam waist radii did not match the specified values as well as the fact that the model of the receiver had diverged too much from the original in both cases. For each optimised system, the changes made to the lens data editor by the optimiser were carried over to the GRASP model for testing with physical optics. Table 3.8 displays the results of fitting performed on the beams from the three modified receivers. Looking to Opt1, the Gaussicity is higher by 0.01% and the output beam waists in  $x$  and  $y$  are 2.73 mm instead of the desired 2.72 mm. The ellipticity has dropped by 0.0006, indicating that the beam has become more symmetrical. Opt2 was designed to constrain the beam waists in  $x$  and  $y$  to 2.72 mm but has failed, most likely due to a conflict that the author was unaware

of. Opt5 was designed to test the standard OpticStudio optimisation. This optimisation achieved a higher Gaussianity than all other optimisations. However, the beam waists have diverged from the desired 2.72 mm and the ellipticity is higher than the unoptimised design. This is not surprising given that constraining beam waists was not a part of this optimisation.

# Chapter 4

## Meshing

### 4.1 Introduction

The goal of this chapter is to describe the process whereby mirror surfaces in a CAD format were transferred into the program GRASP for physical optics analysis in a way that ensures complete fidelity of the surface and rim definition. With numerous schemes to define 3D solid objects, it is important to conserve information when exchanging objects between different software packages. This specific process is known as meshing, where the density of points that represent the surface profile are defined within a formatted framework. This can vary between packages. My thanks to Mr. Donnacha Gayer, a PhD student here in the Department of Experimental Physics, who first introduced me to this method. A mesh is a representation of a surface obtained by fitting points to that surface and then recreating the surface using discrete points on the surface. Meshing was an essential part of the analysis procedures presented in this thesis. The various analysis packages available for use (GRASP, OpticStudio, CST etc.) all define mirror surfaces in different, proprietary ways. There is no straightforward method of transferring an optical system in OpticStudio to GRASP. Meshes of CAD models, however, allow the constituent parts of that optical system to be defined using points fitted across the surface and grouped into triangular/quadrilateral areas (though only triangular meshes were used). With CAD meshes as the intermediary, the options for analysis one has available broaden. This chapter will begin by explaining meshing definitions, specifically for the CAD program FreeCAD which was used to create meshes. Both *CORE* and LLAMA system definitions involved

meshing to greater or lesser extents and will be used as examples to demonstrate the utility of these meshes in exporting mirror profiles.

A comparison of the different meshing options is presented. As meshes were used to import mirror surfaces into GRASP, it is important to quantify the effect that each mesh type and density will have on beams propagated through those mirrors and compare them to a standard GRASP single-surface reflector definition. The question may be asked at this point: “Why not always make the finest, most dense meshes possible?” In programs such as GRASP, computation times can be quite long especially for large reflectors. This point also holds for reflectors that are meshed finely. Currents must be worked out for each mesh segment; the more of these there are, the longer and more demanding the computation time.

## 4.2 FreeCAD and Meshing

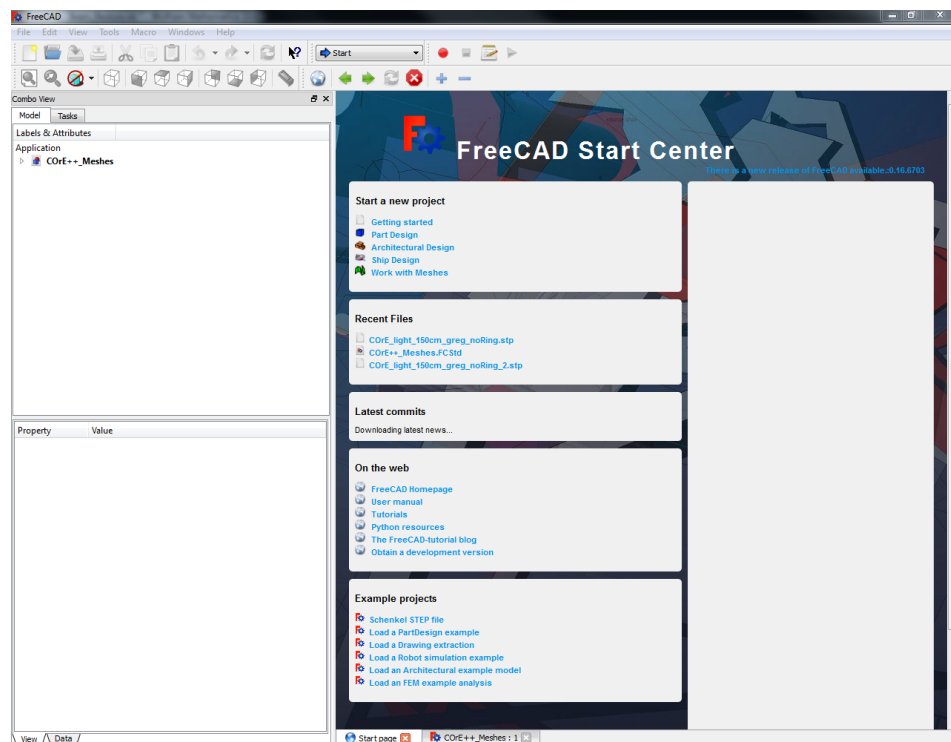


Figure 4.1: The start page presented upon opening FreeCAD. The “start” selection at the top is used to select workbenches.

FreeCAD is an open source CAD program available to download for free ([www.freecadweb.org](http://www.freecadweb.org)). It handles 3D modelling akin to other CAD programs. It is supported by online documentation and active forums. FreeCAD can operate in different modes, known as workbenches. Only the mesh workbench will be discussed here as it is relevant to surface definition.

Subsequent to launching FreeCAD, the user will be presented with the screen shown in Figure 4.1. Note the drop-down menu currently displaying “Start”. This menu allows the user to navigate between the different workbenches. The meshing workbench is named “Mesh Design”. Upon choosing this option the user can create, import and export meshes. Meshing requires a pre-existing object to be loaded into FreeCAD. This can be executed simply by opening a CAD file with FreeCAD. In addition to Binary STL, STEP, IGES and many more formats can be opened by FreeCAD. Figure 4.2 shows the Offset Gregorian design of *CORE* after being imported into FreeCAD. The design was given in a STEP file produced by CODE V. This mirror system required meshes of its mirror to be read into GRASP.

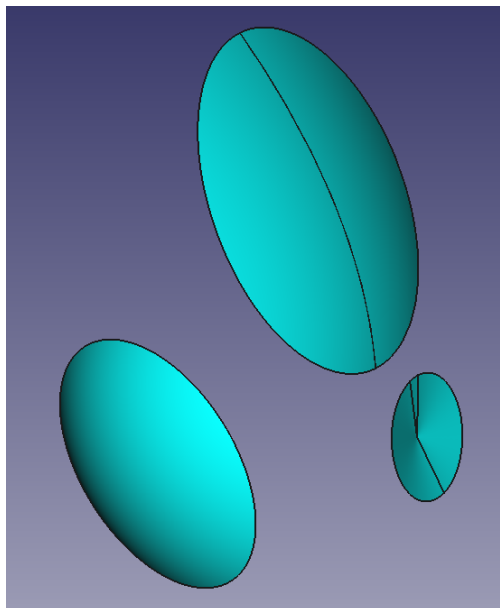


Figure 4.2: *CORE* Offset Gregorian mirrors and focal plane in FreeCAD. Note the workbench has been changed to “Mesh Design”.

Once an object has been loaded into FreeCAD, a mesh of that object can now be created. Three types of mesh are available to the user: Standard, Mefisto and Netgen. Each type fits and joins points in different ways.

Standard meshes use combinations of polygons to represent a surface. The only parameter the user can change is “Surface Deviation”. This parameter sets the maximum allowable deviation between surface point and fitted mesh point. The smaller the value of the parameter, the finer the mesh becomes. The typical values range from 0.1 mm to 0.001  $\mu\text{m}$  at the lower limit. However, this type suffers from a difficulty in meshing plane surfaces, preferring curved elements. An example of this mesh is shown in Figure 4.3.

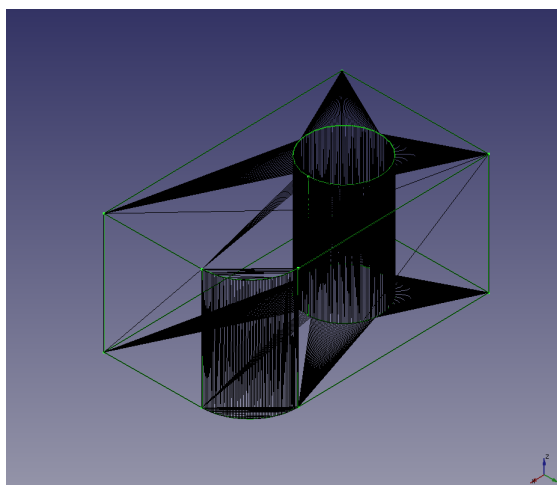


Figure 4.3: Standard mesh type applied to an object. Credit: <http://open-shelf.appspot.com/FreeCAD/en-US/15.html>

Mefisto meshing involves fitting triangles of equal area to an object. The name is drawn from the algorithm which performs the meshing, which is not unique to FreeCAD. Again, the user has only one parameter to set: “Maximum Edge Length”. This parameter sets the upper limit on the maximum edge length of the equilateral triangular areas. Typical values range from 500 mm to 0.1 mm at the lower limit. The smaller this value, the smaller the triangles will be and hence, the finer the meshes will be. This mesh type is able to create meshes of

complex shapes and is useful should regular meshing be required. An example of this mesh is shown in Figure 4.4.

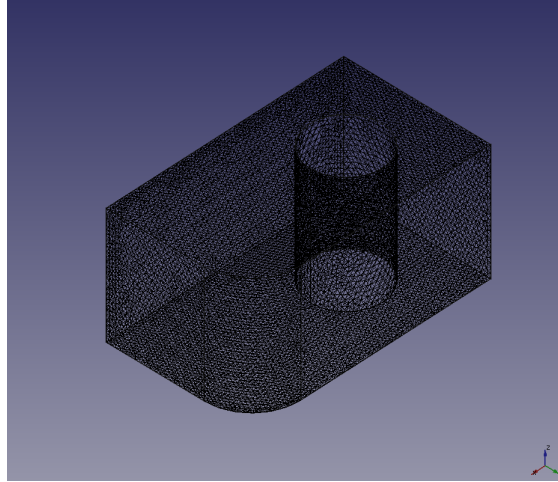


Figure 4.4: Mefisto mesh type applied to an object. Credit: <http://open-shelf.appspot.com/FreeCAD/en-US/15.html>

Finally Netgen meshing is a popular mesh type (again named after its algorithm) which knits together points on a surface into irregular triangles. The advantage of this over the Mefisto method is that the mesh can become denser around edges, which is crucial in dealing with mirrors in physical optics calculations. Diffraction at the rim of a mirror can have a significant effect on the results of PO calculations and beam profile. The user has more options when creating these meshes than the previous two: “Mesh size grading” controls the fineness of the meshes that will be produced (Typical values: 0.3 - 0.1), “Element per edge” sets the number of points that will be created along object edges (Typical values: 1 - 10) and “Elements per curvature radius” does an equivalent operation for curved elements (Typical values: 2 - 10). Finally, the user can choose whether the mesh will be optimised, whether second order elements of the surface will be meshed and whether the mesh will be arranged like a hexahedron. Netgen meshes were used heavily to transfer mirror surfaces between analysis programs. An example of this mesh is shown in Figure 4.5.

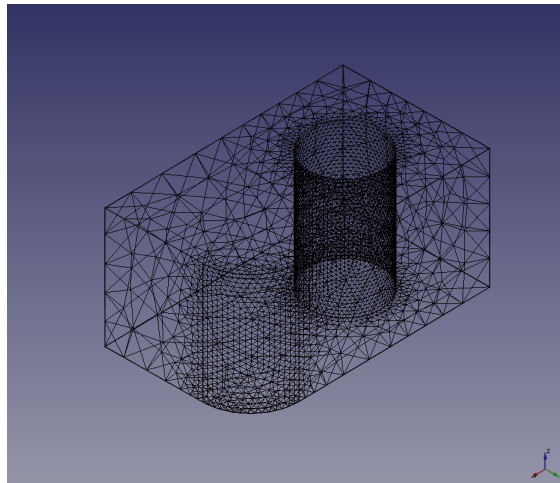


Figure 4.5: Netgen mesh type applied to an object. Credit: <http://open-shelf.appspot.com/FreeCAD/en-US/15.html>

### 4.3 Creating Meshes using CAD Files

Once the model of an optical system is loaded into FreeCAD, meshes of the mirrors and associated objects can be created via the “Meshing Workbench”. The subreflector was the first mirror to be meshed in the *CORE* Offset Gregorian system. With the object selected, the “Create mesh from shape...” interaction becomes available on the “Meshes” workbench.

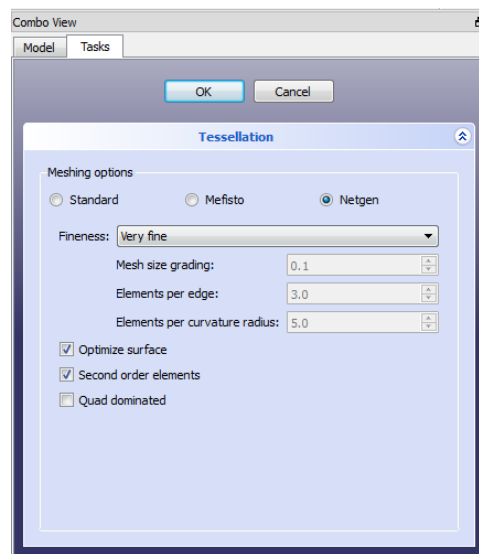


Figure 4.6: The mesh creation window for Netgen meshes. Note the preset fineness selector, which alters the parameters of the beneath it.

Figure 4.6 shows the window that will appear. Netgen meshes are the default type of mesh proffered to the user and were chosen to mesh all the mirrors. Figure 4.6 also displays the mesh creation options (mentioned previously for Netgen meshes) that the user can tweak to produce their desired mesh. The mesh fineness contains presets that range from “Very Coarse” to “Very Fine”. These presets change the values of “Mesh size grading”, “Element per edge” and “Elements per curvature radius”. Additionally the options “Optimize Surface” and “Second order elements” can be checked increase the fidelity of the mesh at the cost of increased creation time and file size (1 KB to 46 KB for *CORE*’s primary mirror, as high as 58 MB for baffling components in the three mirror design). Once the options have been set satisfactorily, clicking the “OK” button at the top of the window will create the mesh.

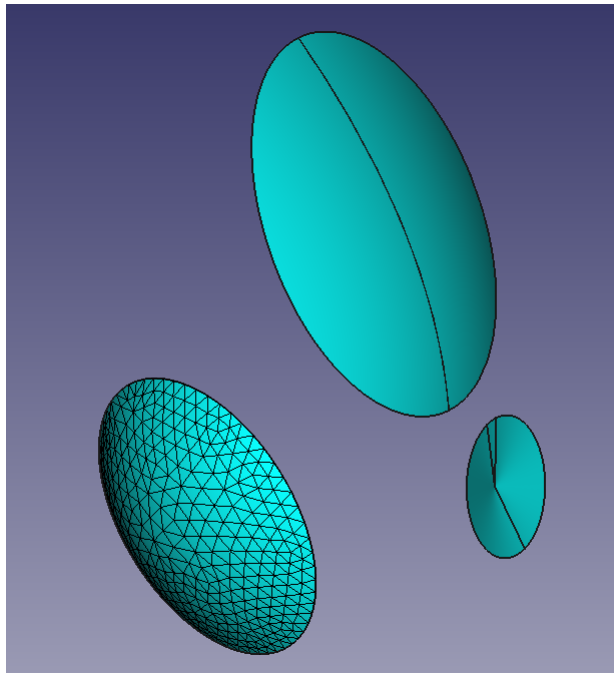


Figure 4.7: *CORE* Gregorian mirrors and focal plane in FreeCAD. A mesh has been placed over the secondary mirror.

Figure 4.7 shows the newly created mesh was overlaid on the subreflector. The mesh itself will be added to the navigation window on the left. The above process was repeated for the primary mirror and focal plane representation.

While the subreflector was represented by a single CAD object, the primary mirror and focal plane were represented by two and three part objects respectively (The joins can be seen in Figure 4.7). This was present in the CAD file from the outset and therefore outside of the author's control. Given this fact, no one mesh can be created to represent the two surfaces. Therefore it was necessary to join the meshes of each object to create a single mesh that suitably represented each object. This option is available in the Mesh workbench. The meshes to be joined are first selected. Then one can simply join them by clicking "Merge" from the "Meshes" drop-down menu. The new merged mesh contains all faces of the previous objects (including inner-facing ones), which differentiates this simple method from Boolean Unions where inner faces will be removed.

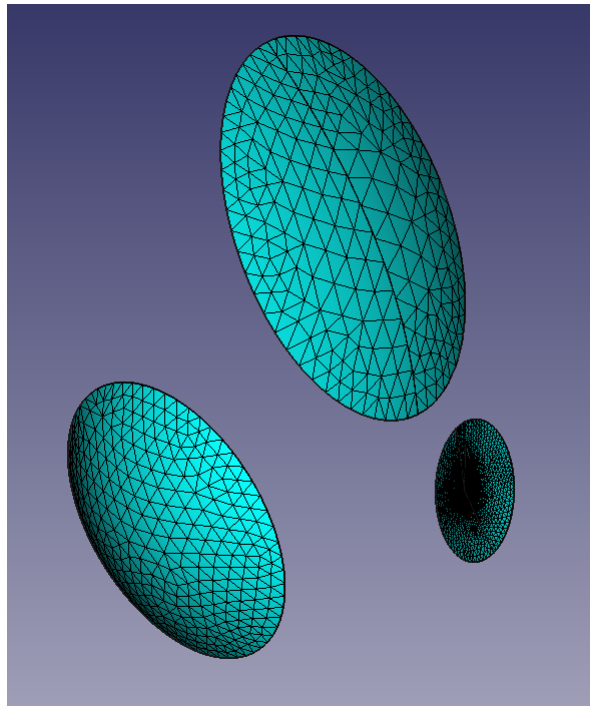


Figure 4.8: The three meshes representing each optical component.

There were then three meshes of the Offset Gregorian system: one for the primary reflector, one for the subreflector and one for the focal plane. They can be seen in Figure 4.8.

The final step of mesh creation was to export the three meshes from FreeCAD. A mesh can be exported by selecting it and choosing the “Export Mesh” option from the “Meshes” menu. The user will be prompted to choose a location to save the exported mesh as well as the file format. There is a wide range of formats from STL files, Nastran Bulk Data Files and FreeCAD’s Python module definition files. The file format chosen was “Python module def” (.py) as this format was easy to reformat as needed and groups constituent points for each triangular mesh section together, which allows the mesh structure to be retained easily while reformatting. They can also be opened by nearly any editor, unlike many CAD-specific formats.

## 4.4 Formatting Mesh Data with Notepad++

GRASP has very strict criteria for importing a surface correctly. The surface in question must be laid out in a specific format which TICRA calls a “.sfc” file:

```

1  .Surface.z values for object:M3_Surface_Output, xy-unit:m, data-unit:mCR LF
2  .....90601CR LF
3  --0.5000000000000000.....-0.5000000000000000.....-0.745918678493398.....CR LF
4  --0.4966666666666667.....-0.5000000000000000.....-0.739961438844399.....CR LF
5  --0.4933333333333333.....-0.5000000000000000.....-0.734040380765427.....CR LF
6  --0.4900000000000000.....-0.5000000000000000.....-0.728154863542366.....CR LF
7  --0.4866666666666667.....-0.5000000000000000.....-0.722304265496447.....CR LF
8  --0.4833333333333333.....-0.5000000000000000.....-0.716487983200074.....CR LF
9  --0.4800000000000000.....-0.5000000000000000.....-0.710705430733735.....CR LF
10 --0.4766666666666667.....-0.5000000000000000.....-0.704956038981396.....CR LF
11 --0.4733333333333333.....-0.5000000000000000.....-0.699239254961966.....CR LF
12 --0.4700000000000000.....-0.5000000000000000.....-0.693554541194607.....CR LF
13 --0.4666666666666667.....-0.5000000000000000.....-0.687901375095812.....CR LF
14 --0.4633333333333333.....-0.5000000000000000.....-0.682279248406324.....CR LF
15 --0.4600000000000000.....-0.5000000000000000.....-0.676687666646133.....CR LF
16 --0.4566666666666667.....-0.5000000000000000.....-0.671126148595844.....CR LF
17 --0.4533333333333333.....-0.5000000000000000.....-0.665594225802920.....CR LF
18 --0.4500000000000000.....-0.5000000000000000.....-0.660091442111327.....CR LF
19 --0.4466666666666667.....-0.5000000000000000.....-0.654617353213243.....CR LF
20 --0.4433333333333333.....-0.5000000000000000.....-0.649171526221585.....CR LF
21 --0.4400000000000000.....-0.5000000000000000.....-0.643753539262185.....CR LF
22 --0.4366666666666667.....-0.5000000000000000.....-0.638362981084508.....CR LF
23 --0.4333333333333333.....-0.5000000000000000.....-0.632999450689916.....CR LF
24 --0.4300000000000000.....-0.5000000000000000.....-0.627662556976489.....CR LF
25 --0.4266666666666667.....-0.5000000000000000.....-0.622351918399542.....CR LF
26 --0.4233333333333333.....-0.5000000000000000.....-0.617067162646973.....CR LF
27 --0.4200000000000000.....-0.5000000000000000.....-0.611807926328674.....CR LF
28 --0.4166666666666667.....-0.5000000000000000.....-0.606573854679256.....CR LF
29 --0.4133333333333333.....-0.5000000000000000.....-0.601364601273405.....CR LF
30 --0.4100000000000000.....-0.5000000000000000.....-0.596179827753218.....CR LF
31 --0.4066666666666667.....-0.5000000000000000.....-0.591019203566890.....CR LF
32 --0.4033333333333333.....-0.5000000000000000.....-0.585882405718223.....CR LF
33 --0.4000000000000000.....-0.5000000000000000.....-0.580769118526356.....CR LF
34 --0.3966666666666667.....-0.5000000000000000.....-0.575679033395259.....CR LF
35 --0.3933333333333333.....-0.5000000000000000.....-0.570611848592493.....CR LF

```

Figure 4.9: The format of a .sfc file including ASCII control characters.

Figure 4.9 shows the format of a .sfc file taken from an exported GRASP mirror surface. The file format itself, while requiring strict formatting, is versatile and can be used for different surface definitions that are all single surfaces. For a standard surface object (above), each line contains a Cartesian  $xyz$  point that makes up the mirror surface (including defined areas that have not been encapsulated by a rim). The points must be ordered regularly for the file to be read in properly. For an irregular surface each line will still contain a Cartesian  $xyz$  point, but these do not need to be ordered; instead they will be grouped into three points and formed into a triangular surface section.

To reformat the python files to be readable to GRASP it was necessary to manually reformat the mesh files. Notepad++ was used for this but any text editor which has a find and replace function and regular expression capability would work just as well.

The Python data file format of a mesh is shown in Figure 4.10:

```

1  faces = [
2  [-601.2809,336.5622,1238.8728], [-562.8213,399.7538,1207.9127], [-505.8040,332.4800,1266.9404],
3  [-523.8931,461.7772,1175.2241], [-467.0298,394.9771,1234.8840], [-562.8213,399.7538,1207.9127],
4  [-409.5905,326.4516,1291.9812], [-505.8040,332.4800,1266.9404], [-467.0298,394.9771,1234.8840],
5  [-562.8213,399.7538,1207.9127], [-467.0298,394.9771,1234.8840], [-505.8040,332.4800,1266.9404],
6  [-409.5905,326.4516,1291.9812], [-315.0914,277.4066,1339.1793], [-433.5848,198.6747,1364.8186],
7  [-219.9912,225.9174,1382.4041], [-338.7383,148.6496,1410.6055], [-315.0914,277.4066,1339.1793],
8  [-456.3024,67.3571,1431.5176], [-433.5848,198.6747,1364.8186], [-338.7383,148.6496,1410.6055],
9  [-315.0914,277.4066,1339.1793], [-338.7383,148.6496,1410.6055], [-433.5848,198.6747,1364.8186],
10 [0.0000,695.7173,1062.6027], [0.0000,623.3840,1120.8020], [-89.0729,669.1481,1082.4393],
11 [0.0000,549.7458,1177.3418], [-89.0826,596.2905,1140.0367], [0.0000,623.3840,1120.8020],
12 [-178.0341,640.4802,1099.6823], [-89.0729,669.1481,1082.4393], [-89.0826,596.2905,1140.0367],
13 [0.0000,623.3840,1120.8020], [-89.0826,596.2905,1140.0367], [-89.0729,669.1481,1082.4393],
14 [-585.4702,574.1296,1076.1588], [-525.0261,629.8791,1049.0662], [-476.6625,572.9415,1105.0024],
15 [-458.5729,679.7874,1024.7866], [-412.9631,625.0413,1078.3322], [-525.0261,629.8791,1049.0662],
16 [-367.0374,569.0496,1130.2969], [-476.6625,572.9415,1105.0024], [-412.9631,625.0413,1078.3322],
17 [-525.0261,629.8791,1049.0662], [-412.9631,625.0413,1078.3322], [-476.6625,572.9415,1105.0024],
18 [-523.8931,461.7772,1175.2241], [-554.8516,518.4196,1126.3258], [-445.7614,516.4233,1154.1371],
19 [-585.4702,574.1296,1076.1588], [-476.6625,572.9415,1105.0024], [-554.8516,518.4196,1126.3258],
20 [-367.0374,569.0496,1130.2969], [-445.7614,516.4233,1154.1371], [-476.6625,572.9415,1105.0024],
21 [-554.8516,518.4196,1126.3258], [-476.6625,572.9415,1105.0024], [-445.7614,516.4233,1154.1371],
22 [-669.8589,46.4245,1384.5333], [-741.6427,78.4554,1343.8429], [-641.0150,121.1119,1354.6450],
23 [-812.6715,109.3848,1301.0325], [-712.7680,153.1098,1313.7955], [-741.6427,78.4554,1343.8429],
24 [-611.4879,194.6004,1322.5364], [-641.0150,121.1119,1354.6450], [-712.7680,153.1098,1313.7955],
25 [-741.6427,78.4554,1343.8429], [-712.7680,153.1098,1313.7955], [-641.0150,121.1119,1354.6450],
26 [0.0000,368.8055,1304.7780], [0.0000,253.9400,1377.2882], [-110.1530,299.2239,1346.5676],
27 [0.0000,136.1479,1444.9460], [-110.1305,182.4862,1416.2323], [0.0000,253.9400,1377.2882],

```

Figure 4.10: Mesh data file before reformatting. Each line represents three vertices that make up a triangular face.

The steps taken to reformat the data file are as follows:

- Open Find and Replace using keyboard shortcut CTRL + H.
- Set search mode to “Extended”
- Find “],” and replace with “\r\n”.
- There should now be three numbers on each line separated by a comma, with every fourth line blank.
- Switch search mode to “Regular expression”
- Find “^\ $(s^*)$ ” and replace with “”
- The blank lines should disappear
- Set search mode back to “Extended”
- Find “[” and replace with “”
- Find “]” and replace with “”
- All of the square brackets will now have been removed
- Find “,” and replace with “, \t”
- N.B. A space must be included between “,” and “\t”
- There should now be three columns of numbers with no commas present in the third column
- Replace line 1 with a header for the file
- Enter the number of rows containing numbers into line 2
- Line 3 should be the start of the data
- Save the file as a .sfc file

Figure 4.11 shows the data file after reformatting had taken place.

```

1  COrE++_Primary_Datafile
2  1320
3  -601.2809, 336.5622, 1238.8728
4  -562.8213, 399.7538, 1207.9127
5  -505.8040, 332.4800, 1266.9404
6  -523.8931, 461.7772, 1175.2241
7  -467.0298, 394.9771, 1234.8840
8  -562.8213, 399.7538, 1207.9127
9  -409.5905, 326.4516, 1291.9812
10 -505.8040, 332.4800, 1266.9404
11 -467.0298, 394.9771, 1234.8840
12 -562.8213, 399.7538, 1207.9127
13 -467.0298, 394.9771, 1234.8840
14 -505.8040, 332.4800, 1266.9404
15 -409.5905, 326.4516, 1291.9812
16 -315.0914, 277.4066, 1339.1793
17 -433.5848, 198.6747, 1364.8186
18 -219.9912, 225.9174, 1382.4041
19 -338.7383, 148.6496, 1410.6055
20 -315.0914, 277.4066, 1339.1793
21 -456.3024, 67.3571, 1431.5176
22 -433.5848, 198.6747, 1364.8186
23 -338.7383, 148.6496, 1410.6055
24 -315.0914, 277.4066, 1339.1793
25 -338.7383, 148.6496, 1410.6055
26 -433.5848, 198.6747, 1364.8186
27 0.0000, 695.7173, 1062.6027
28 0.0000, 623.3840, 1120.8020
29 -89.0729, 669.1481, 1082.4393

```

Figure 4.11: Mesh data file after reformatting. Each line now represents a vertex point location.

## 4.5 Importing Mirror Surfaces into GRASP

This section will explain how the mirrors were imported into GRASP. The reformatting meshes were imported using an “Irregular xy-Grid, Triangulation” surface.

This can be found under the *Geometrical Objects/Tabulated Surfaces* menu.

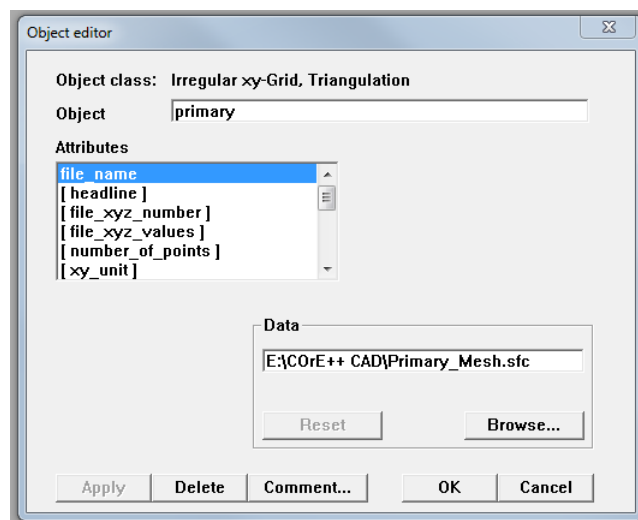


Figure 4.12: The triangulation surface Object Editor.

The object editor for triangulation surfaces can be seen in Figure 4.12. The file path to the .sfc file was entered into the “file name” field. The “xy unit” and “z unit” fields were also changed to millimetres for all three surfaces. The other parameters can be set in the menu or read in automatically from the supplied .sfc file.

The mirrors could then be implemented like any other in GRASP. Three reflector objects were used: one for the primary mirror, one for the secondary mirror and one for the focal plane. Rims for the mirrors in this case were elliptical rims, which require a radius in  $x$  and  $y$ . The half-axis values for the three objects were found by analysing the original parts in FreeCAD. There is also a decentre value needed, which can be thought of as a translation from the reference coordinate system of the mirror to the centre of the mirror. All three objects share the global coordinate system as their base coordinate system. Hence, by setting this as the reference coordinate system for each, the mirrors will retain their positions and orientations relative to each other. This is an important factor to consider when importing mirrors into GRASP. The final design can be seen in Figure 4.13 below:

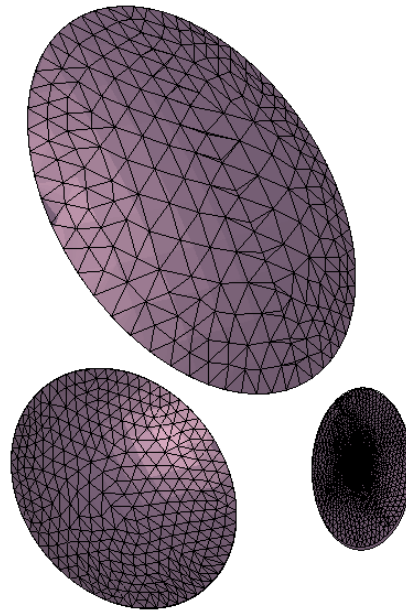


Figure 4.13: The *CORE* Offset Gregorian design in GRASP.

## 4.6 Comparison of Mesh Types

A comparison of different mesh densities will be presented for the LLAMA receiver. LLAMA has the advantage over *CORE* in that standard GRASP mirror definitions existed for its mirrors (M3 and M4); *CORE* only had meshed versions of its mirrors. This would allow a direct comparison between meshed surfaces and standard, mathematically defined conics. Three densities of mesh were used; their associated values are displayed below in Tables 4.1 and 4.2:

M3 Mesh Values			
Mesh Type	Faces	Edges	Vertices
Custom Density	1344	2070	727
Very Fine Density	520	810	291
Fine Density	176	282	107

Table 4.1: Face, edge and vertex values for the three mesh densities used for M3.

M4 Mesh Values			
Mesh Type	Faces	Edges	Vertices
Custom Density	1312	2022	711
Very Fine Density	520	810	291
Fine Density	176	282	107

Table 4.2: Face, edge and vertex values for the three mesh densities used for M4.

Note that custom mesh density refers to a mesh that was made to be as dense, point-wise, as FreeCAD allowed. The LLAMA Band 9 frequency (660 GHz) was chosen for this comparison due to its lengthier computation times (a result of the higher frequency). This was done to limit any inherent variability in computation time. The results for each different surface type are shown in Table 4.3:

Variable Surface PO Results (Band 9)			
Surface Type	Co-Polar Power (dB)	Cross-Polar Power (dB)	Calc. Time (s)
Conic Mirror Surface	-22.69	-49.53	3.36
Standard Surface	-22.69	-49.56	7.36
Custom Mesh	-22.69	-49.57	15.88
Very Fine Mesh	-22.69	-49.57	10.5
Fine Mesh	-22.69	-49.57	16.4

Table 4.3: Results of Band 9 calculations for varying surface types.

Plots were constructed on the above data to more easily discern the difference between the five surface types used. They can be seen in Figures 4.14 - 4.16:

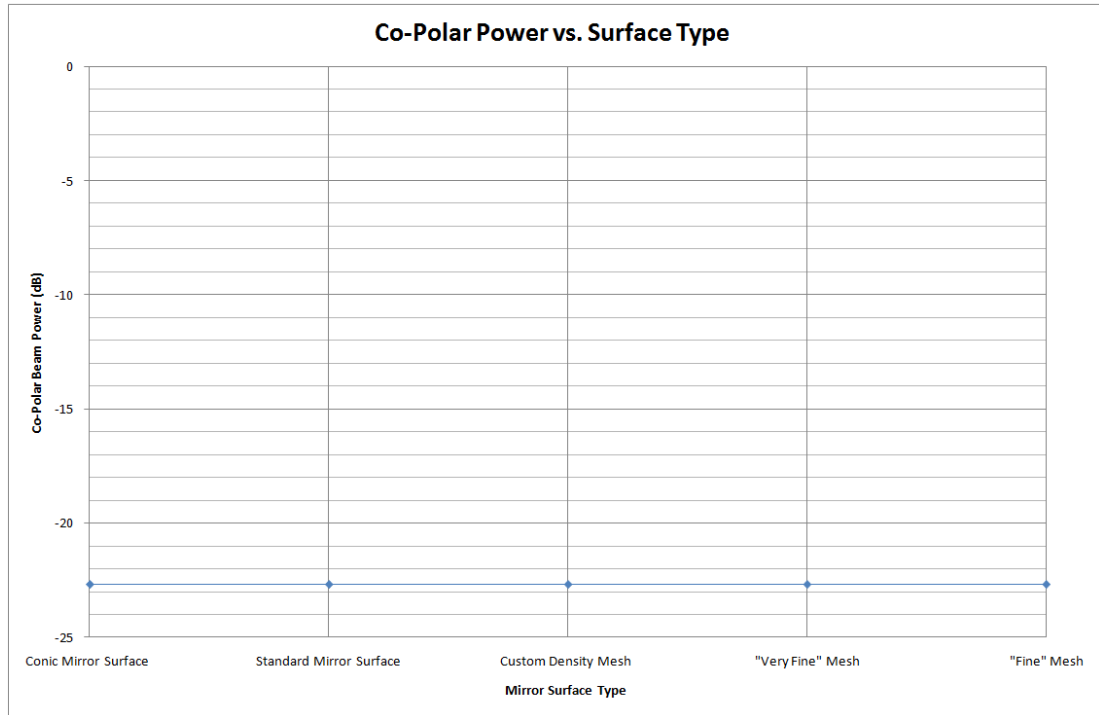


Figure 4.14: Co-Polar power per surface type.

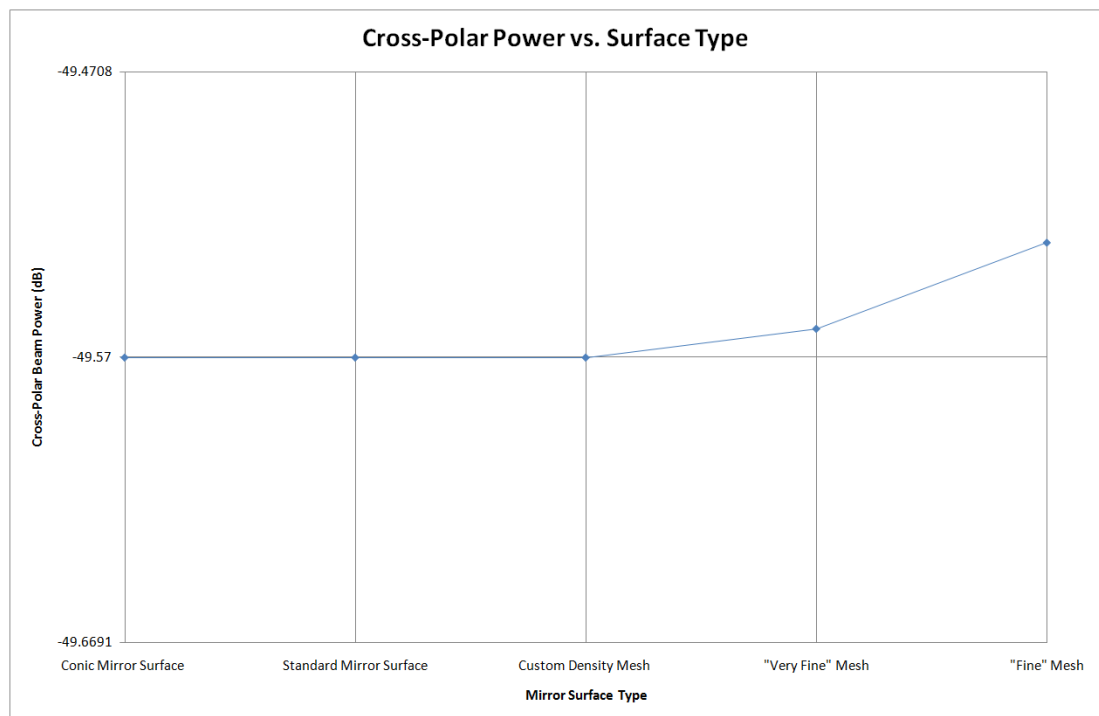


Figure 4.15: Cross-Polar power per surface type.

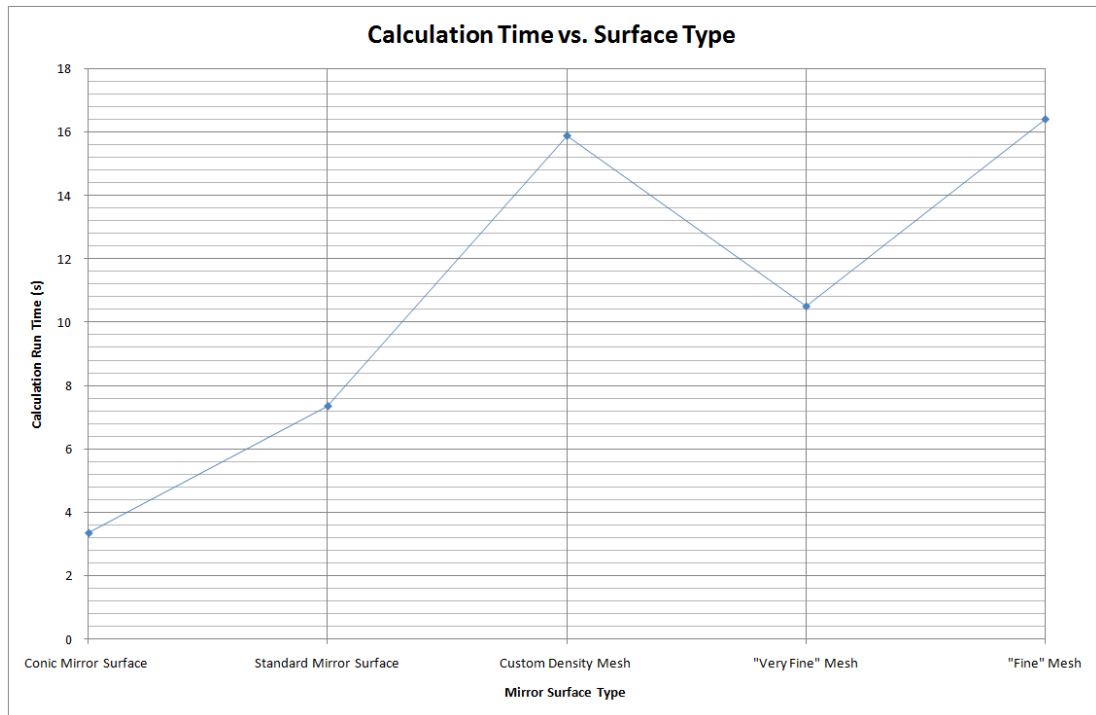


Figure 4.16: Time taken for computation per surface type.

### 4.6.1 Conclusions

Looking at the data presented, there seems to be little variation with surface used. The conic mirror surfaces were chosen as the control. Both they and the standard mirror surfaces set the bar for co-polar and cross-polar power levels and computation time. The meshed surfaces vary in their computation times but are longer for the initial two surface types. The time difference between these surface types may be down to the generation of PO evaluation points, but timing will be discussed in a moment. More concretely we have the co-polar and cross-polar power levels. Co-Polar power levels are identical across the board, which is unsurprising. GRASP smooths the surface before calculations commence. However, the cross-polar power levels exhibit minor differences across the surface types. The levels reduced down to a minimum when the two GRASP-defined surfaces were used and also the custom, high point density mesh. Unlike measurements of time, these power level measurements are reproducible. Therefore, common sense

holds out and the most representative mesh matches its progenitors the closest.

Now, the timing will be discussed. The time taken to complete a PO calculation is complex and therefore is rarely reproducible. When performing convergence tests to PO points on a surface and subsequently calculating induced currents, GRASP will always follow the same pattern for a certain reflector. However, the speed at which this can be done is dependent on the machine GRASP is running on. Better processors and memory will allow the calculations to proceed much faster. Mundane factors like running another intensive program alongside GRASP can dramatically affect runtimes as well. This is all obvious to the computer-literate. Therefore, the only reasonable conclusion to draw from the timing results is that meshes seem to take longer to run. This makes sense given the difference in how GRASP must prepare meshed surfaces when compared to its own conic based ones.

The best mesh density for optimal accuracy without excessive over-sampling is a difficult matter to determine. There is a method in GRASP to control the minimum distance between mesh points in the  $xy$ -plane, with those points closer than this distance being removed. By default, this distance is set to zero. Also, GRASP will fit a polynomial to a meshed surface in order to smooth it. As a result, one could justify using less dense meshes. However, finding out the lower limit on mesh density is complex. First, the number of points fitted by a meshing algorithm will vary by surface. Figure 4.15 demonstrates that the highest density mesh matches the GRASP surfaces perfectly in terms of co-polar and cross-polar power, while the less dense meshes start to diverge (if only very slightly). Considering that high mesh density can be seen to translate to more accurate surfaces (despite the previously mentioned systems to bolster lower density meshed surfaces) and that the lower density limit will vary by surface, the author recommends using the highest density meshes where possible as a

precaution while recognising that the polynomial fit feature of GRASP makes less dense meshes far more viable.

# Chapter 5

## LLAMA Optical Analysis

### 5.1 Background

The purpose of this section is to deliver preliminary results from PO analysis of the proposed unfolded configuration of the receiver for the Large Latin American Millimetre Array (LLAMA) Bands 5, 6 and 9 (which is based on an ALMA receiver design). The two mirrors (which will be known as M3 and M4) were defined using alternate surface definitions in order to allow the mirrors themselves to be exported in a CAD format to facilitate CNC manufacturing and to verify that different mirror definitions give equivalent performance.

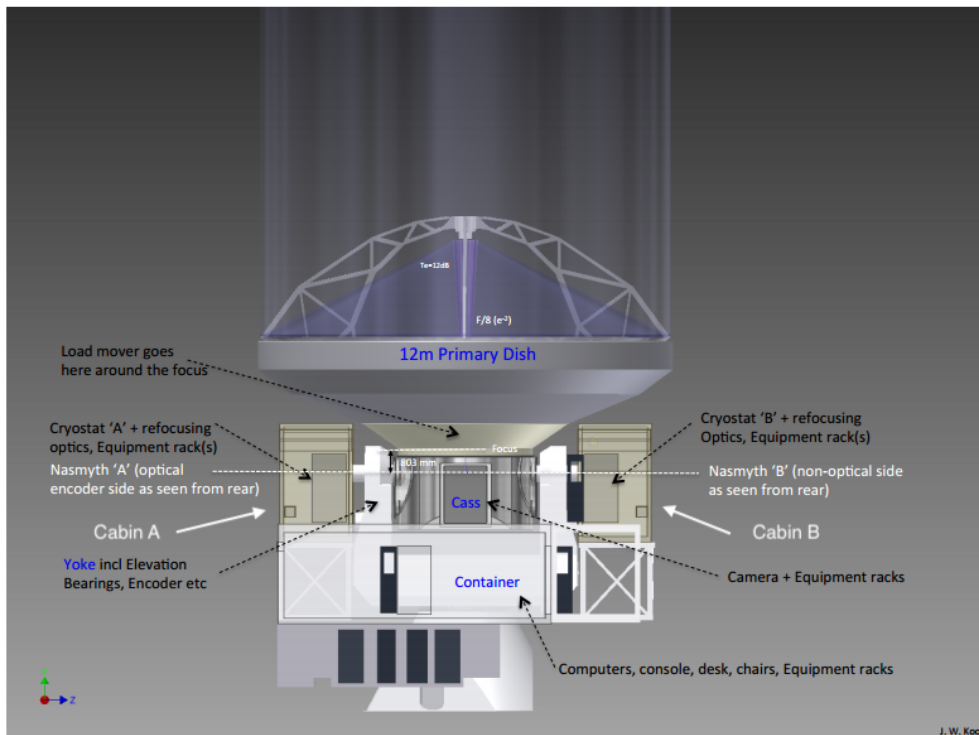


Figure 5.1: LLAMA elements showing telescope and Nasmyth cabins.

LLAMA is a 12 m telescope under construction in the Puna region of the Atacama desert in Argentina using similar configurations as ALMA. It is a Cassegrain design telescope with ALMA-equivalent front-end optics (12 m telescope built by Vertex AntennenTechnik GmbH as reported by LLAMA (2016)) but with Nasymth receiver architecture. Figure 5.1 is a figure taken from the LLAMA “First Light Unfolded Optics” report Kooi (2016). It shows the telescope with two Nasmyth focus cabins, designated Cabin A and Cabin B. Cabin A contains an optical encoder which converts the received signal to light pulses. Cabin B houses a non-optical encoder. LLAMA (2016) claims that LLAMA will observe from 35 GHz up to 1 THz. According to Kooi (2016) it is desirable to have simultaneous observations between both receivers. Cabin A has a narrower entrance aperture than B, which means that it can only accommodate the higher frequencies ( $> 220$  GHz). In order for Cabin B to cover this wide range of frequencies, the entrance aperture must be frequency-independent. Frequency-independence here means that beams of different frequencies (which ordinarily have different beam sizes) must be made to have a fixed beam size in order to fit through the window to the cryostat unit housing the detectors with high optical throughput and low truncation levels at the aperture edges where the aperture dimension is at least  $4\omega_a$  in diameter (where  $\omega_a$  is the beam radius at the aperture).

LLAMA bands 5 (163 - 211 GHz), 6 (211 - 275 GHz) and 9 (602 - 720 GHz) were chosen for the first light observations. As LLAMA is planned to work alongside primarily ALMA in a VLBI configuration as well as a single reflector, the frequency bands were matches for those used by ALMA. A frequency-independent receiver design known as a Gaussian beam telescope was chosen, consisting of an elliptical mirror M3 and a hyperboloidal mirror M4 (see Figure 5.4). The point of contact for this work was Dr. Jacob Kooi, a receiver engineer at JPL and technical advisor for the LLAMA optical interface, including the GBT under investigation. The design of the GBT needed to be validated in GRASP for

physical optics analysis and subsequently verify that the current design meets LLAMA optical system requirements. Figure 5.2 shows the simplified LLAMA optical train implemented in GRASP.

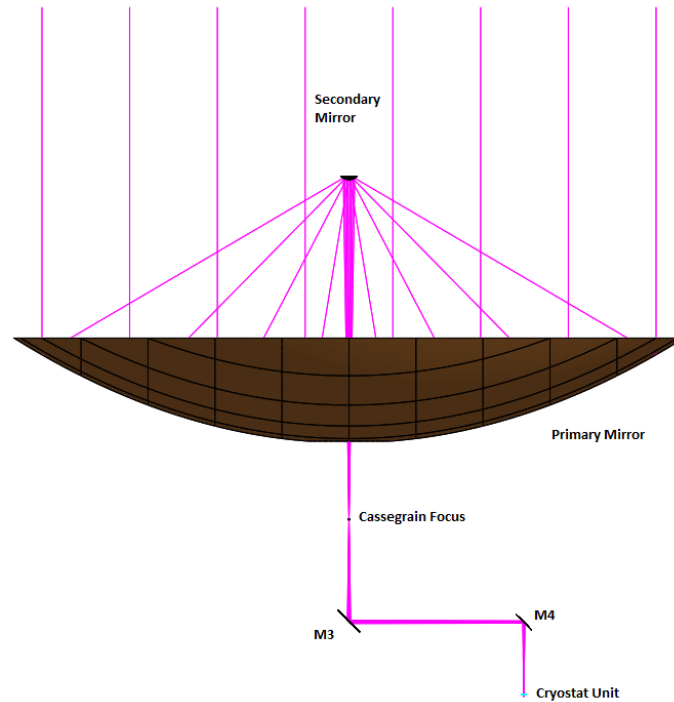


Figure 5.2: LLAMA simplified optical train for Nasmyth B receiver.

## 5.2 GRASP Implementation

Maynooth's role in LLAMA was to verify the design of the receiver and also to carry out detailed PO analysis to verify ultimate optical performance. A memo by Kooi (2016) was sent to the department containing information on the receiver including expected beam radii at optical surfaces, system geometry, mirror parameters and frequency bands to be tested. Verification of the design involved confirming that the expected beam waists (acquired through ray matrix analysis) from the memo matched those acquired from physical optics calculations. Once verified, the mirrors would need to be exported from GRASP and sent to the LLAMA technicians for manufacture.

The system was first created in GRASP9. Simple Gaussian beams of the correct dimension were used as sources given their good approximation to the intended corrugated scalar horn antennae, which would be located inside the cryostat unit. The effect of a GBT will be such that the input waist and output waist will be identical and system is reciprocal, so choice of which focus to propagate from is irrelevant. Following the propagation chain in the memo, the source was placed at the Cassegrain focus of the main reflector dish and beams were propagated towards a planar detection grid, placed at the cartridge focus, to record the output beam profile. Regarding band cartridge layout, Kooi (2016) states that LLAMA will not adopt ALMA's radial cartridge layout as it does not make sense given their Nasmyth configuration. See Figure 5.3 for a schematic layout of the receiver and Figure 5.4 for the representative optical system in GRASP.

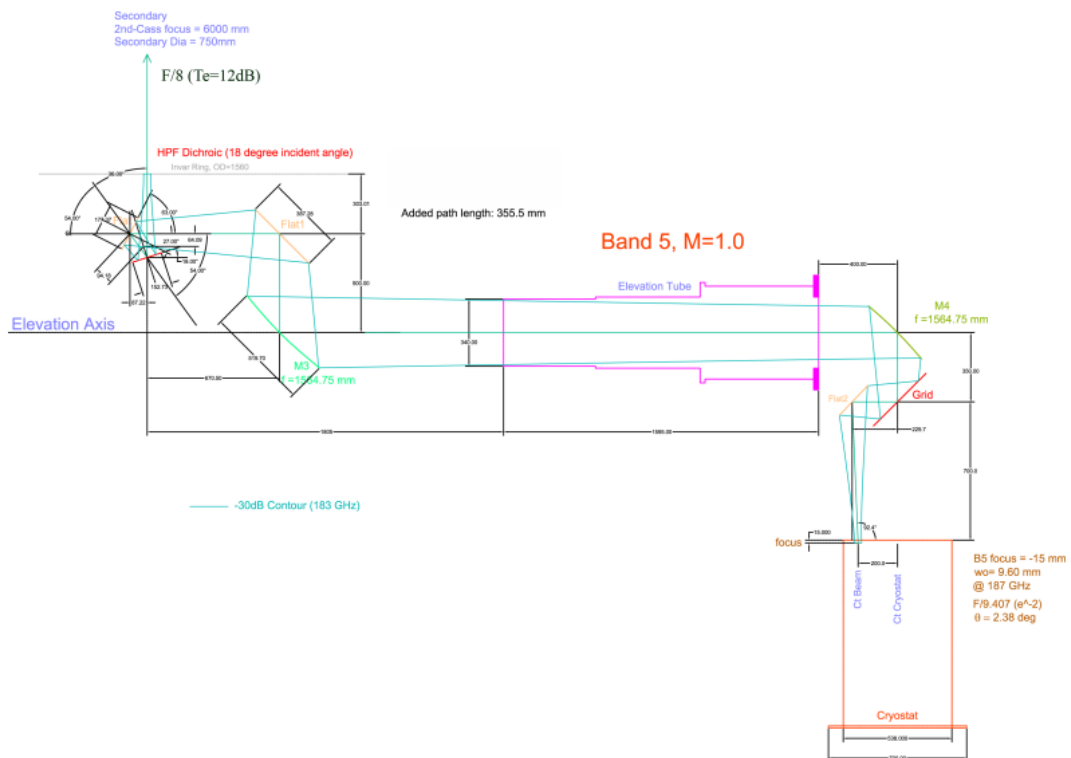


Figure 5.3: The fully unfolded LLAMA GBT from Kooi (2016).

Figures 5.3 and 5.4 show the two mirrors placed according to the layout in first light report. The global  $x$ ,  $y$  and  $z$  directions can be seen in the lower left corner

of Figure 5.3. One focus of M3 was placed over the Cassegrain focus (where the input analysis beam is located). M4 (at this stage an ellipsoidal mirror) was placed a distance of 3129.50 mm from M3. The radius of M4 was 140.1 mm and the radius of M3 was 197.5 mm. Finally, the output grid (whose coordinate system can be seen in the bottom right of Figure 5.3) was placed 1300 mm away from M4 at an angle of  $90^\circ$ . Note that the output plane must be oriented  $180^\circ$  about the global  $y$ -axis in order to function properly.

### 5.3 GRASP Analysis

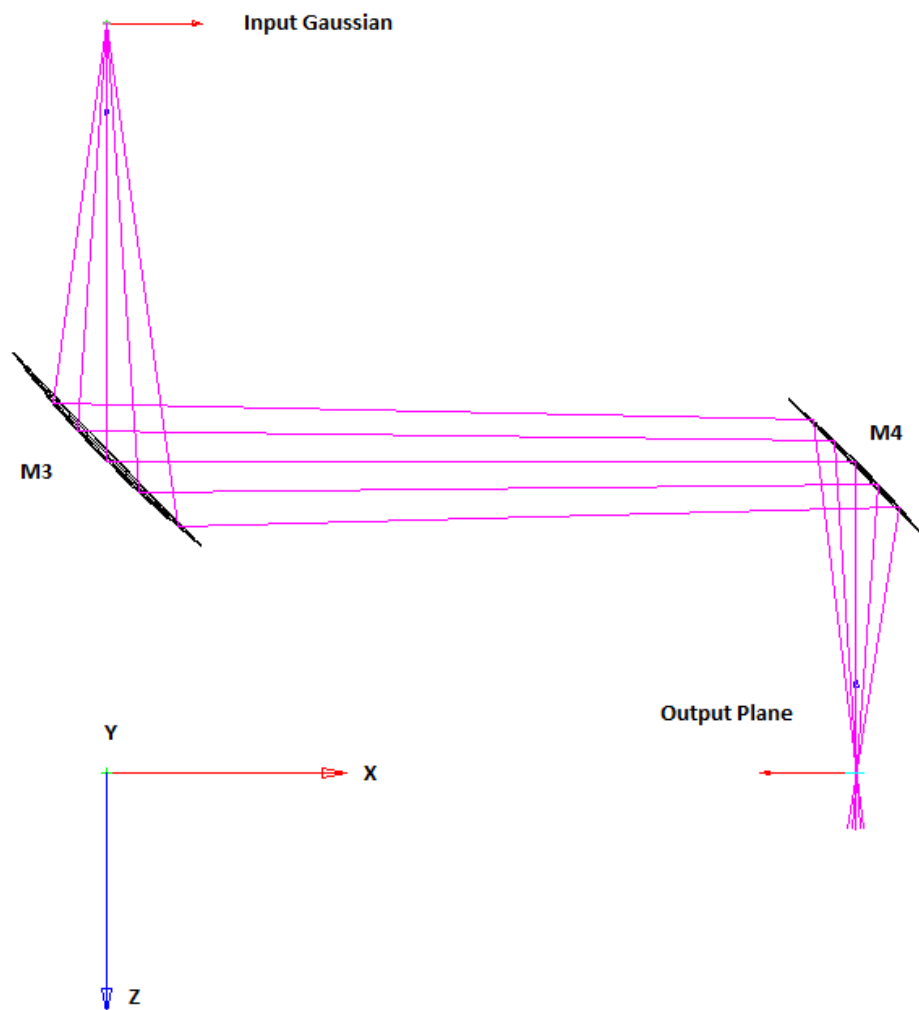


Figure 5.4: OpenGL plot of the folded LLAMA GBT in GRASP.

The initial implementation of the mirrors in GRASP was done using Conic Mirror Surfaces. A conic mirror surface in GRASP is a precursor class of surfaces from which the others (Ellipsoidal, Hyperbolic, etc.) are derived. These surfaces require two distances,  $r1$  and  $r2$ , which are the distances from the surface of the mirror to the two foci that defines the surface of the mirror. Two angles are also required,  $\theta_i$  and  $\theta_n$ , which are half the bending angle of the mirror and the direction of the surface normal measured from the positive  $x$ -axis.

As the Conic Mirror Surface (CMS) requires two foci, it can be used to recreate both elliptical and hyperbolic mirrors. If either  $r1$  or  $r2$  are negative, then a hyperbolic mirror will be created. If both are positive, then an elliptical mirror will be created. If  $r1$  or  $r2$  have a value of infinity, then a parabolic mirror will be created. Figures 5.5, 5.6 and 5.7 should help to illustrate this concept:

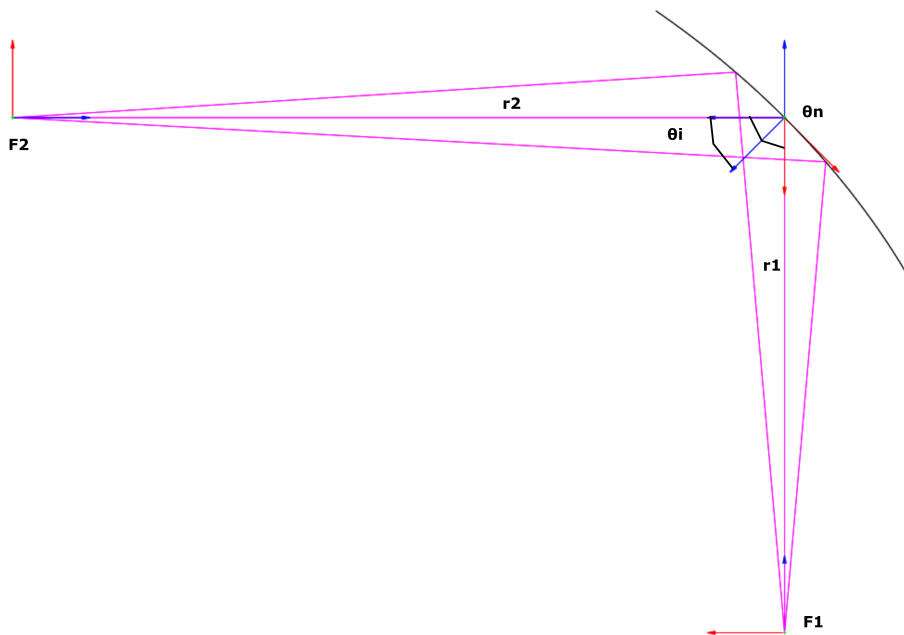


Figure 5.5: Elliptical mirror design using CMS.

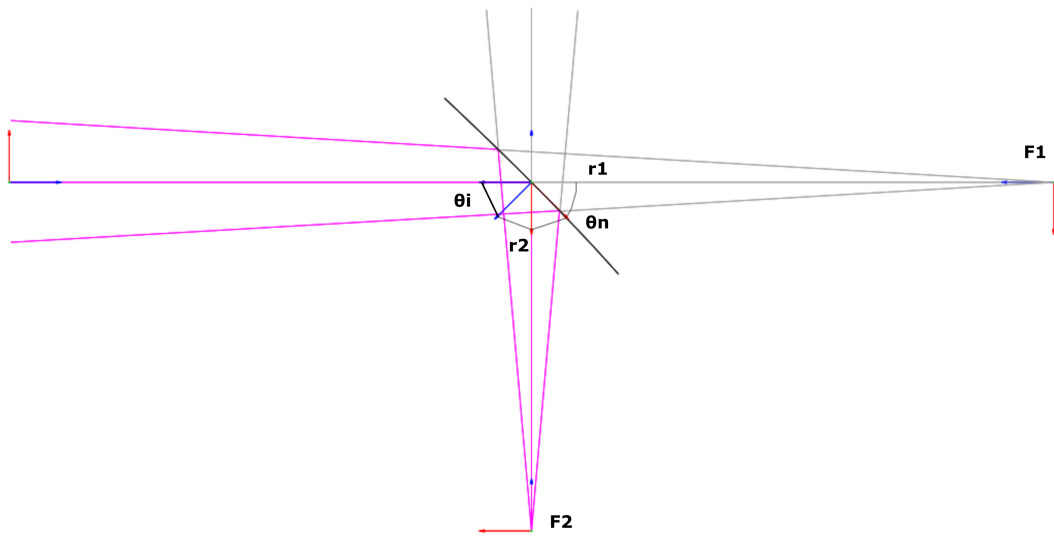


Figure 5.6: Hyperbolic mirror design using CMS.

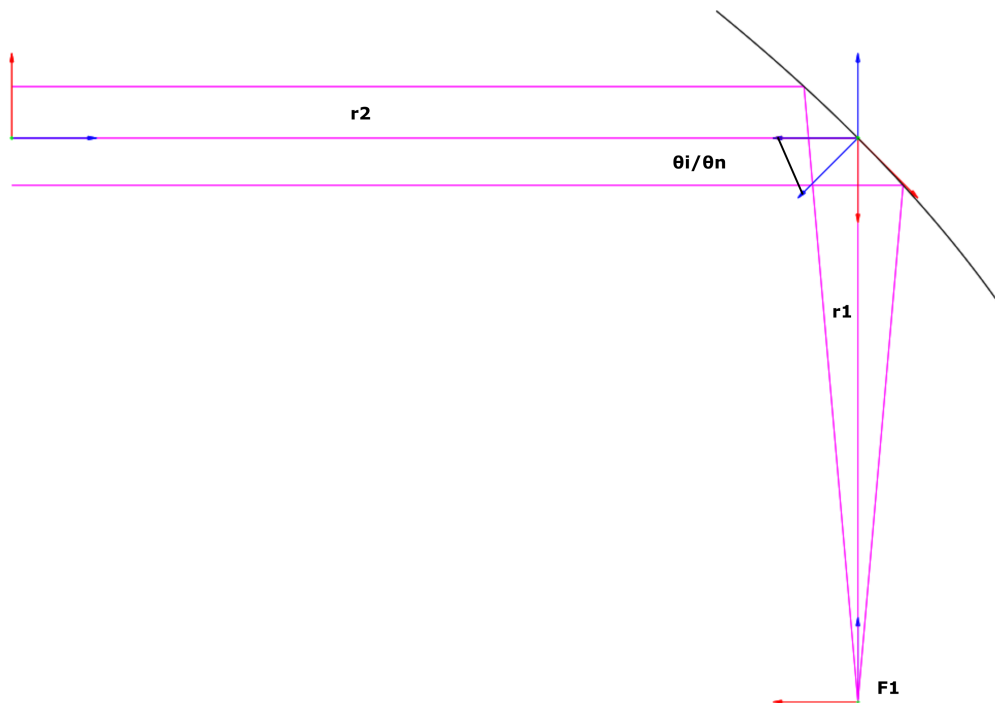


Figure 5.7: Parabolic mirror design using CMS.

The parameters used to construct M3 and M4 are listed in Tables 5.1 and 5.2

and are derived from the LLAMA optical design:

<b>M3 CMS Parameters</b>	
<b>r1 (mm)</b>	1829.0
<b>r2 (mm)</b>	10830.38
$\theta_i$ (°)	-45.0
$\theta_n$ (°)	135.0

Table 5.1: M3 parameters for implementation in GRASP.

<b>M4 CMS Parameters</b>	
<b>r1 (mm)</b>	1300.0
<b>r2 (mm)</b>	-7683.38
$\theta_i$ (°)	135.0
$\theta_n$ (°)	-45.0

Table 5.2: M4 parameters for implementation in GRASP.

## 5.4 Results of the Physical Optics Analysis

The results of the GRASP analysis will be presented in this section. A Gaussian beam was propagated from the feed placed at the Cassegrain focus to M3 (representing a beam from the 12 m LLAMA telescope), then to M4 and finally to a planar output grid placed at the cartridge focus. The centre frequency of each band (B5, B6 and B9) was used to carry out the analysis. Band 5 covers frequencies 163 - 211 GHz with centre frequency 187 GHz. Band 6 covers 211 - 275 GHz with centre frequency 243 GHz. Finally, Band 9 covers 602 - 720 GHz with 660 GHz as the centre frequency.

For each plot presented in this chapter, the **E** and **H**-cuts of the copolar beam are presented along with a Gaussian equivalent beam using the expected beam waist at the output grid for each band. Please note that, for all plots in this chapter, “**E**” refers to the electric field, which lies along the  $x$ -direction of the output grid. “**H**” refers to the magnetic field which itself follows the  $y$ -direction of the grid. Figure 5.4 shows the positive  $x$ -direction heading towards M4 and

positive  $y$ -direction heading out of the page. This convention holds for all plots and results presented in this chapter.

Gaussicity is calculated with the best fit overlap of an equivalent Gaussian field with the output field from GRASP. The beam waists in the  $x$  and  $y$  direction ( $\omega_{0x}$  and  $\omega_{0y}$  respectively) are the beam waists of the equivalent Gaussian beam. Finally,  $\omega_{0 \text{ Expected}}$  is the expected beam waist. Figure 5.8 shows the grids used to record the beams overlaid on each other.

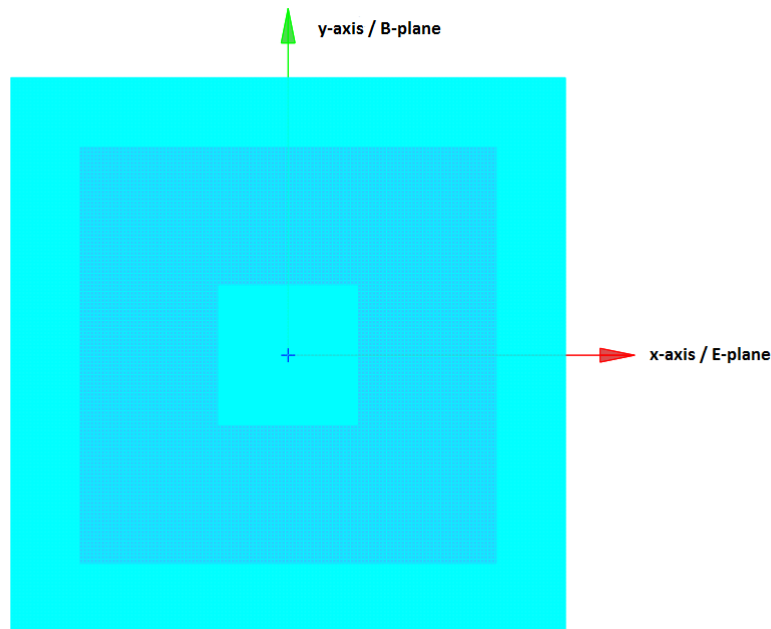


Figure 5.8: Output grids for Bands 5, 6 and 9. Note the orientation of the grid and how it relates to the recorded  $\mathbf{E}$  and  $\mathbf{B}$  fields.

#### 5.4.1 Band 5 Results (163 - 211 GHz)

This section lists plots (linear and logarithmic) of the beam at the cartridge focus for Band 5. A plane grid of size 80 mm by 80 mm and located at the cartridge focus was used with 201 samples in both directions. The convergence for the beam in GRASP was set to -120 dB, which ensures accuracy above these levels.  $\omega_0$  was set to 9.6 mm. The centre frequency was 187 GHz. Results of a Gaussian

beam fitting routine applied to the beam are also included. Please note that in Figures 5.9 - 5.16, “E” refers to the E-plane and “H” refers to the H-plane.

### 5.4.2 Band 5 Plots

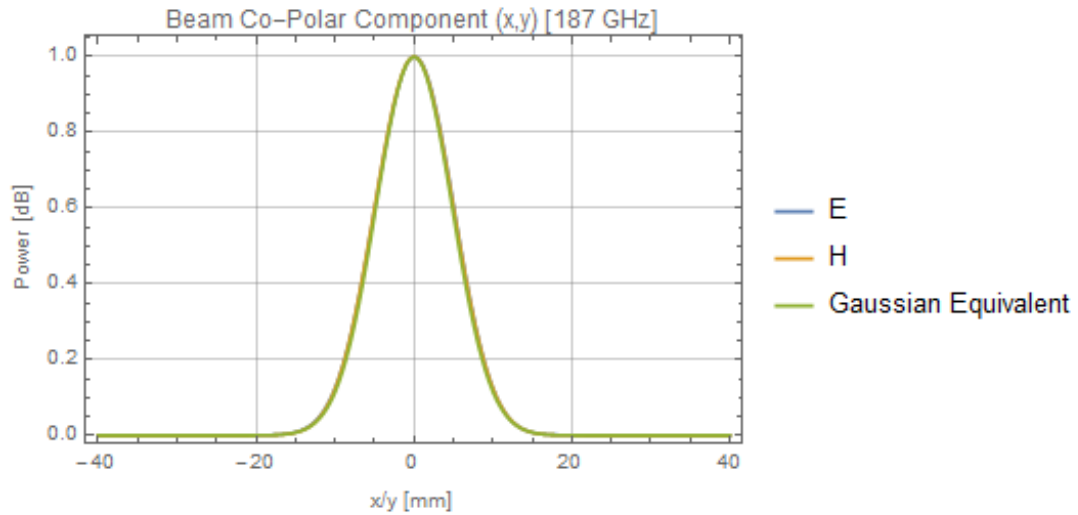


Figure 5.9: Band 5 linear plot of the co-polar beam at 187 GHz. An equivalent Gaussian function ( $\omega_0 = 9.6$  mm) has been included for comparison.

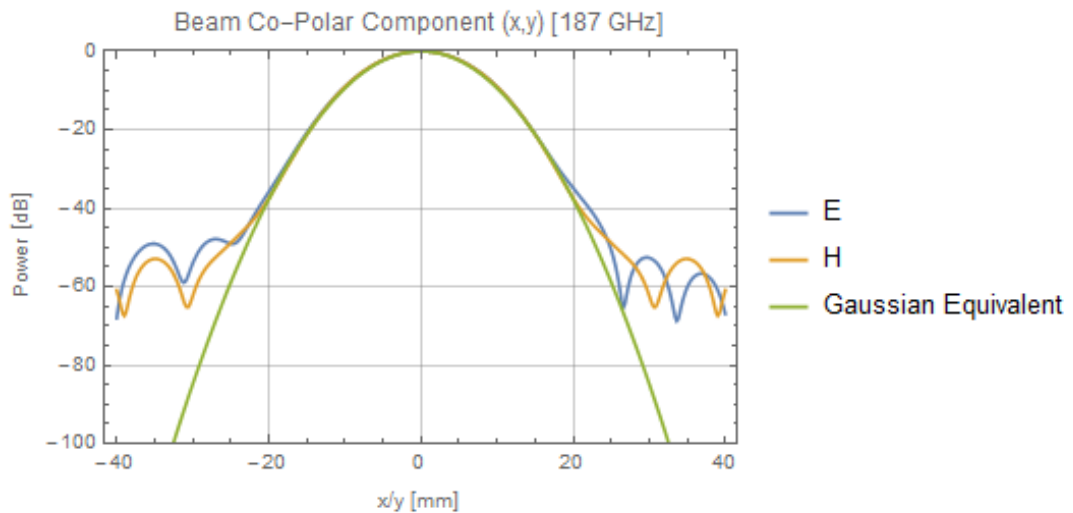


Figure 5.10: Band 5 log-plot of the co-polar beam at centre frequency 187 GHz. An equivalent logarithmic Gaussian function ( $\omega_0 = 9.6$  mm) has been included for comparison.

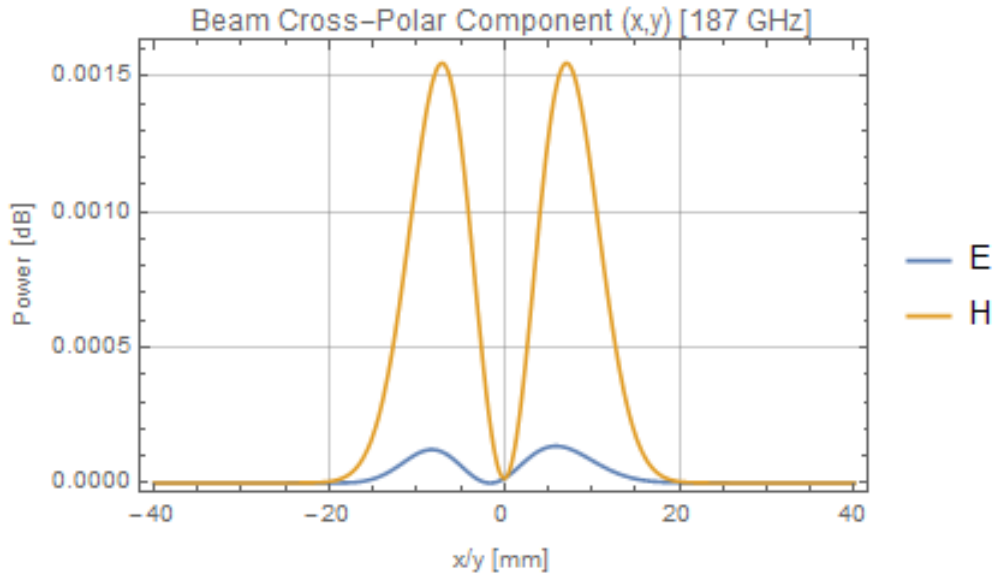


Figure 5.11: Band 5 linear plot of the cross-polar beam at 187 GHz.

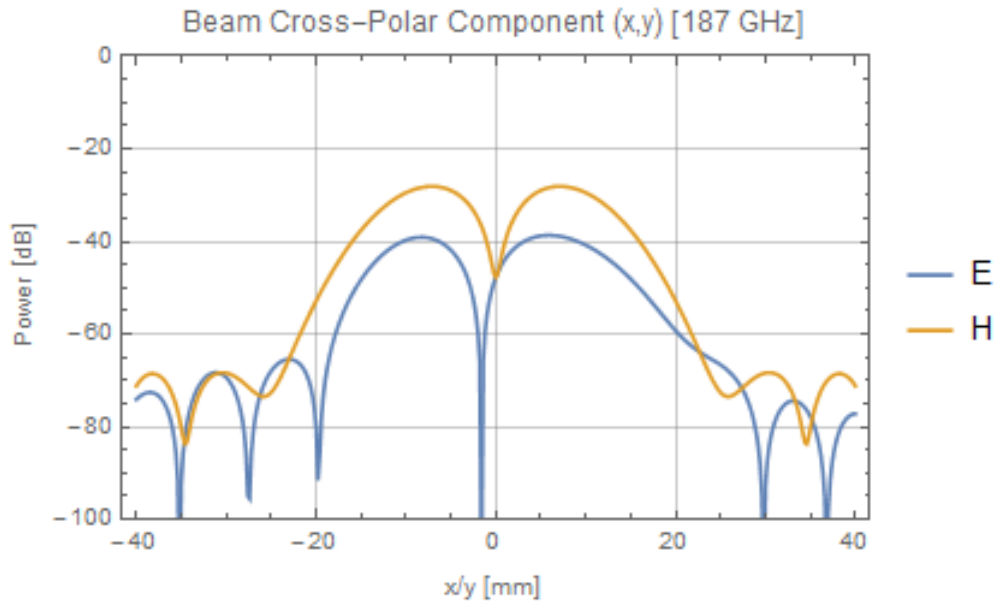


Figure 5.12: Band 5 log-plot of the cross-polar beam plot at 187 GHz.

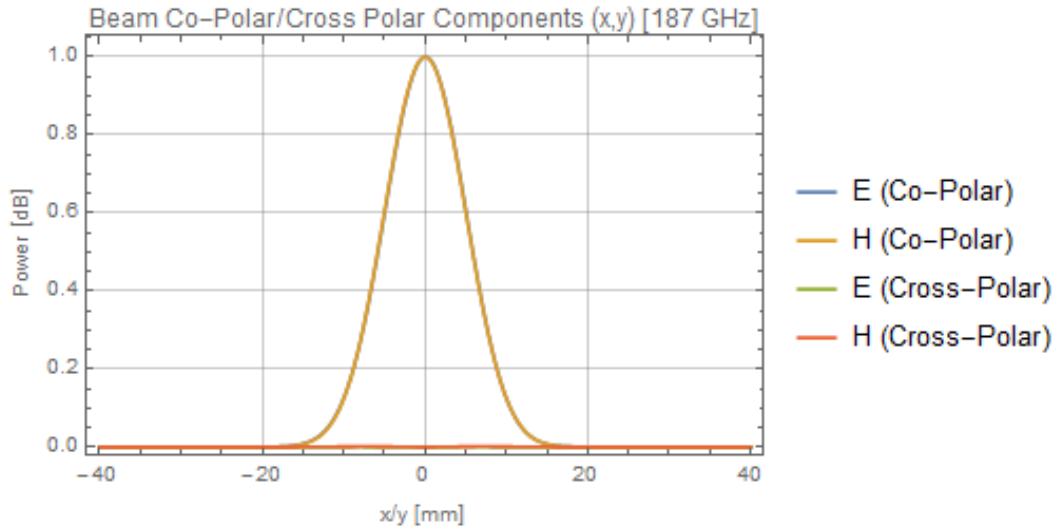


Figure 5.13: Band 5 combined beam linear plot at 187 GHz. The equivalent Gaussian is no longer present.

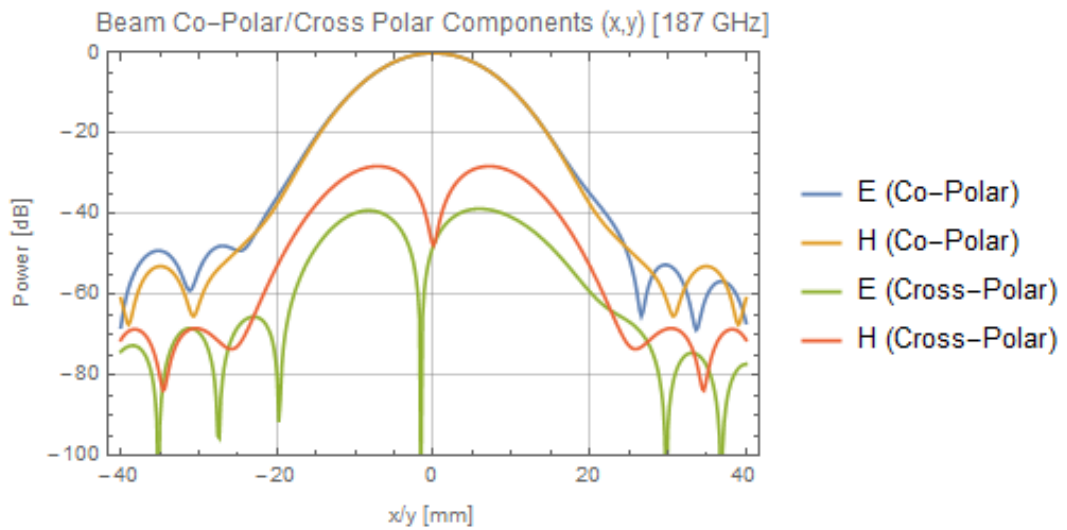


Figure 5.14: Band 5 combined beam log-plot at 187 GHz. Again, the equivalent Gaussian is no longer present. Note the low sidelobe levels and high beam symmetry.

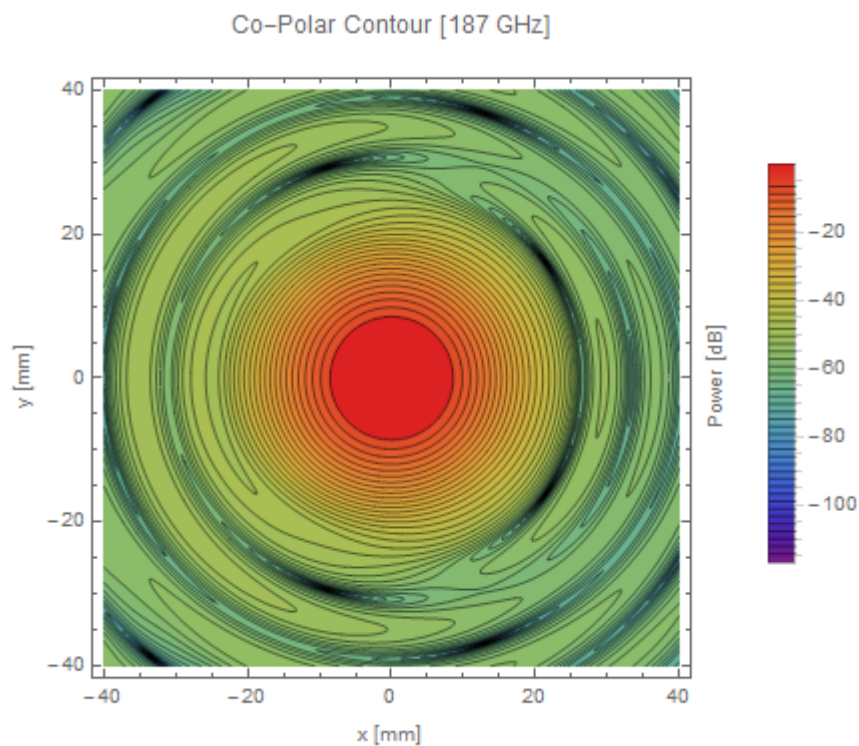


Figure 5.15: Band 5 co-polar contour plot at 187 GHz.

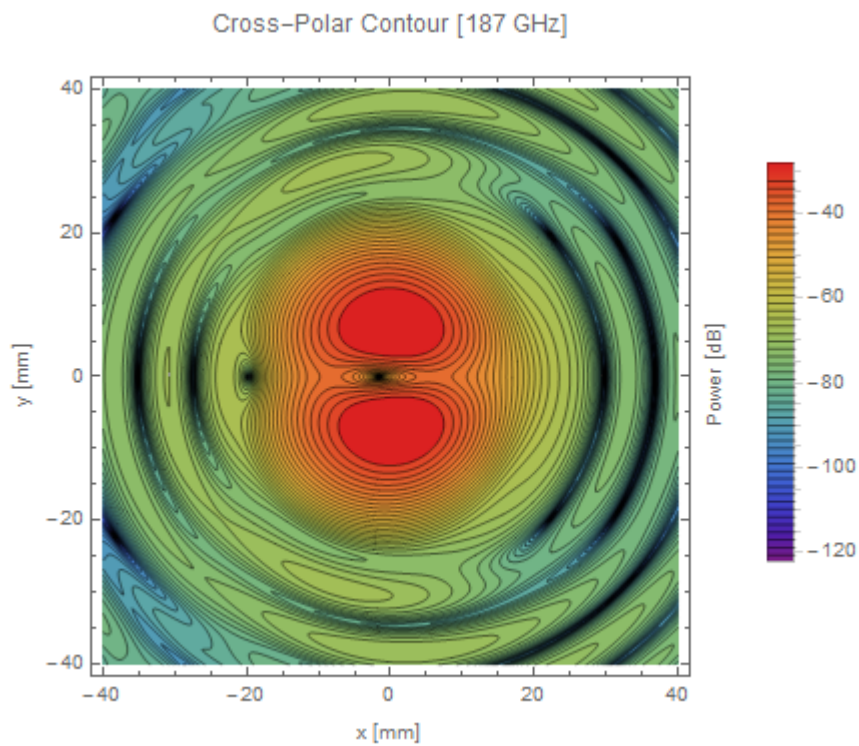


Figure 5.16: Band 5 cross-polar contour plot at 187 GHz.

### 5.4.3 Band 5 Results and Discussion

Physical Optics Results (Band 5)							
Gaussianity (%)	$\omega_{0x}$ (mm)	$\omega_{0y}$ (mm)	X offset (mm)	Y Offset (mm)	X Tilt (°)	Y Tilt (°)	$\omega_0$ Expected (mm)
99.81	9.85	9.84	0.024	0	0	0.001	9.60

Table 5.3: Band 5 results. Note that tilt here refers to phase tilt.

As can be seen in Table 5.3, the beam waists at the cryostat in both  $x$  and  $y$  match the expected beam waists supplied in Kooi (2016) to the order of  $\pm 0.25$  mm. The cause of the difference was found to be the size of the mirrors. Diffraction effects would occur at the mirror edge. If the mirror size is doubled (M4 radius: 391.4 mm, M3 radius: 280.2 mm), the beam waists will match the sizes reported in Kooi (2016), which themselves are derived from ray matrix analysis. The diffraction effect from the finite size of the mirror surfaces has a significant effect in reality but could not be included in basic optical analysis. Despite the small discrepancy, the beam was found to be over 99 % Gaussian after fitting, indicating low aberration after propagation through the receiver. The levels of the cross-polar beam component is around the -30 dB level, indicating low beam distortion being generated by the receiver. Having satisfied the conditions that the fitted beam waists match the expected beam waists the receiver design can be considered verified for Band 5.

### 5.4.4 Band 6 Results (211 - 275 GHz)

The following section lists plots (linear and logarithmic) of the beam at the cryostat focus for Band 6. The beam ( $\omega_0 = 7.385mm$ ) was launched from the Cassegrain focus and propagated from M3, to M4 and to the focus in the band cartridge. The planar output grid was located at the cartridge focus, the detector horn location. The grid size was decreased to 60 mm by 60 mm, with 201 samples in both  $x$  and  $y$  directions. The convergence for the beam was set to -120 dB. The frequency was 243 GHz. Also included are the results of Gaussian fitting on

the beam. Please note that in Figures 5.17 - 5.24, “E” refers to the E-plane and “H” refers to the H-plane.

### 5.4.5 Band 6 Plots

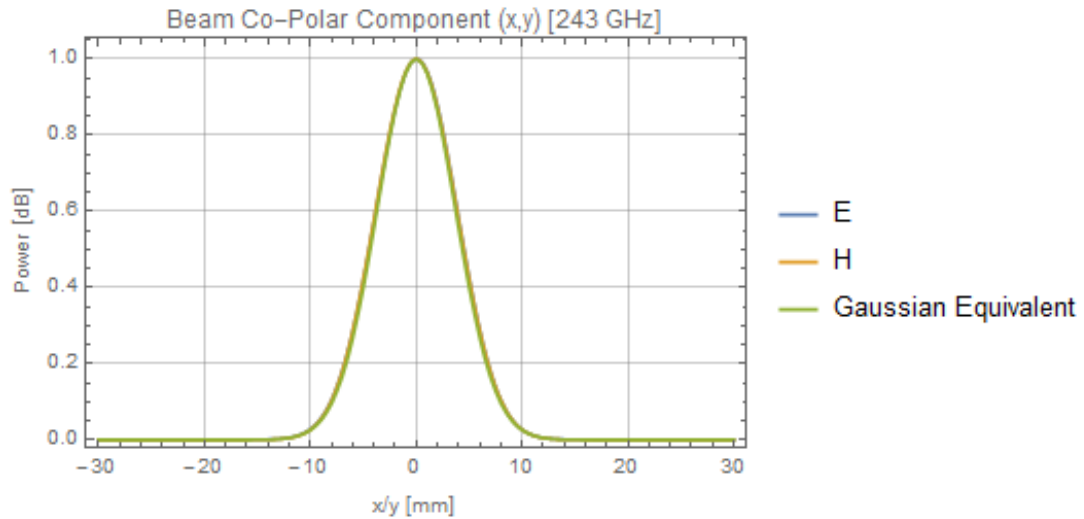


Figure 5.17: Band 6 linear plot of the co-polar beam at centre frequency 243 GHz. An equivalent Gaussian function ( $\omega_0 = 7.385$  mm) has been included for comparison.

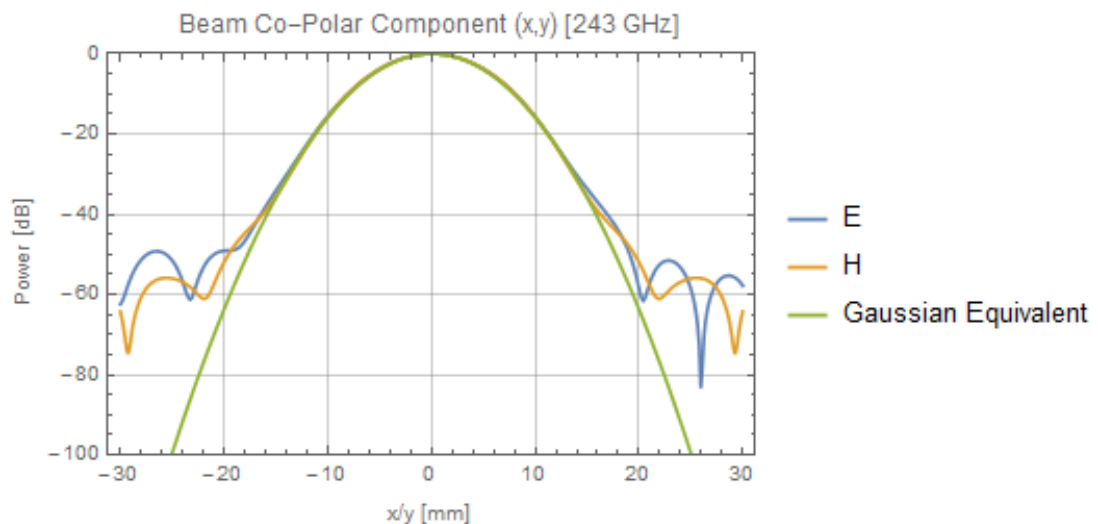


Figure 5.18: Band 6 log-plot of the co-polar beam at centre frequency 243 GHz. An equivalent logarithmic Gaussian function ( $\omega_0 = 7.385$  mm) has been included for comparison.

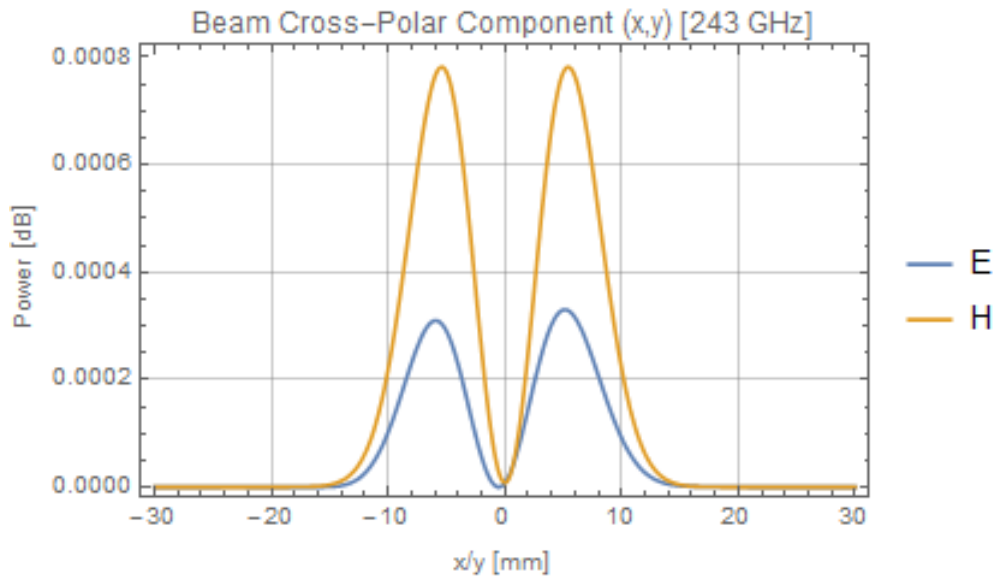


Figure 5.19: Band 6 linear plot of the cross-polar beam at 243 GHz.

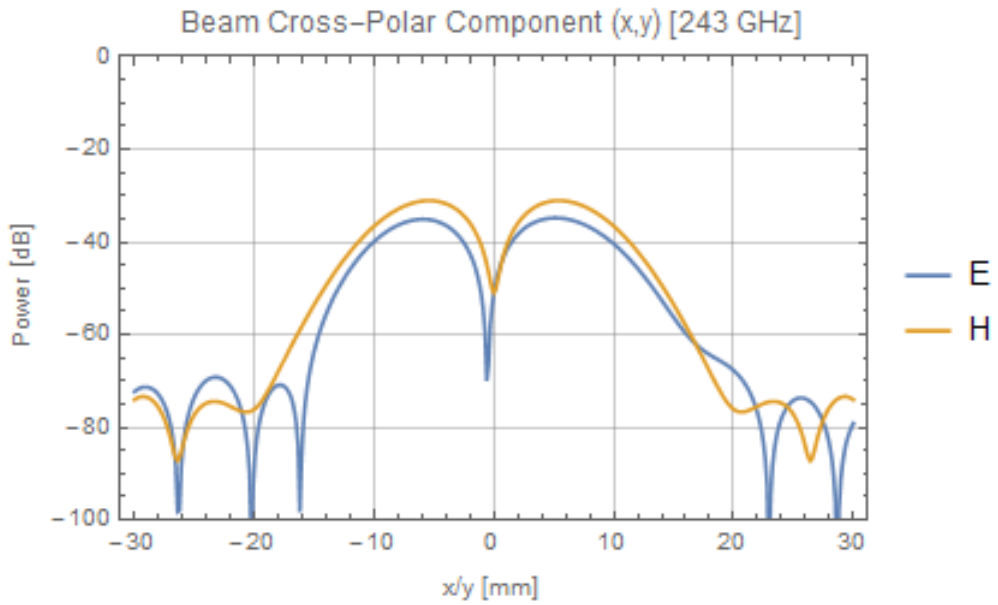


Figure 5.20: Band 6 log-plot of the cross-polar beam at 243 GHz.

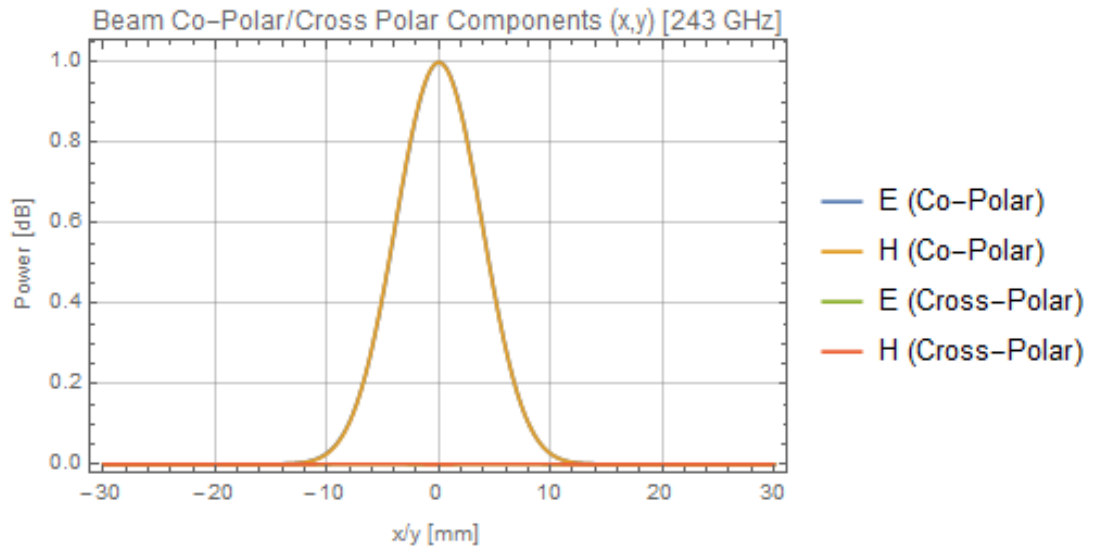


Figure 5.21: Band 6 combined beam linear plot at 243 GHz.

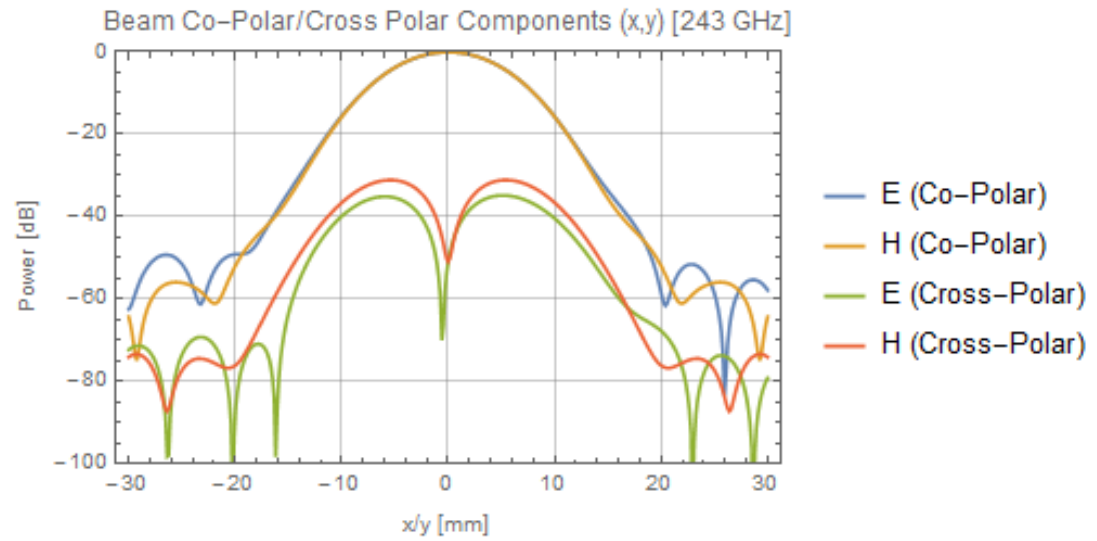


Figure 5.22: Band 6 combined beam log-plot at 243 GHz. Note the low sidelobe levels (-50 dB) and consistent level of symmetry from Band 5.

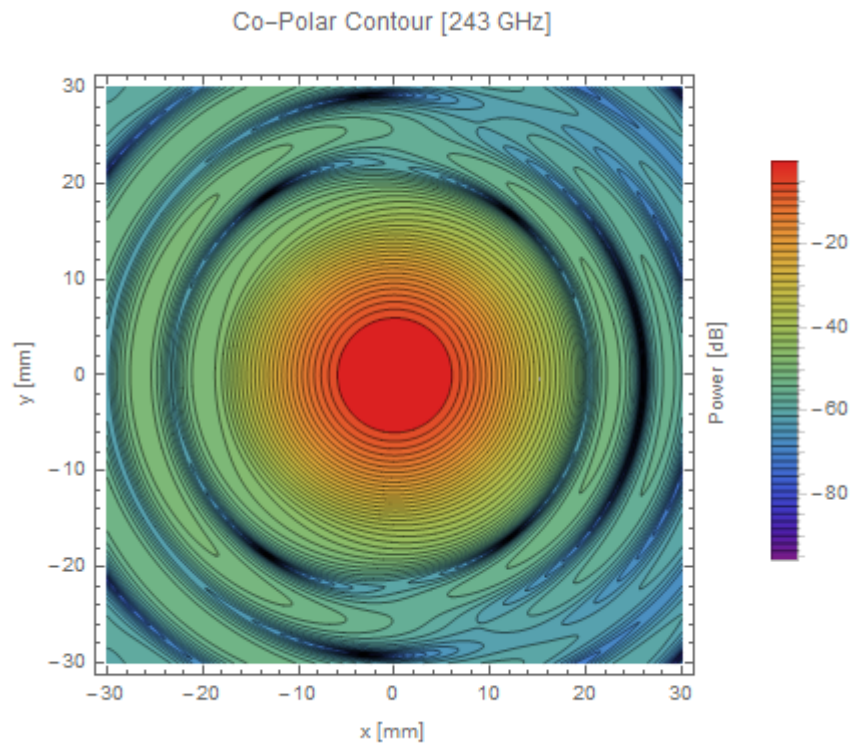


Figure 5.23: Band 6 co-polar contour plot at 243 GHz.

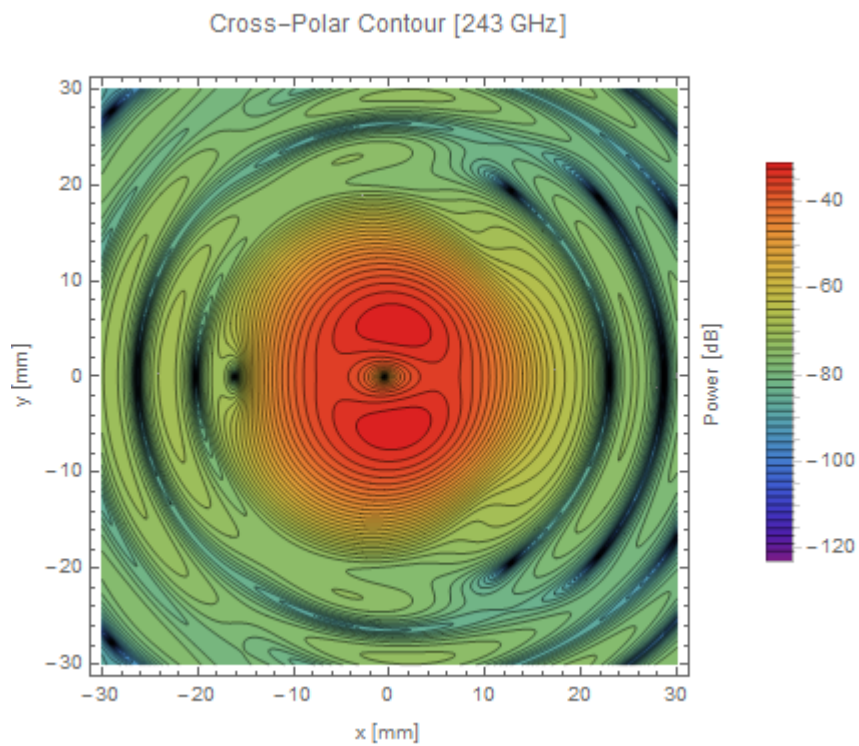


Figure 5.24: Band 6 cross-polar contour plot at 243 GHz.

### 5.4.6 Band 6 Results and Discussion

Physical Optics Results (Band 6)							
Gaussicity (%)	$\omega_{0x}$ (mm)	$\omega_{0y}$ (mm)	X Offset (mm)	Y Offset (mm)	X Tilt ( $^{\circ}$ )	Y Tilt ( $^{\circ}$ )	$\omega_0$ Expected (mm)
99.84	7.58	7.58	0.015	0	-0.0009	0	7.385

Table 5.4: Band 6 results. Note that tilt here refers to phase tilt.

As can be seen in Table 5.4, the beam waists at the cryostat in both  $x$  and  $y$  match well the expected beam waists supplied in Kooi (2016) to the order of  $\pm 0.195$  mm. Again diffraction effects at the mirror rim will affect the beam but, due to the smaller beam profile at this higher frequency the discrepancy is less than that found for Band 5. The beam was found to be over 99 % Gaussian after fitting, indicating low aberration after propagation through the receiver for this higher frequency band. It is higher than the Gaussicity reported for Band 5, which is expected due to the lower aberration and smaller beam size relative to the mirror size due to the higher frequency. The levels of the cross-polar beam component is around the -30 dB level again, indicating high polar purity being generated by the receiver. Having satisfied the conditions that the fitted beam waists match the expected beam waists the receiver design can be considered verified for Band 6.

### 5.4.7 Band 9 Results (602 - 720 GHz)

The following section lists plots (linear and logarithmic) of the beam at the cartridge focus for Band 9. A plane grid of size 20 mm by 20 mm was used with 201 samples in both directions. Again, the output grid was located at the cartridge (the detector horn location). The convergence for the beam was set to -120 dB.  $\omega_0$  was given a value of 2.7196 mm. The frequency was 660 GHz. As before, fitting results will be presented after the plot section. Please note that in Figures 5.25 - 5.32, “E” refers to the E-plane and “H” refers to the H-plane.

### 5.4.8 Band 9 Plots

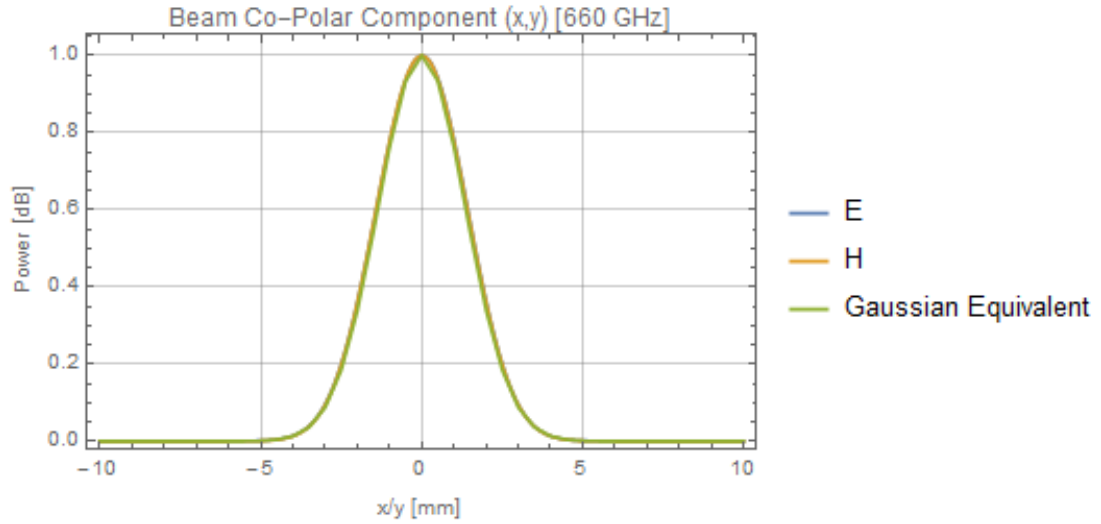


Figure 5.25: Band 9 linear plot of the co-polar beam for 660 GHz. An equivalent Gaussian function ( $\omega_0 = 2.7196$  mm) has been included for comparison.

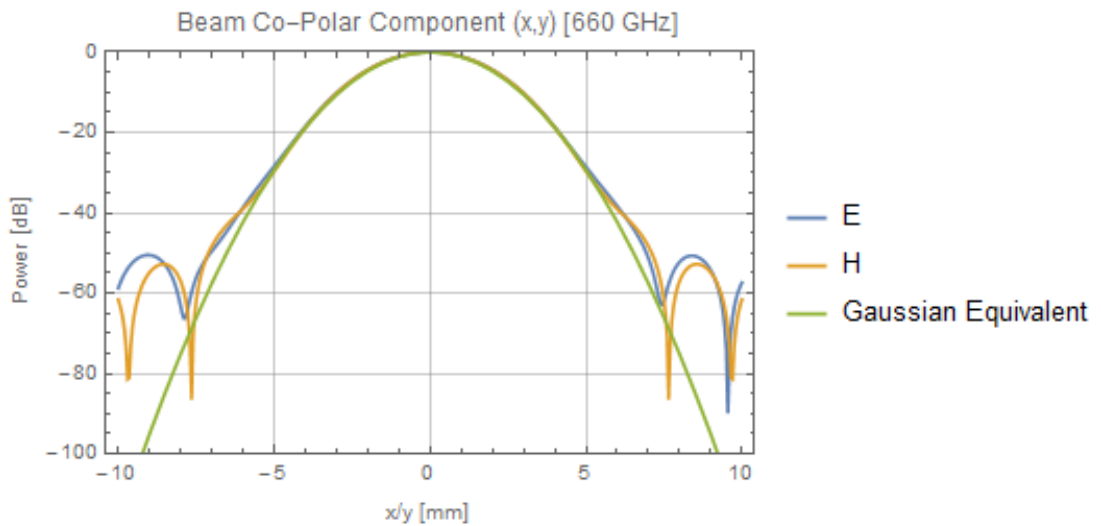


Figure 5.26: Band 9 log-plot of the co-polar beam for 660 GHz. An equivalent logarithmic Gaussian function ( $\omega_0 = 2.7196$  mm) has been included for comparison.

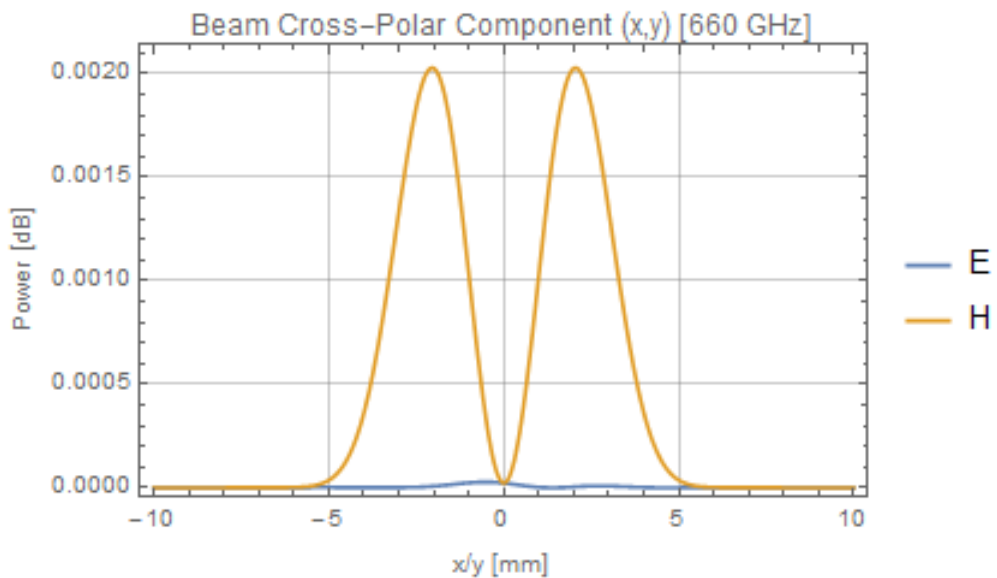


Figure 5.27: Band 9 linear plot of the cross-polar beam for 660 GHz.

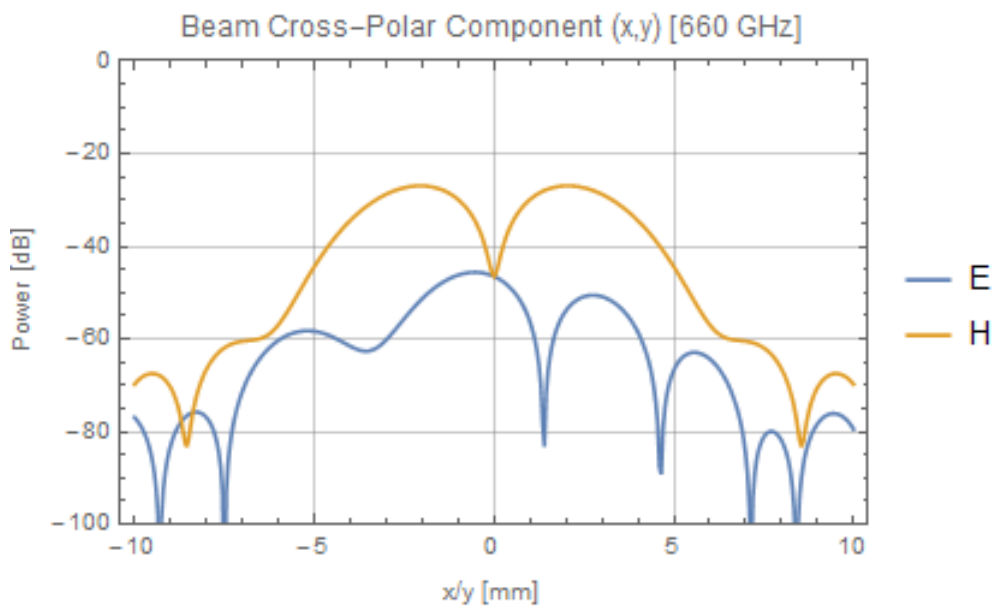


Figure 5.28: Band 9 log-plot of the cross-polar beam for 660 GHz.

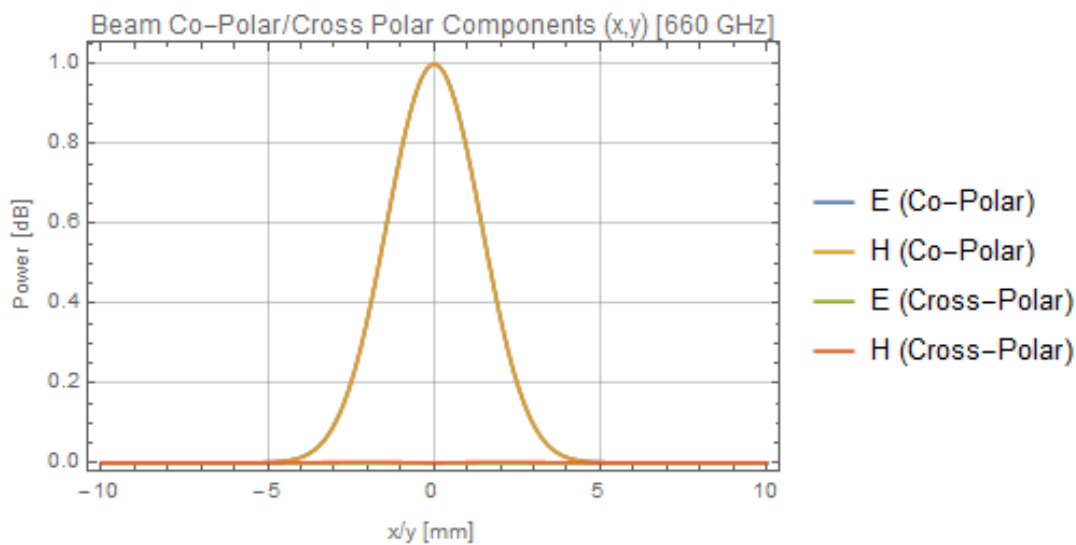


Figure 5.29: Band 9 combined beam linear plot for 660 GHz.

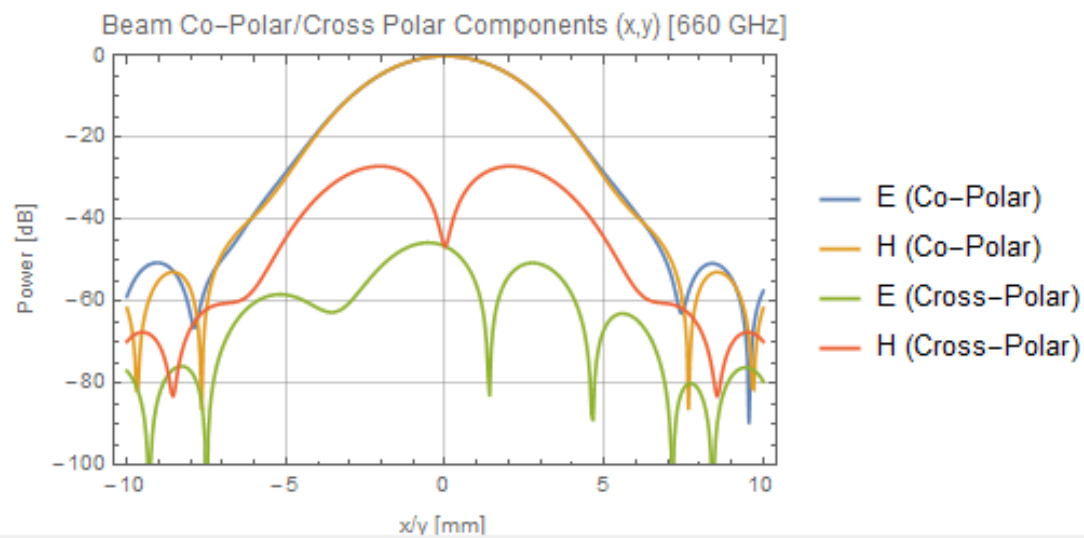


Figure 5.30: Band 9 combined beam log-plot for 660 GHz. The sidelobe levels remain at -50 dB and high levels of beam symmetry are still present at this higher frequency.

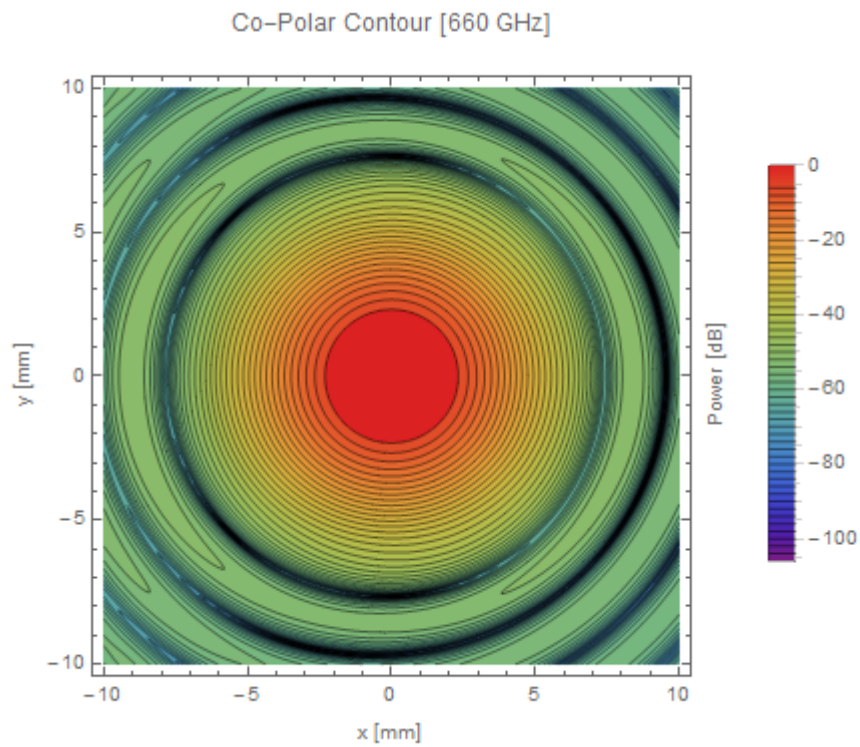


Figure 5.31: Band 9 co-polar contour plot for 660 GHz.

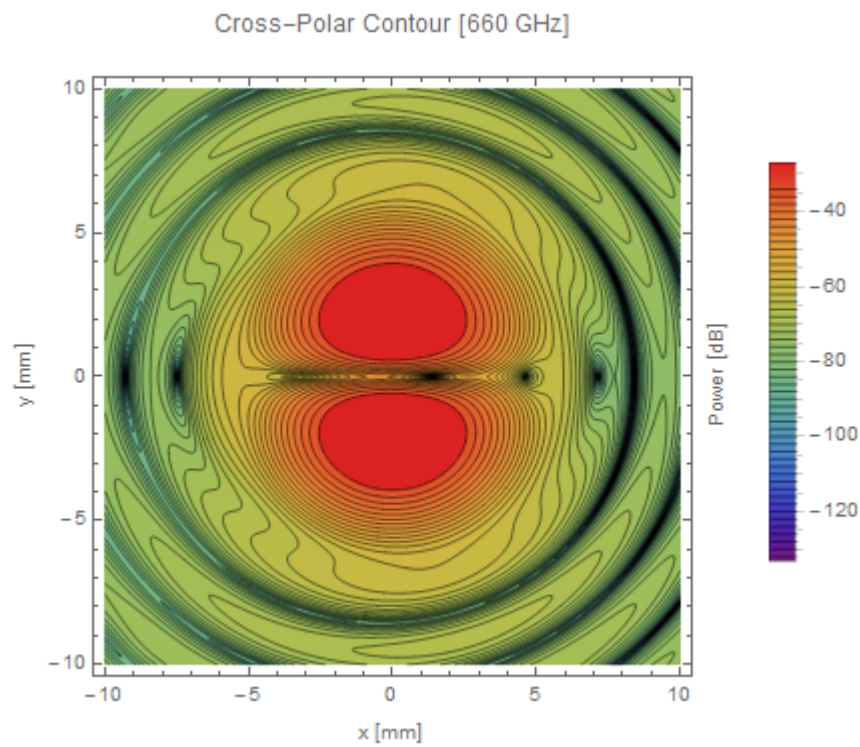


Figure 5.32: Band 9 cross-polar contour plot for 660 GHz.

### 5.4.9 Band 9 Results and Discussion

Physical Optics Results (Band 9)							
Gaussicity (%)	$\omega_{0x}$ (mm)	$\omega_{0y}$ (mm)	X Offset (mm)	Y Offset (mm)	X Tilt ( $^{\circ}$ )	Y Tilt ( $^{\circ}$ )	$\omega_{0 \text{ Exp}}$ (mm)
99.84	2.79	2.79	0.004	0	0.00035	0	2.72

Table 5.5: Band 9 results. Note that tilt here refers to phase tilt.

As can be seen in Table 5.5, the beam waists at the cryostat in both  $x$  and  $y$  seem to match the expected beam waists supplied in Kooi (2016) to the order of  $\pm 0.07$  mm. The lessened diffraction effects, thanks to the narrower beam profile, result in a much lower discrepancy compared to the other two bands. The beam was found to be over 99 % Gaussian after fitting, indicating low aberration after propagation through the receiver. The fitted value is lower by 0.05 % compared with the other bands. The jump in frequency from 243 GHz to 660 GHz for Band 9 may be responsible, as higher frequency beams are more collimated and smaller relative to the mirror surface, given the narrower beam profile. The levels of the cross-polar beam component is around the -30 dB level, indicating low levels of cross-polar radiation being generated by the receiver. Having satisfied the conditions that the fitted beam waists match the expected beam waists the receiver design can be considered verified for Band 9.

## 5.5 Mirror Verification and CAD Exportation

Given that they would be used to machine the surface profiles of M3 and M4, it was necessary to validate the conic mirror surface definitions. This was done in GRASP by creating an equivalent surface using an alternative surface description to ensure the correct surface curvatures were being realised independent of the surface definition being used. The following sections will detail this process.

### 5.5.1 Elliptical Mirror

Ellipsoidal surfaces are derived from the conic mirror surface definitions mentioned previously, though they use three different parameters: vertex distance ( $2a$ ), foci distance ( $2c$ ) and axis angle. The vertex distance is the distance between the two vertices of the representative ellipsoid. The foci distance is the distance between the two foci of the representative ellipse. The axis angle is the angle between the major axis of the ellipse and the reflector coordinate system  $z$ -axis. This along with the mirror radius selects the part of the ellipsoid to be used. Figure 5.33 shows the definition of the ellipsoid.

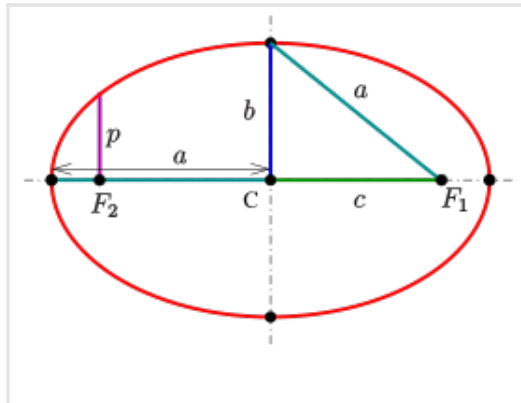


Figure 5.33: Ellipsoidal mirror definition used by GRASP. Credit: By Ag2gaeh - Own work, CC BY-SA 4.0, <https://commons.wikimedia.org/w/index.php?curid=57428275>

An ellipsoidal surface type in GRASP does not use  $r1$  and  $r2$  values. Those values instead inform the vertex and foci distances of the ellipsoidal surface. The resulting for surface parameters for M3 are listed in Table 5.6:

<b>M3 Ellipsoidal Parameters</b>	
<b>Major Axis <math>2a</math> (mm)</b>	6329.69
<b>Minor Axis <math>2b</math> (mm)</b>	3147.12
<b>Interfocal Distance <math>2c</math> (mm)</b>	5491.87
<b>Focal Length (mm)</b>	1564.75
<b>Eccentricity</b>	0.868
<b>Axis Angle (<math>^{\circ}</math>)</b>	-260.415

Table 5.6: Ellipsoidal parameters used to define M3.

### 5.5.2 Hyperbolic Mirror

Hyperbolic mirror definitions require two parameters: vertex distance ( $2a$ ) and foci distance ( $2c$ ). These parameters are defined as they are above in the elliptical mirror section. However, for a hyperbola, the foci distance ( $2c$ ) is larger than the vertex distance ( $2a$ ). The axis angle is used to rotate the hyperbola to its correct orientation. M4 was previously constructed as an ellipsoid, but was corrected to be a hyperboloid. Figure 5.34 shows the definition of the hyperboloid.

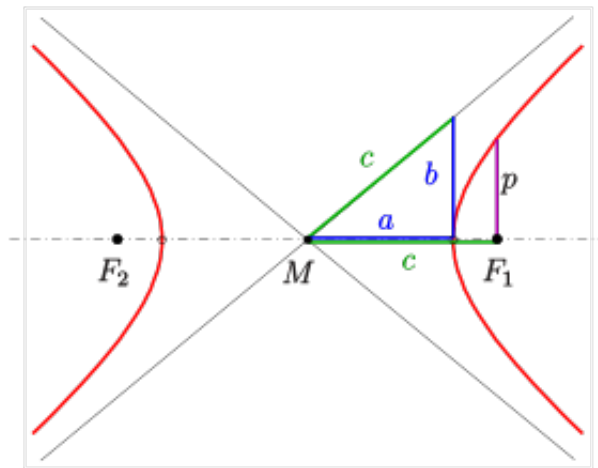


Figure 5.34: Hyperbolic mirror definition used by GRASP. Credit: By Ag2gaeh - Own work, CC BY-SA 4.0, <https://commons.wikimedia.org/w/index.php?curid=57127253>

The parameters of the hyperboloid are listed in Table 5.7:

M4 Hyperboloidal Parameters	
Major Axis $2a$ (mm)	3191.69
Minor Axis $2b$ (mm)	2234.77
Interfocal Distance $2c$ (mm)	3896.29
Focal Length (mm)	1564.75
Eccentricity	1.22
Axis Angle ( $^{\circ}$ )	9.603

Table 5.7: Hyperboloidal parameters used to define M4.

### 5.5.3 Irregular XY Grid Mirrors

The final method of the defining the two mirrors was to use the Irregular X-Y Grid, Triangulation surface. This surface allows a shape in CAD format (see **Chapter 4**) to be re-entered into GRASP and investigated. This was deemed necessary as the mirrors had been sent in CAD format to the LLAMA team. As such, it was necessary to ensure that no optical performance degradation had occurred in the exporting process and how the mirror surfaces are defined to ensure the integrity of the design in exporting the surfaces to the LLAMA consortium. Meshes of the mirrors were created by using GRASP to export the mirrors in STEP format. Once imported to FreeCAD triangulation meshes were fitted to the surfaces of M3 and M4. These meshes were then exported, reformatted to be readable by GRASP and reimported into GRASP. To check the integrity of import/export processes, the results with the original surfaces would be compared with the results from the meshed surfaces. Two Irregular X-Y Grid, Triangulation surfaces were created to represent M3 and M4 and can be seen in Figure 5.35.

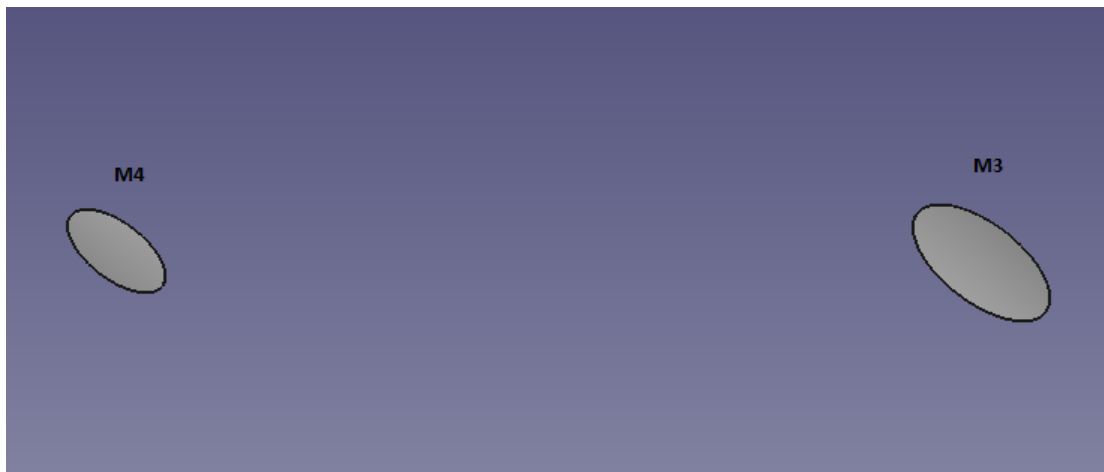


Figure 5.35: Newly imported M3 and M4 in FreeCAD.

### 5.5.4 Verification of Standard Mirror Geometries

The ellipsoidal version of M3 can be seen in Figure 5.36. Parameters in Table 5.6 were used to construct this mirror. An ellipsoidal mirror (possessing two foci) can redirect radiation emerging from one focus towards the other focus, a property that makes it useful in receiver design. The coordinate system of this mirror was placed over the feed at the Cassegrain focus, which can be considered as one of the foci of the system. The other focus of M3 was located behind M4, designating this as a “focusless” type of GBT. As the axis angle has been accounted for in the surface definition of the mirror, there is no need to change the orientation of this mirror.

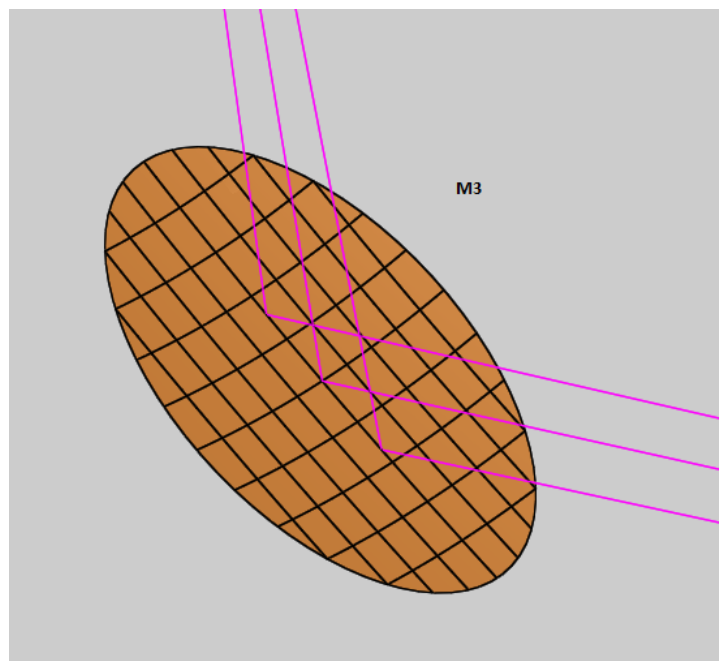


Figure 5.36: Ellipsoidal M3 in GRASP.

The hyperboloidal version of M4 can be seen in Figure 5.37. Table 5.6 contains the parameters used to create this mirror.

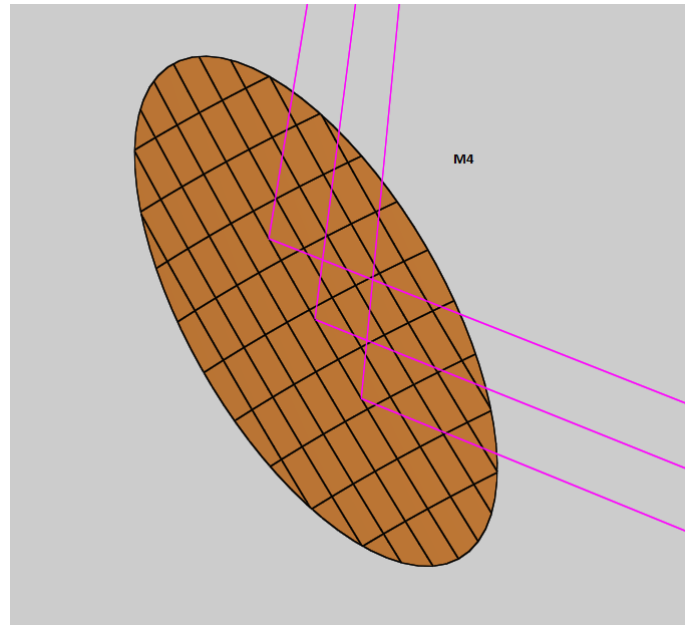


Figure 5.37: Hyperbolic M4 in GRASP.

These surfaces are more complex to set up than their ellipsoidal counterparts. Figure 5.38 shows M4, fully set up and integrated with the rest of the GBT. The full hyperboloid has one focus placed on the output grid and the other at the secondary focus of M3. Unlike the ellipsoidal surfaces, hyperboloidal surfaces do not take in an axis angle as an input though this parameter is still required. This value was found by using the cosine rule to determine the angle between the axis joining the two foci of the hyperbola and the axis joining the centre point of M4 to the second focus of the hyperbola. This rotation ensures that the bending angle of M4 will be  $90^\circ$  as required. This axis angle was found to be  $9.603^\circ$ . Figure 5.38 shows the full hyperbola in GRASP. Both the base coordinate system and rotated coordinate system are located at the focus of the hyperbola. Figure 5.39 shows the rotation in greater detail. Next, the surface must be enclosed by a de-centred rim. This de-centring is taken care of by the ellipsoidal surface but not for the hyperboloidal surface. An alternative method is to export the rim from the Conic Mirror Surface version of M4 and use it again for the hyperboloid version. The latter method is more complicated but ends up being the superior

method as it eliminates a lot of the user adjustments. Figure 5.38 shows M4 as the usable part of the whole hyperbola.

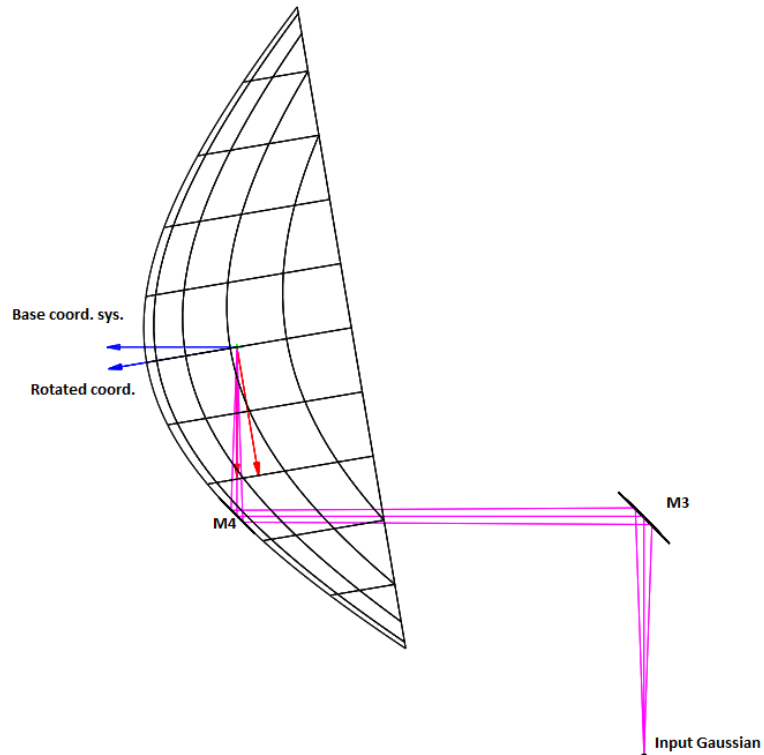


Figure 5.38: M4 hyperbola integrated into the LLAMA GBT.

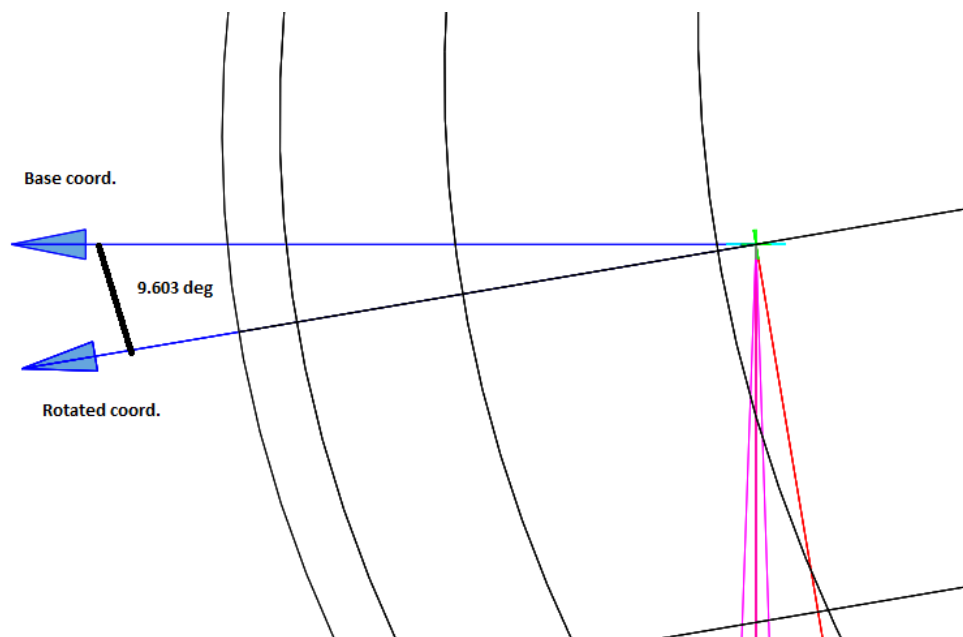


Figure 5.39: The axis angle rotation implemented in GRASP.

The same physical optics calculations as performed on the CMS mirrors were carried out for the standard geometry mirrors. The custom, highest fidelity meshes were used for this analysis. This process of creating these meshes is detailed in **Chapter 4**. The mesh of M3 consists of 727 points with 1344 faces and the M4 mesh consists of 711 points with 1312 faces. The standard mirrors are constructed of a single surface, the user can only influence the tolerances of the mirrors by importing pre-generated distortions.

The results are shown in Figures 5.40 - 5.45. Both the co-polar and cross-polar beam components will be presented, to demonstrate the change (if any) in the power level and sidelobe structure:

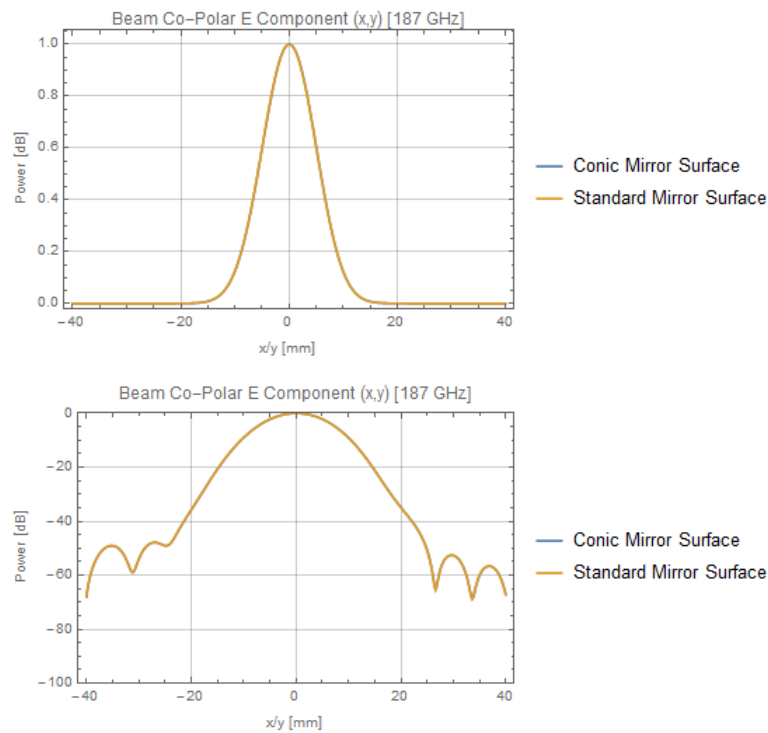


Figure 5.40: Linear and logarithmic co-polar E cuts for CMS and Standard Mirrors (187 GHz).

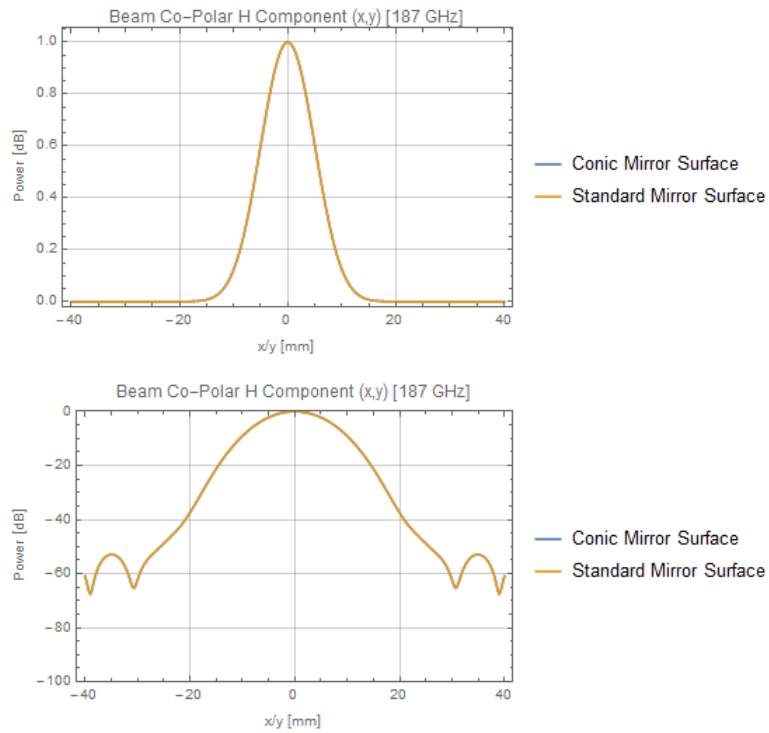


Figure 5.41: Linear and logarithmic co-polar H cuts for CMS and Standard Mirrors (187 GHz).

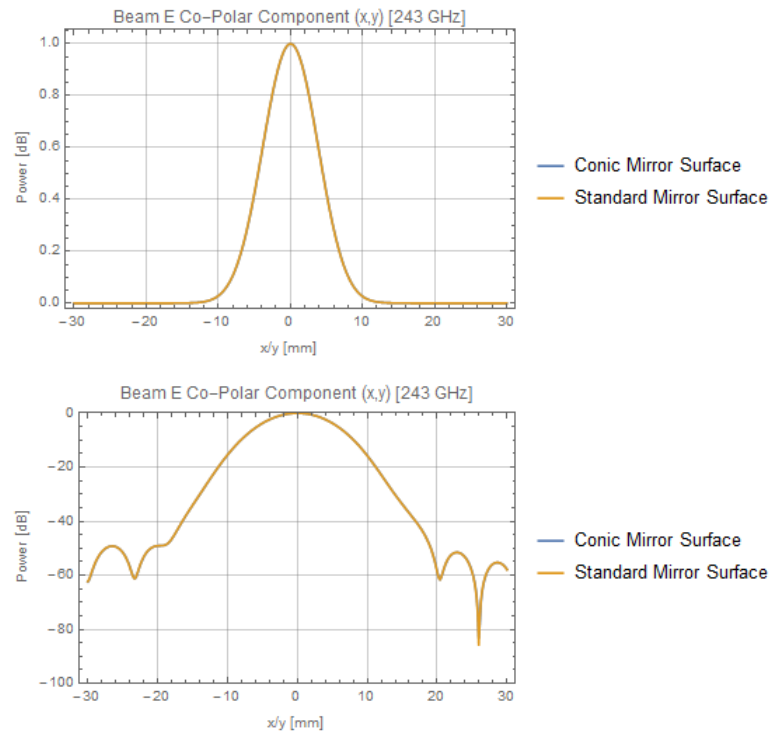


Figure 5.42: Linear and logarithmic co-polar E cuts for CMS and Standard Mirrors (243 GHz).

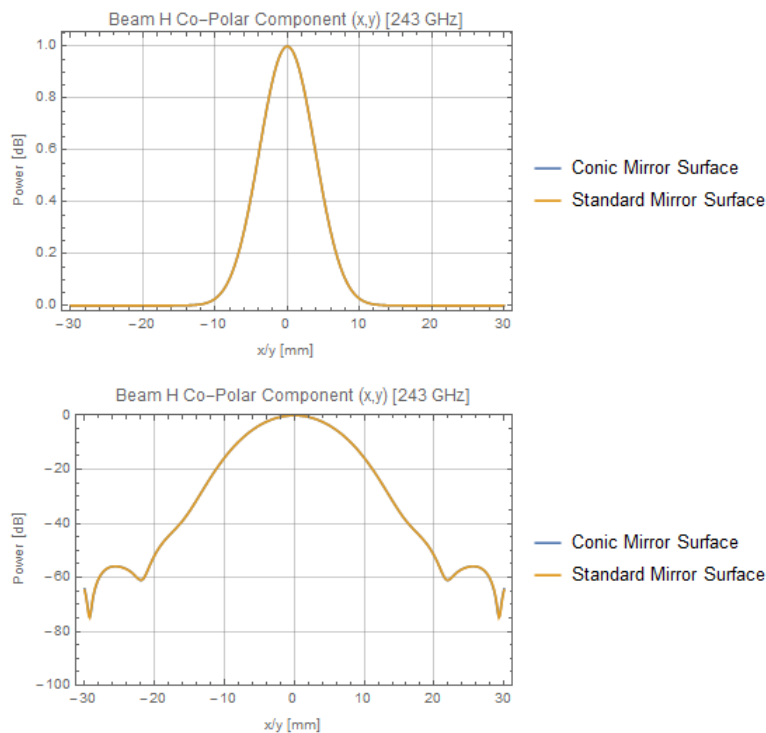


Figure 5.43: Linear and logarithmic co-polar H cuts for CMS and Standard Mirrors (243 GHz).

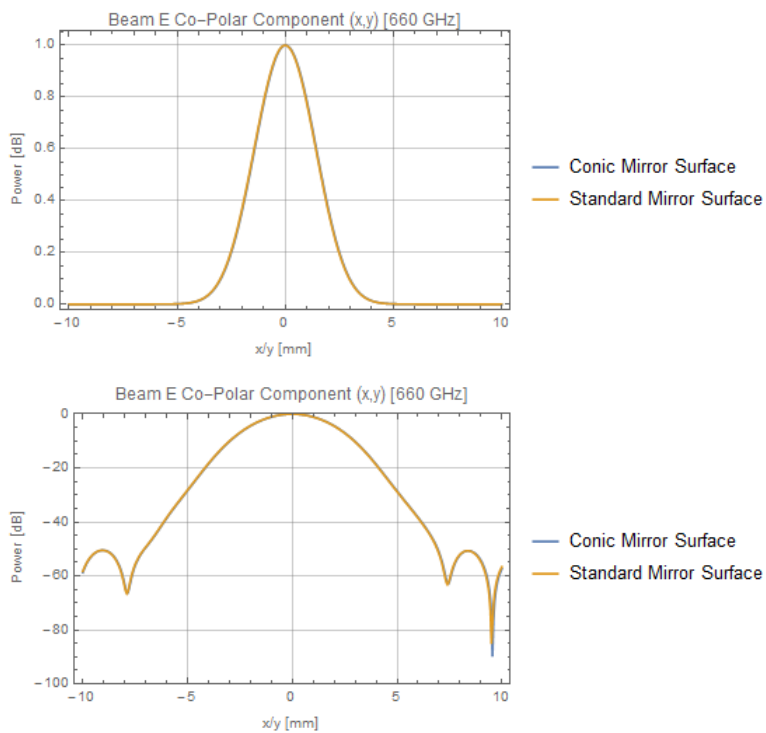


Figure 5.44: Linear and logarithmic co-polar E cuts for CMS and Standard Mirrors (660 GHz).

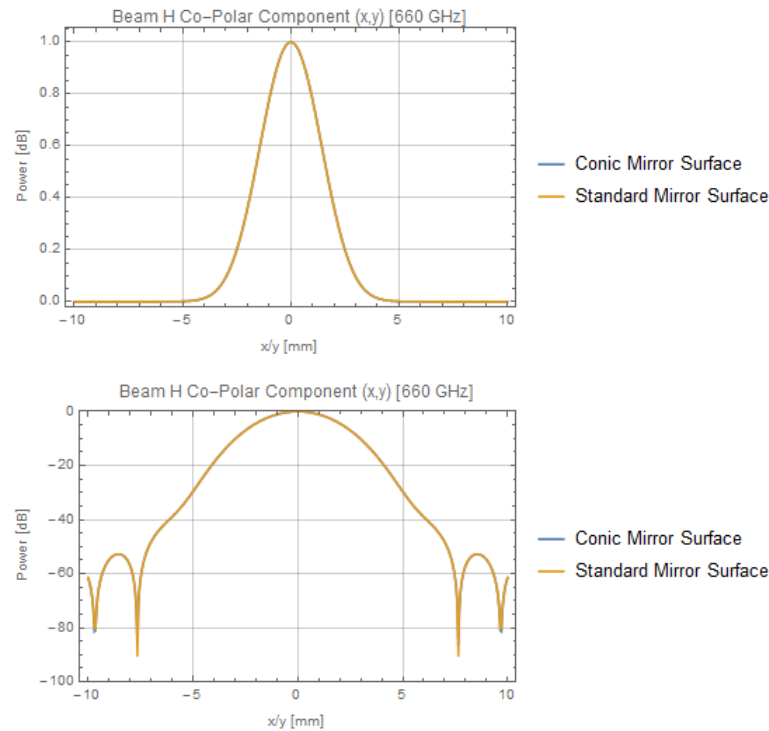


Figure 5.45: Linear and logarithmic co-polar H cuts for CMS and Standard Mirrors (660 GHz).

Looking at the comparison images, it is difficult to discern any difference between each band. Gaussian fitting was performed on the standard mirror data and the results can be viewed in Tables 5.8 - 5.10 below:

Physical Optics Results (Band 5)			
Gaussicity (%)	$\omega_{0x}$ (mm)	$\omega_{0y}$ (mm)	$\omega_0$ Expected (mm)
99.81	9.85	9.84	9.60

Table 5.8: Band 5 standard mirror results.

Physical Optics Results (Band 6)			
Gaussicity (%)	$\omega_{0x}$ (mm)	$\omega_{0y}$ (mm)	$\omega_0$ Expected (mm)
99.84	7.58	7.58	7.385

Table 5.9: Band 6 standard mirror results.

Physical Optics Results (Band 9)			
Gaussicity (%)	$\omega_{0x}$ (mm)	$\omega_{0y}$ (mm)	$\omega_0$ Expected (mm)
99.84	2.79	2.79	2.7196

Table 5.10: Band 9 standard mirror results.

Gaussicity and waist values are identical to those shown previously. This result is unsurprising given that the conic mirror surfaces are a progenitor class for the standard mirror geometry surfaces. The only notable difference between the two methods is in their implementation.

### 5.5.5 Comparison of CAD Mirrors with Conic Mirror Surfaces

As stated previously, the optical performance of the meshed mirror surfaces needed to be tested against the smooth surfaces generated by GRASP. Tests were carried out for three different mesh densities, two of which are presets of FreeCAD's Netgen meshing tool and a custom one which is the densest Netgen mesh FreeCAD could produce. These results can also be seen in **Chapter 4**. The peak co-polar power levels were compared to ensure there had been no loss in power.

Triangulation meshes are the only type of mesh GRASP will accept for single-surface reflectors. These meshes represent their parent surface using many flat, triangular segments. One of the potential issues with using meshes in GRASP is that the triangles may not stitch together well, causing the surface to appear rough. Increasing the density of the mesh increases the number of triangular segments that will be used to represent the surface, causing the area of each segment to decrease. In addition, GRASP employs a fifth-order polynomial function to smooth over the surface before it is used in calculations. Meshed mirrors are placed differently to the other mirror types in GRASP. The reference point for them is the Global coordinate system by default, though the user can change the reference point in GRASP when exporting mirrors in CAD format. A standard rim object can be applied to them.

The two mesh presets used were “Fine” and “Very Fine”. Of these, two versions were used: one with and one without second order elements included. The custom mesh included second order elements. The meshes were exported using the procedure set out in **Chapter 4**. Physical optics calculations were carried out in the same manner as the others presented in the chapter. Below the plots of beam power the results of Gaussian fitting per band are shown. The E cuts are illustrated for each band as these cuts contain asymmetries. Each cut is compared with the conic mirror surface E cut for reference. The H cuts, as can be seen in the previous section, match up exactly for each mesh density tested. The results are set out in Figures 5.46 - 5.54:

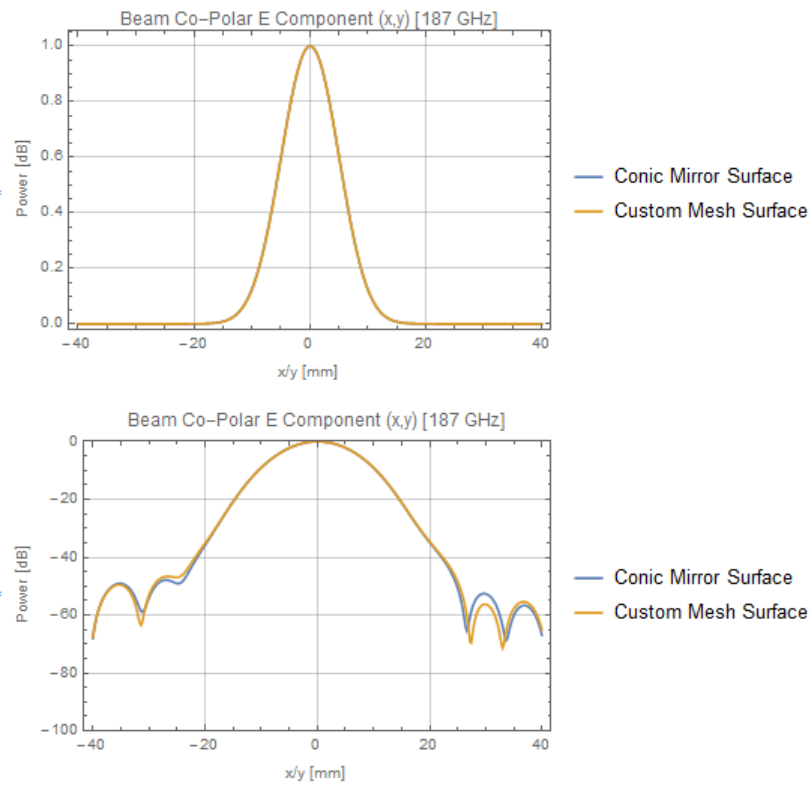


Figure 5.46: E cut co-polar levels for custom mesh and CMS (187 GHz).

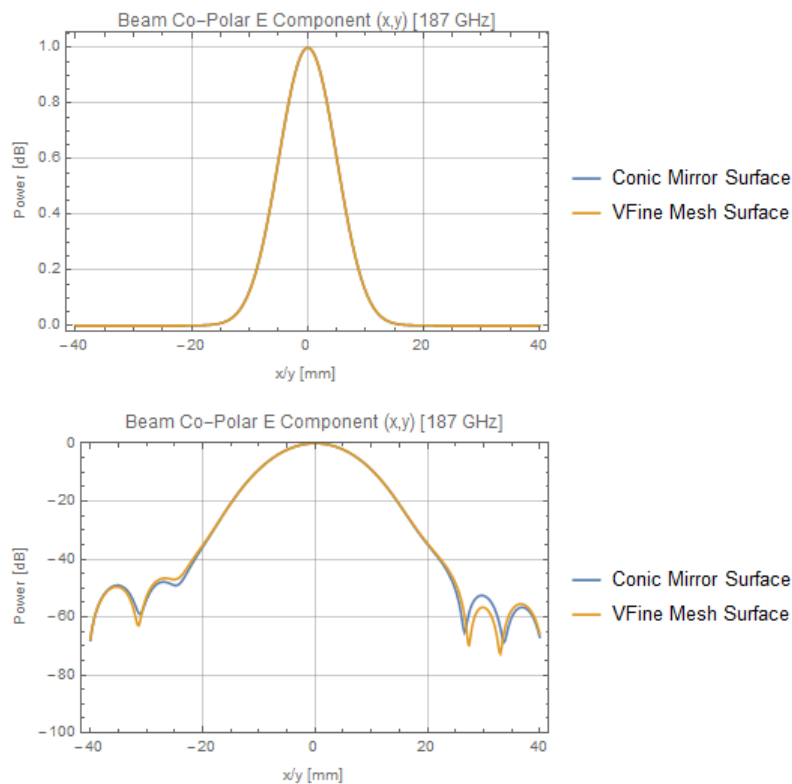


Figure 5.47: E cut co-polar levels for very fine mesh and CMS (187 GHz).

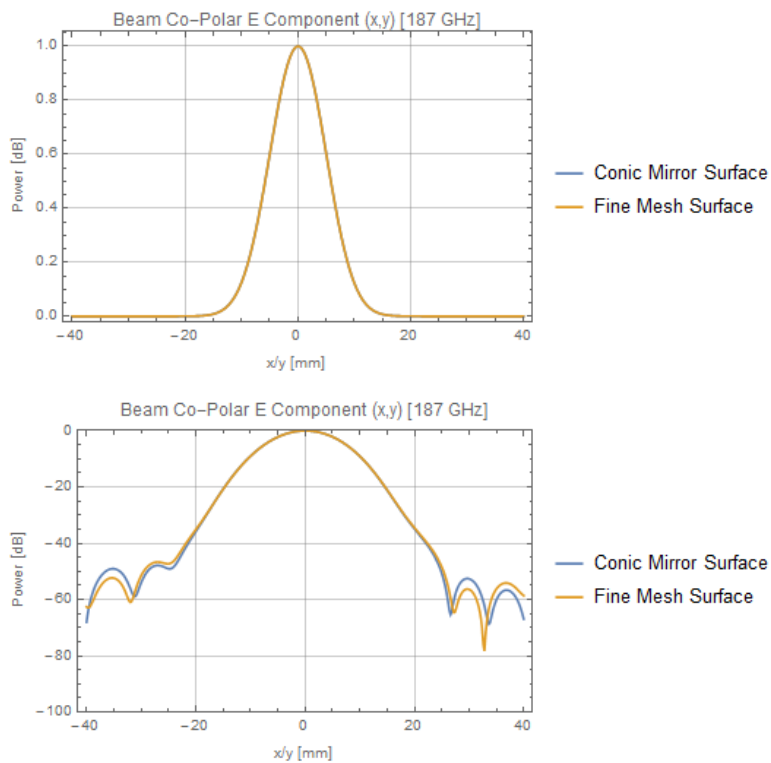


Figure 5.48: E cut co-polar levels for fine mesh and CMS (187 GHz).

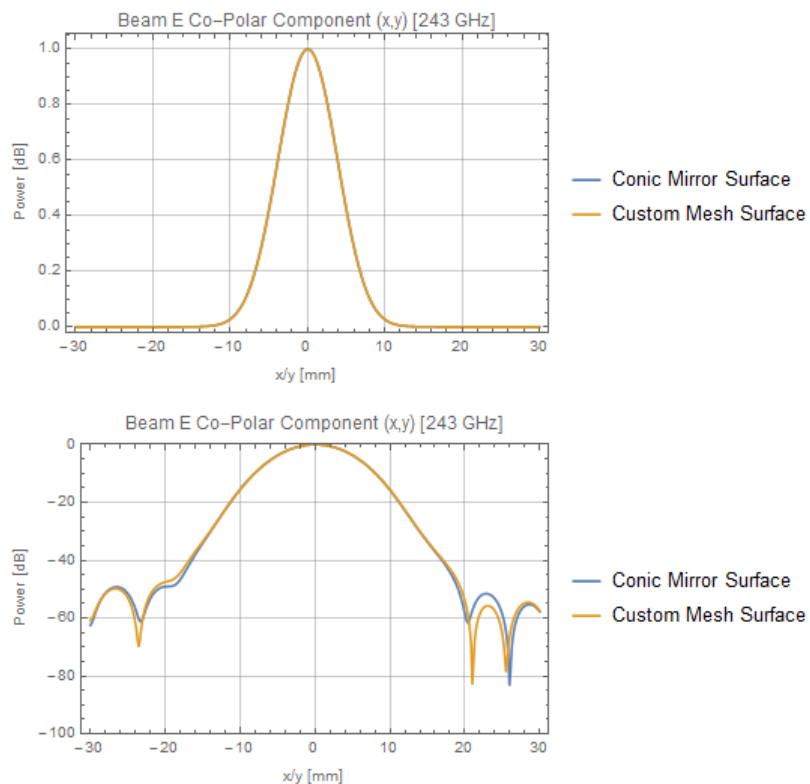


Figure 5.49: E cut co-polar levels for custom mesh and CMS (243 GHz).

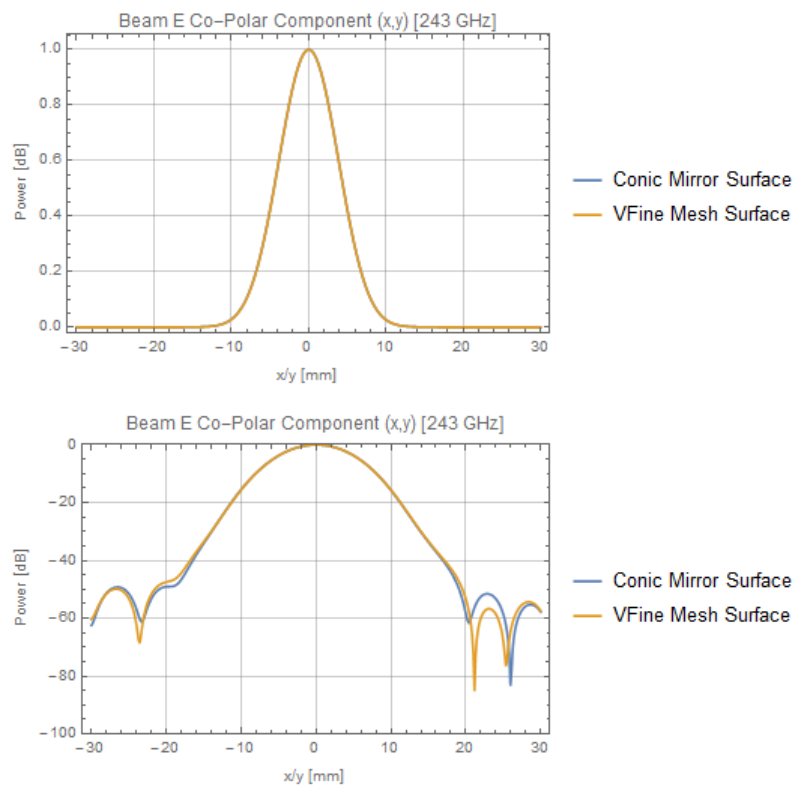


Figure 5.50: E cut co-polar levels for very fine mesh and CMS (243 GHz).

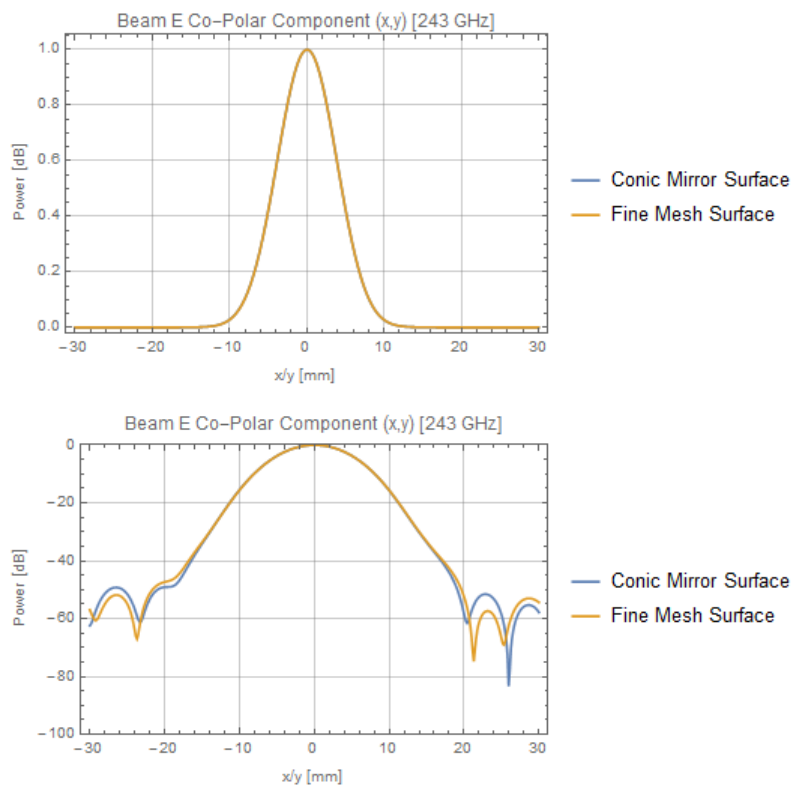


Figure 5.51: E cut co-polar levels for fine mesh and CMS (243 GHz).

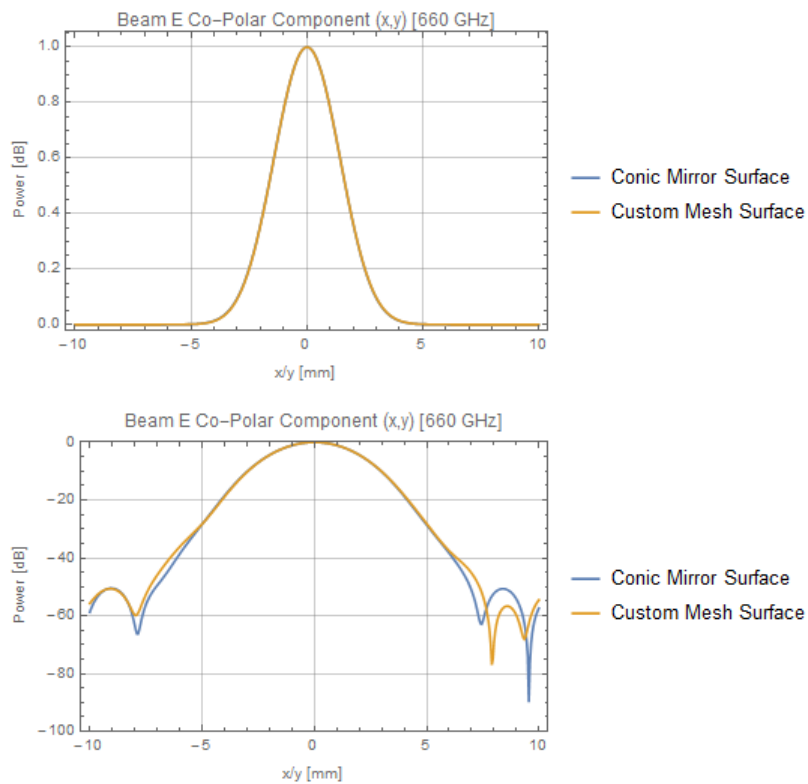


Figure 5.52: E cut co-polar levels for custom mesh and CMS (660 GHz).

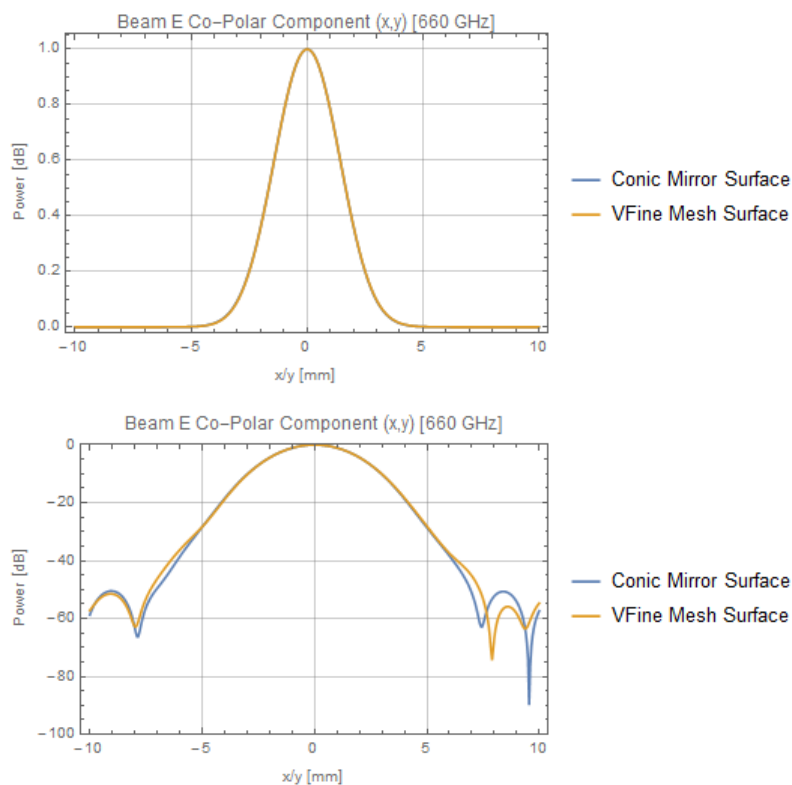


Figure 5.53: E cut co-polar levels for very fine mesh and CMS (660 GHz).

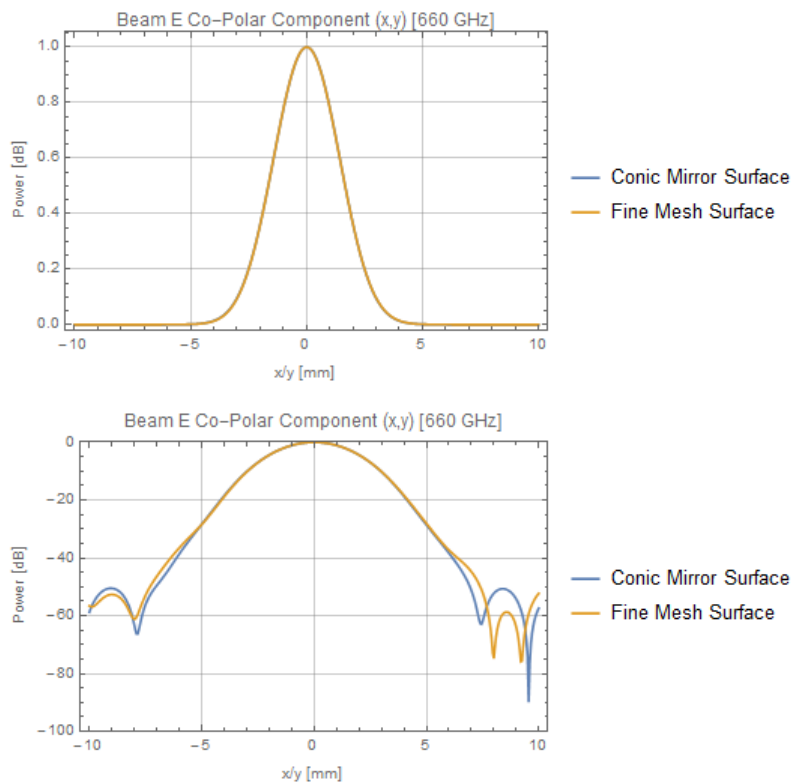


Figure 5.54: E cut co-polar levels for fine mesh and CMS (660 GHz).

The results of Gaussian fitting on the mesh mirrors are located in Tables 5.11 - 5.13. The results are split by band for ease of reference:

<b>Physical Optics Results (Band 5)</b>				
<b>Mesh Type</b>	<b>Gaussicity (%)</b>	$\omega_{0x}$ (mm)	$\omega_{0y}$ (mm)	$\omega_{0 \text{ Exp}}$ (mm)
Custom	99.81	9.84	9.84	9.60
Very Fine	99.81	9.84	9.84	9.60
Fine	99.806	9.85	9.84	9.60

Table 5.11: Band 5 meshed mirror results.

<b>Physical Optics Results (Band 6)</b>				
<b>Mesh Type</b>	<b>Gaussicity (%)</b>	$\omega_{0x}$ (mm)	$\omega_{0y}$ (mm)	$\omega_{0 \text{ Exp}}$ (mm)
Custom	99.84	7.58	7.58	7.385
Very Fine	99.84	7.58	7.58	7.385
Fine	99.83	7.58	7.58	7.385

Table 5.12: Band 6 meshed mirror results.

<b>Physical Optics Results (Band 9)</b>				
<b>Mesh Type</b>	<b>Gaussicity (%)</b>	$\omega_{0x}$ (mm)	$\omega_{0y}$ (mm)	$\omega_{0 \text{ Exp}}$ (mm)
Custom	99.83	2.8	2.79	2.7196
Very Fine	99.83	2.79	2.79	2.7196
Fine	99.82	2.79	2.79	2.7196

Table 5.13: Band 9 meshed mirror results.

Looking at the results per band, it can be seen that at higher power levels (0-40 dB) the meshed mirrors are in good agreement with the control conic mirror surfaces. Deviation occurs at the -40 dB level and seems to worsen for both higher frequencies and lower mesh densities. The latter makes sense as the lower densities result in cruder surface definitions. The former is also expected as higher frequency beams have narrower profiles. The increased size of the triangular areas coupled with the smaller beam sizes means that effects will be larger for Band 9 than for Band 5. In effect, the higher frequency beams are influenced by the rougher parts of a surface much more than the lower frequency ones. It is for this reason that tolerances for optical surfaces used in the visible region are much lower than for the infrared region. Tables 5.11, 5.12 and 5.13 contain the Gaussian

fitting results from the meshed mirrors. A drop in Gaussicity of 0.04% for Band 5 and at most 0.01% for Bands 6 and 9 indicates that the lower quality meshes are having a negligible effect on the already-existing aberration experienced by the beams. The waists for all bands are functionally identical to those obtained with the conic mirrors in Tables 5.3, 5.4 and 5.5.

### 5.5.6 Exporting the Mirrors in CAD Format

The final piece of work to carry out with the LLAMA GBT was to export the mirror geometry to a CAD format. The mirrors would be produced using Computer Numerical Control (CNC) milling. The mirrors, in CAD format, would define the dimensions of a part to be milled. Computer aided manufacturing (CAM) software converts the CAD model into a series of instructions that a milling machine can follow.

Exporting mirror surfaces in GRASP can be done in the following ways. To export a mirror as a GRASP-readable file, a “Surface Data Output” object must be instantiated. This object can represent a mirror surface as a grid of irregular  $xyz$  points, a regular  $xy$  grid or as a  $\rho - z$  arc. The data is stored as a “.sfc” file, a file type bespoke to GRASP. The user must provide a range in  $x$  and  $y$  as well as a number of points they wish to sample. The units for the  $x$ ,  $y$  and  $z$  distances must also be specified. The “Values” option selects which values are generated for the surface. The choices are either  $z$ -values of the surface, or either first, second order derivatives of the surface along either the  $x$  or  $y$  directions (or a mix of both). A reference coordinate system must be chosen in which the surface will be tabulated. Finally, the “List” option will set whether or not the points generated will be displayed on the output window. The “Get Reflector Data” command will then generate the “.sfc” file. Note that this method will not export the rim of the mirror, just the surface.

To export a mirror as a CAD file, a command must be used with no object required. Surfaces can be exported to either a STEP or IGES format. The mirror to be exported is chosen as the target of the command. A file name and location must be entered. The “Tolerance” parameter sets the allowed deviation between the GRASP definition and the CAD representation in units of distance. Should a mirror/scatterer contain more than one body (i.e. support struts or composite mirrors) there is the option to group these bodies together or not. Finally, the reference coordinate system must be selected. This method will include the rim, exporting a full mirror rather than a surface.

The latter method was used to export M3 and M4. The STEP format was chosen for both mirrors. The tolerance for the two mirrors was set to 0.1 mm. The Global coordinate system was used for both mirrors to keep the geometry of the GBT intact should they be imported to a CAD program.

Once created and checked in FreeCAD, the CAD files were sent to the LLAMA consortium for manufacture. Figures 5.55 and 5.56 (courtesy of Dr. Jacob Kooi) are AstroCAD design drawings of the M3 and M4 mirrors respectively:

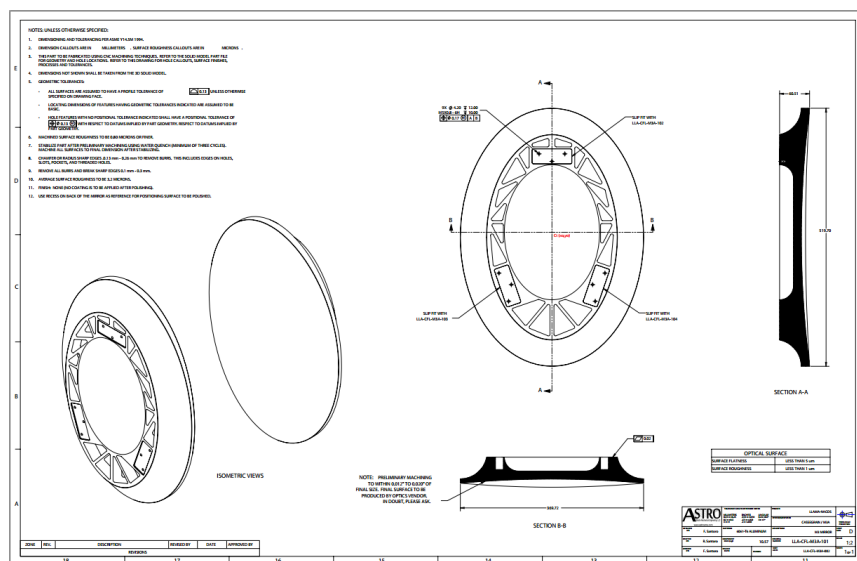


Figure 5.55: AstroCAD design drawing of M3.

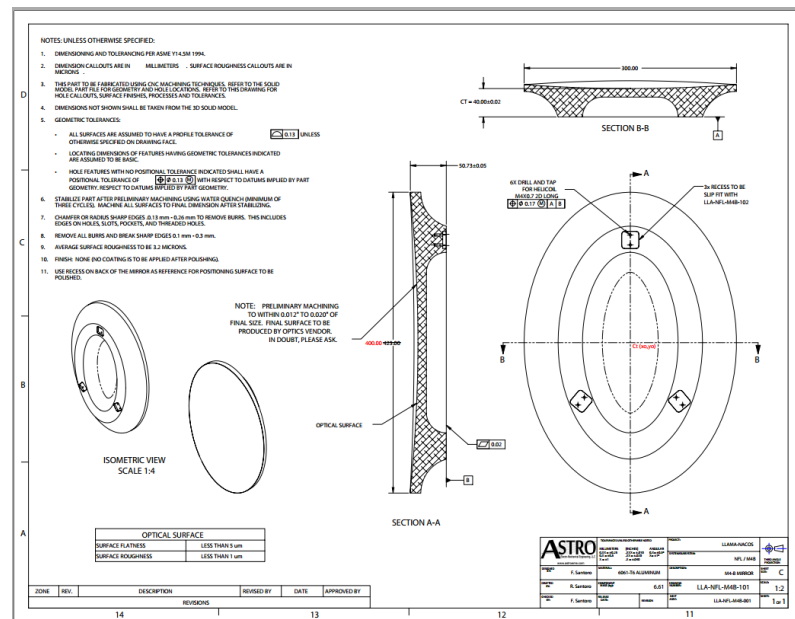


Figure 5.56: AstroCAD design drawing of M4.

## 5.6 Conclusions

To recap, the goal of this work was to implement and analyse the GBT required for the LLAMA Nasmyth B receiver cabin. The analysis was carried out for three frequency bands: LLAMA Bands 5, 6 and 9. The beam contour plots shown in previous sections confirm that the beams measured are symmetric and highly Gaussian, indicating low aberration being induced by the receiver. All co-polar beam components were found to be over 99 % Gaussian. Though no expected Gaussicity were provided, the results nonetheless indicate low aberration through the optical system. The power level of the cross-polar beam components were found to be low with respect to the power of the co-polar beam components. Finally, the fitted beam waists in both  $x$  and  $y$  were almost identical to the expected beam waists from Kooi (2016).

Looking at the comparison between conic mirror surfaces and standard GRASP surface definitions, it can be seen for all bands that the beam components are identical. The largest difference to be seen in all bands is the depth of the cross-

polar central dip, though this is for all intents and purposes an aesthetic difference as the levels of these features are -80 to -100 dB. As stated in the relevant section, this result is expected. The choice of the two types of mirror definition will therefore be up to the user themselves. The only noticeable difference between the two functionally is the mirror rim definition, which is far simpler for conic mirror surfaces. No decentre value is required nor does the size of the mirror have to be adjusted depending on whether an ellipse or hyperbola is being used.

Regarding the meshing portion of this section, the results show that, at the lowest level, all of the mesh densities can be said to replicate a GRASP single face reflector well. The custom meshes (highest number of points) can replicate the conic mirror surfaces almost identically. The “Very Fine” meshes show slight deviation in the co-polar levels around -30 to -40 dB. The “Fine” meshes have deviations at the same level which are more pronounced. There do not seem to be any deviations at higher power levels. The deviation at lower power levels ( $\approx$  -50 dB) can be explained due to the degradation of the focus as mesh density drops. Figures 5.57 and 5.58 illustrate this point rather clearly. The fewer points that constitute the mesh surface of a mirror, the larger the triangular sections become. This causes the surface to become more poorly defined, even with the help of the smoothing polynomial used by GRASP. This shows that mesh density is an important factor when using meshed surfaces; the higher the number of points, the better the surface will represent the smooth, mathematically defined single-surface reflectors of GRASP.

Finally, the mirrors M3 and M4 were successfully exported to a CAD format. Both the spacing and positions of the mirrors were verified with FreeCAD. The CAD files were deemed satisfactory, as evidenced by the AstroCAD drawings seen in the previous section.

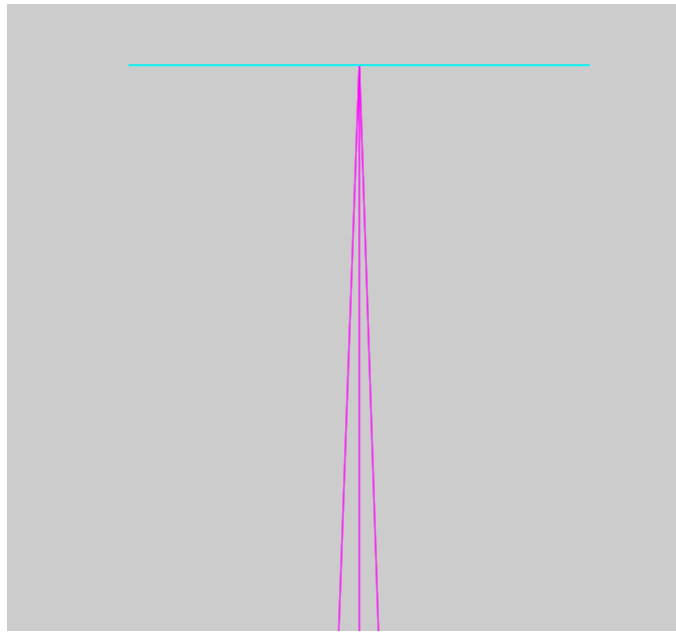


Figure 5.57: Focus at the band cartridge/output grid using CMS mirrors.



Figure 5.58: Focus at the band cartridge/output grid using “Fine” density preset meshed mirrors. The focus has become somewhat distributed when compared with the above figure.

# Chapter 6

## *CORE* Analysis

### 6.1 Introduction

The purpose of this chapter is to discuss the telescope analysis carried out in Maynooth of the proposed **Cosmic ORigins Explorer (CORE)** space telescope. Two iterations of the telescope design were tested initially to establish which design offered the best optical performance and solution to the mission. Due to the constraints of a fixed launcher volume, optical configuration was critical. After this, more detailed analysis was carried out on the chosen design. Detailed descriptions of the construction of the optical models in GRASP will be provided. The detector arrays on the focal plane were positioned and aligned. Mirror meshes from a CAD model were defined and positioned to recreate the telescope layout. Most importantly, the beams of radiation produced by *CORE* over its designated frequency bands will be presented, having been simulated in GRASP to predict the beam patterns on the sky. An introduction to the *CORE* concept mission will now follow.

### 6.2 Information on the *CORE* Mission

*CORE* was a proposed mission submitted to the ESA Cosmic Visions M5 call in 2016. Its goal was to study the CMB with a focus on polarisation, specifically attempting to detect the elusive primordial B-modes outlined in **Chapter 1**.

The telescope and instrument would have to fit the strict requirements of an ESA medium M-class mission with limited budget overall which narrows the

technical options available. The stated goal for the scalar-to-tensor ratio achievable (i.e. the level of B-mode power detectable in relation to E-mode power) is  $r \approx 1 \times 10^{-3}$ . de Bernardis et al. (2017) explain that this level of sensitivity will mean that a non-detection would indicate the absence of large-scale inflation signatures on the CMB. Being a space-based instrument allowed *CORE* to aim for angular resolutions on the order of a few arcminutes and a polarisation sensitivity of less than  $2.5 \mu K$ , which is 20 times that of the aggregated polarisation sensitivity of the detectors on-board *Planck*. To achieve this exquisite sensitivity, the focal plane will contain 2100 linearly polarised, cryogenically cooled detectors (limited by cost). The telescope will possess 1.2 m aperture similar to *Planck*, leading to a focal plane that will be about 50 cm in diameter (limited again by cost). The frequency range was chosen to be 60 - 600 GHz, a suitably long range required to perform background subtraction (again limited by budgetary constraints). This range would be broken up into 19 bands in three general groupings: Low Frequencies (60 - 155 GHz), CMB Frequencies (130 - 220 GHz) and High Frequencies (255 - 600 GHz).

KIDs were selected as the detector technology. As KIDS can be printed en masse onto silicon boards, they can be tiled onto a flat surface to drastically increase the detector density. This necessitates a telescope system capable of producing a flat focal plane to allow optimum structuring of the detectors in a mosaic fashion.

The satellite was planned to be located at the Sun-Earth  $L_2$  Lagrangian point ( $1.5 \times 10^6$  km from the Earth). This is a popular location due to the thermal and gravitational stability of this region.  $L_2$  is constantly in the shadow of the Earth, avoiding the disastrous possibility of Sun exposure on the cryogenic systems. A Lissajous orbit was chosen for the satellite. Orbits at  $L_2$  are non-periodic, and Lissajous orbits require a modest amount of station-keeping to maintain. The scan strategy would be to cross sky pixels multiple times to eliminate systematic

effects like bias and thermal noise and the pickup of sidelobes from near/foreground sources.

Two telescope designs of *CORE* were submitted to Maynooth for PO testing. The first was an Offset Gregorian design that had been created in Maynooth with OpticStudio and optimised with CODE V at the University of Minnesota. The program mismatch therefore required surface meshing in order to import the design into GRASP. The second was an Offset Dragonian design that was created and under test in Maynooth using GRASP. The two designs would be compared and the superior design would be recommended.

### 6.2.1 Focal Plane

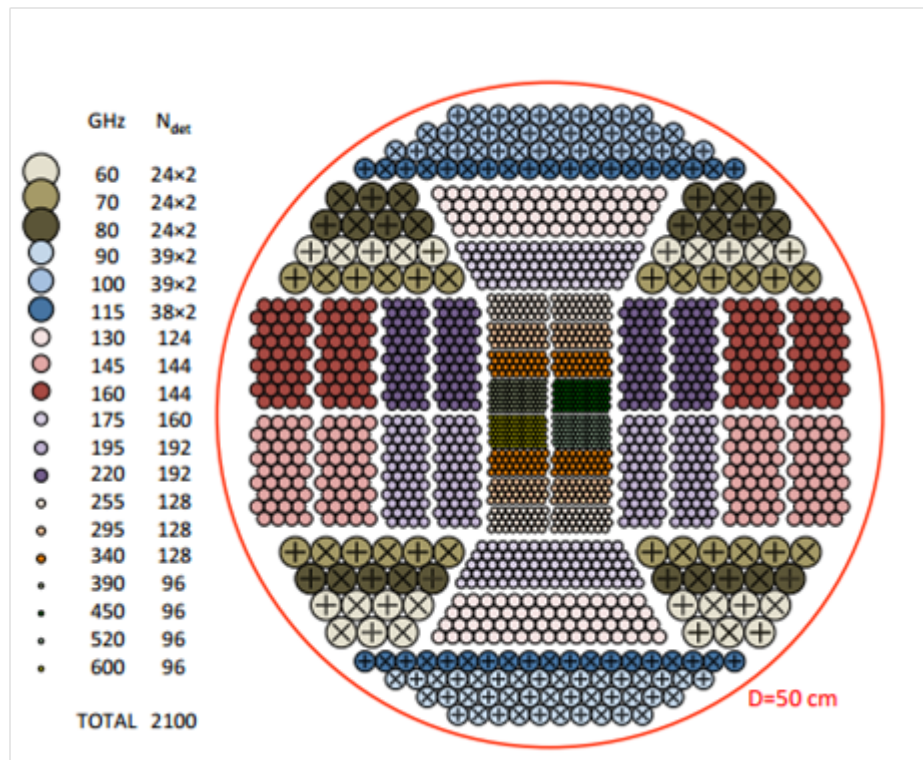


Figure 6.1: Outline of the *CORE* focal plane showing detector placement and the detector frequencies.

The potential layout of detectors is shown in Figure 6.1. The small circular objects represent tiled KID detectors. The larger circles with the crosses repre-

sent Lumped Element KIDS (LEKIDS) that are coupled to planar meta-material lenselets. The crosses represent the polarisation sensitivity of the detector. Ortho-mode transducers will be used to split the polarisation into two orthogonally polarised channels. The focal plane is 0.5 m in diameter, yielding a diffraction limited field of view (DLFOV) of up to  $12^\circ$  on the sky (reported in de Bernardis et al. (2017)) with an Offset Dragonian telescope. The scan direction is horizontal. Due to the use of superconducting detection technology, the focal plane will be located in a cryostat unit at a temperature of 100 mK. The focal plane must also be located close to the service module of the satellite for the engineering of the cryogenic systems. This is another constraint on the optical design.

## 6.3 Offset Gregorian Design

The first telescope design of *CORE* that was tested was an Offset Gregorian telescope. The design was created using OpticStudio in Maynooth, optimised with CODE V in Minnesota and returned to Maynooth for PO analysis. It was returned in a STEP file format, meaning meshing was required to translate the design into a form readable by GRASP so that PO analysis could be performed.

### 6.3.1 Implementation in GRASP

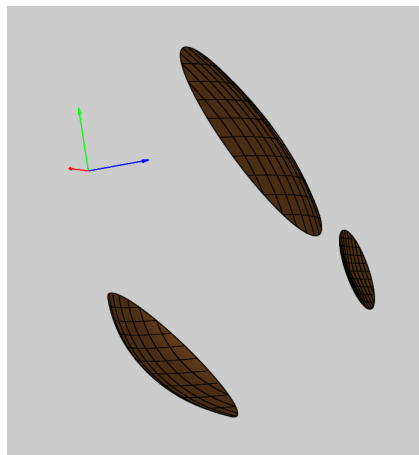


Figure 6.2: The implemented meshed objects of the Offset Gregorian telescope.

The process of importing the meshed mirrors of the Offset Gregorian design has been covered in **Chapter 4**. Both reflectors (primary and secondary) and the focal plane representation shared a common global coordinate system. As a result, no manual adjustments were needed to return the meshed mirrors to their proper positions. The GRASP model is shown in Figure 6.2.

The rims of the three objects required decentering from the global coordinate system. These values were found via geometrical information contained in the CAD model. The values are contained in Table 6.1:

Offset Gregorian Rim Data				
Object	Centre (x) (m)	Centre (y) (m)	Radius (x) (m)	Radius (y) (m)
<b>Primary</b>	0	0	0.819	0.819
<b>Secondary</b>	0	-1.543	0.65	0.564
<b>Focal Plane</b>	0	-1.1422	0.3232	0.3232

Table 6.1: Rim data for the Offset Gregorian mirrors and focal plane.

The model now needed to be prepared for physical optics calculations. Two *PO, Analysis* objects were created for the primary and secondary mirrors. The focal plane material was adjusted to be 100% transmitting, given that it is merely a representation of the circle of least confusion and therefore not designated as a reflector. The analysis frequency was chosen to be 100 GHz. Feeds of radiation would be placed at the focal plane to be propagated through the mirrors and captured by offset grids placed on the sky. Gaussian beams were used to represent the detector feeds in the first instance as an exact input field description is not available.

Feeds and grids would need to be aligned before any PO calculations could commence. The plan was to test the beams produced by the telescope up to  $8^\circ$  off-axis on the sky. This would take the form of 17 feeds; one placed at the centre of the FOV and the others offset along either azimuth  $\theta$  or elevation  $\phi$ . Focal plane locations were spaced by  $1^\circ$  to a maximum of  $4^\circ$ . This allowed a sizeable

portion of the FOV to be analysed.

A vector approach was used to place and align the feeds on the focal plane. Propagation in the telescope system is reciprocal, so a beam incident at an angle of  $+2^\circ$  elevation will meet the focal plane at a specific coordinate and angle. A feed placed at that point on the focal plane and oriented  $180^\circ$  opposite to that angle will produce a beam that follows the same path and travels onto the sky offset at  $+2^\circ$  in elevation. This principle would allow all the offset feeds to be positioned and oriented correctly.

Taking the  $z$ -axis of the global coordinate system as the centre ray, plane ray objects were constructed in GRASP at offsets ranging from  $+4^\circ$  to  $-4^\circ$  in both azimuth and elevation. These objects are intended as a visual aid, but the points where rays contact a surface can be recorded. Additionally, a plot of the mirror system allows those points to be obtained manually. The chief ray was used as the guide since the majority of the power propagates along that direction. The point of contact of a ray with the focal plane will become the location of a Gaussian feed. To compute the orientation of that feed, a vector was constructed using the contact point with the focal plane as point A and the point of contact with the subreflector as point B. The resulting unit vector  $\hat{\mathbf{R}}$  can be computed with the following equations:

$$|\mathbf{R}| = \sqrt{(A_x - B_x)^2 + (A_y - B_y)^2 + (A_z - B_z)^2} \quad (6.1)$$

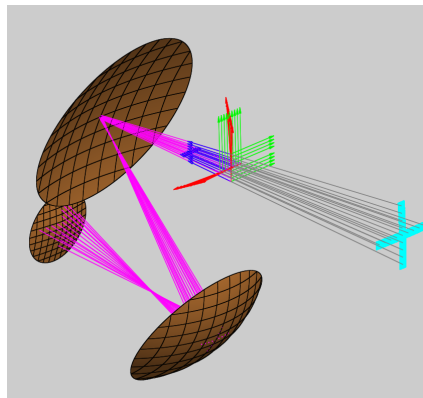
$$\hat{\mathbf{R}} = \frac{A_x - B_x}{|\mathbf{R}|} \hat{\mathbf{x}} + \frac{A_y - B_y}{|\mathbf{R}|} \hat{\mathbf{y}} + \frac{A_z - B_z}{|\mathbf{R}|} \hat{\mathbf{z}} \quad (6.2)$$

This unit vector  $\hat{\mathbf{R}}$  will serve as the  $z$ -axis of a particular Gaussian feed. Once entered into the coordinate system, the ray from the feed and the incident plane ray will be aligned. The locations and orientations of the feeds used in the Offset Gregorian design are listed in Table 6.2:

Feed Coordinate System Values						
Coord. Sys.	x (m)	y (m)	z (m)	$\alpha$ ( $^\circ$ )	$\beta$ ( $^\circ$ )	$\gamma$ ( $^\circ$ )
Central	0.0	-1.09	1.99 1	-90.035	163.658	-0.0332
$\theta+1^\circ$	-0.0528	-1.092	1.991	-79.971	163.4806	-26.3087
$\theta+2^\circ$	-0.108	-1.0952	1.991	-70.121	162.8870	179.6862
$\theta+3^\circ$	-0.1615	-1.1022	1.991	-61.115	162	117.6853
$\theta+4^\circ$	-0.216	-1.11	1.99	-53.0176	160.7650	121.0770
$\theta-1^\circ$	0.0564	-1.089	2.0	-100.36	163.4537	260.0571
$\theta-2^\circ$	0.1116	-1.095	2.0	-110.24	162.95	250.5824
$\theta-3^\circ$	0.1893	-1.054	2.15	-118.975	161.9222	242.2373
$\theta-4^\circ$	0.2197	-1.1067	2.0	-127.161	160.7145	234.4190
$\phi+1^\circ$	0.00174	-1.1446	1.99	-90.2316	166.4835	179.7749
$\phi+2^\circ$	0.00147	-1.1977	2.01	-90.2466	169.3913	179.7576
$\phi+3^\circ$	0.0	-1.255	2.029	-90.0	172.361	180.0
$\phi+4^\circ$	0.00018	-1.314	2.04935	-90.0	175.3436	180.0
$\phi-1^\circ$	0.00134	-1.036	1.99282	-90.0	160.8586	90.0
$\phi-2^\circ$	0.00092	-0.9825	1.99449	-90.0	158.1138	90.0
$\phi-3^\circ$	-0.00011	-0.9275	1.99621	-90.0	155.3786	90.0
$\phi-4^\circ$	-0.00024	-0.8755	1.99784	-90.0	152.7568	90.0

Table 6.2: Offset Gregorian feed coord. system parameters using Euler angles.

A similar, albeit far simpler, process is used to align the output grids. Take for example the  $-3^\circ$  elevation output grid. The coordinate system of the grid is based on the coordinate system of the  $-3^\circ$  elevation plane ray. The grid coordinate system is then rotated by  $180^\circ$  to place the grid behind the incident plane ray. This grid will now be primed to collect radiation from the aligned  $-3^\circ$  elevation feed. The fully aligned system is illustrated in Figure 6.3:

Figure 6.3: The aligned Offset Gregorian *CORE* telescope.

### 6.3.2 Physical Optics Analysis

When analysing the Offset Gregorian telescope, the feed beam waists were chosen to be 10 mm (representative of an equivalent Gaussian for a detector feed). The frequency was set to 100 GHz. The far-field grid size was chosen to be  $2^\circ$  elevation by  $2^\circ$  azimuth, which collects all of the beam pattern on the sky. Those feeds offset in  $\phi$  were selected for PO analysis. The results of the physical optics analysis are presented in Table 6.3:

Physical Optics Results (Gregorian)					
Beam Offset	Gaussicity (%)	$\omega_x$ ( $^\circ$ )	$\omega_y$ ( $^\circ$ )	$x_0$ ( $^\circ$ )	$y_0$ ( $^\circ$ )
$\phi+4^\circ$	97.02	0.188	0.168	0	-0.085
$\phi+3^\circ$	99.11	0.187	0.175	0	-0.096
$\phi+2^\circ$	99.55	0.188	0.181	0	-0.120
$\phi+1^\circ$	99.73	0.189	0.187	0	-0.129
$\phi=0^\circ$	99.75	0.188	0.194	0	-0.121
$\phi-1^\circ$	99.64	0.186	0.201	0	0.124
$\phi-2^\circ$	98.90	0.120	0.132	0	0.124
$\phi-3^\circ$	97.53	0.118	0.136	0	0.160
$\phi-4^\circ$	94.55	0.128	0.139	0	0.144

Table 6.3: Results of the Offset Gregorian PO analysis.

Included below in Figure 6.4 is the co-polar beam pattern for the centre feed ( $\theta=0^\circ$ ,  $\phi=0^\circ$ ). Note that due to the optimisation of the mirror surfaces in CODE V, this beam is not as symmetric as might be assumed as it is completely on-axis:

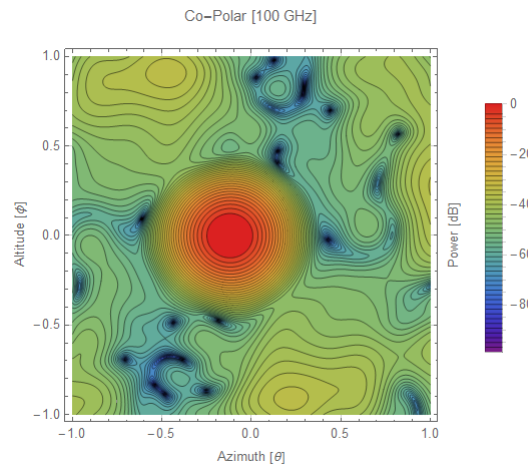


Figure 6.4: The co-polar beam pattern for central feed at 100 GHz.

### 6.3.3 Depth of Field Analysis

A depth of field analysis was also carried out on the Offset Gregorian design. This arose due to the fact that the design had been optimised in OpticStudio and CODE V. The focal plane has a peculiar conic shape as a result and it was deemed necessary to examine the evolution of the beams along the local  $z$ -axis of the focal plane. The flatness of the focal plane is important for the detector tiling. The feeds were gradually stepped back in 5 mm increments to a maximum distance of 40 mm and the Gaussicity of each beam was recorded. This served to give a broad idea as to how the quality of the beams would change with distance from the nominal focus. The Gaussicity results give an indication of the depth of field of the beams and are shown in Table 6.4:

Depth of Field Gaussicity Results									
Field	$z$ (mm)								
	0	5	10	15	20	25	30	35	40
0°	99.745	99.75	99.694	99.7113	99.7561	99.7543	99.7502	99.7447	99.7373
+1°	99.7291	99.7306	99.5724	99.6758	99.7206	99.7308	99.7284	99.712	99.7045
+2°	99.5473	99.5495	99.5516	99.4764	99.5497	99.5446	99.5567	99.5568	99.5564
+3°	99.1082	99.1203	98.8064	99.0307	99.1427	99.1592	99.0946	99.2004	99.2004
+4°	97.0169	98.2834	98.3194	98.0829	98.2768	98.4006	98.4597	98.4939	98.5271
-1°	99.6353	99.6414	99.6453	99.6465	99.6173	99.6408	99.6337	99.6238	99.6119
-2°	98.8977	99.3816	99.376	99.3672	99.3548	99.3389	99.3196	99.2973	99.2716
-3°	97.5321	98.8488	98.8156	98.7852	98.7548	98.7078	98.6487	98.6214	98.568
-4°	94.5527	94.102	93.6847	93.2416	92.7726	92.2895	91.795	91.29	90.7744

Table 6.4: Gaussicity values recorded in the Depth of Field analysis.

Narrowing in on  $z = 25$  mm for examination in greater detail, a finer step size (1 mm) was used in the analysis. The results are set out in Table 6.5:

Depth of Field Gaussicity Results				
Field	$z$ (mm)			
	26	27	28	29
0°	99.754	99.7527	99.7394	99.7513
+1°	99.7302	99.7292	99.7276	99.729
+2°	99.5359	99.5252	99.5567	99.5568
+3°	99.192	99.194	99.1924	99.1134
+4°	98.4325	98.4394	98.4435	98.4528

Table 6.5: Gaussicity values for the finer Depth of Field results.

### 6.3.4 Evolution of Beam along Local Z-Axis

In this section, the far-field beam patterns originating from the different  $z$  positions of the central feed will be shown. This will give an indication as to how the beam is evolving with increasing distance along the local  $z$ -axis from the designated focal plane position, similar to Tables 6.4 and 6.5. The beam characteristics remain quite consistent.

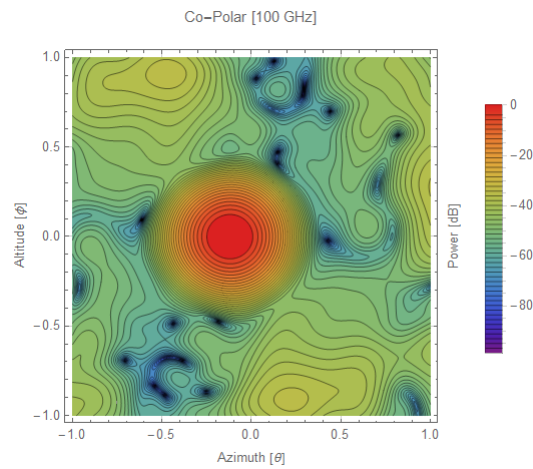


Figure 6.5: The co-polar beam pattern for  $z=0$  mm.

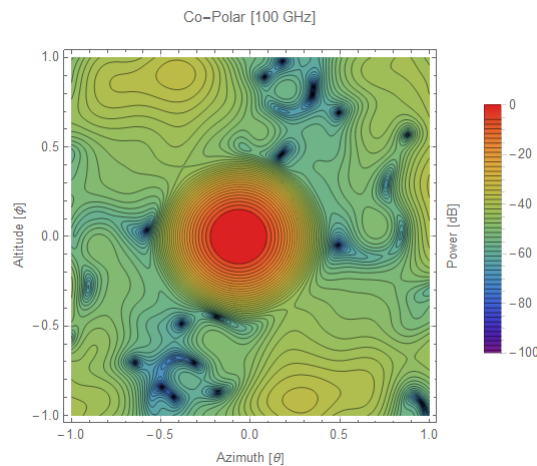
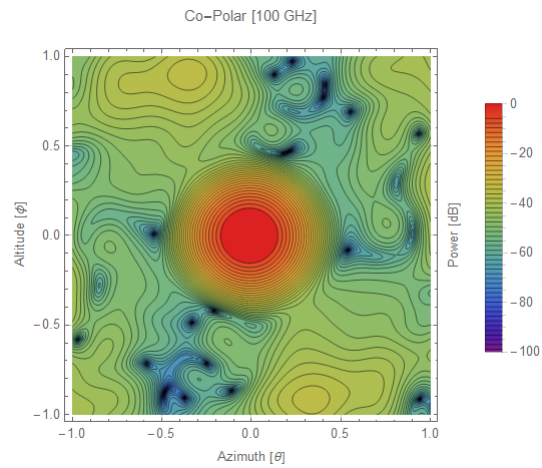
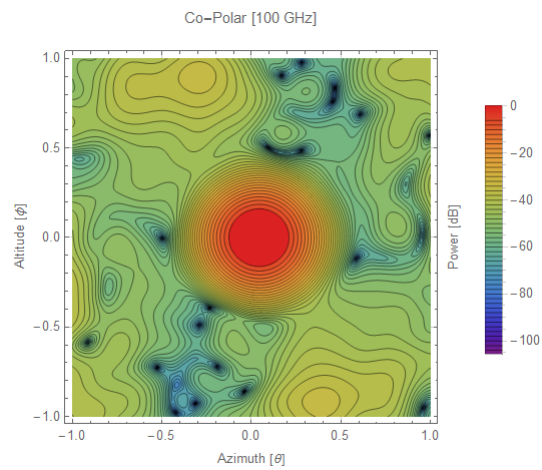
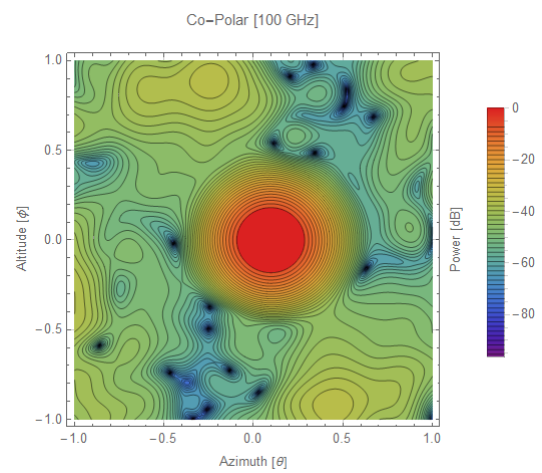


Figure 6.6: The co-polar beam pattern for  $z=10$  mm.

Figure 6.7: The co-polar beam pattern for  $z=20$  mm.Figure 6.8: The co-polar beam pattern for  $z=30$  mm.Figure 6.9: The co-polar beam pattern for  $z=40$  mm.

As Figures 6.5 - 6.9 show, the Gaussicity rise occurs when the beam begins to move towards the centre of the focal plane. What appears to be happening is that, for a particular beam, the focal plane is moving from the compromise focus where it sits in the model and towards the actual focus of that beam. Rises and falls in Gaussicity can be seen to occur for all offset beams as their particular foci are reached and passed by. This is indicative of the issue with the curved focal plane; a compromise location will always be sought.

## 6.4 Offset Dragonian Design

The other design under consideration was an Offset Dragonian design. The model of this telescope had been created in Maynooth, so the work for this design was primarily to establish the feed network as with the Offset Gregorian and to test the mirror system using PO.

### 6.4.1 Implementation in GRASP

The model of the Offset Dragonian had been constructed in GRASP using optimised parabolic and hyperbolic mirror surfaces for the primary and secondary.

<b>Primary Mirror Data</b>	
<b>Focal Length (mm)</b>	6545.46
<b>Vertex (x) (mm)</b>	0.0
<b>Vertex (y) (mm)</b>	0.0
<b>Vertex (z) (mm)</b>	0.0
<b>Rim Centre (x) (mm)</b>	6534.3962
<b>Rim Centre (y) (mm)</b>	0.0
<b>Rim Radius (x) (mm)</b>	900.0
<b>Rim Radius (y) (mm)</b>	800.0
<b>x coord. (mm)</b>	0.0
<b>y coord. (mm)</b>	0.0
<b>z coord. (mm)</b>	0.0
$\alpha$ (°)	0.0
$\beta$ (°)	0.0
$\gamma$ (°)	0.0

Table 6.6: Offset Dragonian primary mirror data.

<b>Secondary Mirror Data</b>	
<b>Vertex Distance (mm)</b>	-3737.037
<b>Foci Distance (x) (mm)</b>	9,081.0
<b>Rim Centre (x) (mm)</b>	-1562.5639
<b>Rim Centre (y) (mm)</b>	0.0
<b>Rim Radius (x) (mm)</b>	950.876
<b>Rim Radius (y) (mm)</b>	796.8631
<b>x (mm)</b>	0.0
<b>y (mm)</b>	0.0
<b>z (mm)</b>	0.0
$\alpha$ ( $^{\circ}$ )	0.0
$\beta$ ( $^{\circ}$ )	114.089
$\gamma$ ( $^{\circ}$ )	180

Table 6.7: Offset Dragonian secondary mirror data.

The parameters of the two mirrors are shown in Tables 6.6 and 6.7. The coordinate system for the primary mirror was located at the global coordinate system. The coordinate system for the secondary mirror was located at the global but moved a distance of 6545.6 mm in  $z$ , a distance equal to the focal length of the primary mirror. Equations to construct an Offset Dragonian system can be found in Chang and Prata (2004).

### 6.4.2 Positioning and Orienting Feeds and Grids

The feeds were placed via the ray-tracing method used with the Offset Gregorian model. With no physical representation of the focal plane this time, the endpoints of the rays were used as a positioning point for the feeds. The central feed and those offset by  $\pm 4^{\circ}$  in  $\phi$  were already positioned in the model, providing useful guide posts. The ray path length was set to 6.515 m, which would position the ray end point at the location of the central feed propagating from the sky. The end points of the other rays would then form an ideal focal plane for the Offset Dragonian. The AB vector approach was used to orient each feed along the path of its chief ray counterpart. The location and orientation each ray is set out in Table 6.8:

Feed Coordinate System Values						
Coord. Sys.	x (mm)	y (mm)	z (mm)	$\alpha$ ( $^\circ$ )	$\beta$ ( $^\circ$ )	$\gamma$ ( $^\circ$ )
Central	8290.1588	0.0	2,839.0	-180	96.1605	270
$\theta+1^\circ$	8290.05	63.0512	2838.87	-179.1572	96.1579	90.1963
$\theta+2^\circ$	8286.9	126.096	2838.12	-178.3155	96.1720	179.3155
$\theta+3^\circ$	8282.73	189.092	2837.12	-177.4707	96.1379	22.4470
$\theta+4^\circ$	8277.37	251.736	2835.79	-176.6322	96.1223	28.8878
$\theta-1^\circ$	8289.5	-63.0512	2838.84	179.1569	96.1585	-90.1960
$\theta-2^\circ$	8286.39	-125.667	2838.12	178.3178	96.1507	-15.3283
$\theta-3^\circ$	8282.82	-188.475	2837.12	177.4804	96.1378	-22.3694
$\theta-4^\circ$	8277.07	-251.55	2835.65	176.6308	96.1202	-28.9066
$\phi+1^\circ$	8296.39	0.0	2776.32	180.0	95.3205	-180.0
$\phi+2^\circ$	8300.48	0.0	2713.19	180.0	94.4779	-180.0
$\phi+3^\circ$	8301.23	0.0	2649.32	180.0	93.6268	-180.0
$\phi+4^\circ$	8300.3	0.0	2585.63	180.0	92.7726	-90.0
$\phi-1^\circ$	8281.85	0.0	2901.57	180.0	96.9937	-180.0
$\phi-2^\circ$	8272.14	0.0	2963.27	180.0	97.8237	180.0
$\phi-3^\circ$	8259.53	0.0	2963.27	180.0	98.64	-180.0
$\phi-4^\circ$	8245.61	0.0	3085.11	180.0	99.47	-90.0

Table 6.8: Offset Dragonian feed coord. system parameters.

The grids were placed in and oriented in exactly the same manner as with the Offset Gregorian. The fully implemented mirror system is shown in Figure 6.10:

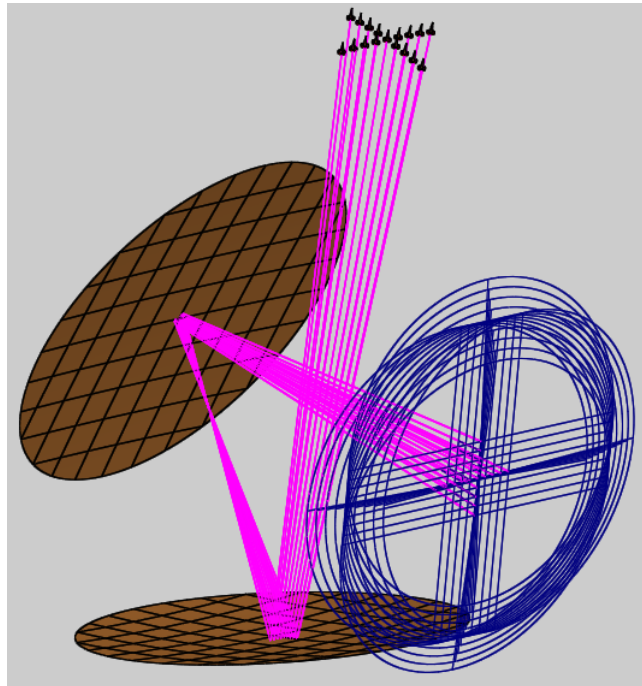


Figure 6.10: The offset rays of the Dragonian design. The dark blue objects are the plane wave sources.

### 6.4.3 Physical Optics Analysis

When analysing the Offset Dragonian telescope, the feed beam waists were chosen to be 10 mm with a frequency of 100 GHz. The far-field grid size was chosen to be  $2^\circ$  elevation by  $2^\circ$  azimuth. The results of the physical optics analysis carried out on this design are located in Table 6.9:

Physical Optics Results (Crossed Dragonian)					
Beam Offset	Gaussicity (%)	$\omega_x$ ( $^\circ$ )	$\omega_y$ ( $^\circ$ )	$x_0$ ( $^\circ$ )	$y_0$ ( $^\circ$ )
$\phi+4^\circ$	99.62	0.162	0.158	0	0.018
$\phi+3^\circ$	99.84	0.160	0.157	0	0.012
$\phi+2^\circ$	99.95	0.159	0.158	0	0.012
$\phi+1^\circ$	99.99	0.159	0.159	0	0
$\phi=0^\circ$	99.99	0.159	0.159	0	0
$\phi-1^\circ$	99.99	0.159	0.159	0	0.003
$\phi-2^\circ$	99.94	0.160	0.159	0	0.007
$\phi-3^\circ$	99.84	0.162	0.160	0	0.007
$\phi-4^\circ$	99.64	0.163	0.162	0	-0.012

Table 6.9: Results of the Offset Dragonian PO analysis.

The co-polar beam pattern for the central beam is included in Figure 6.11:

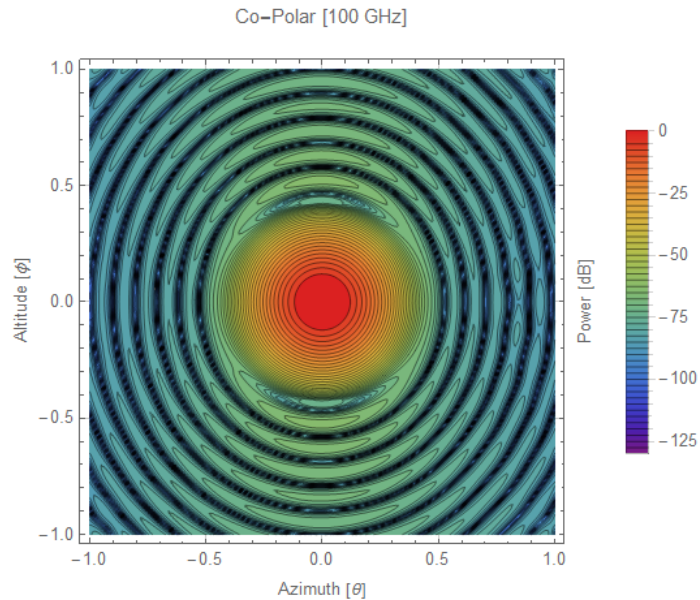


Figure 6.11: The co-polar beam pattern for  $\theta=0^\circ$ .

## 6.5 Comparison of Designs

Ultimately, the two mirror Offset Gregorian was excluded due to its inability to meet the stringent design requirements. The justifications can be found in de Bernardis et al. (2017) and will be discussed in the following sections.

### 6.5.1 Design

Offset Gregorian telescopes were used in *WMAP* and *Planck*, granting this design a high Technological Readiness Level (TRL). The mirrors of this design can be small and therefore lighter than an equivalent Dragonian. The vertical layout of the telescope combined with the reverse orientation of the secondary mirror makes them easy to baffle against stray light. However, the DLFOV of these telescopes is naturally smaller than that of *CORE*. A lens would be needed to flatten the focal plane, but given that the lens and the anti-reflection coating would not be space-proven technology, this would lower the TRL of the mission.

The Offset Dragonian telescope grants a large, flat and telecentric focal plane, as is required. The design also induces low instrumental/polarisation rotation. That said, the mirrors required for this telescope are bigger and heavier. The secondary mirror in particular must be of the same size as the primary, which is not the case with the Offset Gregorian. The positioning of the primary and secondary mirrors so close to one another makes baffling more of a challenge. Despite the larger overall design, the telescope would still fit inside the fairing of an Ariane 5/6, the intended launch vehicle of M-class missions.

### 6.5.2 Focal Plane

Due to the nature of the detectors (ideally flat tiles), the shape of the focal plane was critical to the *CORE* mission. A large, telecentric and flat focal plane is required. Any excessive curvature of that focal plane would lead to shadowing of

detectors and require a large depth of field. Beginning with the Offset Gregorian, its focal plane (represented as a surface) can be seen in Figure 6.12:

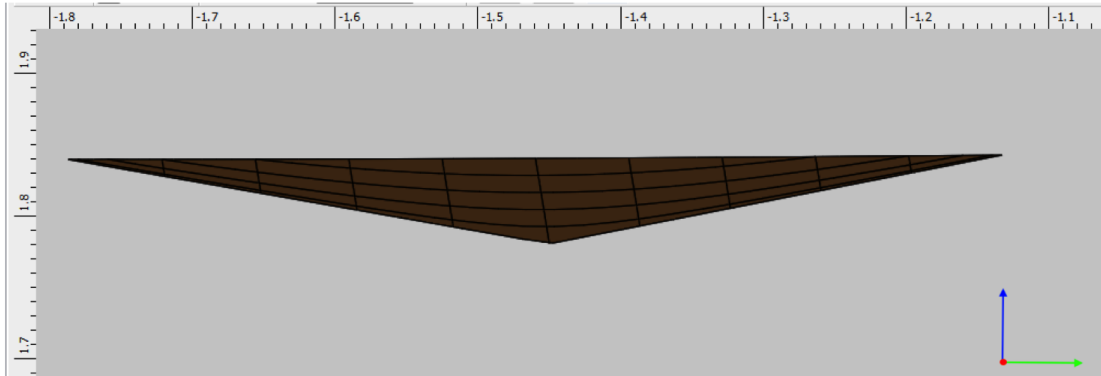


Figure 6.12: The focal plane of the Gregorian design.

Detectors would be placed along the surface, much like a mosaic. What is immediately noticeable is the curvature of this focal plane. This is a result of optimisations carried out in CODE V. The subreflector was optimised to increase the field of view of the telescope, but the focal plane adopted a non-flat shape as a result. It is formed from the circle of least confusion of the telescope, which is the best possible focus for a non-ideal system.

The shape of the Offset Dragonians focal plane can be seen in Figure 6.13:

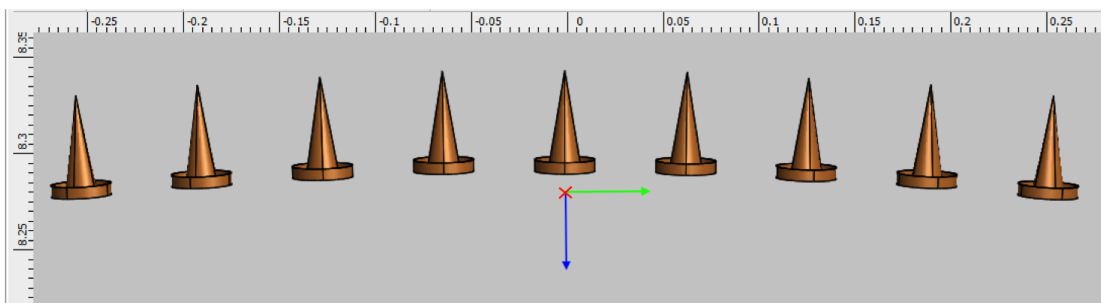


Figure 6.13: The focal plane of the Dragonian design.

Note that the scales of the above two figures are in metres. The ruler function is tied to the global coordinate system, hence the different values displayed for both figures. While the focal plane is not flat, it is much more so than the

Gregorian designs focal plane, which covers a distance of 6 cm along the local  $z$ -axis from centre to edge (see Figure 6.12). Please note that the figure shows the focal planes shape in the  $x$ -direction. The focal plane is formed from a wave front whose central point meets the central feed of the model. Large, flat and telecentric focal planes are hallmarks of Offset Dragonian designs, with trade-offs taking the form of the larger subreflector. This flatter focal plane (roughly 0.3 cm along the local  $z$ -axis) was one of the primary reasons the Offset Dragonian design was chosen.

### 6.5.3 Conclusion

It was the conclusion of the *CORE* Consortium that the larger DLFOV of the Offset Dragonian telescope (which the Offset Gregorian could not meet) rendered it more suitable for fulfilling the requirements of the mission. The limitations of the Offset Dragonian design can be addressed without lowering TRL levels, which is a major factor in ESA mission evaluation. The same is not true of the Offset Gregorian telescope. The curvature of the Offset Gregorian could be rectified with an additional lens but this would add complexity and lower the usable FOV of the telescope further.

## 6.6 *CORE* Finalised Design

The finalised design of *CORE* took the form of the Offset Dragonian with additional optimisation to obtain an even flatter focal plane and a folding mirror to keep the design compact within the launcher volume. The redirection offered by the new mirror also allows the focal plane and cryogenic systems to be located near the base of the satellite, which is crucial for cryogenic containment purposes. This was based off of a JAXA/NASA telescope design known as Lite-BIRD. The design was given to Maynooth in CAD format from collaborators Mr. Karl Young and Dr. Shaul Hanany of Minnesota University, so meshing was

required to import the mirrors. The CAD model is shown in Figure 6.14.

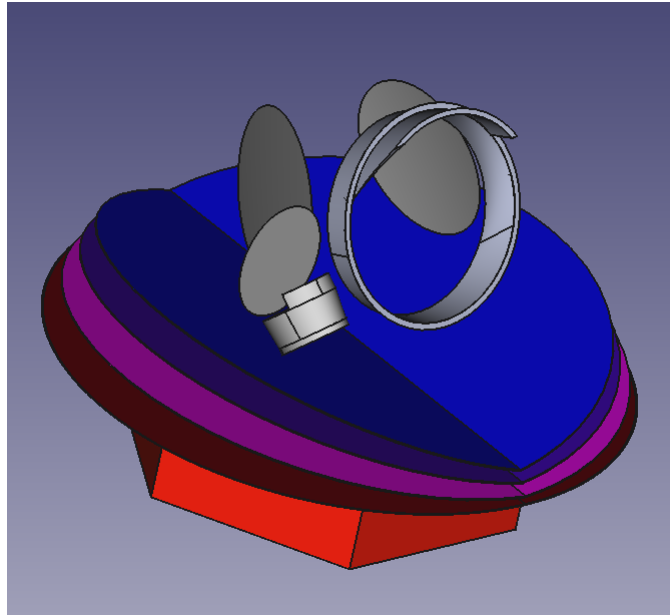


Figure 6.14: The CAD model of the finalised *CORE* telescope.

### 6.6.1 Meshing the New Design

The procedure of meshing the new mirrors will now be discussed. Three STEP files were given to Maynooth: one containing the mirrors, one with mirrors and baffling and one with shielding, baffling and the mirrors. At this point the important thing was to get the mirrors imported to GRASP successfully. Hence the mirror-only file was imported.

FreeCAD was used to mesh the mirrors. Netgen was again chosen for the mesh type due to its superior ability to mesh the mirror edges well. Each mirror has its coordinate system base at a common global position at the telescope aperture. A translation and rotation had been applied to the mirrors because they had been taken from the full *CORE* CAD model. These changes had been necessary to position the mirrors among the other components. However, the repositioning would make it impossible to import the meshes to GRASP. With an existing translation/rotation, the mirror rims would need to be decentered and rotated

in a manner similar to the two-mirror Offset Dragonian design mentioned previously. The difficulty here lay in the fact that the only solid positional information available from the model was vertex position. No centre points could be retrieved as none existed. The rim rotations in GRASP are not the same as model rotations in FreeCAD, so these values would also be unobtainable. Therefore, the simpler and more robust option was to remove the rotation and translation from the FreeCAD model. The removal of inherent offsets and rotations also make analysis of the design far easier to accomplish. The initial format of the design can be seen in Figure 6.15:

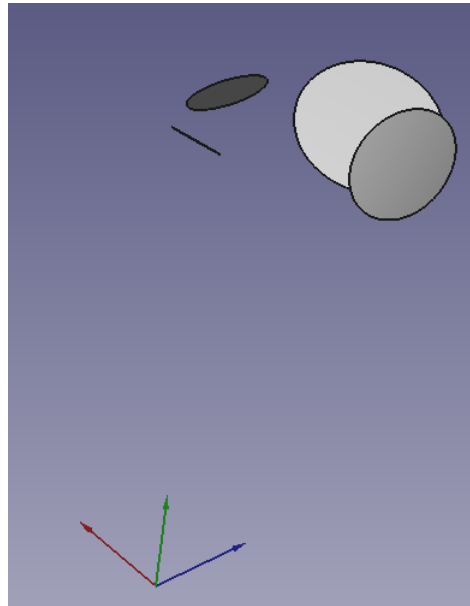


Figure 6.15: The initial, translated *CORE* mirrors.

The values required to undo the translation are shown in Table 6.10:

<b>Translation Values</b>	
<b>Parameter</b>	<b>Value</b>
x (mm)	-2065.36
y (mm)	-3152.14
z (mm)	-2951.46
Yaw (°)	102.927
Pitch (°)	-24.095
Roll (°)	7.1376

Table 6.10: Position/Rotation information to relocate the model.

The results of the changes to the mirror coordinates can be seen in Figure 6.16:

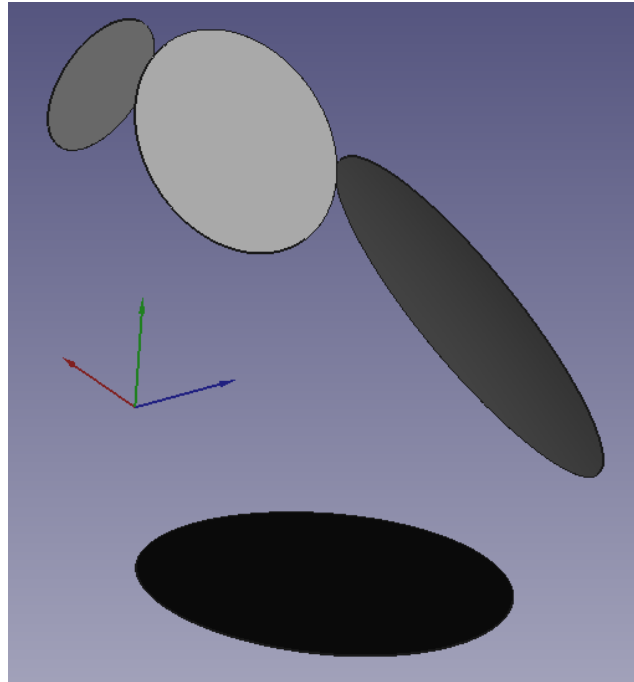


Figure 6.16: The repositioned mirrors of the *CORE* telescope.

Now the model would be aligned with the sky correctly. As with the previous Offset Dragonian design, the  $x$ -axis follows azimuth ( $\theta$ ) and the  $y$ -axis follows elevation ( $\phi$ ). The model was now ready to be meshed.

To create meshes that would be compatible with GRASP, two conditions needed to be fulfilled. First, the mirror would need to have a vertex placed over the global coordinate system. The position of the vertex is one of the few aspects of the CAD model which will return a positional value, so by placing the vertex over the global the intervening offset will be eliminated and the placement of the mesh can be controlled precisely. Secondly, the surface normal of a mirror object must be parallel to the global  $z$ -axis. If this is not done then GRASP will experience difficulty in rendering the model. The reason for this effect is unknown, but is certainly associated with the GRASP algorithm which joins up the meshed points into the irregular triangular faces that comprise the meshed mirror surface.

Taking the meshing of the secondary mirror as an example, the meshing process will now be explained. The first piece of information required was the position of the vertices of that mirror. The value of a vertex can be found by selecting the vertex in the 3D view or retrieving it with python commands. The python commands have the advantage of listing all vertex positions in a format that is easy to copy. The first command is “`ev=App.ActiveDocument.Part.Shape.Vertexes`”. When entered in FreeCAD’s python console, the *xyz* values of the vertexes of object “Part” will be retrieved. The second command is “`for v in ev: v.X,v.Y,v.Z`”. This simple loop will extract all of the stored values in the *ev* array. For the secondary mirror, the vertex locations are shown in Table 6.11:

Subreflector Vertex Values		
Parameter	Vertex 1	Vertex 2
x (mm)	620	-579.99
y (mm)	-953.12	-955.93
z (mm)	928.46	926.63

Table 6.11: Position of the vertices of the secondary mirror.

The mirror must now be rotated to such that its surface normal will be parallel with the global *z*–axis. This was done simply by setting the **roll** of the mirror to 90°. This rotation can then be cancelled in GRASP via rotation in the opposite direction. Note that an additional reposition may be required after re-orienting the mirror. Figure 6.17 shows the repositioned subreflector in FreeCAD.

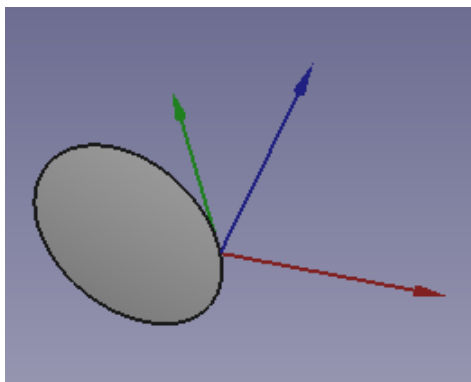


Figure 6.17: The repositioned *CORE* subreflector, showing the vertex location centred on the global coord. system.

### 6.6.2 Implementing *CORE* in GRASP

The meshes were reformatted and imported into GRASP. The coordinate system values and rim data are shown in Table 6.12:

<i>CORE</i> Mirror Values				
Parameter	Primary	Secondary	Folding Mirror	Focal Plane
x (mm)	670.0	620.0	279.597	511.629
y (mm)	-1.7075	-953.119	1299.32	1276.33
z (mm)	1480.874	928.46	321.878	162.303
$\alpha$ ( $^\circ$ )	0	90	90	0
$\beta$ ( $^\circ$ )	0	90	90	0
$\gamma$ ( $^\circ$ )	0	-90	-90	0
Rim Centre (X) (mm)	-669.9964	-599.99	-300.83	-0.0009
Rim Centre (Y) (mm)	1.56155	0.9135	-30.583	-238.675
Rim Radius (X) (mm)	669.995	600.0	302.38	114.815
Rim Radius (Y) (mm)	669.88	720.16	419.82	241.455

Table 6.12: Parameters of the four *CORE* mesh objects.

The fully established system can be seen in Figures 6.18 and 6.19:

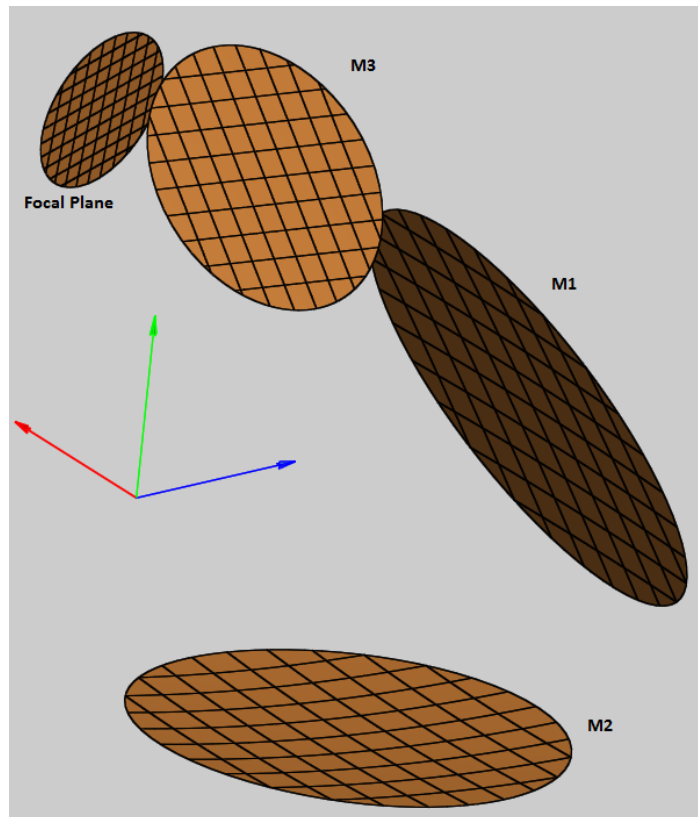


Figure 6.18: The imported mirrors of the *CORE* telescope in GRASP.

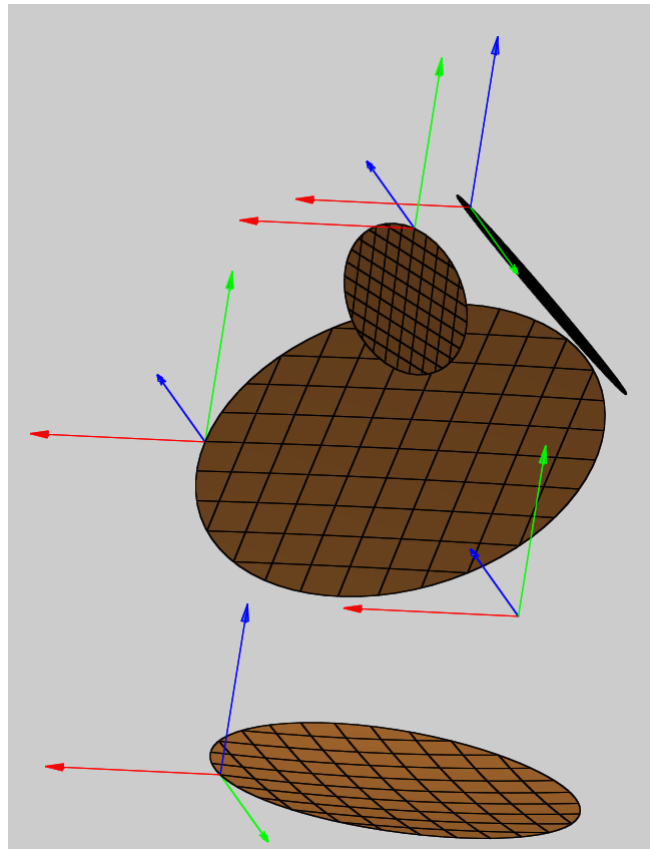


Figure 6.19: The *CORE* telescope showing vertex locations and the mirror global coordinate system.

The vertex placement approach allows a one-to-one comparison with the FreeCAD model, which in turn makes verification of the correct implementation of the design straightforward. With the mirrors in place, feed placement can now begin over the focal plane.

### 6.6.3 Modelling Information

The goal of this section is to clarify aspects of the positioning and orienting of Gaussian pattern feeds on the working *CORE* model in Maynooth. The first section will detail how feeds were placed onto the focal plane. The second section will describe how the feeds were subsequently oriented to project beams to the sky correctly for analysis. The third section contains information on the set-up of the detector grids. Finally, section four will contain a number of projections

of the current *CORE* system showing the path of the edge (i.e.  $+4^\circ$ ,  $-4^\circ$ )  $\theta$  and  $\phi$  offset rays.

#### 6.6.4 Positioning Feeds on the Focal Plane

In order to determine the location where each feed would have to be placed correctly and oriented to receive radiation on-axis from the equivalent sky angular position each time. Plane rays at various offsets were propagated through the telescope aperture. The rays would travel through the mirror system and come to a focus at the equivalent focal plane. A feed would be placed at the location on the focal plane where its corresponding chief ray intersected the focal plane. The chief ray was used for this purpose as the majority of the transmitted power lies along this ray.

The position of the contact point of a ray with the focal plane was found using the “Show Position” feature available on GRASP’s plots. Figure 6.20 shows the feature in use. This feature displays the position of the mouse pointer in Cartesian  $xyz$  coordinates, depending on the projection. For example, if one was looking along the XZ plane, the coordinates displayed would be the  $x$  and  $z$  coordinates of the pointer. The coordinates themselves would all be based on the global coordinate system.

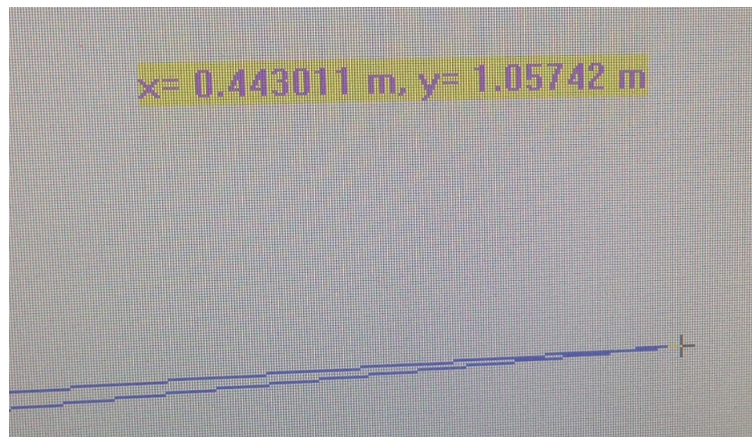


Figure 6.20: Show position feature. The ray being investigated is  $\phi = +4^\circ$ .

Each feed was given its own coordinate system. Each one used the global coordinate system as its reference and used the coordinates of the contact point as its  $xyz$  coordinates. Figure 6.21 shows the coordinates entered in GRASP. The end result is that the centre of the feed (and the location of the beam waist  $\omega_0$ ) would sit at the point where the offset ray struck the focal plane. Giving the focal plane temporary reflective properties makes this point of contact easy to determine.

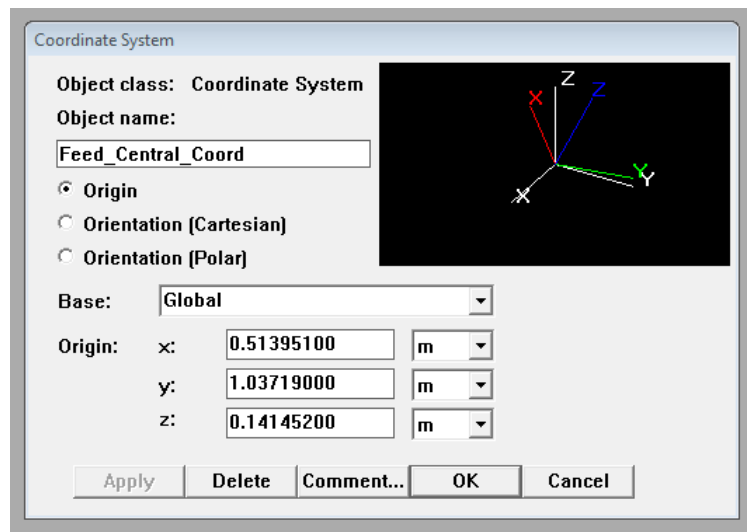


Figure 6.21: Coordinate system window for the central feed.

### 6.6.5 Orienting Feeds on Focal Plane

Having positioned the feeds, they now needed to be oriented correctly to transmit radiation along their intended offset path. A vector based approach was used to correctly point the feeds over the focal plane.

For any offset ray, the ray path from the folding mirror to the focal plane was treated as a vector. The point of contact with the folding mirror for a ray was found in an identical manner to the point of contact with the focal plane. Having two points A and B, a vector  $\mathbf{AB}$  could be constructed between them.

GRASP handles coordinate system orientation as follows. Three angles  $\theta$ ,  $\phi$  and  $\psi$  are used in a spherical coordinate system.  $\theta$  and  $\phi$  control the direction of the  $z$ -axis while  $\psi$  controls the rotation of the  $x$  and  $y$  axes. This system is favourable to positioning feeds. In effect,  $\theta$  and  $\phi$  control the pointing of the feed (since the emitted radiation follows the  $z$ -axis) and  $\psi$  controls the polarisation rotation. GRASP allows coordinate systems to be oriented in two ways: entering values for  $\theta$ ,  $\phi$  and  $\psi$  or entering unit vectors to represent each axis of the coordinate system. Figure 6.22 displays the rotation of the central feed entered in GRASP.

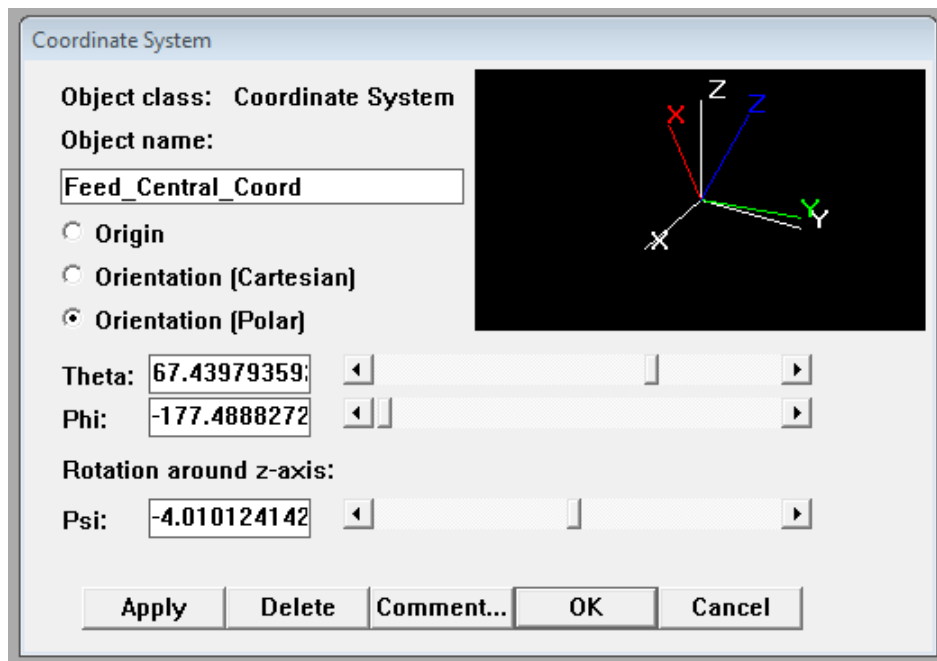


Figure 6.22: Polar orientation window for central feed coordinate system.

The new unit vector was entered in as the  $z$ -axis of the coordinate system. The  $x$  and  $y$  axes were then generated by GRASP so as to be orthogonal to the  $z$ -axis. The result was that the feed was now oriented in a such a way as to emit radiation along the path of the incident rays. According to the Theory of Reciprocity, the beams generated by these feeds, positioned as they are, will correspond to the offset sky beams.

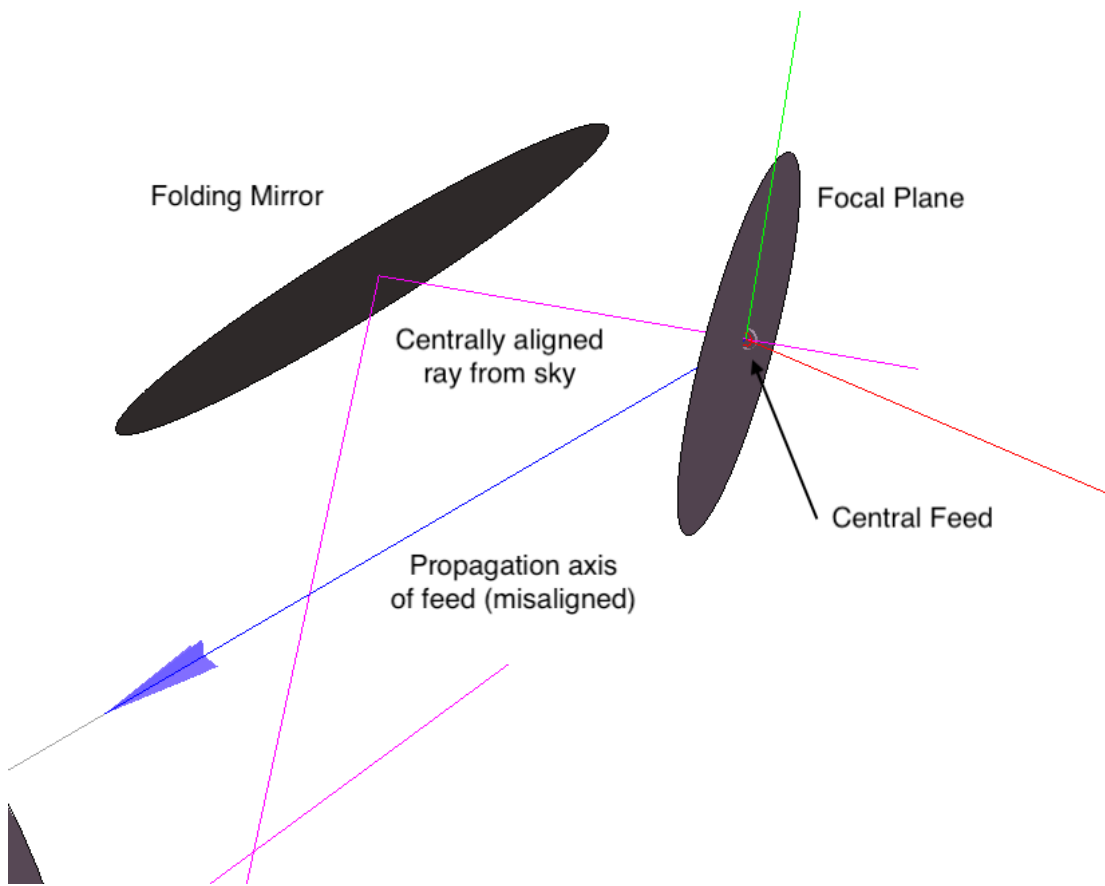


Figure 6.23: Unoriented central feed. Note that ray travels along  $z$ -axis of coordinate system.

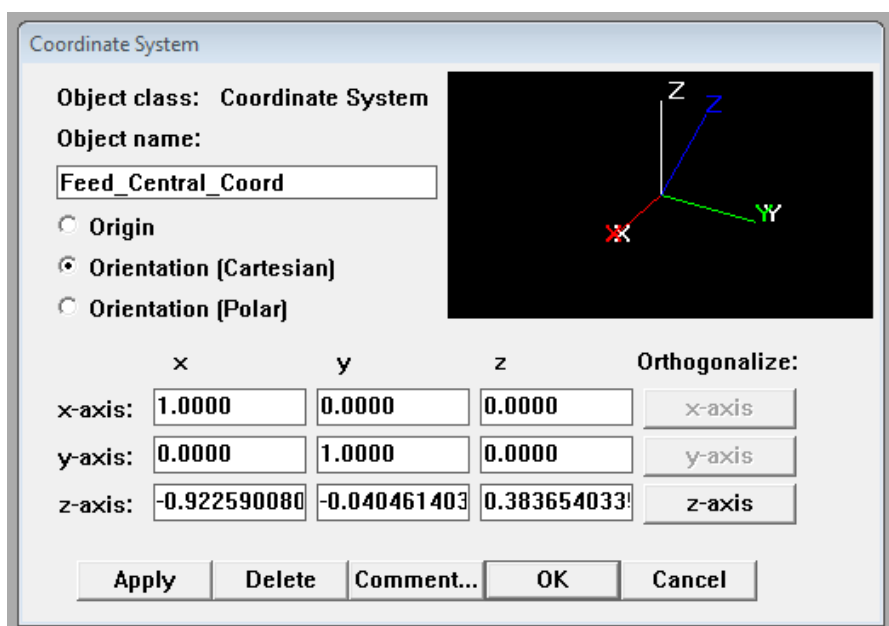


Figure 6.24: Unit vector orientation window prior to orthogonalisation of  $x$  and  $y$  axes. Unit vector describing ray path has been set as  $z$ -axis unit vector.

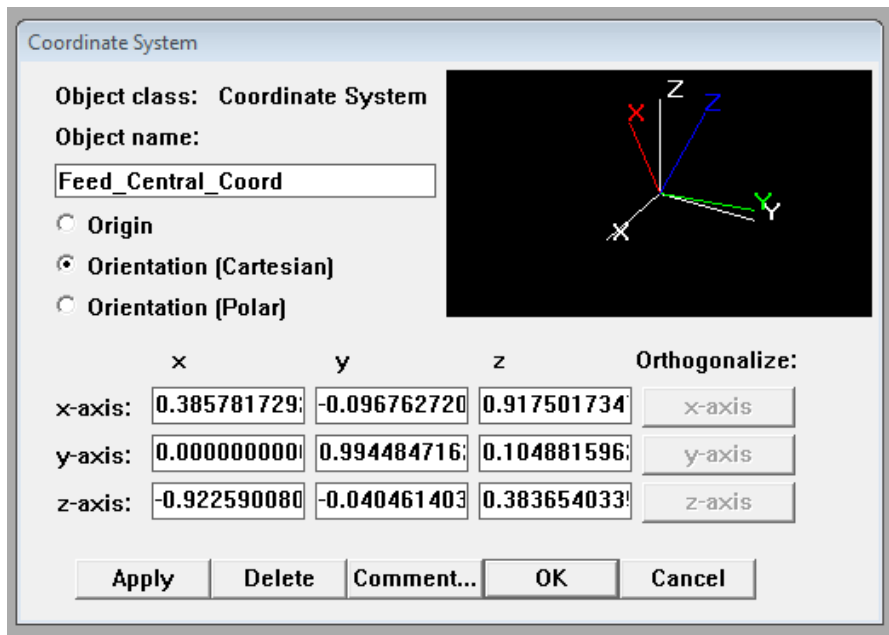


Figure 6.25: Unit vector orientation window after orthogonalisation of  $x$  and  $y$  axes.

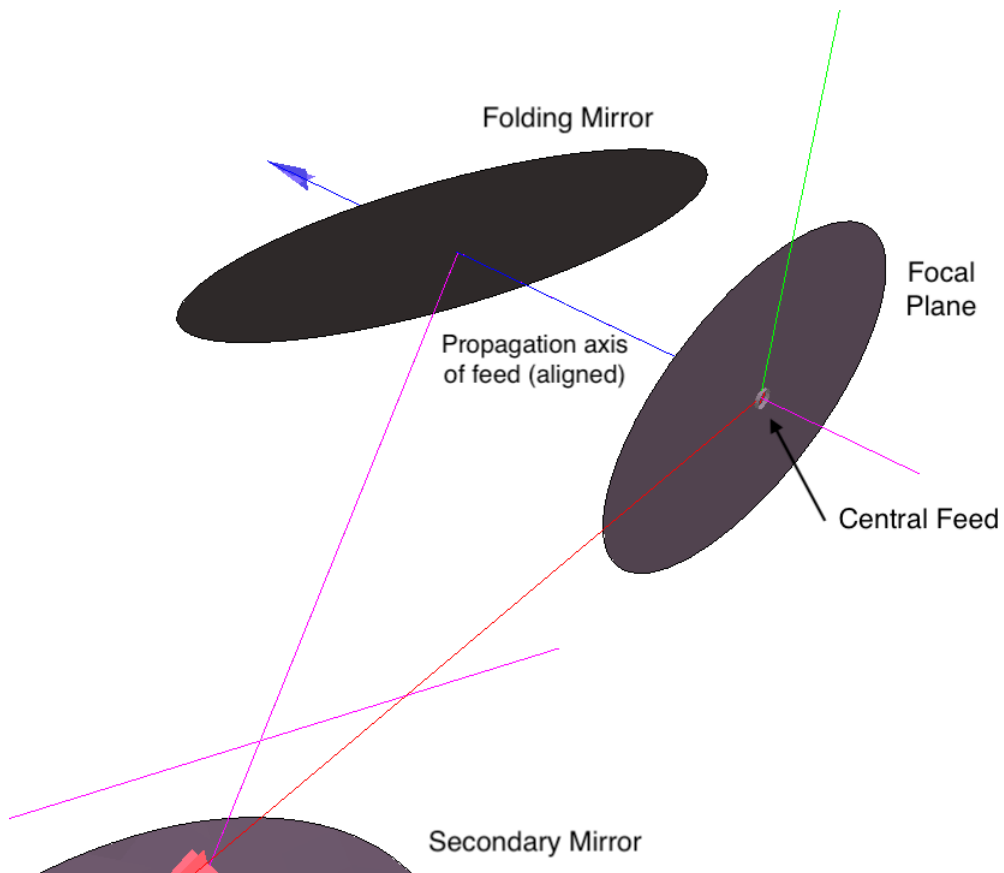


Figure 6.26: The feed is now aligned with the incoming rays.

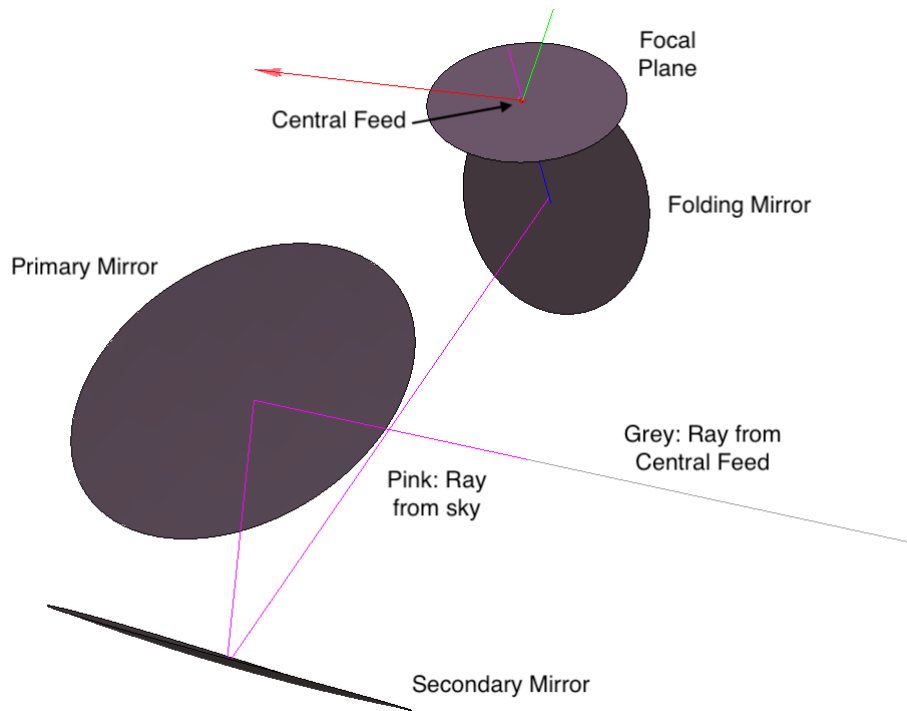


Figure 6.27: The grey feed ray retraces the exact path of the aperture ray.

Figures 6.23 - 6.27 detail the steps taken as the feed is oriented. The final item to fix was to negate projection effects for those feeds that were offset on the sky in azimuth ( $\theta$ ). As these feeds moved away from the axis of symmetry of the primary and secondary mirror, the radiation produced by them would experience unexpected polarisation rotations. The aberration is caused when the  $x$ -axis of the feed becomes misaligned from the  $x$ -axis of the incident radiation. The manifestation of the projection effect is that power will leak from the co-polar beam component to the cross-polar beam component, causing it to lose the characteristic on-axis dipole structure. Rather than rotate the grid to match the rotation of the feed, it made more sense to rotate the feed to negate the projection effect. In reality linearly polarised light will enter through the aperture and be detected at the focal plane. Thus the detectors will need to be rotated such that they can receive this polarised light with maximum response to the correct polarisation angles (i.e. the grids on the sky need to be correctly orientated with the corresponding input co-polar direction in each case).

The solution to the problem is quite simple and relies on GRASP’s ability to redefine coordinate systems to new bases. By setting the base of an affected feed to that of one which was unaffected by projection, the difference between the polarisation rotation of the two can be seen. Note that the method of feed orientation used contains no data on the polarisation rotation. This difference must be eliminated for the projection effect to be nullified. In terms of changes made to the model, the Euler angle  $\gamma$  (which controls polarisation rotation) must be set to zero. In the  $ZY'Z''$  rotation scheme of GRASP, this means that the feed will be pointed by rotating about the  $z$ -axis and then rotating about the new  $y'$ -axis. However, the additional rotation will take place about the new  $z''$ -axis and will be required to match up again with the polarisation rotation of the incident radiation. The polarisation rotations of both feeds will then match and the projection effect will have been resolved for that feed.

A worked example will now be provided dealing with the  $\theta = +1^\circ$  feed. The cross-polar component of the incorrectly rotated feed is shown in Figure 6.28:

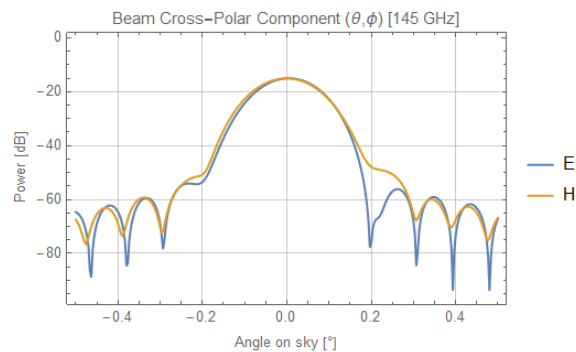


Figure 6.28: Cross-Polar component of the incorrectly rotated  $\theta+1^\circ$  feed.

The base of the  $\theta + 1^\circ$  feed was redefined to the central feed coordinate system. Moving across to the Euler angle tab, the relative orientation of the feed compared to the central can be seen. The  $\gamma$  angle (or  $\psi$  in GRASP angles) controls the polarisation rotation. The central feed has the correct polarisation rotation as it is placed along the telescopes axis of symmetry. The non-zero value of  $\gamma$  indicates

that the polarisation rotation of the  $\theta + 1^\circ$  feed is not the same as the central feed. Setting  $\gamma = 0$  in Euler notation (or  $\psi = \phi$  in GRASP angles) will align the polarisation rotation of the two feeds. the effect of projection should therefore be nullified. The cross-polar component of the resolved feed is shown in Figure 6.29:

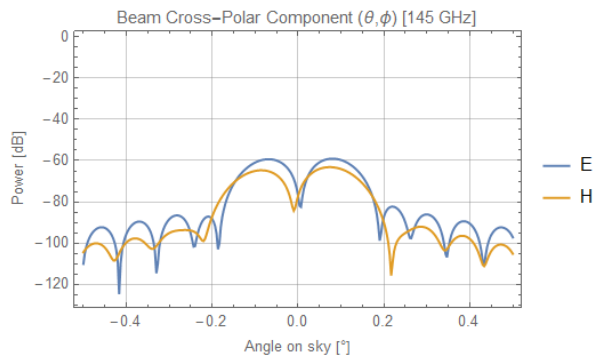


Figure 6.29: Cross-Polar component of the resolved  $\theta+1^\circ$  feed.

Figure 6.30 shows the fully established *CORE* model, ready for PO analysis:

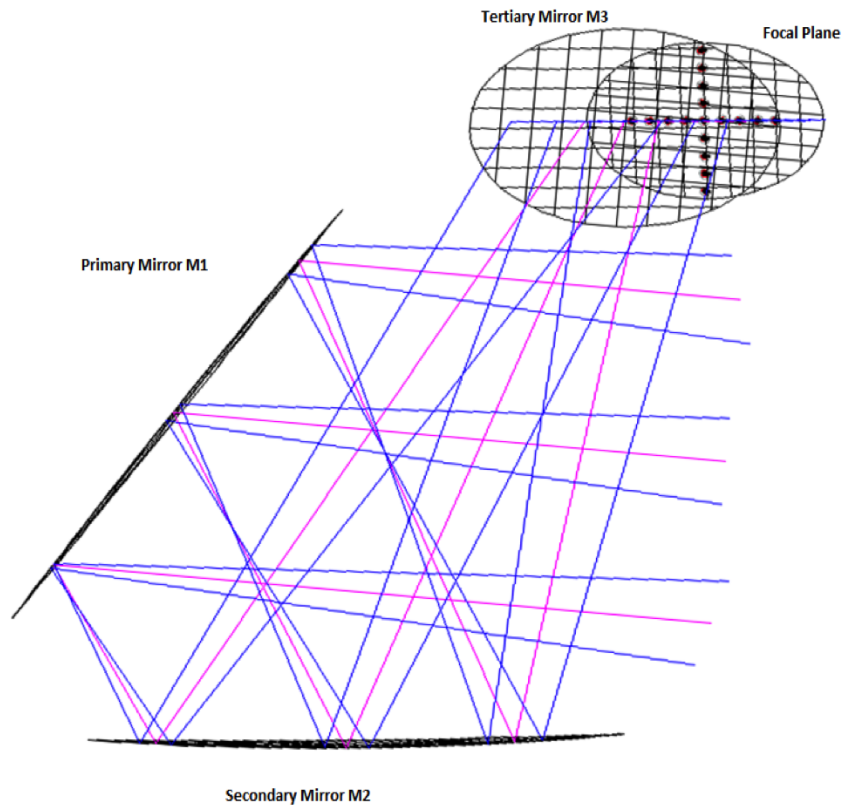


Figure 6.30: *CORE* mirrors showing centre and  $\phi$  offset rays. The full extent of the mirror is being utilised in this diagram.

### 6.6.6 Verification of Feed Positioning

The above method of positioning is straightforward and fast when dealing with large numbers of feeds. However, the human element in this method leaves open the possibility of error. The design must also be oriented so that the focal plane is viewed edge-on. A superior method is to use stored ray data to position and orient the rays. Rays in GRASP are stored in a .txt file. The start and end points are stored as well as all the positions where the ray contacts a reflector. Grouping is done by ray object. Once this method was utilised, the feed coordinates were rechecked and the orientations adjusted if needed. All PO calculations shown were computed after the feed verification. The locational parameters are located in Table 6.13. Note that all feeds have the “Mirror Global” coordinate system as their base:

Feed Coordinate System Values						
Coord. Sys.	x (m)	y (m)	z (m)	$\alpha$ ( $^\circ$ )	$\beta$ ( $^\circ$ )	$\gamma$ ( $^\circ$ )
Central	0.5133	1.0371	0.1417	-177.4894	67.439	83.48
$\theta+1^\circ$	0.5133	1.09	0.1474	-176.555	67.543	83.013
$\theta+2^\circ$	0.5134	1.144	0.1534	-175.6225	67.6546	82.5537
$\theta+3^\circ$	0.5136	1.198	0.1594	-174.692	67.775	82.0904
$\theta+4^\circ$	0.5139	1.252	0.1658	-173.765	67.9069	81.5785
$\theta-1^\circ$	0.5133	0.9835	0.1361	-178.4255	67.3455	-96.0576
$\theta-2^\circ$	0.51343	0.9299	0.1307	-179.3633	67.2598	-95.589
$\theta-3^\circ$	0.5136	0.876	0.1255	179.698	67.183	-95.1139
$\theta-4^\circ$	0.5138	0.8223	0.1205	178.758	67.115	-94.638
$\phi+1^\circ$	0.4957	1.0422	0.0936	-177.388	66.625	173.44
$\phi+2^\circ$	0.478	1.0473	0.0455	-177.2857	65.8137	173.399
$\phi+3^\circ$	0.4606	1.052	-0.0024	-177.1825	65.01	173.356
$\phi+4^\circ$	0.443	1.0574	-0.0503	-177.078	64.204	173.311
$\phi-1^\circ$	0.531	1.032	0.1899	-177.59	68.2591	173.5184
$\phi-2^\circ$	0.5486	1.027	0.2382	-177.69	69.082	173.554
$\phi-3^\circ$	0.5664	1.0219	0.2867	-177.7896	69.9082	173.5892
$\phi-4^\circ$	0.5842	1.0167	0.3353	-177.888	70.7383	173.6221

Table 6.13: Three mirror *CORE* feed coord. system parameters.

### 6.6.7 Setting up Detector Grids

Detector grids were used to obtain farfield beam patterns emanating from each feed. Spherical grids were used to mimic the celestial sphere/sky. Each grid type was set to Elevation over Azimuth. The size was kept constant for all grids initially:  $1^\circ$  elevation by  $1^\circ$  azimuth, but this would change as the analysis demanded. The base sampling was set to 201 by 201 points, though again this would change with the analysis requirements. The coordinate system of each grid was set  $180^\circ$  opposite its corresponding aperture ray coordinate system. That way, rays emanating from the feeds on the focal plane would pass through the centre of each grid. All grids used were farfield grids. Figure 6.31 shows the detector grids with the  $\phi$  feed rays passing through them:

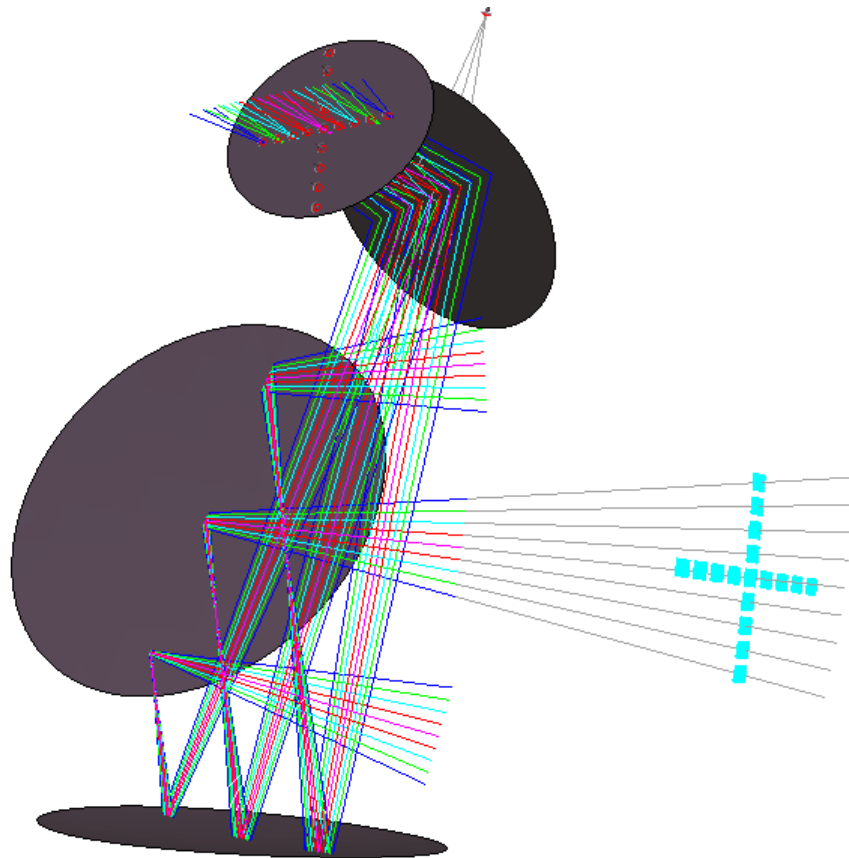


Figure 6.31: The grids used in the PO analysis. Coloured rays represent plane rays, grey rays represent feed rays.

## 6.7 PO Analysis of the *CORE* Design

PO analysis was carried out identically to the previous *CORE* models. The introduction of the folding mirror meant it needed to be included into the PO calculations, though it would ultimately have no effect on the beams other than to redirect them. The analysis carried out on *CORE* took two forms. First, the design was analysed in the centre of the CMB frequency band. These data would be included in the *CORE* instrument paper as a proof of concept, showing that the design could produce beams of a high quality at the frequency band of prime interest. The second form was an expanded PO analysis that roughly gauged the position of the different detectors (see Figure 6.1) and performed calculations at their frequencies, which spanned the whole frequency range of *CORE*.

### 6.7.1 Analysis at CMB Frequencies

PO Analysis objects were created for the primary, secondary and folding mirrors. Frequency bands were created to span the range of 60 - 600 GHz. These tests would utilise a frequency  $f$  of 145 GHz, beam waist  $\omega_0$  of 5.13946 mm. These values were requested by the *CORE* consortium for inclusion into the *CORE* instrument paper, part of the larger M5 proposal. 145 GHz is in the CMB frequency band mentioned in the chapter introduction (130 GHz - 220 GHz). The accuracy level was set to -120 dB. The PO objects maintained a frequency of 145 GHz. The central feed and those feeds that were offset in azimuth ( $\theta$ ) or elevation ( $\phi$ ) exclusively were those selected for analysis. Their position information can be found in Table 6.13.

The 17 feeds which are mentioned in Table 6.13 were used as sources. The results of fitting performed on the resultant beams are presented below in Table 6.14. At the consortium's request, the Full Width at Half Maximum (FWHM)

for each offset beam was calculated and shown rather than the beam radii on the sky. This was calculated via:

$$FWHM_{x/y} = \omega_{x/y} \sqrt{2 \ln(2)} \quad (6.3)$$

The ellipticity calculations also used FWHM values. After the results in Tables 6.14 and 6.15, plots of the beams will be produced in Figures 6.33 - 6.59. These plots exist for all 17 feeds (which can be seen in Figure 6.32). However, due to volume considerations, the central plots and those offset in  $\pm 2^\circ$  and  $\pm 4^\circ$  in  $\theta$  and  $\phi$  will be presented. The hope is that the reader will still gain an sense of how the beams evolve from the centre to the edge of the focal plane.

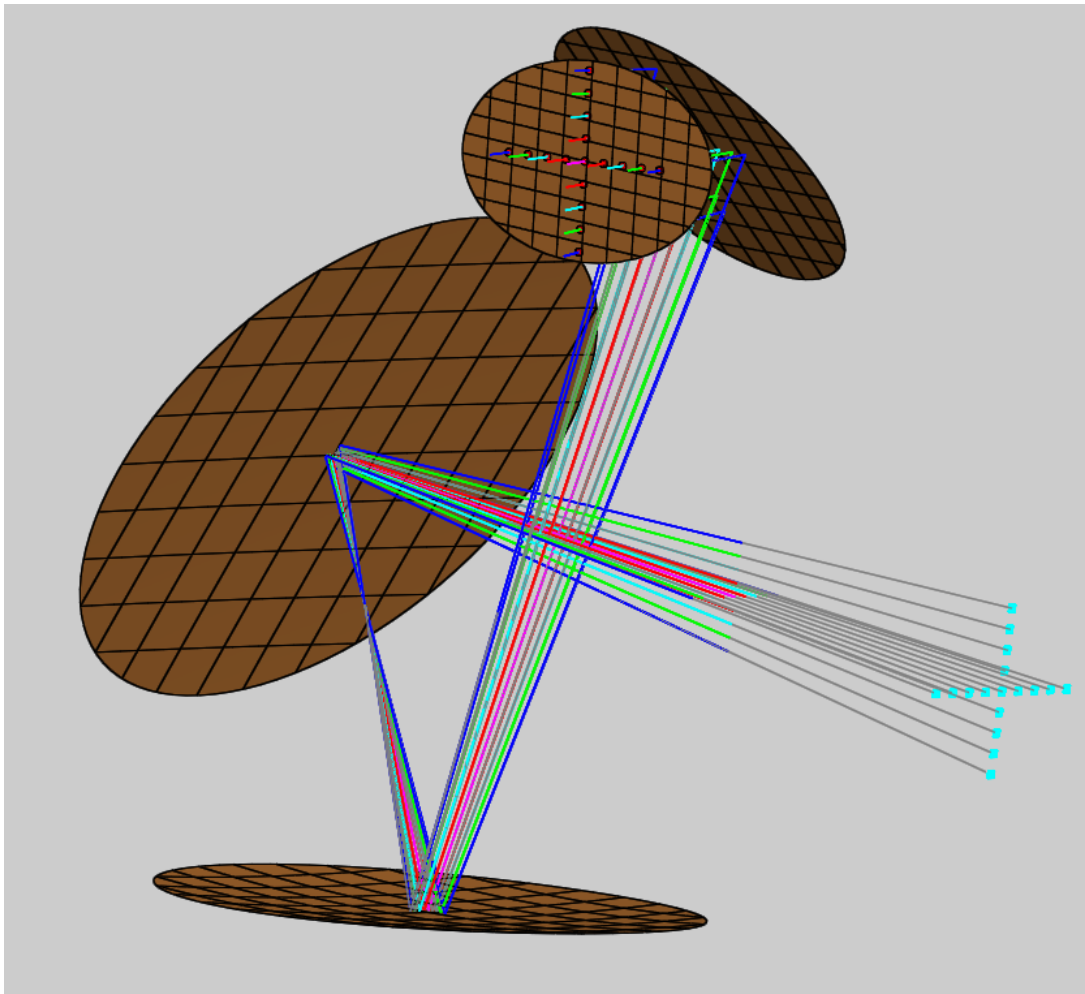


Figure 6.32: The extent of the PO analysis at 145 GHz. The output grids are shown in light blue.

<b>Physical Optics Results (145 GHz) Linear X Pol.</b>					
<b>Beam</b>	<b>FWHM<math>_{\theta}</math> (°)</b>	<b>FWHM<math>_{\phi}</math> (°)</b>	<b><math>\theta_0</math> (°)</b>	<b><math>\phi_0</math> (°)</b>	<b>Ellipticity</b>
Centre	0.12	0.1246	0.0	0.0	0.0366
$\theta + 1^\circ$	0.12	0.1246	0.0043	0.0	0.0368
$\theta + 2^\circ$	0.1204	0.1248	0.008	0.0	0.0354
$\theta + 3^\circ$	0.1216	0.1252	0.0112	0.0	0.0291
$\theta + 4^\circ$	0.124	0.1256	0.0147	0.0	0.01327
$\theta - 1^\circ$	0.1204	0.1247	-0.0034	0.0	0.0341
$\theta - 2^\circ$	0.1213	0.125	-0.0072	0.0	0.0298
$\theta - 3^\circ$	0.123	0.125	-0.0108	0.0	0.0195
$\theta - 4^\circ$	0.126	0.1293	-0.015	0.0	0.0263
$\phi + 1^\circ$	0.1198	0.1249	0.0	0.0056	0.0407
$\phi + 2^\circ$	0.1195	0.1265	0.0	0.0128	0.0556
$\phi + 3^\circ$	0.1193	0.13	0.0	0.02	0.0827
$\phi + 4^\circ$	0.1191	0.1354	0.0	0.025	0.12
$\phi - 1^\circ$	0.1202	0.1252	0.0	-0.009	0.0393
$\phi - 2^\circ$	0.1205	0.1267	0.0	-0.016	0.0489
$\phi - 3^\circ$	0.1207	0.1289	0.0	-0.023	0.0641
$\phi - 4^\circ$	0.1209	0.1322	0.0	-0.028	0.0856

Table 6.14: Linear X Pol. 145 GHz PO results. Note that  $\theta_0$  is the beam offset in  $\theta$  and  $\phi_0$  is the beam offset in  $\phi$ .

<b>Physical Optics Results (145 GHz) Linear Y Pol.</b>					
<b>Beam</b>	<b>FWHM<math>_{\theta}</math> (°)</b>	<b>FWHM<math>_{\phi}</math> (°)</b>	<b><math>\theta_0</math> (°)</b>	<b><math>\phi_0</math> (°)</b>	<b>Ellipticity</b>
Centre	0.12	0.1246	0.0	0.0	0.0366
$\theta + 1^\circ$	0.12	0.1246	0.0043	0.0	0.0368
$\theta + 2^\circ$	0.1204	0.1248	0.008	0.0	0.0355
$\theta + 3^\circ$	0.1216	0.1252	0.0112	0.0	0.0292
$\theta + 4^\circ$	0.1239	0.1256	0.01475	0.0	0.0134
$\theta - 1^\circ$	0.1204	0.1247	-0.0034	0.0	0.034
$\theta - 2^\circ$	0.1213	0.125	-0.0072	0.0	0.0298
$\theta - 3^\circ$	0.123	0.1254	-0.0108	0.0	0.0195
$\theta - 4^\circ$	0.1259	0.1292	-0.0151	0.0	0.026
$\phi + 1^\circ$	0.1198	0.1249	0.0	0.0056	0.0407
$\phi + 2^\circ$	0.1195	0.1265	0.0	0.0128	0.0556
$\phi + 3^\circ$	0.1193	0.1301	0.0	0.0195	0.0826
$\phi + 4^\circ$	0.1191	0.1354	0.0	0.025	0.12
$\phi - 1^\circ$	0.1202	0.1252	0.0	-0.009	0.0394
$\phi - 2^\circ$	0.1205	0.1267	0.0	-0.016	0.0489
$\phi - 3^\circ$	0.1207	0.1289	0.0	-0.023	0.0641
$\phi - 4^\circ$	0.1209	0.1322	0.0	-0.028	0.0827

Table 6.15: Linear Y Pol. 145 GHz PO results.

### 6.7.2 145 GHz *CORE* Beam Contour Plots

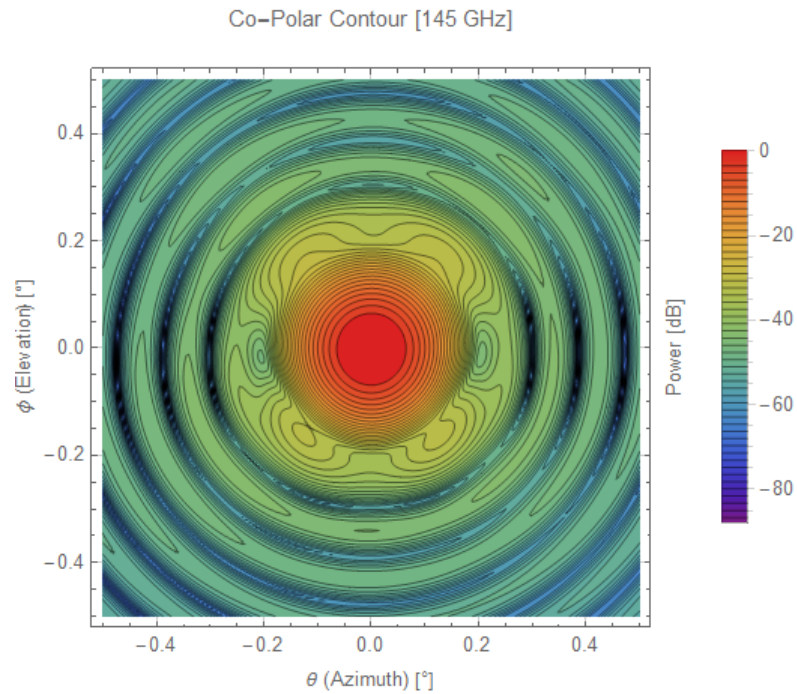


Figure 6.33: Co-Polar beam contour plot for centre beam at 145 GHz.

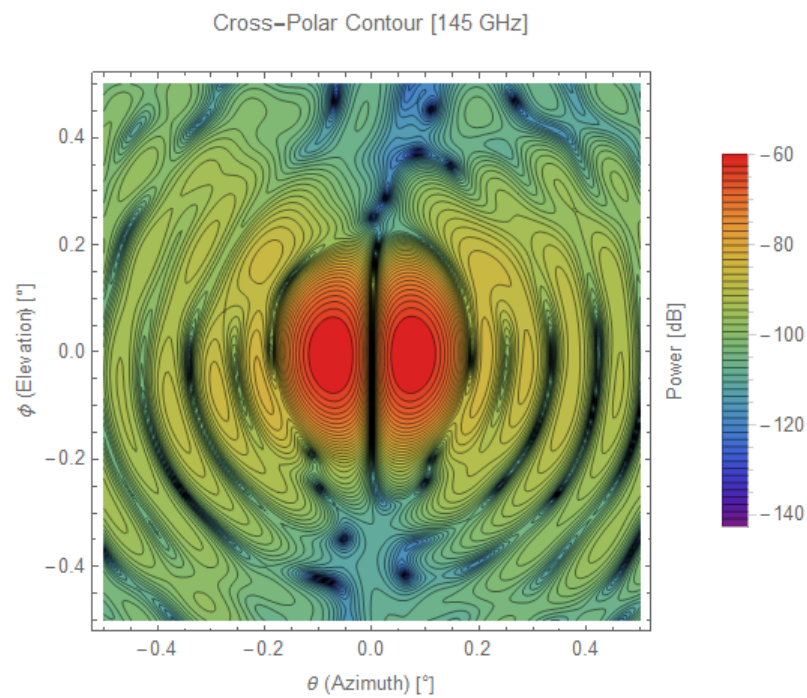
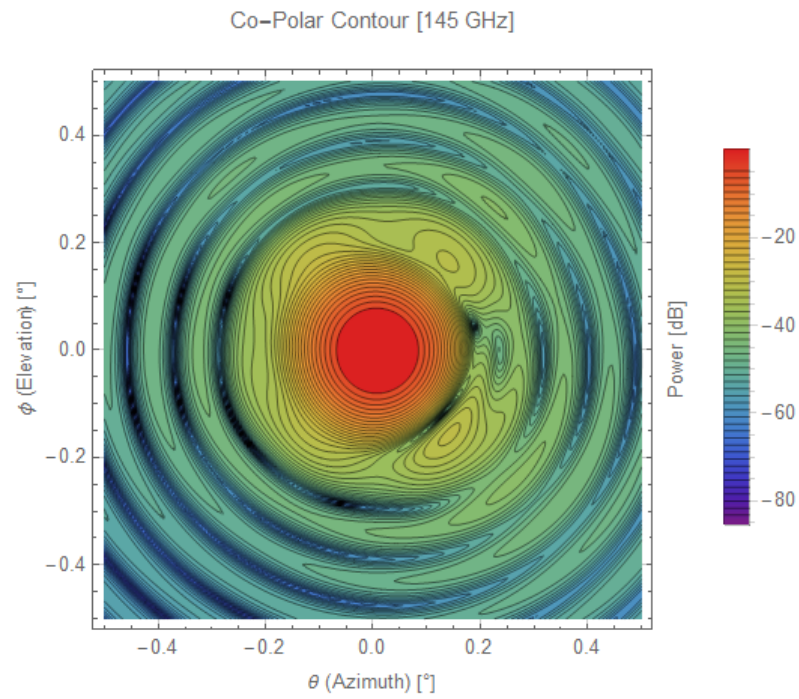
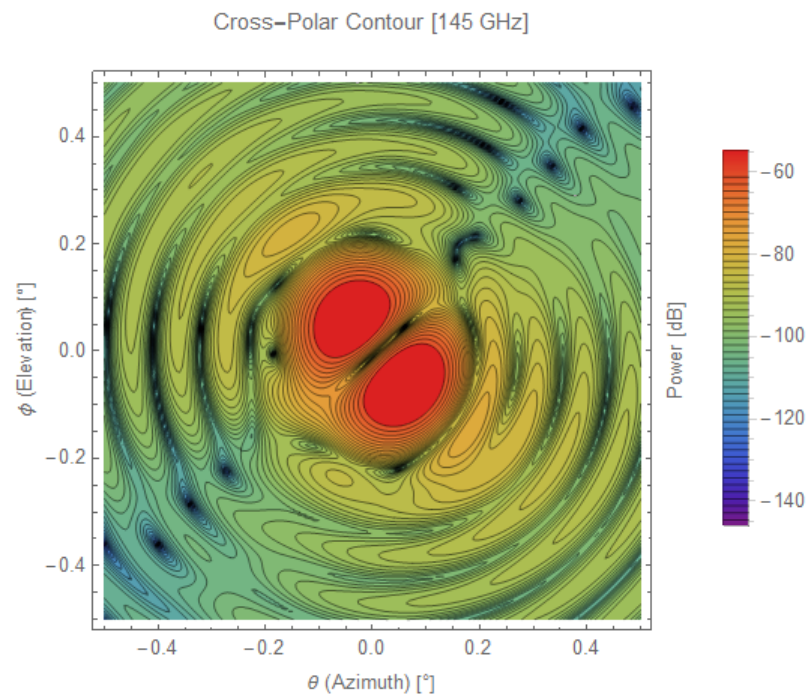


Figure 6.34: Cross-Polar beam contour plot for centre beam at 145 GHz.

Figure 6.35: Co-Polar beam contour plot for  $\theta = +2^\circ$  beam at 145 GHz.Figure 6.36: Cross-Polar beam contour plot for  $\theta = +2^\circ$  beam at 145 GHz.

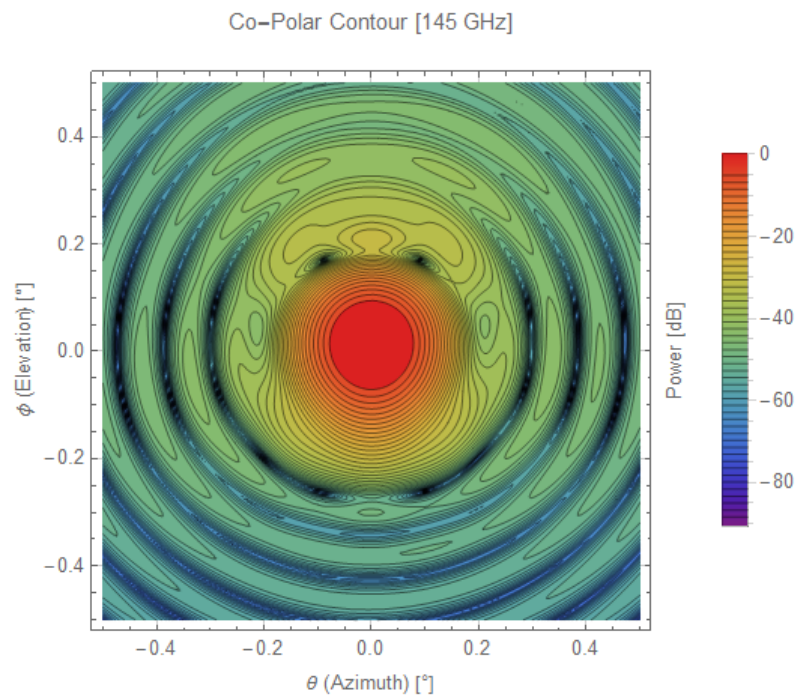


Figure 6.37: Co-Polar beam contour plot for  $\phi = +2^\circ$  beam at 145 GHz.

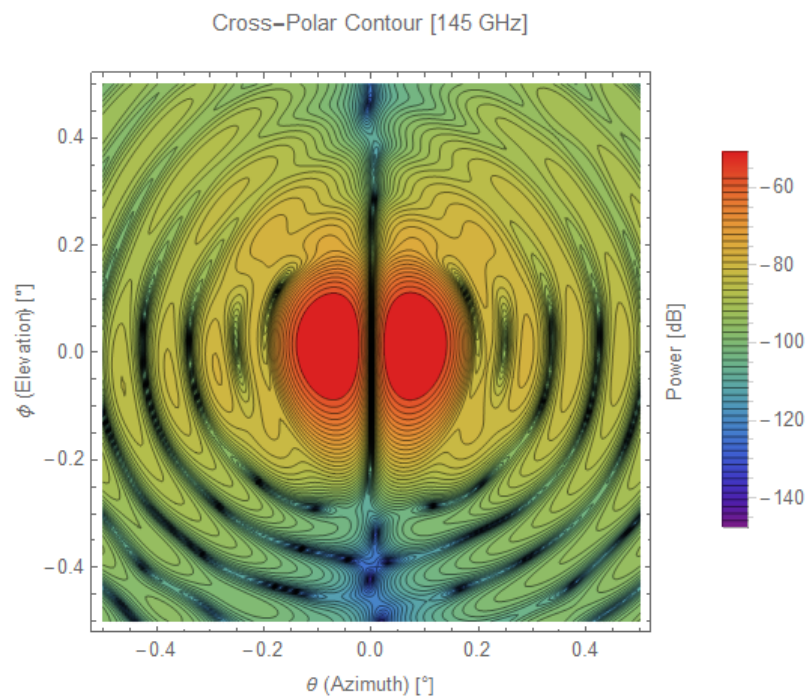
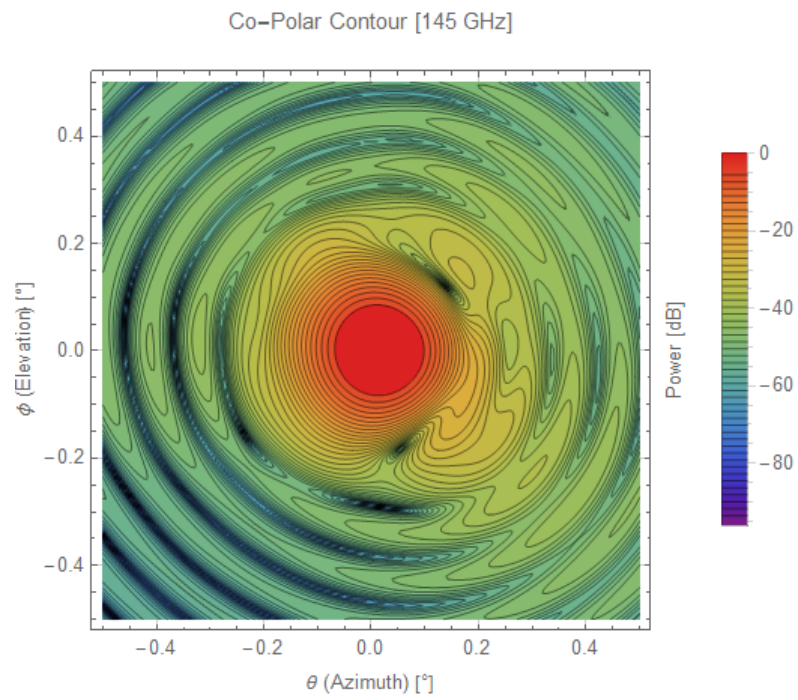
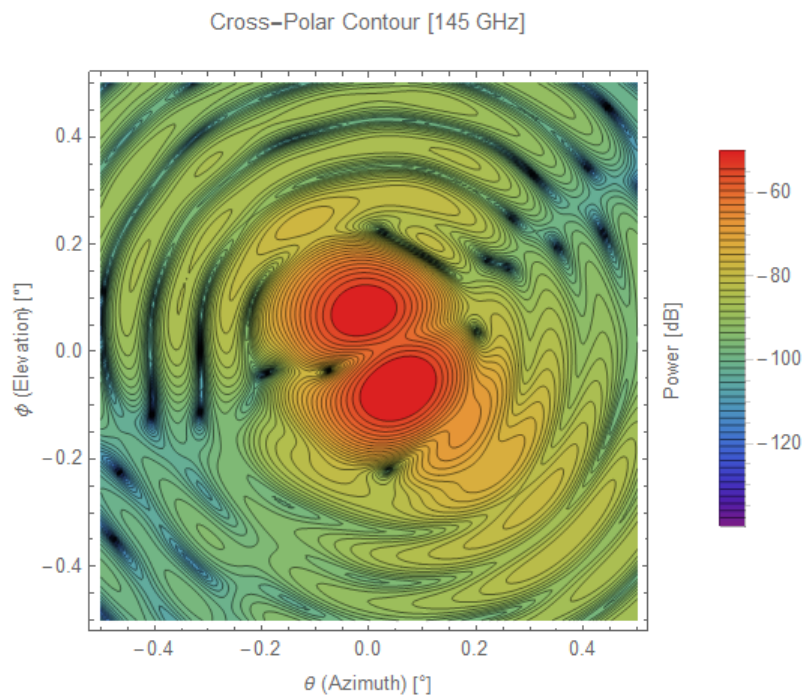


Figure 6.38: Cross-Polar beam contour plot for  $\phi = +2^\circ$  beam at 145 GHz.

Figure 6.39: Co-Polar beam contour plot for  $\theta = +4^\circ$  beam at 145 GHz.Figure 6.40: Cross-Polar beam contour plot for  $\theta = +4^\circ$  beam at 145 GHz.

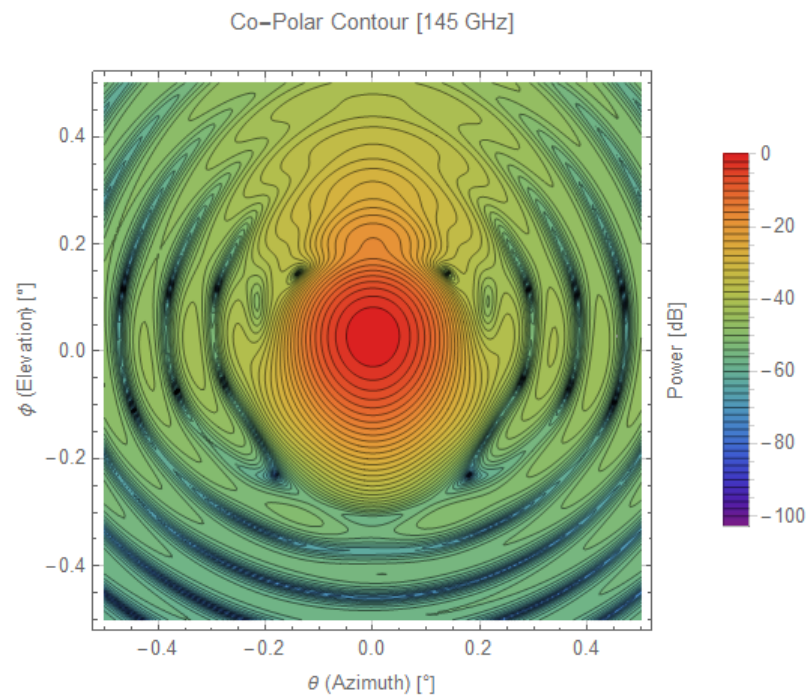


Figure 6.41: Co-Polar beam contour plot for  $\phi = +4^\circ$  beam at 145 GHz.

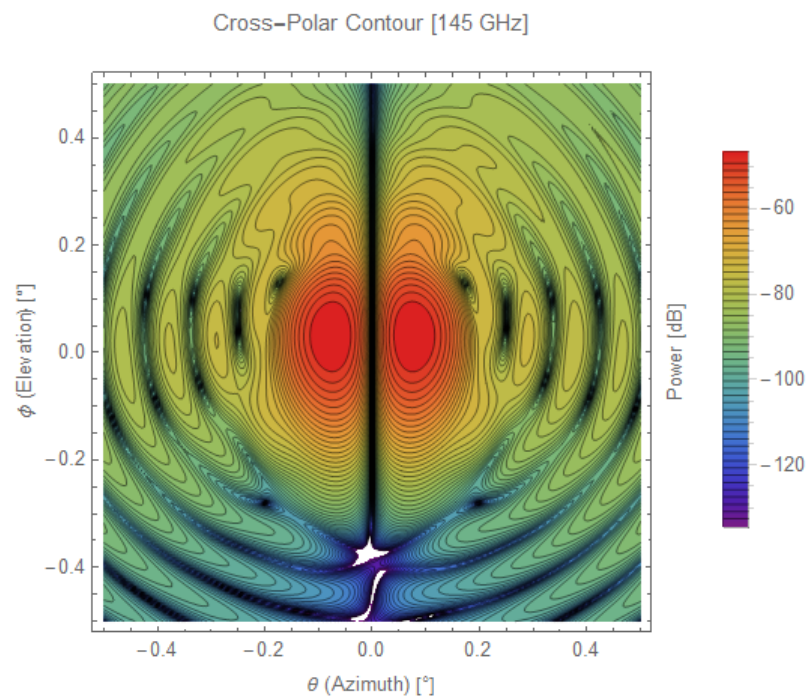
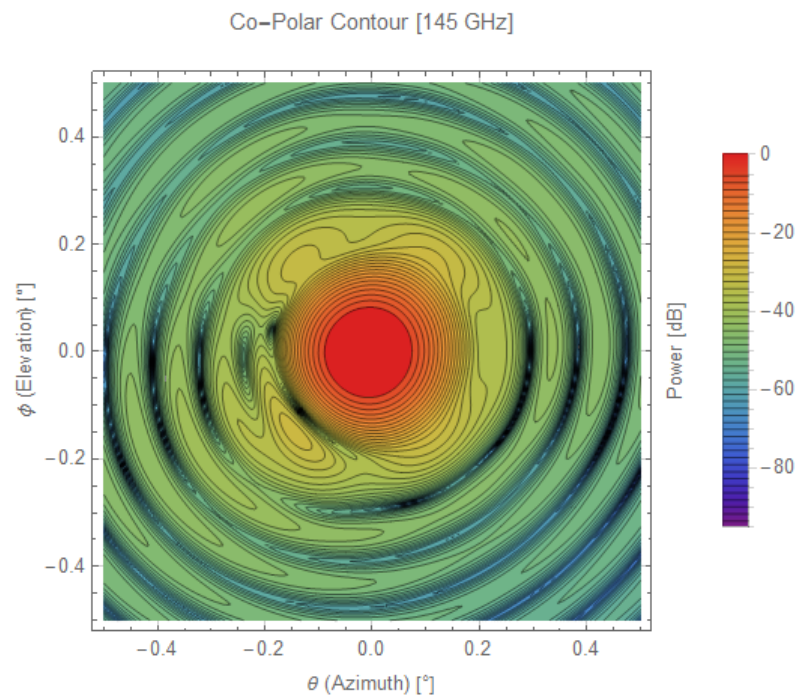
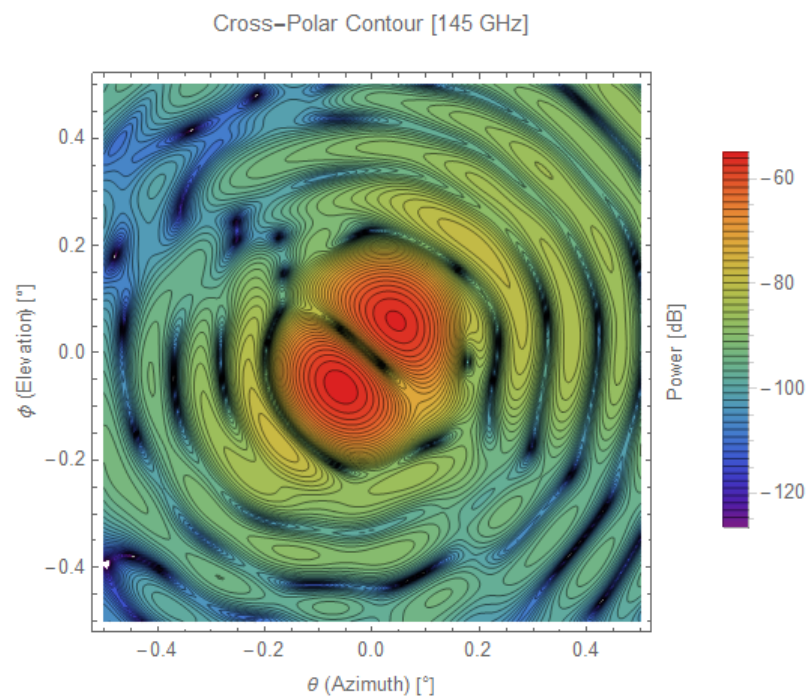
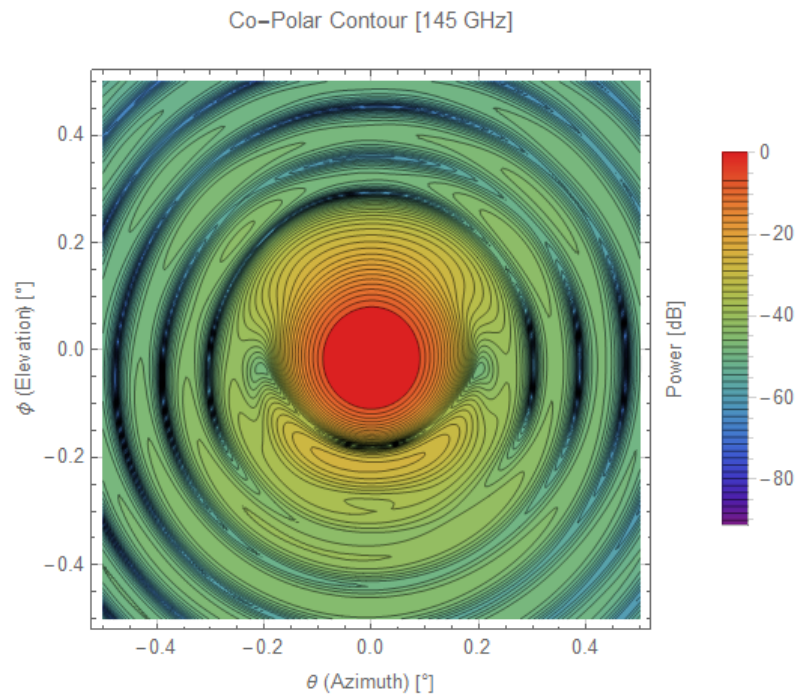
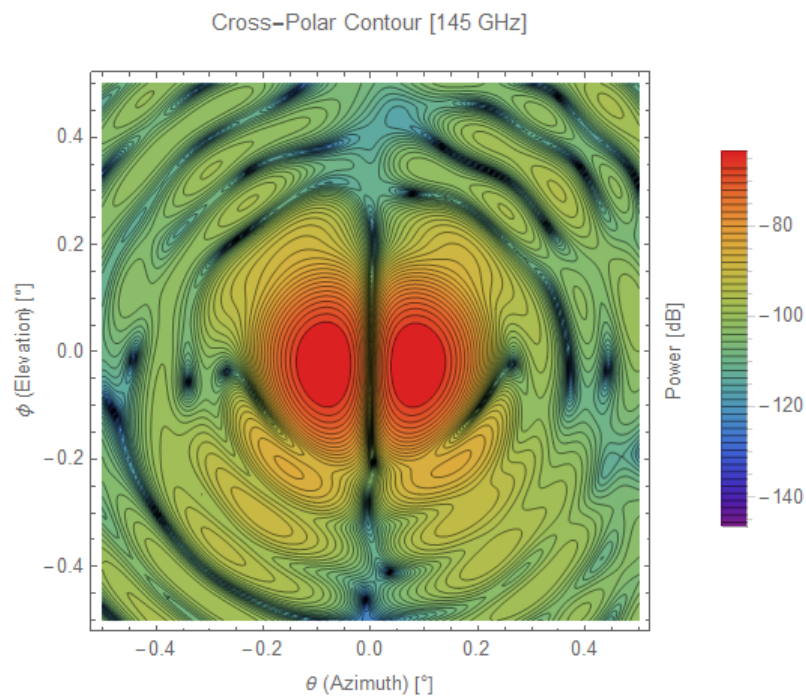


Figure 6.42: Cross-Polar beam contour plot for  $\phi = +4^\circ$  beam at 145 GHz.

Figure 6.43: Co-Polar beam contour plot for  $\theta = -2^\circ$  beam at 145 GHz.Figure 6.44: Cross-Polar beam contour plot for  $\theta = -2^\circ$  beam at 145 GHz.

Figure 6.45: Co-Polar beam contour plot for  $\phi = -2^\circ$  beam at 145 GHz.Figure 6.46: Cross-Polar beam contour plot for  $\phi = -2^\circ$  beam at 145 GHz.

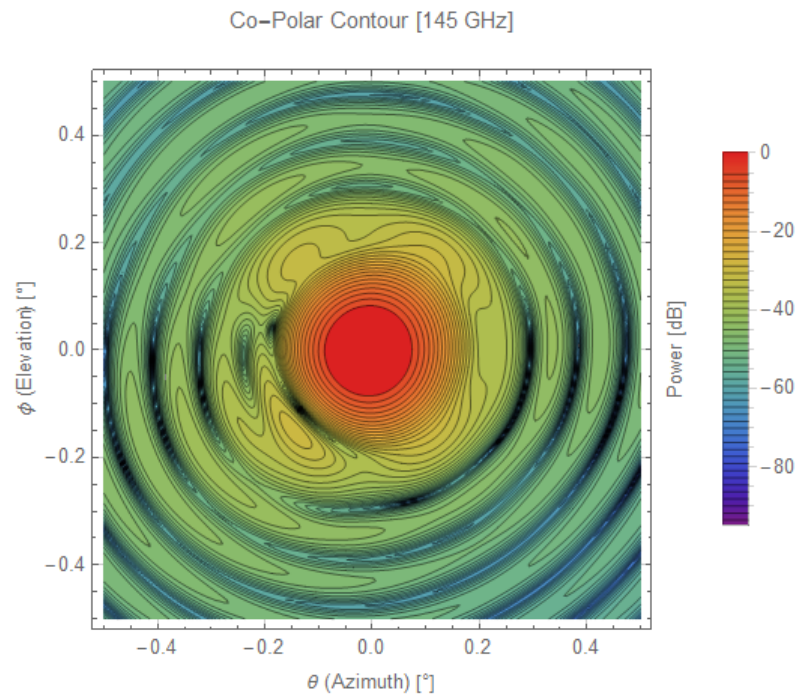


Figure 6.47: Co-Polar beam contour plot for  $\theta = -4^\circ$  beam at 145 GHz.

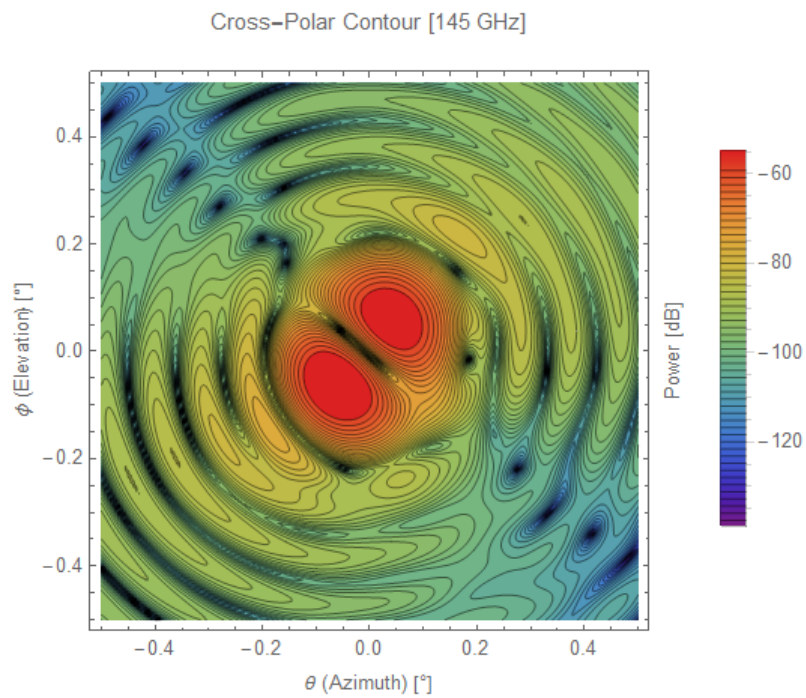
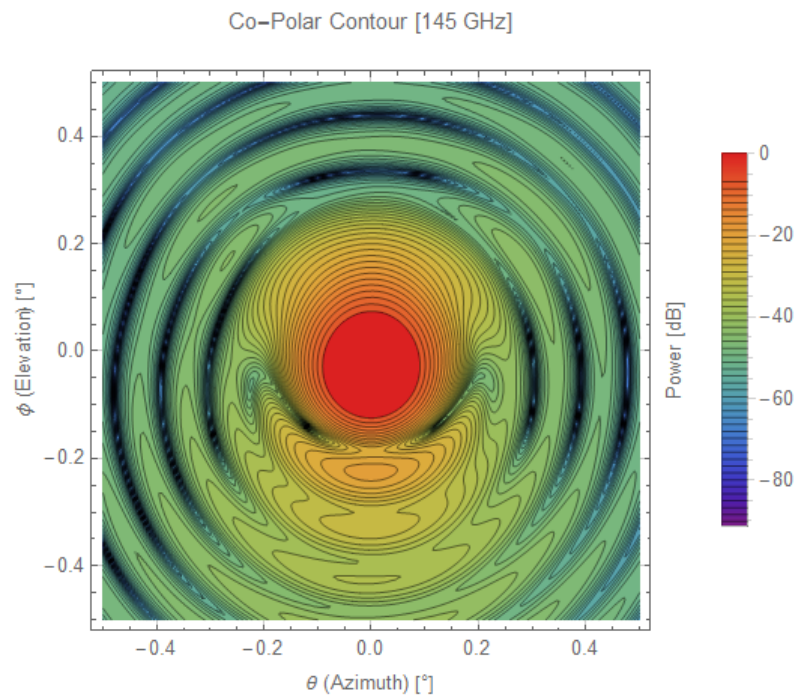
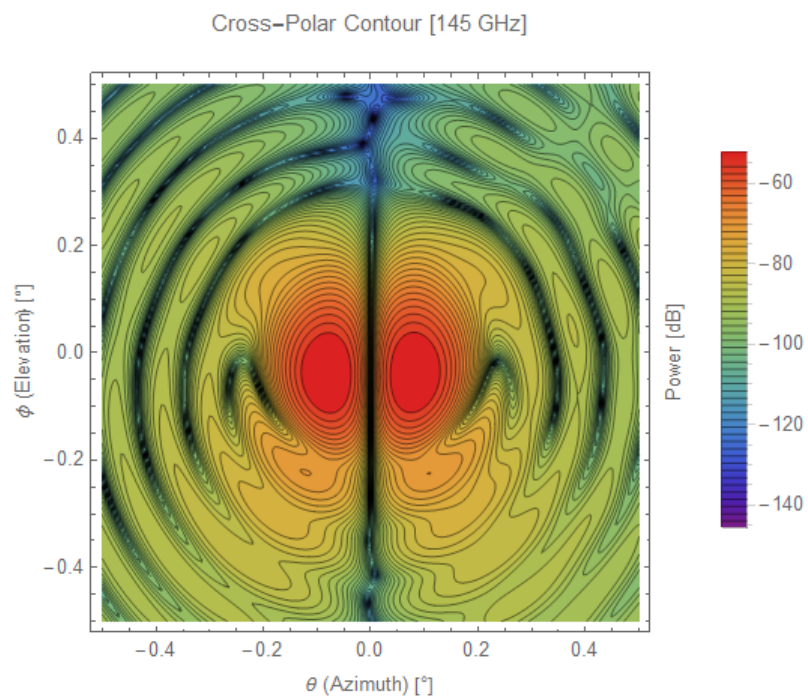


Figure 6.48: Cross-Polar beam contour plot for  $\theta = -4^\circ$  beam at 145 GHz.

Figure 6.49: Co-Polar beam contour plot for  $\phi = -4^\circ$  beam at 145 GHz.Figure 6.50: Cross-Polar beam contour plot for  $\phi = -4^\circ$  beam at 145 GHz.

### 6.7.3 145 GHz *CORE* Beam Log Plots

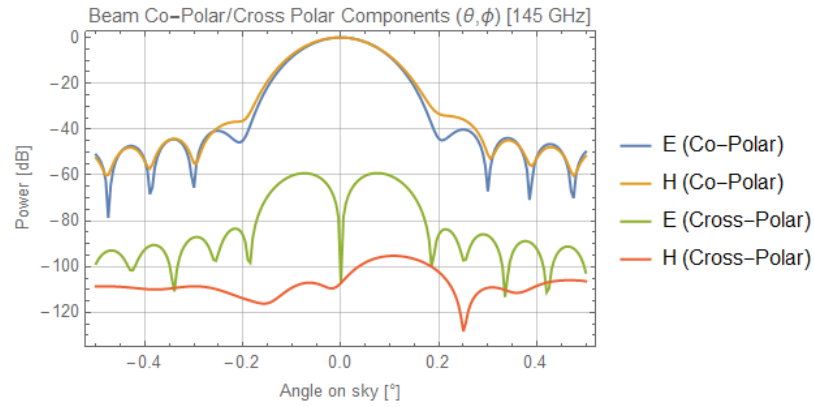


Figure 6.51: Co/Cross-Polar beam log plot for centre beam at 145 GHz.

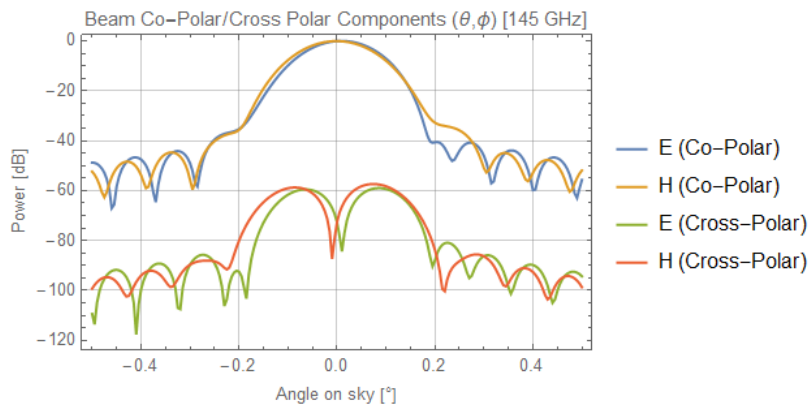


Figure 6.52: Co/Cross-Polar beam log plot for  $\theta = +2^\circ$  beam at 145 GHz.

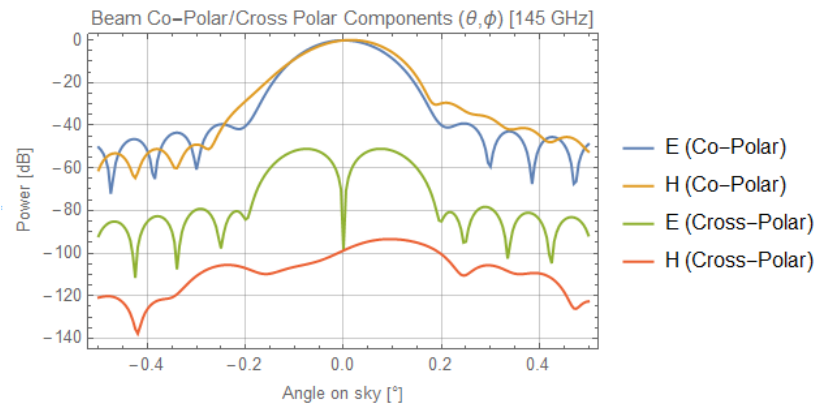
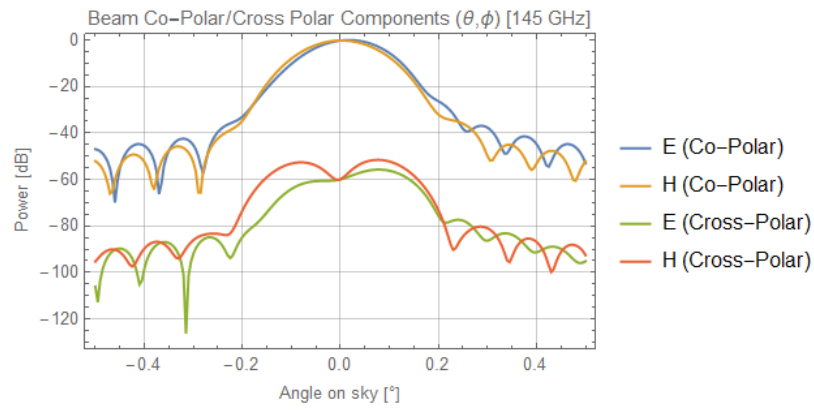
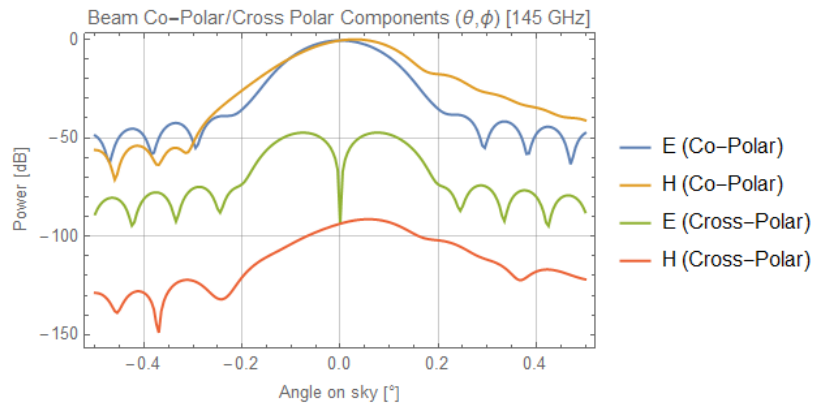
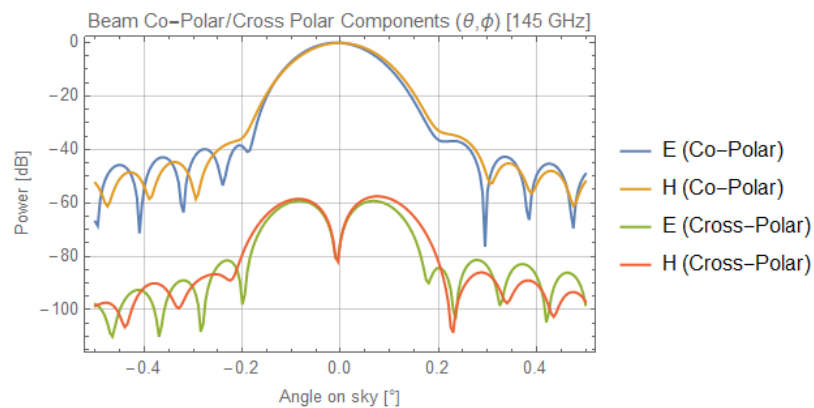
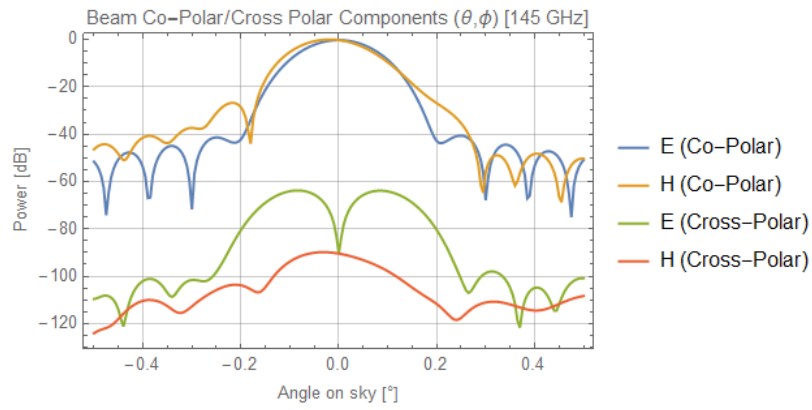
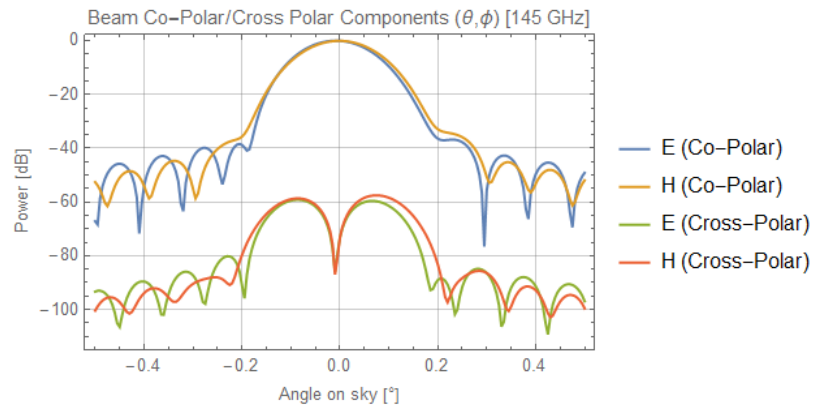
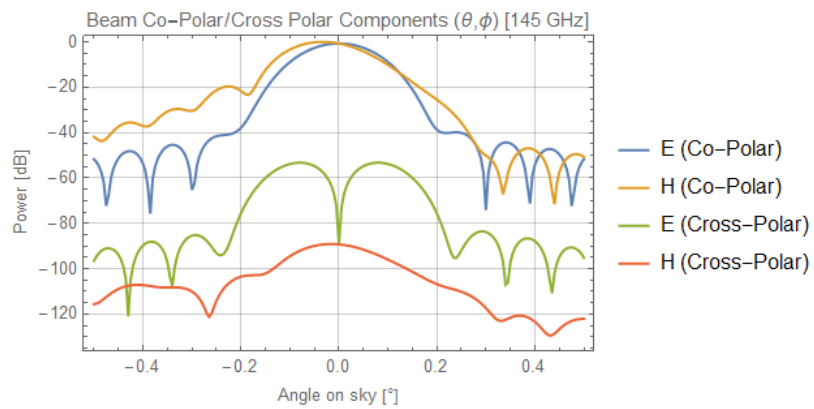


Figure 6.53: Co/Cross-Polar beam log plot for  $\phi = +2^\circ$  beam at 145 GHz.

Figure 6.54: Co/Cross-Polar beam log plot for  $\theta = +4^\circ$  beam at 145 GHz.Figure 6.55: Co/Cross-Polar beam log plot for  $\phi = +4^\circ$  beam at 145 GHz.Figure 6.56: Co/Cross-Polar beam log plot for  $\theta = -2^\circ$  beam at 145 GHz.

Figure 6.57: Co/Cross-Polar beam log plot for  $\phi = -2^\circ$  beam at 145 GHz.Figure 6.58: Co/Cross-Polar beam log plot for  $\theta = -4^\circ$  beam at 145 GHz.Figure 6.59: Co/Cross-Polar beam log plot for  $\phi = -4^\circ$  beam at 145 GHz.

### 6.7.4 Conclusions on 145 GHz Analysis

Starting with Tables 6.14 and 6.15, the beam offsets can be seen to generally increase moving from the centre of the focal plane to the edge. Distortion in the beams is higher for those offset in elevation  $\phi$  due to symmetry breaking along the corresponding axes of the primary and secondary mirrors. The logarithmic plots bear this out as well. Both linear X and Y polarisations show similar results to one another as would be expected. An ellipticity of 5% (0.05) was judged to be the standard for beams suitable for performing CMB research. Returning to the results tables, ellipticities stay below 0.05 for beams offset in azimuth  $\theta$ . For those offset in  $\phi$  (which are more distorted) ellipticities rise above 5% at  $\pm 2^\circ$  in both polarisations. The maximum ellipticity is 12% at a beam offset of  $\phi = +4^\circ$ . The 145 GHz detectors will be placed at the  $\phi$  offsets, which follows the local horizontal  $x$ -axis of the focal plane (the folding mirror causes a  $90^\circ$  rotation). Further refinements would need to take place to remedy this issue. In general though, all beams are of acceptable quality and serve to verify the three-mirror Offset Dragonian telescope.

### 6.7.5 Analysis across the Focal Plane

Feeds were oriented from highest frequency pixels at the centre and lower frequency pixels near the edge of the focal plane. Aberration effects are analysed for different frequencies and focal plane positions.

Additional feeds were required to extend the coverage off the main  $\theta/\phi$  axes and onto the unused focal plane area. These rays still required guidance from plane rays in order to have the correct position and orientation. The existing feeds projected beams onto the sky along either the azimuth or elevation axes. These new feeds would need to project an composite angles of  $\theta$  and  $\phi$ , like  $\theta + 1^\circ$ ,  $\phi + 1^\circ$ . The map of new feeds is shown in Figure 6.60. The feeds were placed using ray

output data and the previously discussed AB vector approach. Projection effects also needed to be resolved for these feeds. The parameters of their coordinate systems are located in Table 6.16. Beam plots are presented in Figures 6.61 - 6.114.

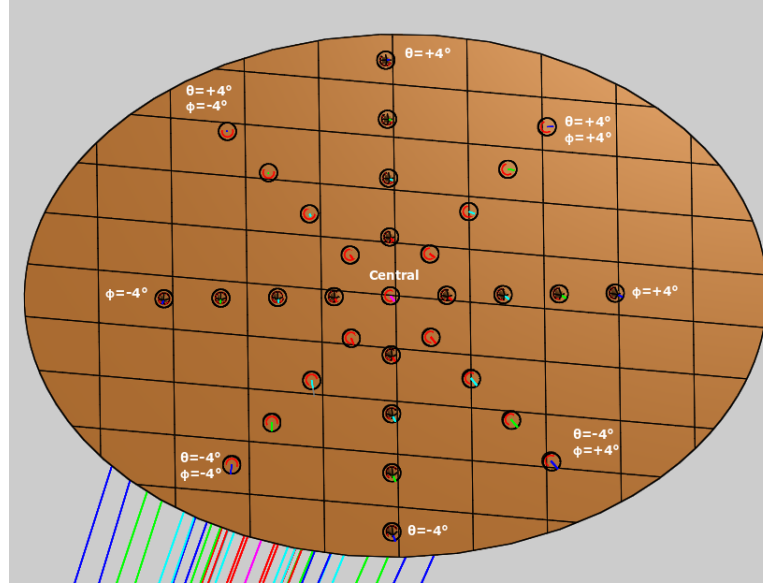


Figure 6.60: The map of feeds used in this multi-frequency analysis.

Feed Coordinate System Values						
Coord. Sys.	x (m)	y (m)	z (m)	$\alpha$ ( $^{\circ}$ )	$\beta$ ( $^{\circ}$ )	$\gamma$ ( $^{\circ}$ )
$\theta+1^{\circ}, \phi+1^{\circ}$	0.501	1.08	0.112	-176.537	66.7713	83.006
$\theta+2^{\circ}, \phi+2^{\circ}$	0.4885	1.1202	0.08189	-175.5755	66.11	82.535
$\theta+3^{\circ}, \phi+3^{\circ}$	0.476	1.1618	0.052	-174.6037	65.4599	82.055
$\theta+4^{\circ}, \phi+4^{\circ}$	0.4638	1.204	0.0224	-173.622	64.8175	81.521
$\theta+1^{\circ}, \phi-1^{\circ}$	0.5258	1.07	0.1798	-176.736	68.296	83.1035
$\theta+2^{\circ}, \phi-2^{\circ}$	0.5383	1.1057	0.218	-175.9924	69.1582	82.779
$\theta+3^{\circ}, \phi-3^{\circ}$	0.5509	1.1399	0.2565	-175.258	70.0268	82.4949
$\theta+4^{\circ}, \phi-4^{\circ}$	0.5636	1.1742	0.295	-174.5325	70.9	82.2057
$\theta-1^{\circ}, \phi+1^{\circ}$	0.5009	1.003	0.1037	-178.2529	66.5901	83.6855
$\theta-2^{\circ}, \phi+2^{\circ}$	0.4885	0.9684	0.0659	-179.027	65.7468	83.9433
$\theta-3^{\circ}, \phi+3^{\circ}$	0.4761	0.9339	0.028	-179.812	64.91	84.2426
$\theta-4^{\circ}, \phi+4^{\circ}$	0.4638	0.8993	-0.0097	179.391	64.08	84.5381
$\theta-1^{\circ}, \phi-1^{\circ}$	0.5258	0.9957	0.1718	-178.432	68.117	83.8537
$\theta-2^{\circ}, \phi-2^{\circ}$	0.5383	0.9542	0.2021	-179.3655	68.802	84.23
$\theta-3^{\circ}, \phi-3^{\circ}$	0.5509	0.9127	0.2325	179.7098	69.4953	84.602
$\theta-4^{\circ}, \phi-4^{\circ}$	0.5636	0.8711	0.263	178.7935	70.1967	84.9724

Table 6.16: Coord. system parameters for additional *CORE* feeds.

### 6.7.6 Multi-Frequency *CORE* Beam Contour Plots

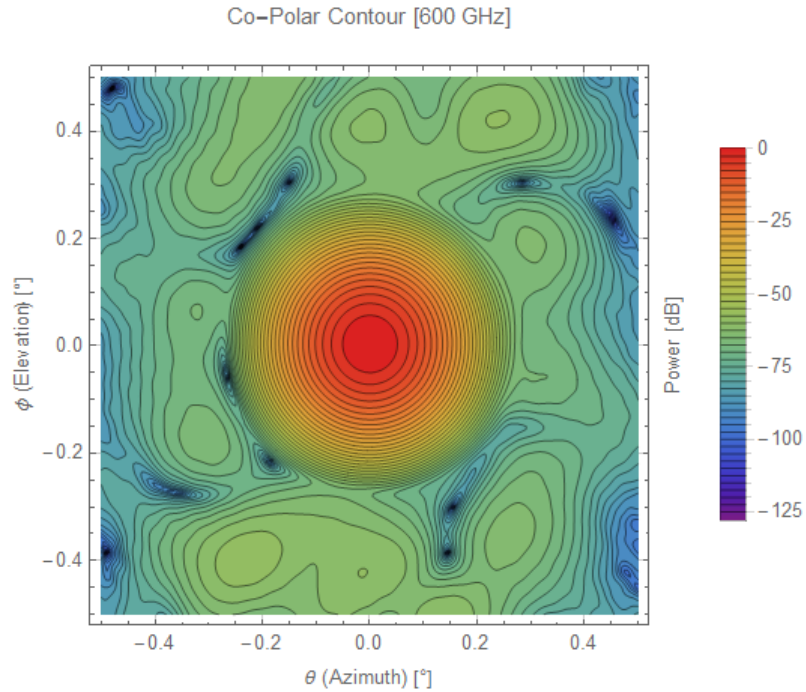


Figure 6.61: Co-Polar beam contour plot for 600 GHz beam launched from the central feed.

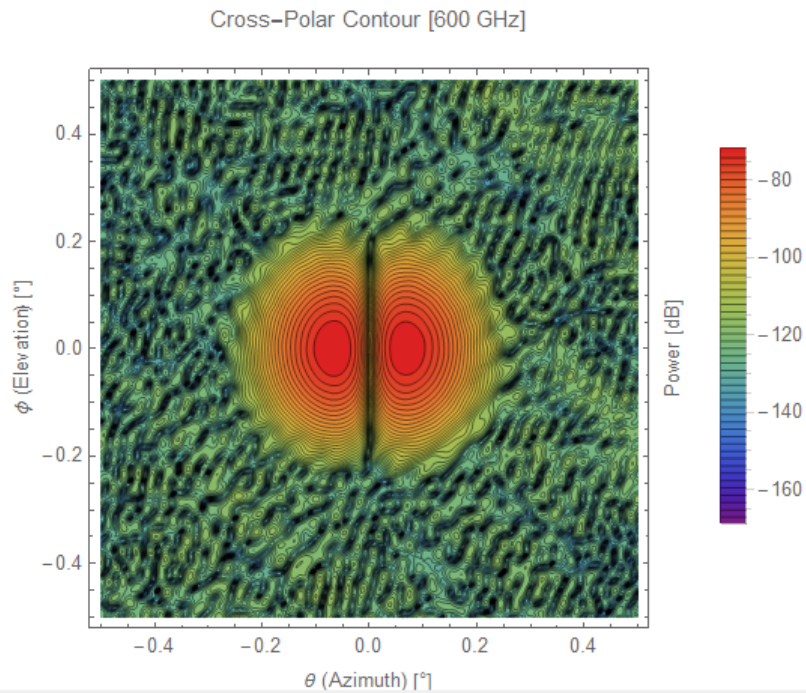


Figure 6.62: Cross-Polar beam contour plot for 600 GHz beam launched from the central feed.

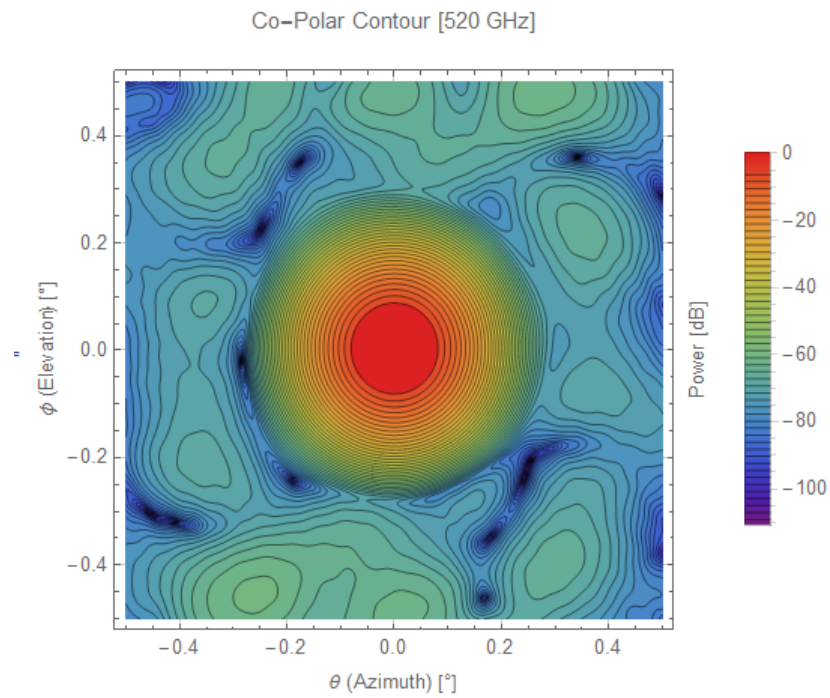


Figure 6.63: Co-Polar beam contour plot for 520 GHz beam launched from the central feed.

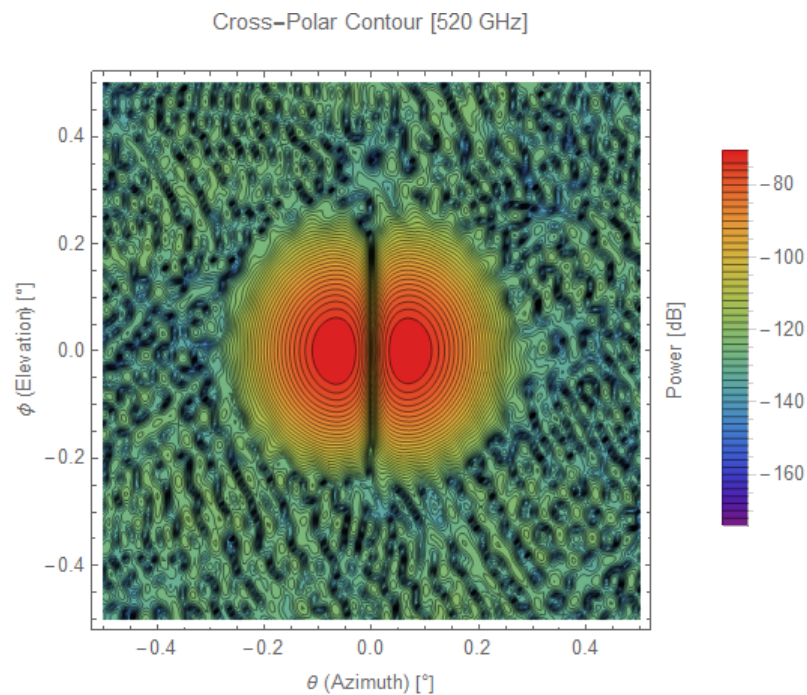


Figure 6.64: Cross-Polar beam contour plot for 520 GHz beam launched from the central feed.

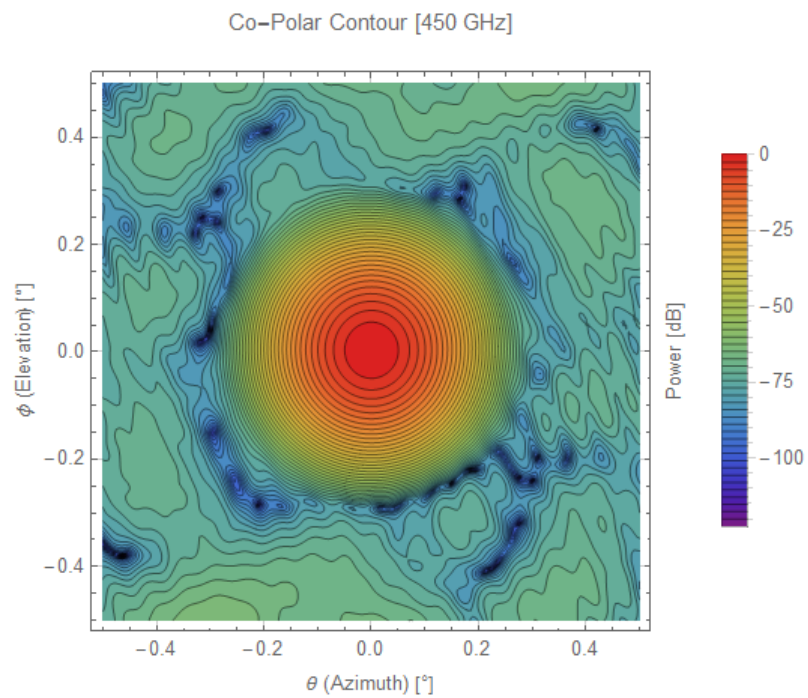


Figure 6.65: Co-Polar beam contour plot for 450 GHz beam launched from the central feed.

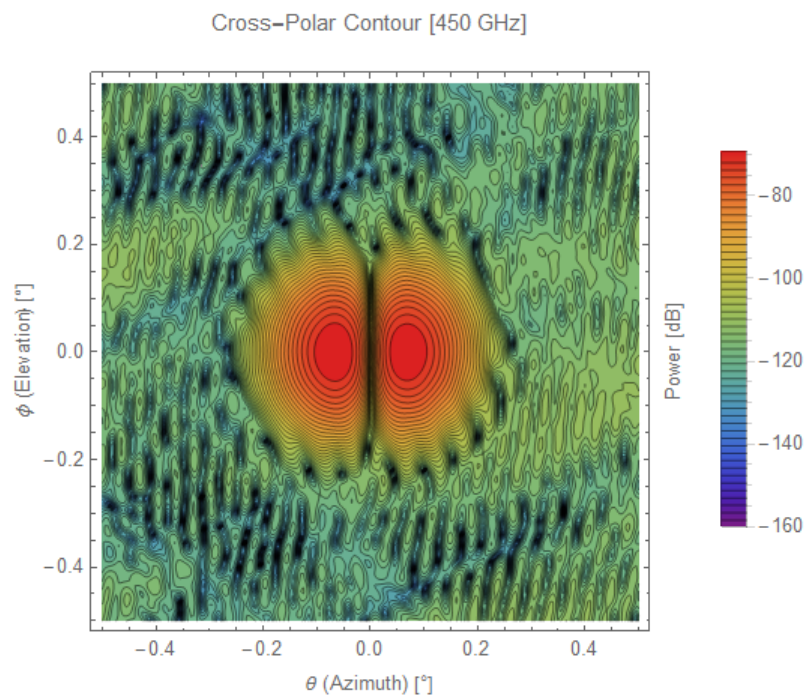


Figure 6.66: Cross-Polar beam contour plot for 450 GHz beam launched from the central feed.

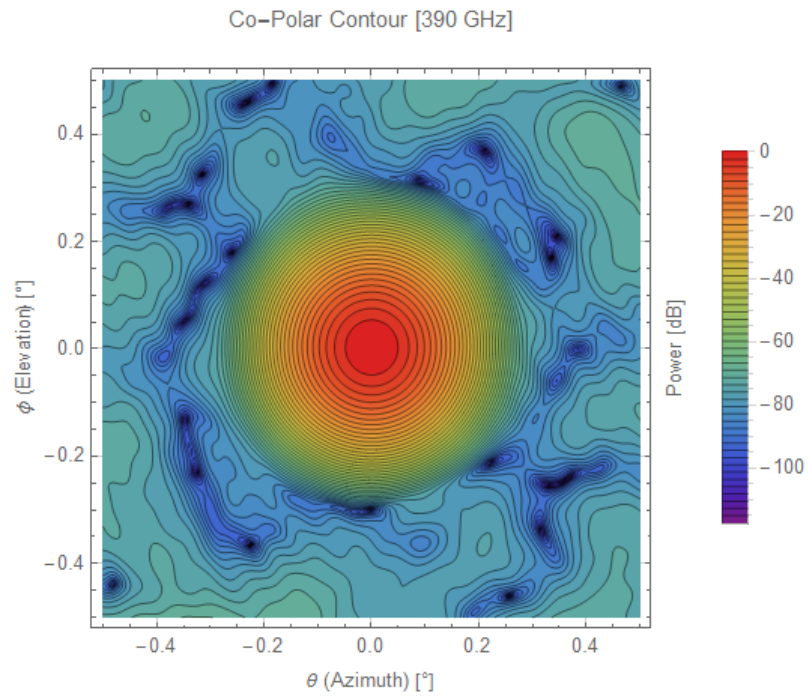


Figure 6.67: Co-Polar beam contour plot for 390 GHz beam launched from the central feed.

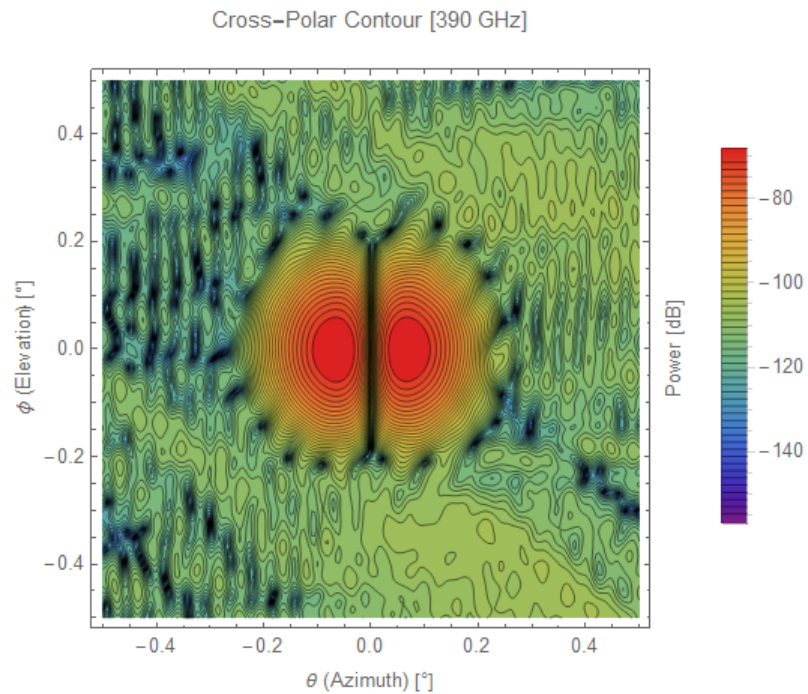


Figure 6.68: Cross-Polar beam contour plot for 390 GHz beam launched from the central feed.

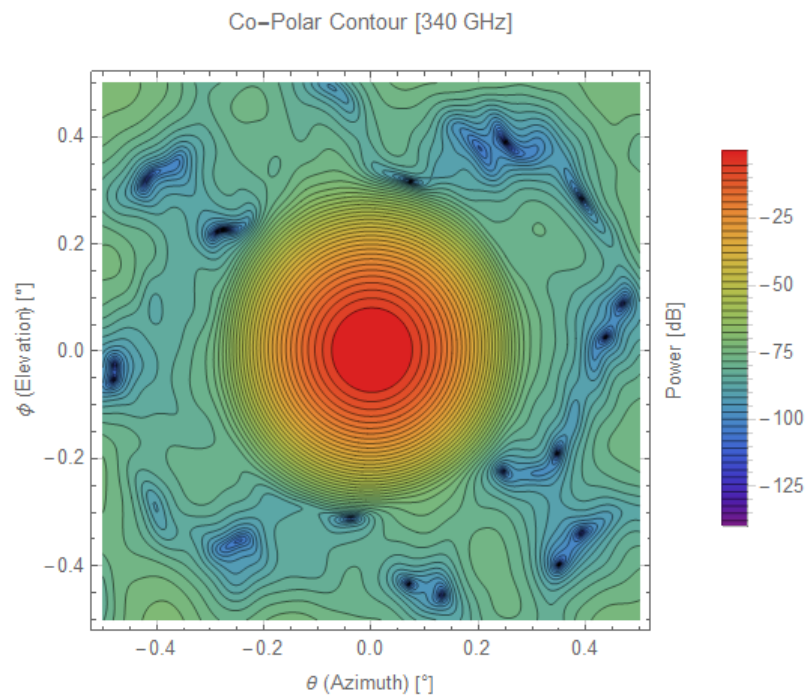


Figure 6.69: Co-Polar beam contour plot for 340 GHz beam launched from the  $\theta = +1^\circ$  feed.

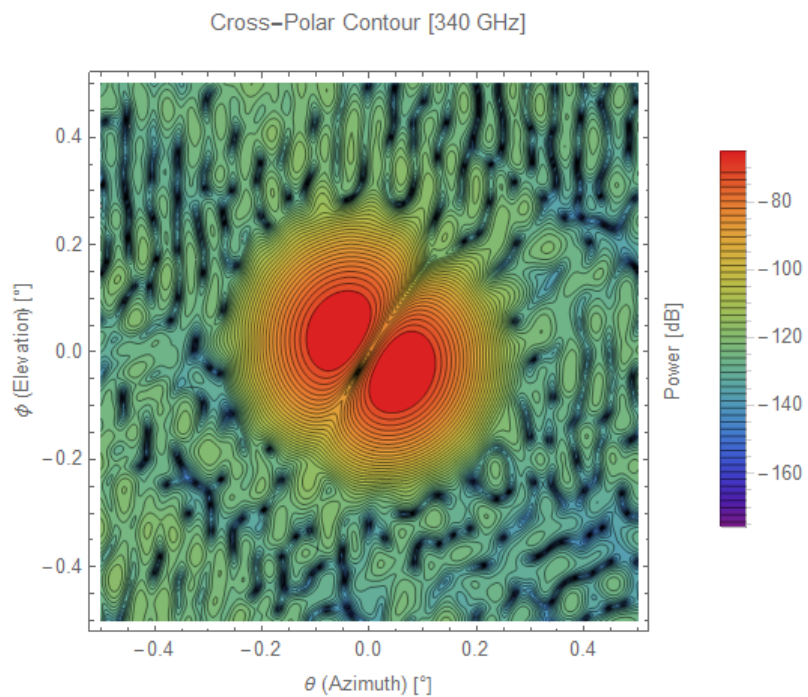


Figure 6.70: Cross-Polar beam contour plot for 340 GHz beam launched from the  $\theta = +1^\circ$  feed.

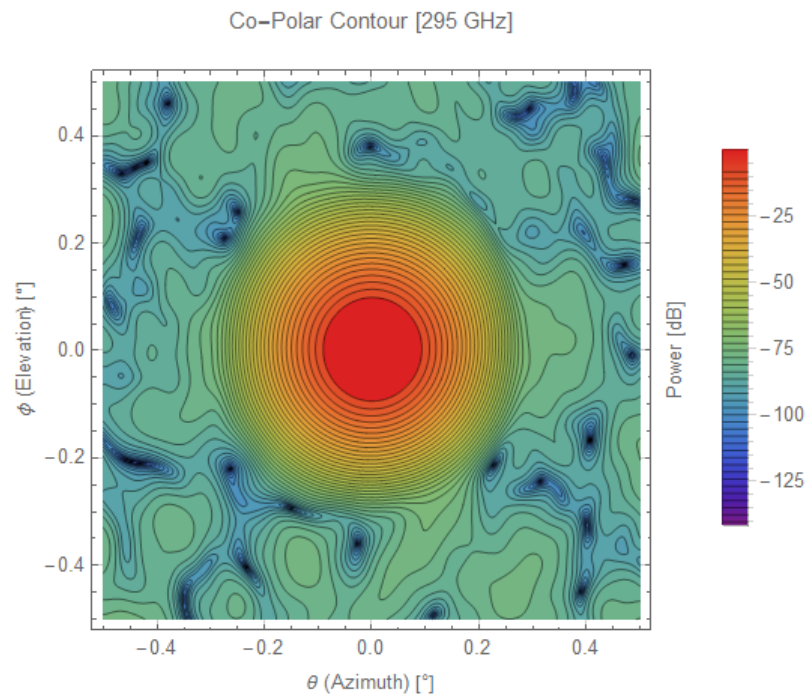


Figure 6.71: Co-Polar beam contour plot for 295 GHz beam launched from the  $\theta = +1^\circ$  feed.

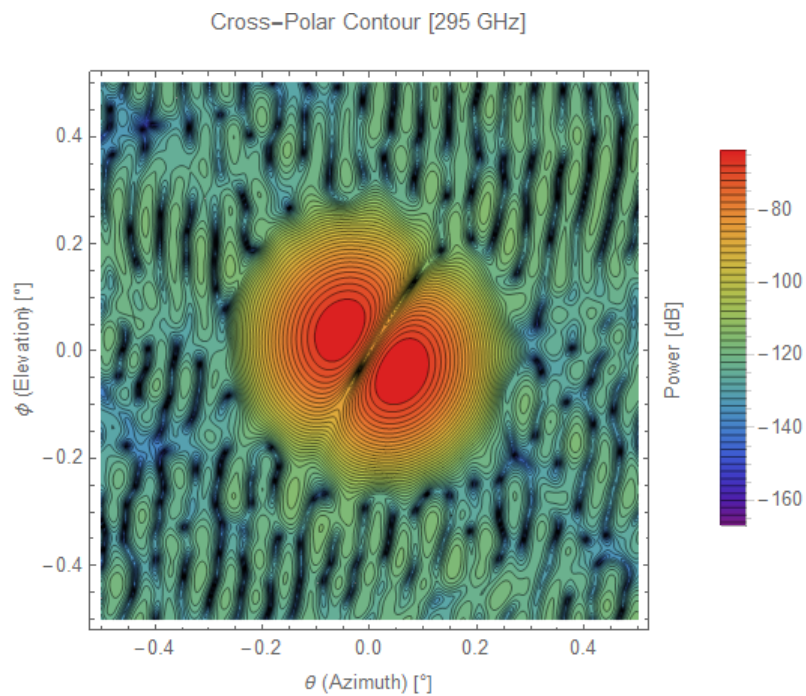


Figure 6.72: Cross-Polar beam contour plot for 295 GHz beam launched from the  $\theta = +1^\circ$  feed.

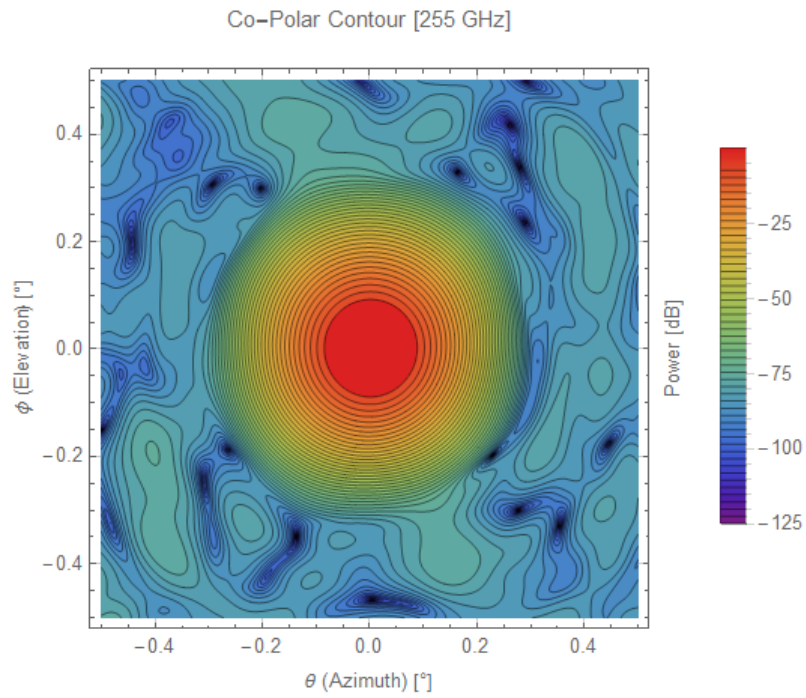


Figure 6.73: Co-Polar beam contour plot for 255 GHz beam launched from the  $\theta = +1^\circ$  feed.

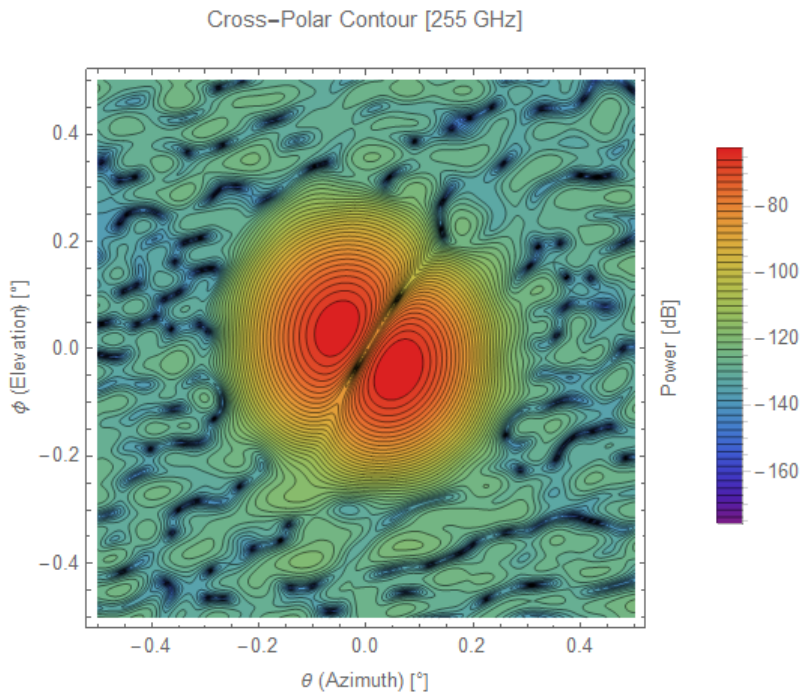


Figure 6.74: Cross-Polar beam contour plot for 255 GHz beam launched from the  $\theta = +1^\circ$  feed.

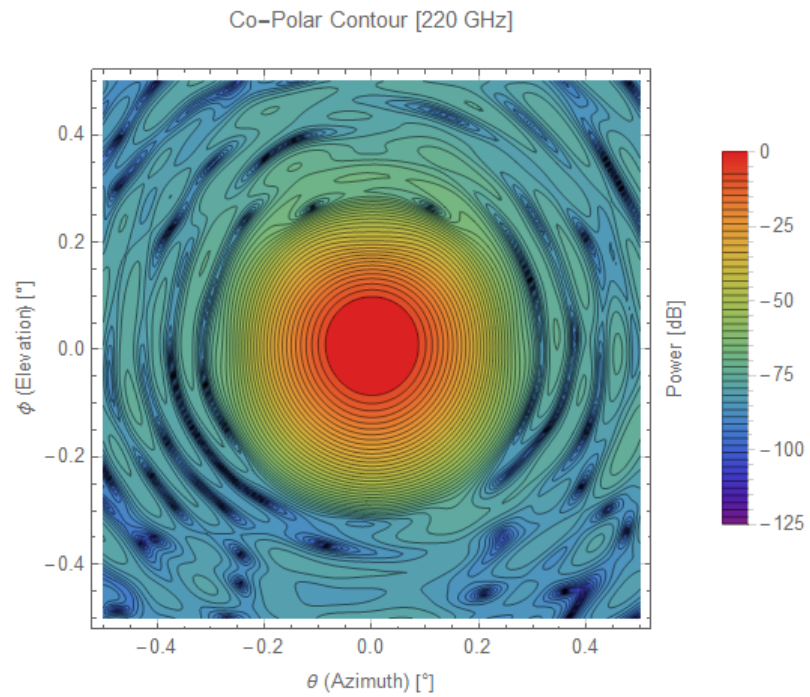


Figure 6.75: Co-Polar beam contour plot for 220 GHz beam launched from the  $\phi = +2^\circ$  feed.

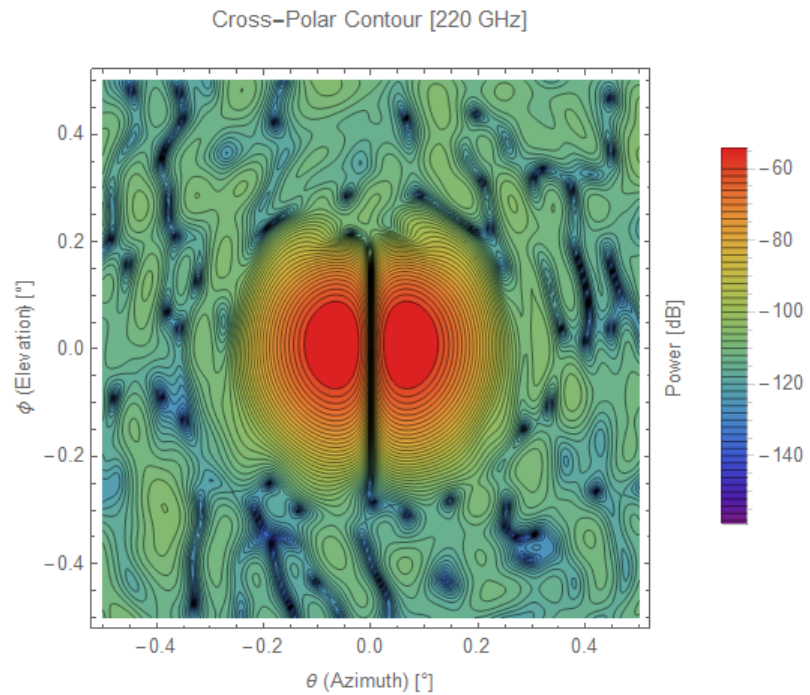


Figure 6.76: Cross-Polar beam contour plot for 220 GHz beam launched from the  $\phi = +2^\circ$  feed.

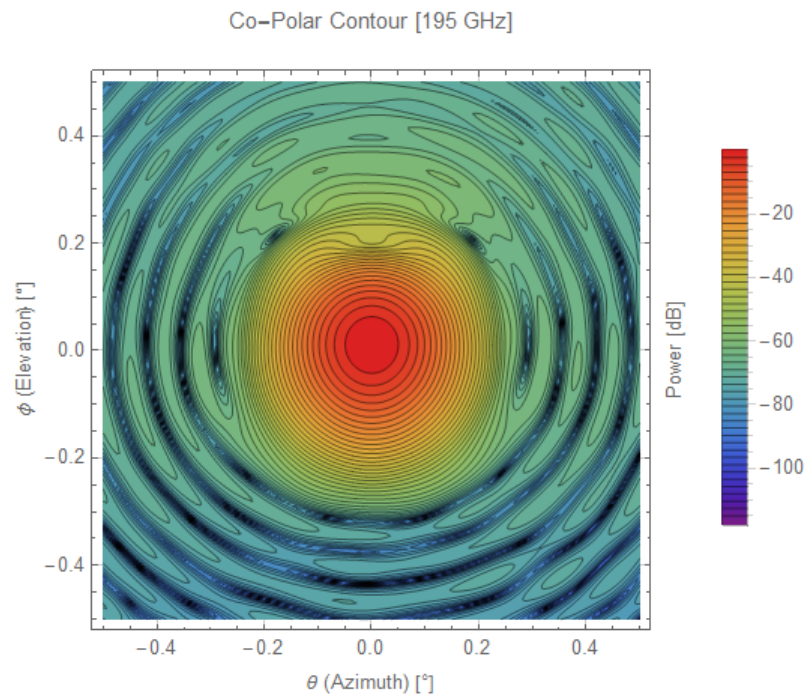


Figure 6.77: Co-Polar beam contour plot for 195 GHz beam launched from the  $\phi = +2^\circ$  feed.

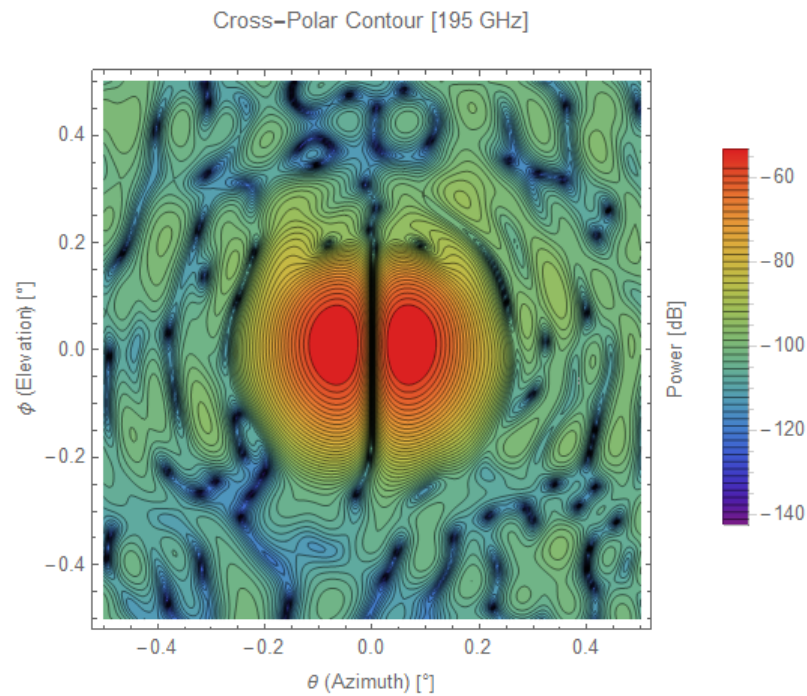


Figure 6.78: Cross-Polar beam contour plot for 195 GHz beam launched from the  $\phi = +2^\circ$  feed.

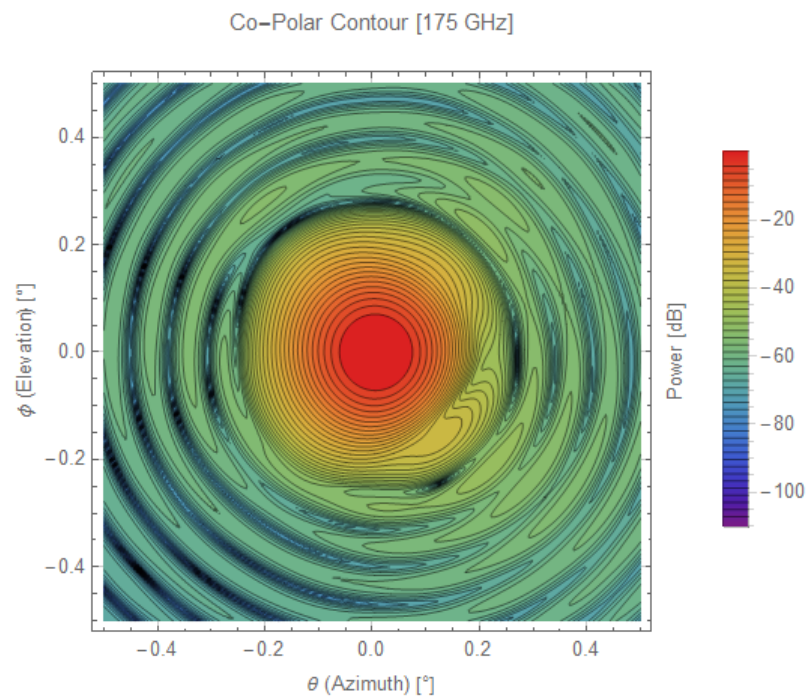


Figure 6.79: Co-Polar beam contour plot for 175 GHz beam launched from the  $\theta = +2^\circ$  feed.

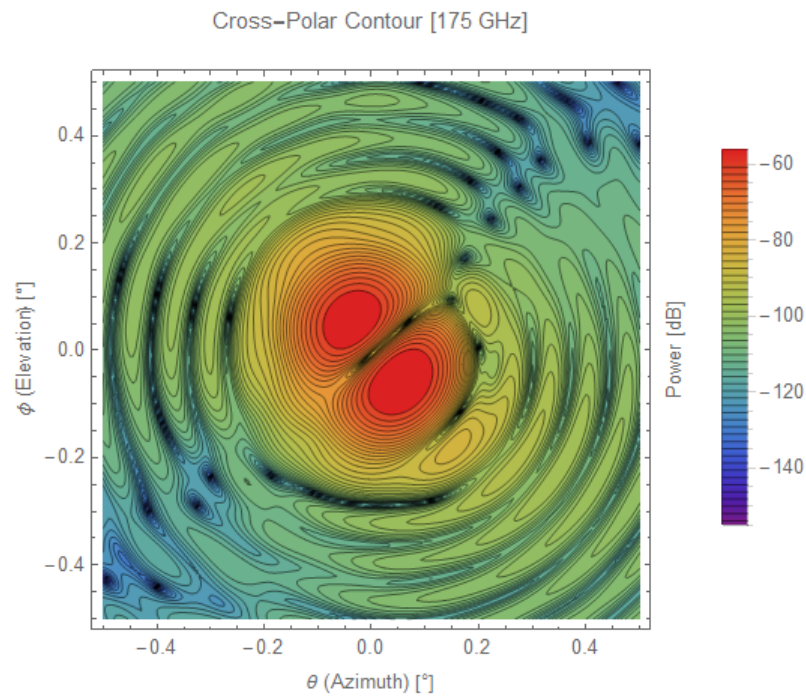


Figure 6.80: Cross-Polar beam contour plot for 175 GHz beam launched from the  $\theta = +2^\circ$  feed.

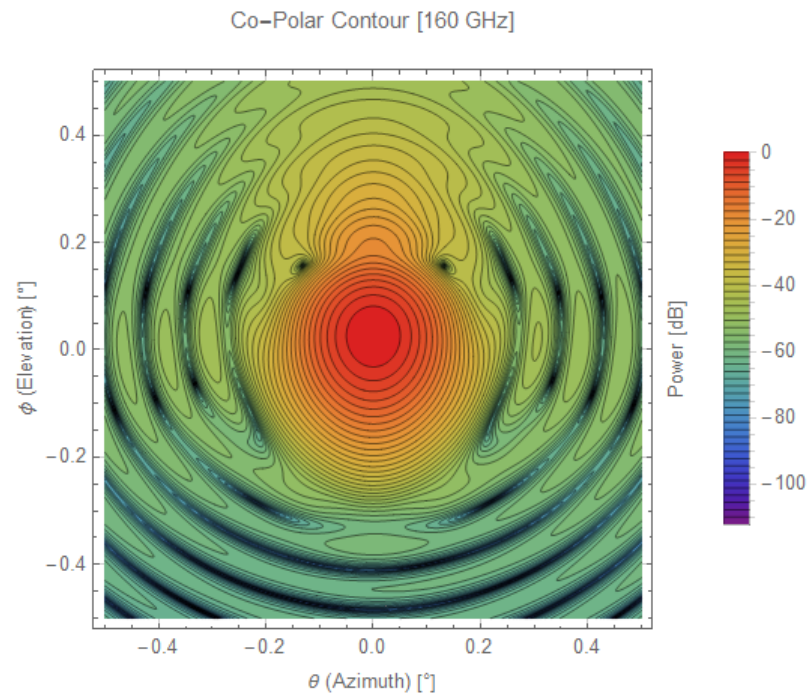


Figure 6.81: Co-Polar beam contour plot for 160 GHz beam launched from the  $\phi = +4^\circ$  feed.

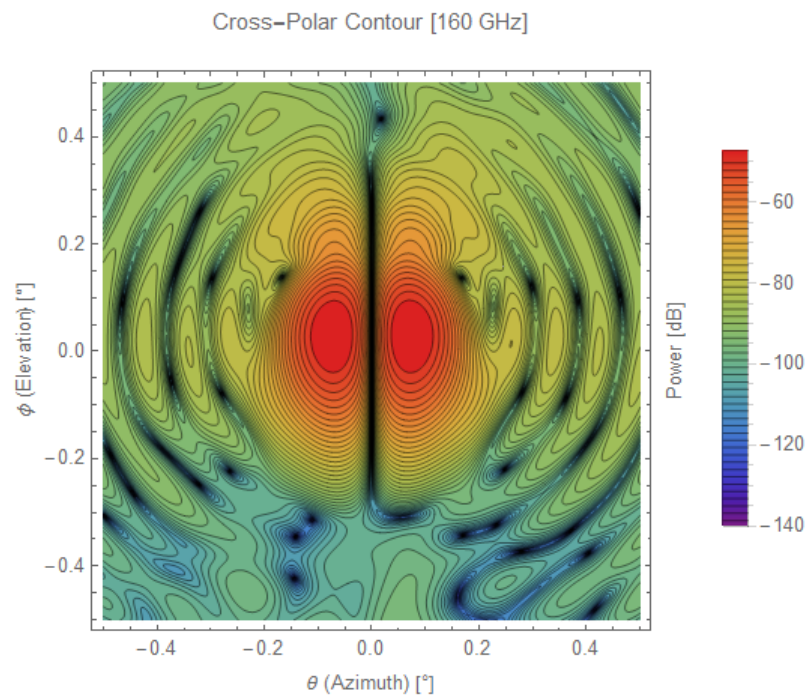


Figure 6.82: Cross-Polar beam contour plot for 160 GHz beam launched from the  $\phi = +4^\circ$  feed.

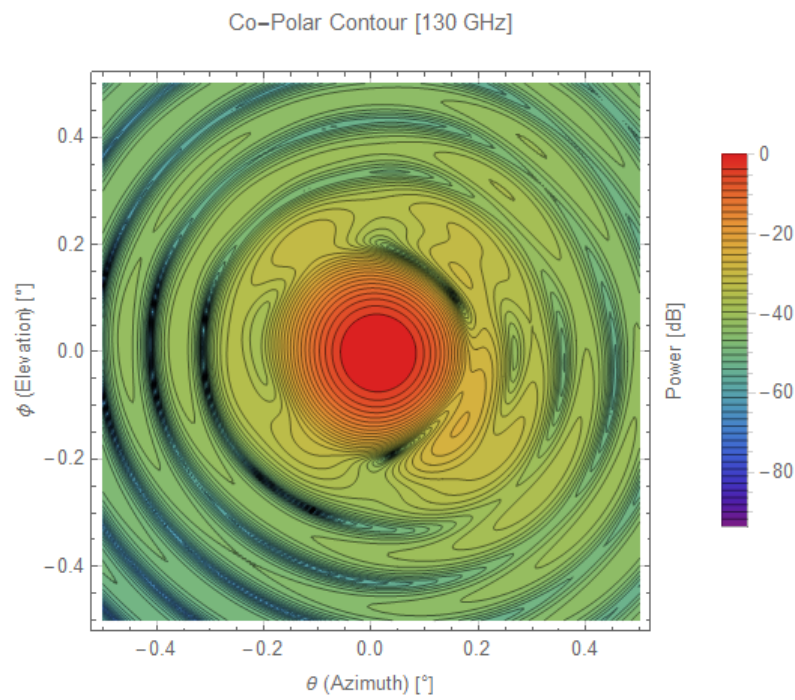


Figure 6.83: Co-Polar beam contour plot for 130 GHz beam launched from the  $\theta = +3^\circ$  feed.

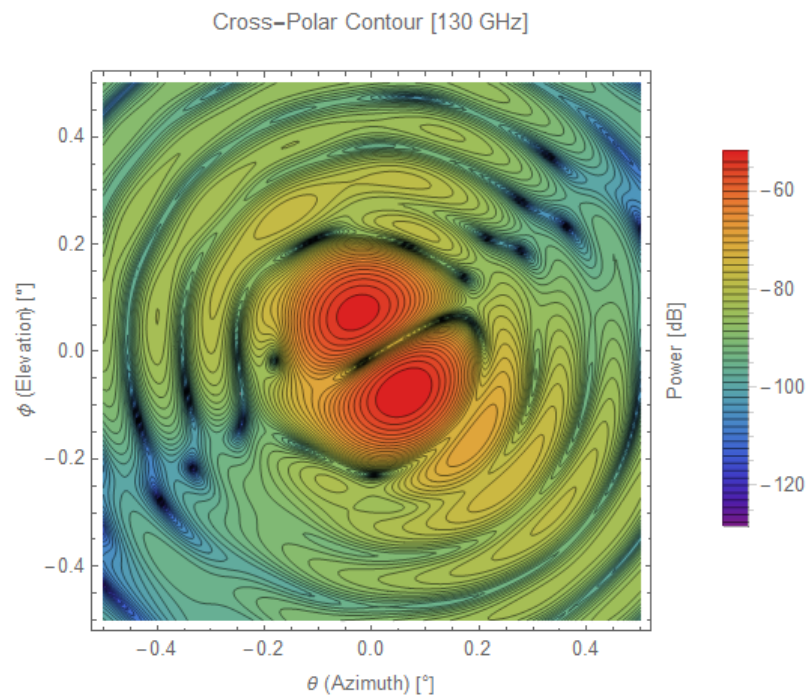


Figure 6.84: Cross-Polar beam contour plot for 130 GHz beam launched from the  $\theta = +3^\circ$  feed.

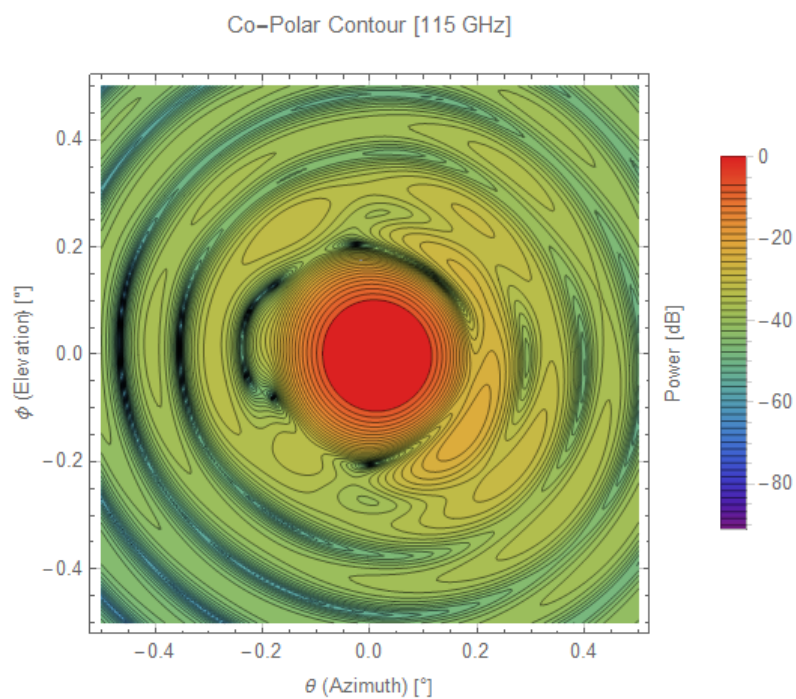


Figure 6.85: Co-Polar beam contour plot for 115 GHz beam launched from the  $\theta = +3^\circ$  feed.

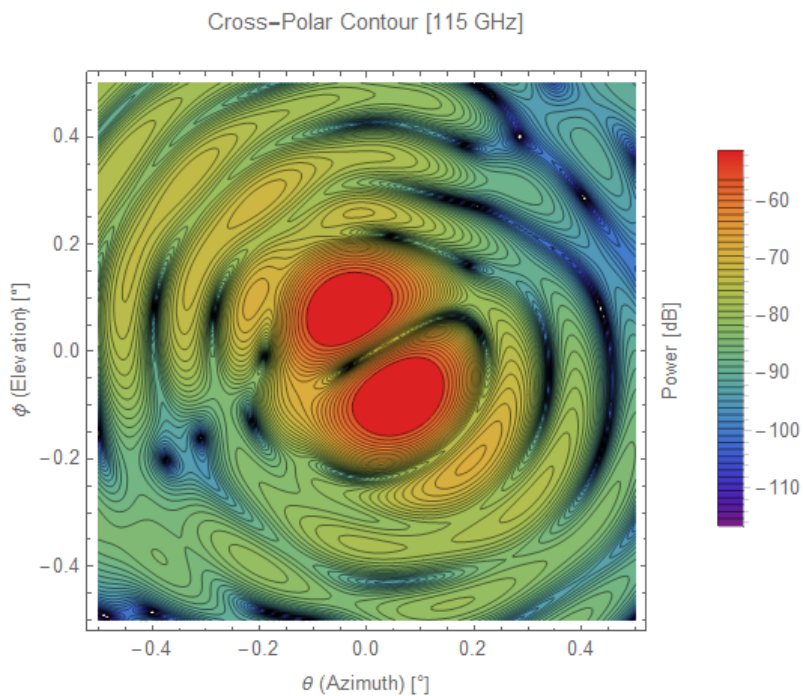


Figure 6.86: Cross-Polar beam contour plot for 115 GHz beam launched from the  $\theta = +3^\circ$  feed.

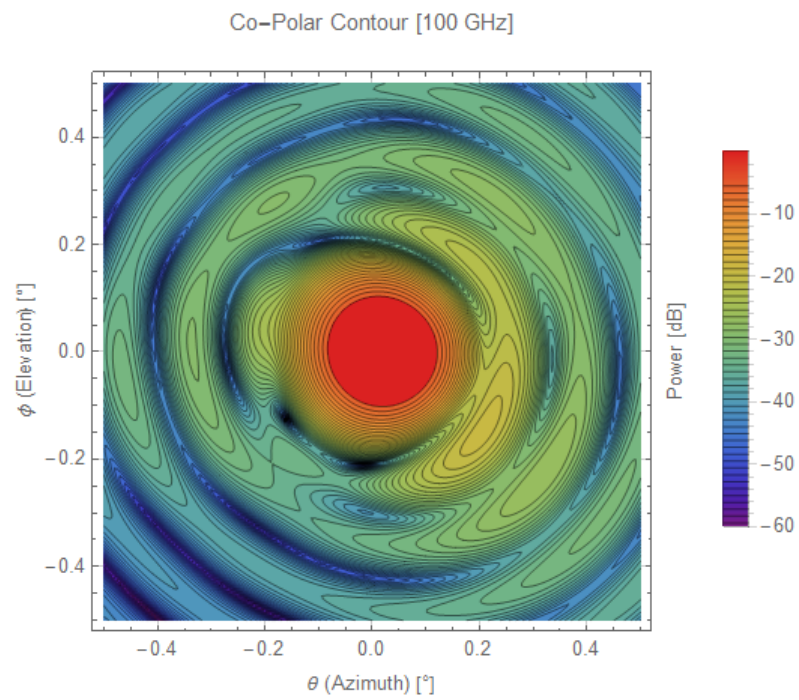


Figure 6.87: Co-Polar beam contour plot for 100 GHz beam launched from the  $\theta = +4^\circ$  feed.

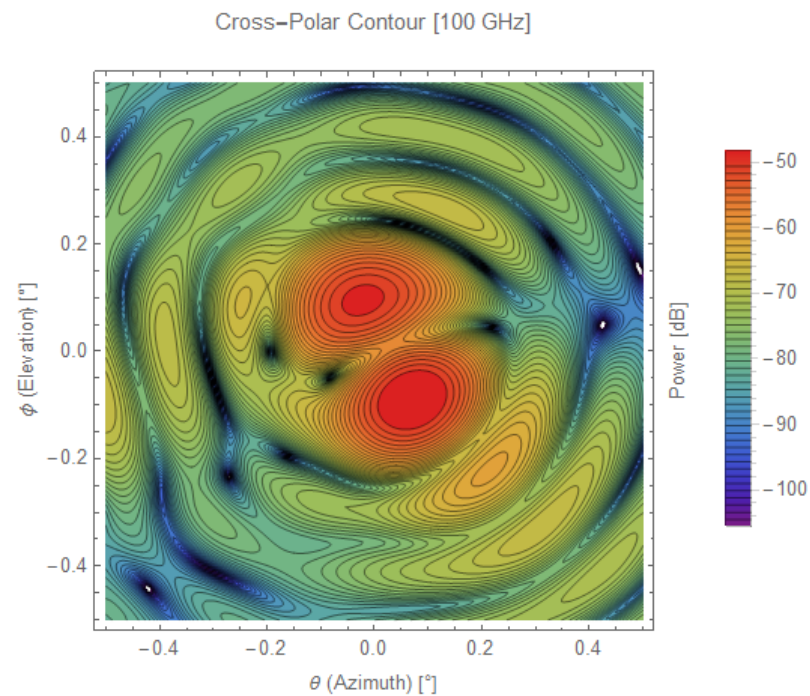


Figure 6.88: Cross-Polar beam contour plot for 100 GHz beam launched from the  $\theta = +4^\circ$  feed.

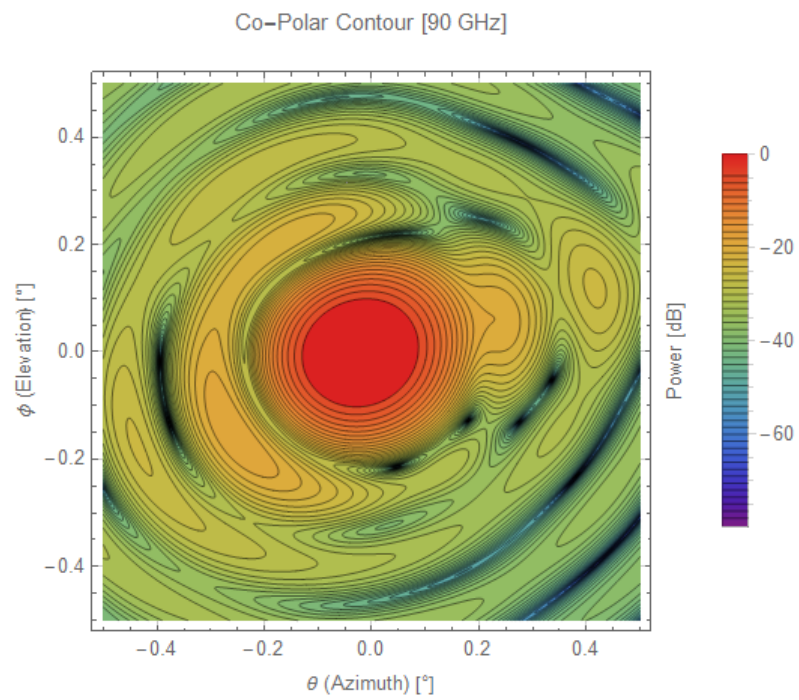


Figure 6.89: Co-Polar beam contour plot for 90 GHz beam launched from the  $\theta = -4^\circ$  feed.

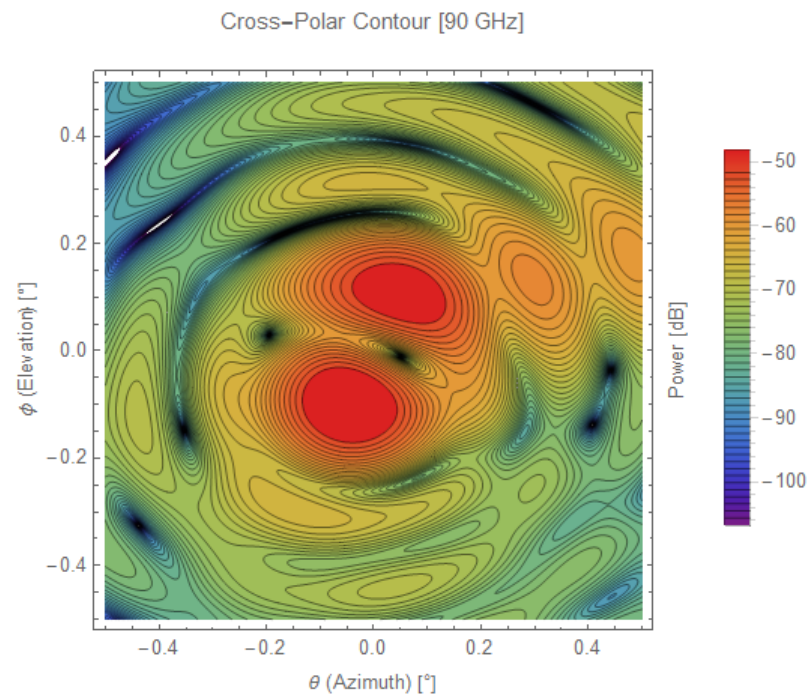


Figure 6.90: Cross-Polar beam contour plot for 90 GHz beam launched from the  $\theta = -4^\circ$  feed.

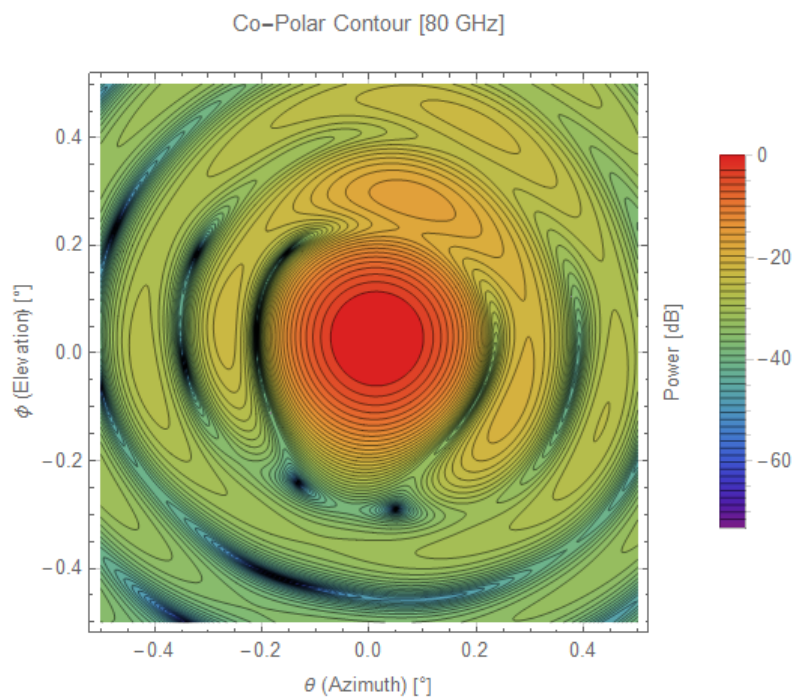


Figure 6.91: Co-Polar beam contour plot for 80 GHz beam launched from the  $\theta = +4^\circ, \phi = +4^\circ$  feed.

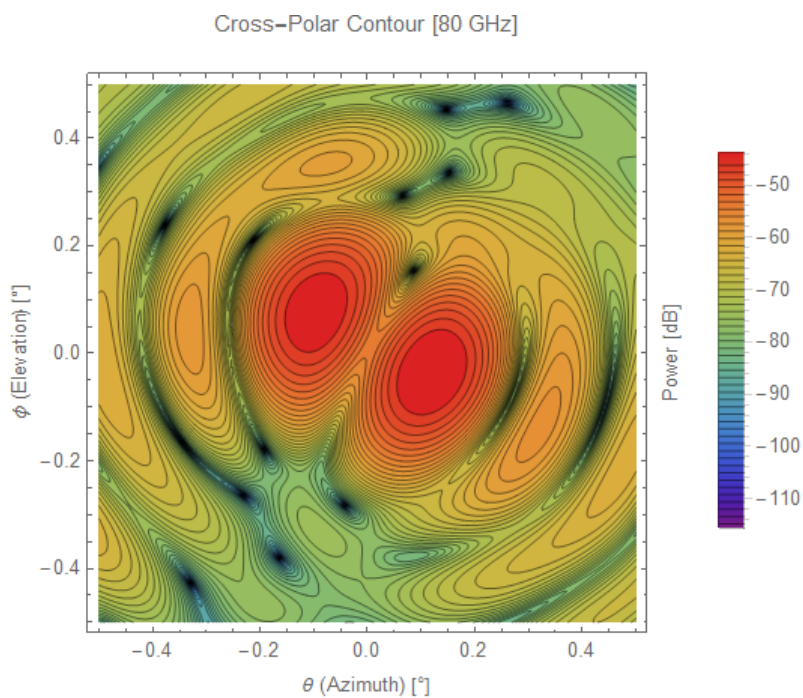


Figure 6.92: Cross-Polar beam contour plot for 80 GHz beam launched from the  $\theta = +4^\circ, \phi = +4^\circ$  feed.

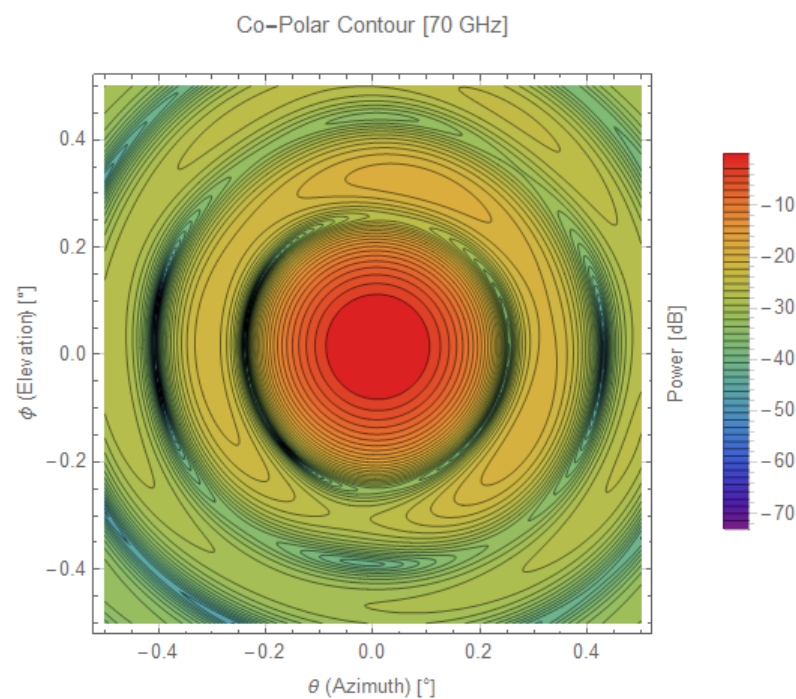


Figure 6.93: Co-Polar beam contour plot for 70 GHz beam launched from the  $\theta = +2^\circ, \phi = +2^\circ$  feed.

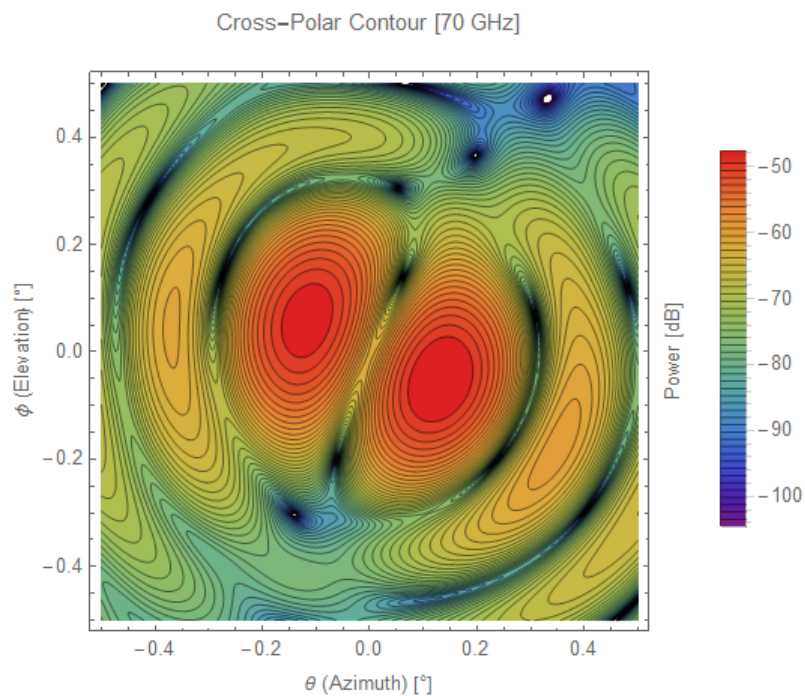


Figure 6.94: Cross-Polar beam contour plot for 70 GHz beam launched from the  $\theta = +2^\circ, \phi = +2^\circ$  feed.

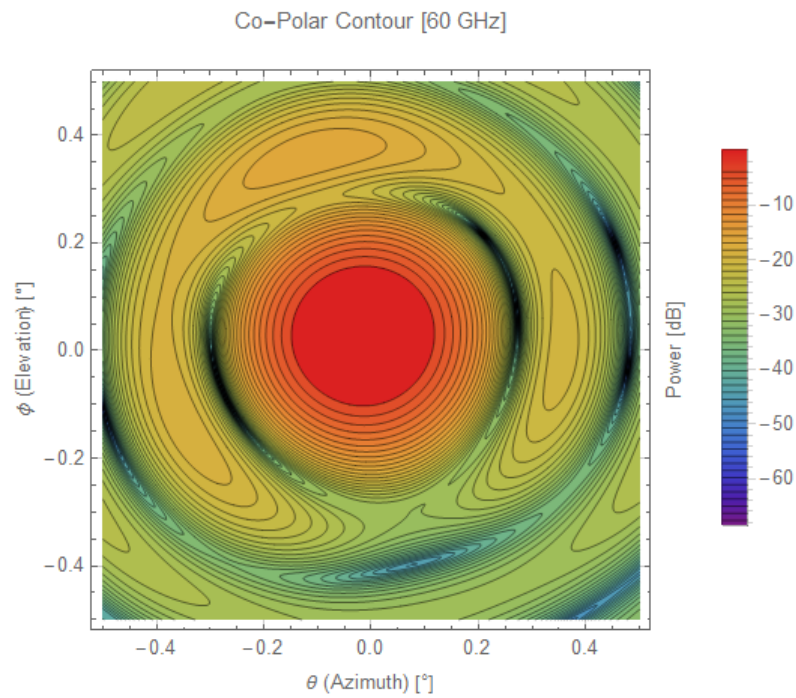


Figure 6.95: Co-Polar beam contour plot for 60 GHz beam launched from the  $\theta = -4^\circ, \phi = +4^\circ$  feed.

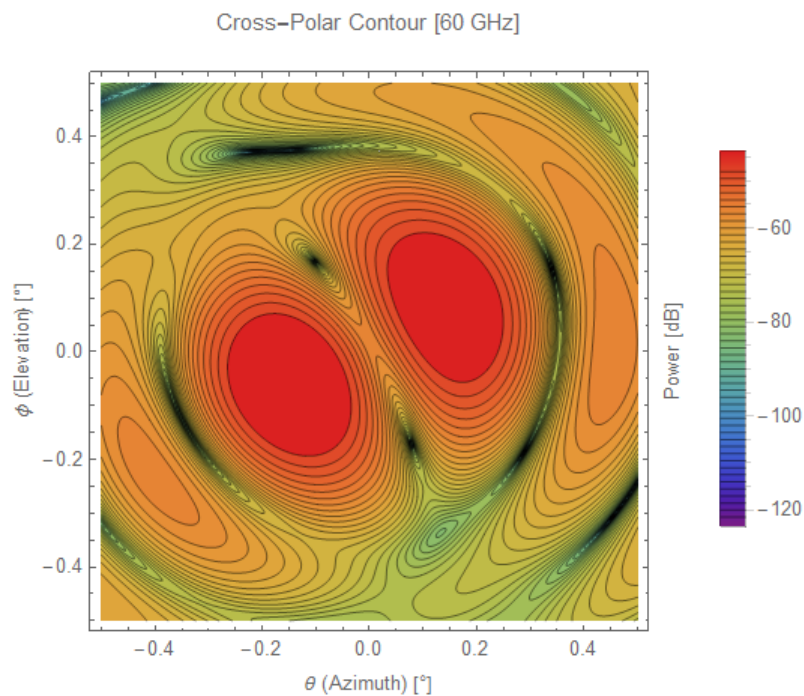


Figure 6.96: Cross-Polar beam contour plot for 60 GHz beam launched from the  $\theta = -4^\circ, \phi = +4^\circ$  feed.

### 6.7.7 Multi-Frequency *CORE* Beam Log Plots

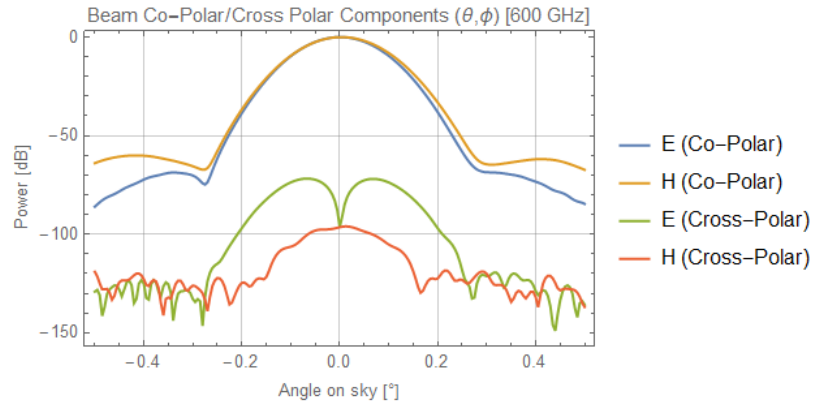


Figure 6.97: Co/Cross-Polar beam log plot for 600 GHz beam.

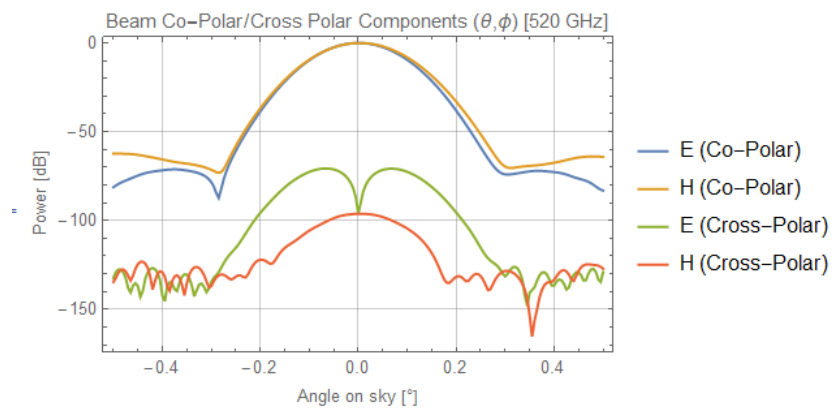


Figure 6.98: Co/Cross-Polar beam log plot for 520 GHz beam.

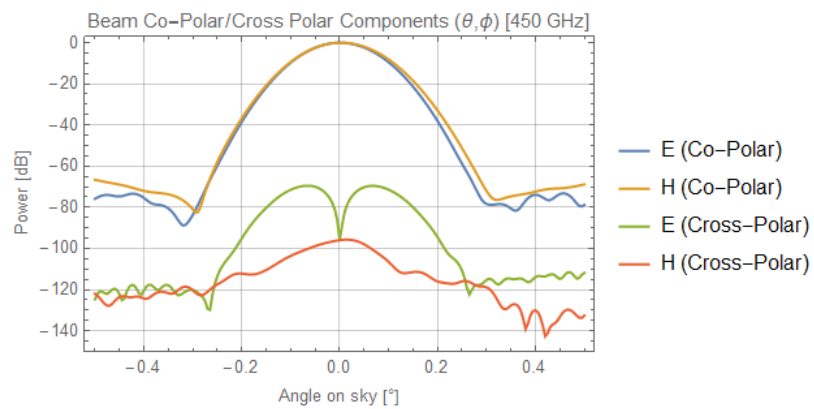


Figure 6.99: Co/Cross-Polar beam log plot for 450 GHz beam.

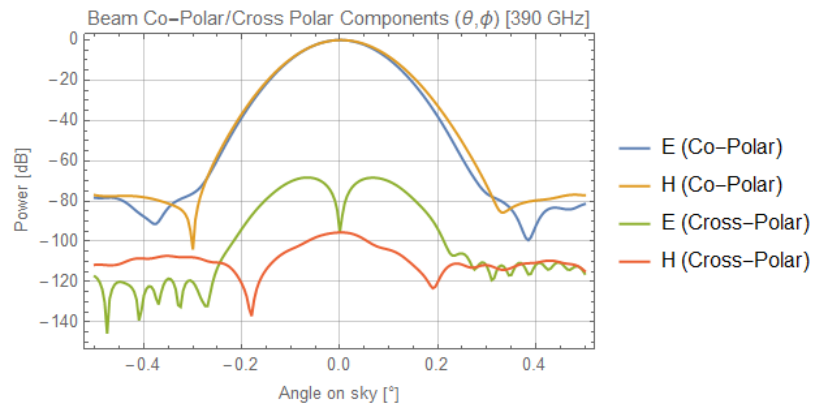


Figure 6.100: Co/Cross-Polar beam log plot for 390 GHz beam.

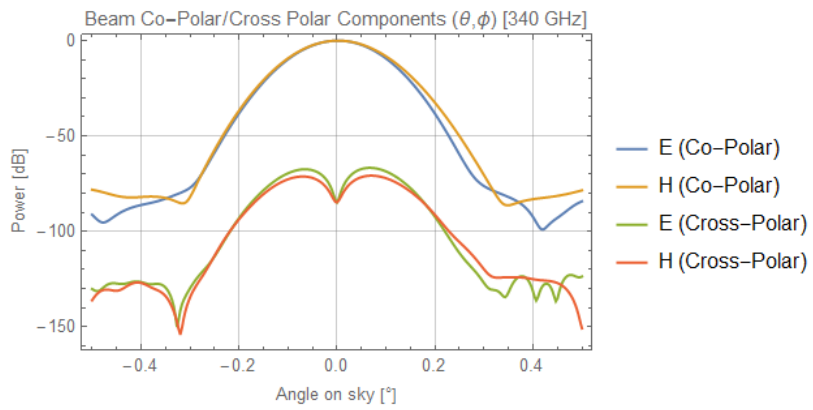


Figure 6.101: Co/Cross-Polar beam log plot for 340 GHz beam.

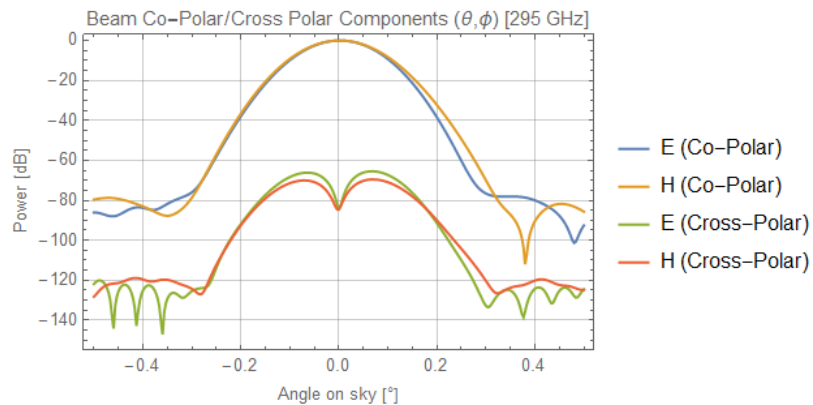


Figure 6.102: Co/Cross-Polar beam log plot for 295 GHz beam.

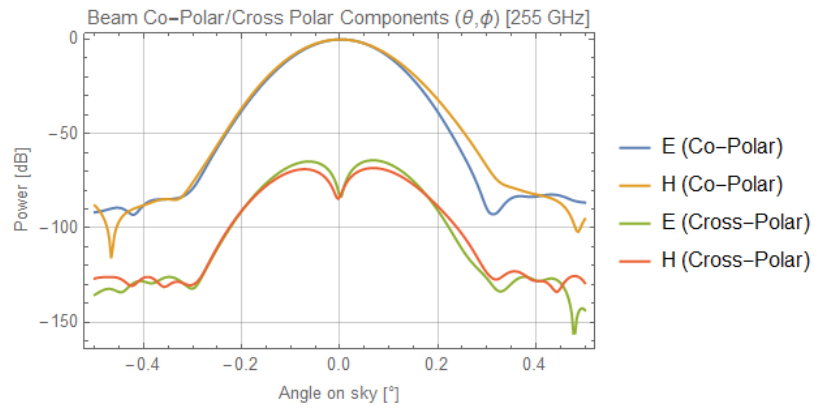


Figure 6.103: Co/Cross-Polar beam log plot for 255 GHz beam.

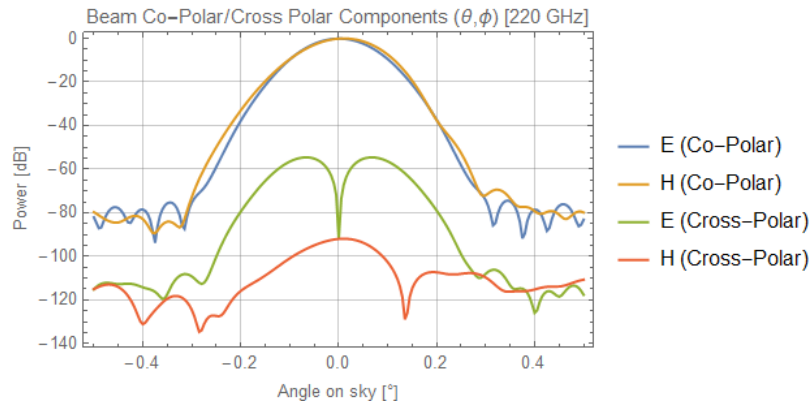


Figure 6.104: Co/Cross-Polar beam log plot for 220 GHz beam.

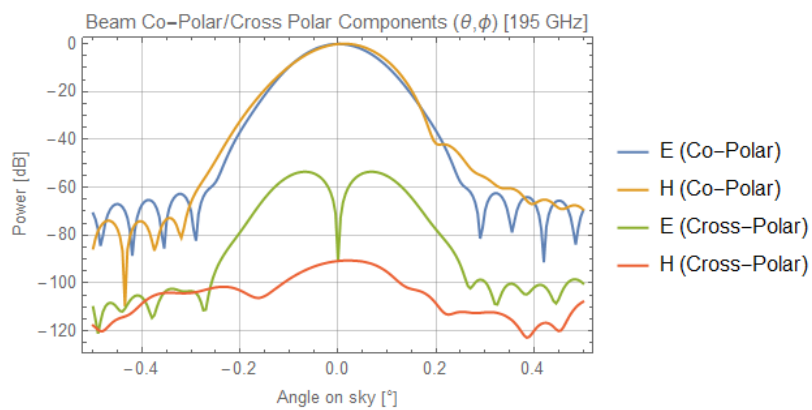


Figure 6.105: Co/Cross-Polar beam log plot for 195 GHz beam.

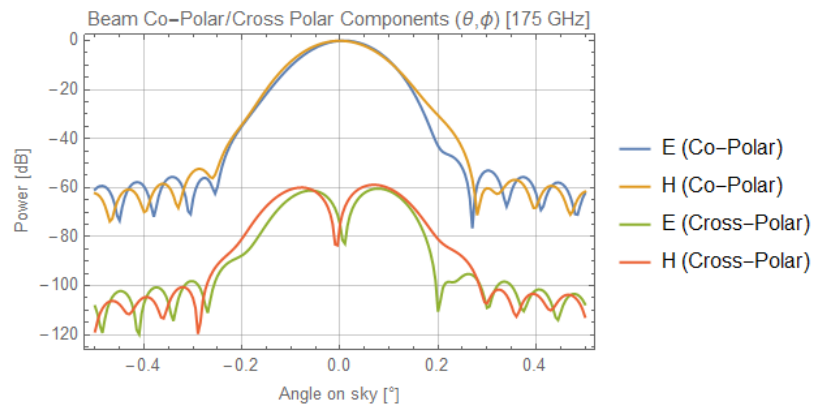


Figure 6.106: Co/Cross-Polar beam log plot for 175 GHz beam.

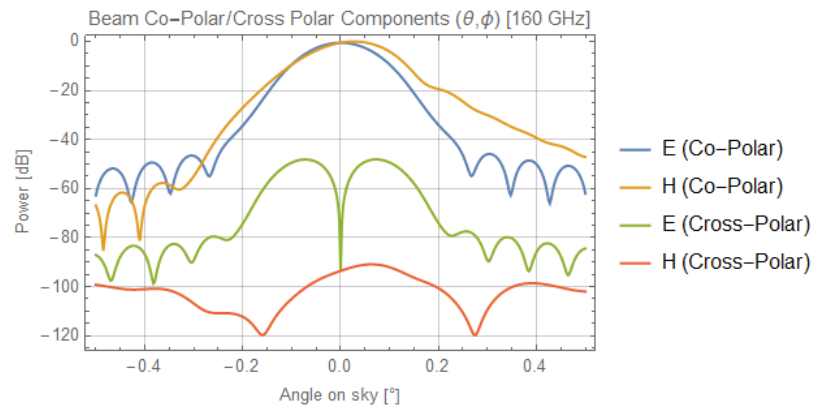


Figure 6.107: Co/Cross-Polar beam log plot for 160 GHz beam.

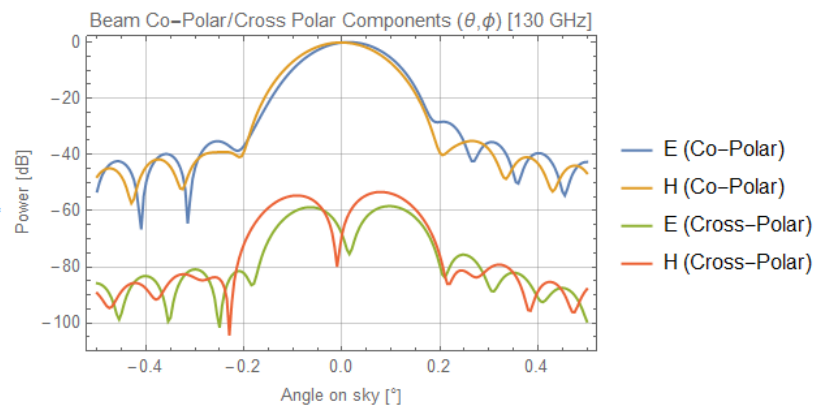


Figure 6.108: Co/Cross-Polar beam log plot for 130 GHz beam.

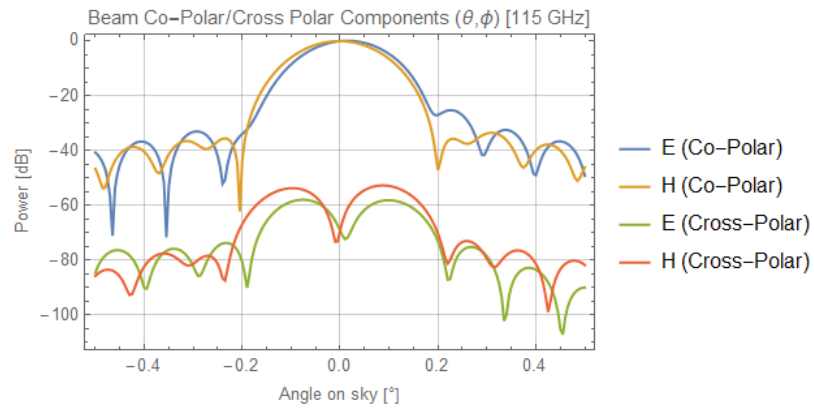


Figure 6.109: Co/Cross-Polar beam log plot for 115 GHz beam.

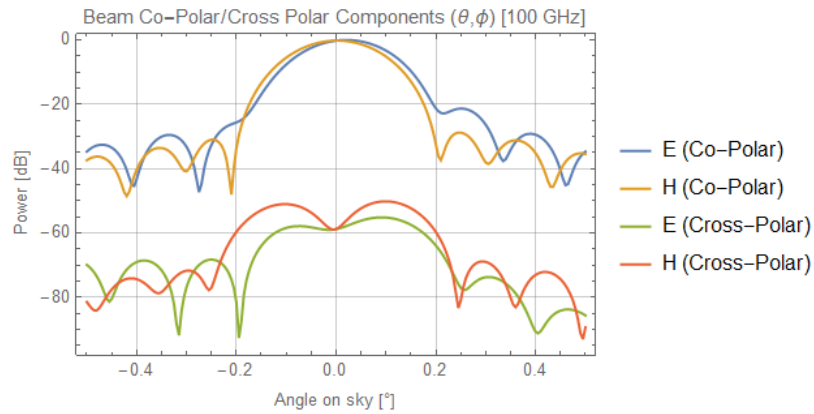


Figure 6.110: Co/Cross-Polar beam log plot for 100 GHz beam.

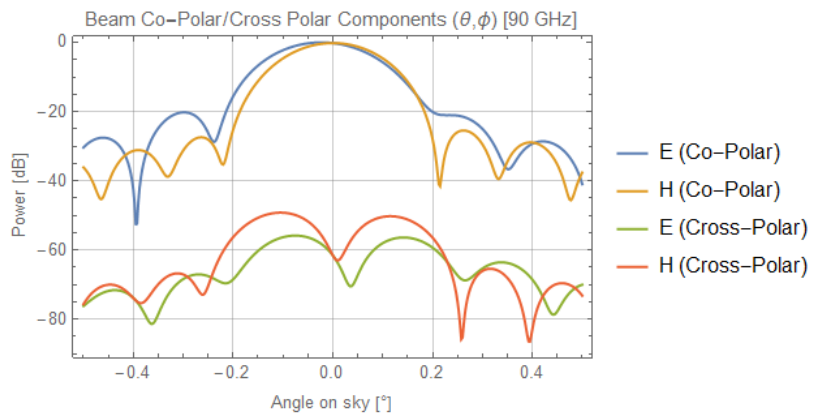


Figure 6.111: Co/Cross-Polar beam log plot for 90 GHz beam.

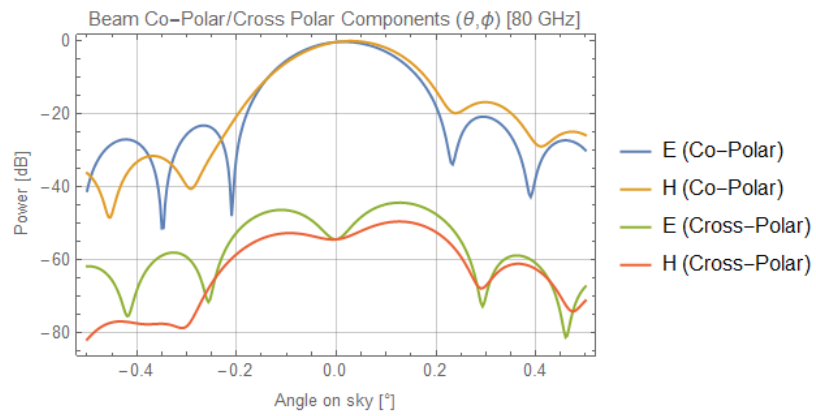


Figure 6.112: Co/Cross-Polar beam log plot for 80 GHz beam.

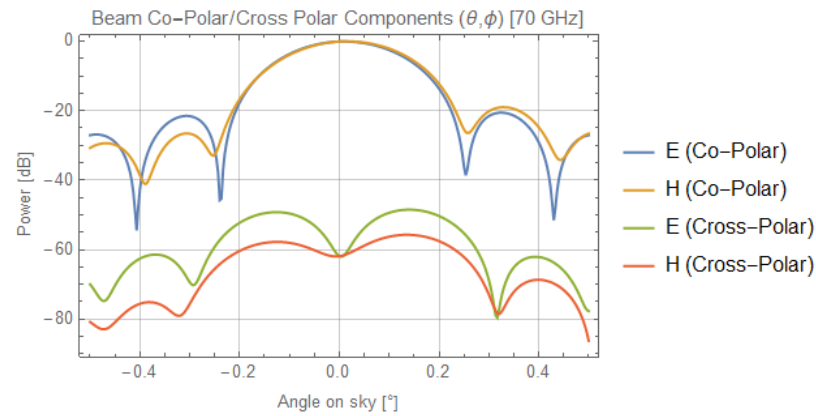


Figure 6.113: Co/Cross-Polar beam log plot for 70 GHz beam.

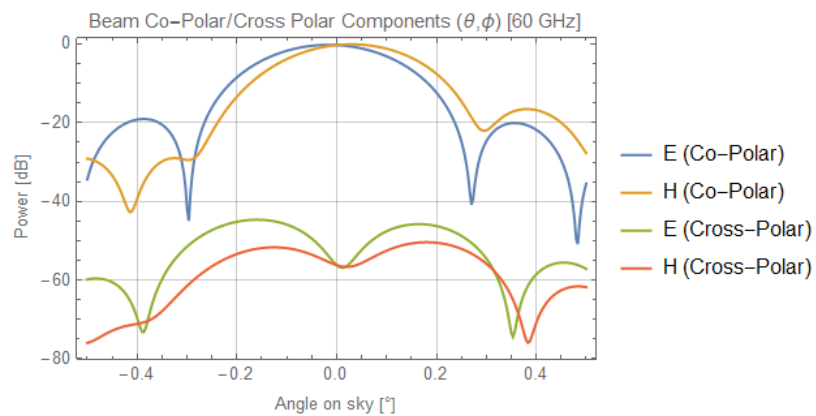


Figure 6.114: Co/Cross-Polar beam log plot for 60 GHz beam.

### 6.7.8 Conclusions

Beginning with the 145 GHz beams, the goal was to provide fields projected onto the sky up to  $4^\circ$  offset in both elevation  $\phi$  and azimuth  $\theta$ . Qualitative analysis was used to determine the shape of the beams in terms of aberrations present and ellipticity as a measure of the difference in FWHM values for one beam. As stated previously, the results of this particular analysis were included in the *CORE* instrument paper de Bernardis et al. (2017). Of particular interest to the *CORE* consortium were the beams at offsets of  $3/4^\circ$  in both directions. The quality of these beams would inform on the telescope design's ability at a fundamental level to produce low-aberration beams. Any issues that may have arisen pertaining to higher than desired distortion or increased cross-polar levels could be assessed initially with a more complete focal plane representation. What can be gleaned from these initial results is that the cross-polar beam components for all tested beams is at or below -40 dB, a rough yardstick which (as with LLAMA) indicates low polarisation leakage being generated in the design. Ellipticity values for both polarisations are consistent and do not rise to substantial levels, the highest values being seen at the very edge offset beams in  $\phi$ . Offsets are consistently lower than  $0.03^\circ$ . The beams can be seen to become more distorted with distance from the centre of the focal plane but the severe aberrations are constricted to one dimension, indicating symmetry breaking along the local  $y$ -axes of the mirrors to be the culprit in this instance. The fact that there is no marked difference at all between results of linear X and Y polarisations is another advantage for the design; considering its role as a polarimeter for the CMB this is a welcome result.

Moving on to the frequency range analysis, this work was not requested by the consortium but was considered to be highly informative nonetheless. Given the lighter aspect of this analysis, no Gaussian fitting was performed on these beams. The higher frequency beams contained at the centre of the focal plane are highly

Gaussian in appearance and exhibit low aberration/offset as expected. Given the size of the mirrors relative to the size of the beams, this is hardly a surprising result. At 160 GHz and below, the effects of diffraction and interference become more apparent with the increasing size of beams relative to the mirrors. Results for 145 GHz can be found in the previous section in abundance. Finally, below 100 GHz the sidelobe structures reach their highest, increasing by 30 dB compared with the other end of the frequency range. Throughout the range, cross-polarised radiation remains fairly low consistently from frequency to frequency and never reaches above -40 dB for any frequency tested.

## 6.8 Importing Telescope Components

The final addition made to the *CORE* model involved importing components from the *CORE* CAD file into the GRASP model. These components include the baffling at the telescope aperture, focal plane shielding, thermal shields and the satellite service module. These components will have a small effect of the beams produced by *CORE* directly, so their inclusion into the model will represent a step towards a more complete model and results that are more representative of reality. In the future, the baffling structure will need detailed modelling for stray-light and far-out sidelobe analysis.

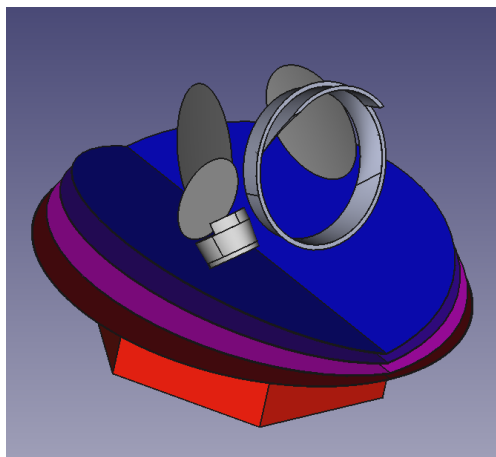


Figure 6.115: The full model of *CORE* in FreeCAD.

The process of importing these objects is different to that used for the mirrors. Though irregular triangulation meshes are still ultimately used, the objects cannot be represented by single-face scatterers. The formatting required for these multi-face scatterers is more complex than that for single-face scatterers, given that an incorrect join between mesh points will result in a heavily warped object.

### 6.8.1 Creating Viable GRASP Meshes

As was stated in the introduction, Netgen meshes were used once again to create representations of the components. The meshing process was simpler this time around as the objects did not need to be moved over the global coordinate system, as was needed for the mirrors. The reasons will be discussed in the multi-face scatterer section. The reference coordinate system for these components was the global coordinate system of the model. Looking to Figure 6.115, the components are much larger than any of the mirrors meaning file size would be an issue going forward. Each component is also composed of multiple smaller objects. Both of these factors informed the choice of mesh density.

The issue with mesh density and these objects is one of rendering. GRASP incorporates a 3D CAD-like environment where the optical system can be viewed. As was discovered early on in this work, highly dense meshes would cause GRASP to slow down to unusable speeds while rendering these components. Any adjustment of the model after rendering would also induce the same effect. Less dense meshes would not impact rendering time to the same degree but would be much rougher surfaces. Therefore, a compromise was made. Two sets of meshes would be made for each component: a high-density version for calculations and a lower-density version for representation outside of calculations.

After all meshes had been created, there was one final step before exportation. The meshes were merged into larger forms to reduce overall complexity and make

the implementation more straightforward. The object groupings are as follows: Baffle, Inner Shield, Middle Shield, Outer Shield, Satellite Shell and Satellite Base. The groupings are shown in Figures 6.116 - 6.119. Merges can be done in the FreeCAD mesh workbench and are simply a joining of the two meshes together without alteration of existing points.

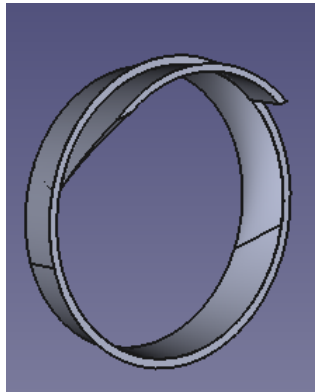


Figure 6.116: The aperture baffling in FreeCAD.

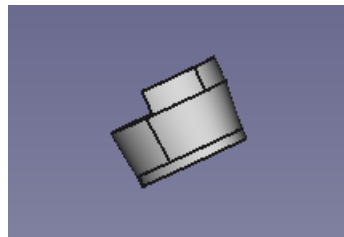


Figure 6.117: The focal plane shield in FreeCAD.

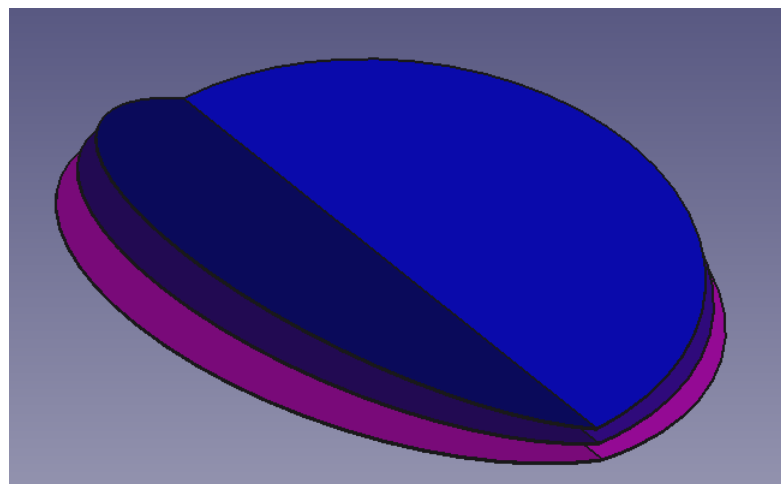


Figure 6.118: The three thermal shielding layers in FreeCAD.

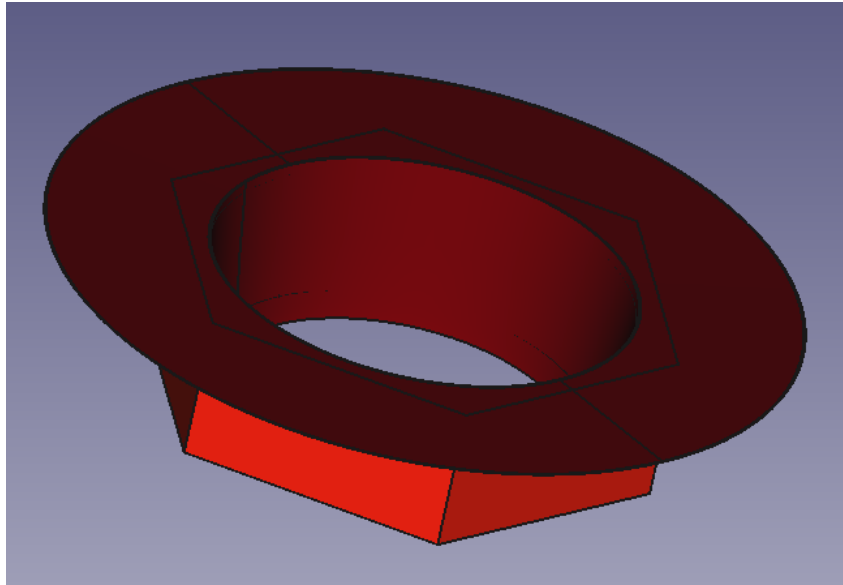


Figure 6.119: Satellite shell and base in FreeCAD.

Due to the different file type requirements, the required file format was the Nastran Bulk Data File (.bdf). This file format saves the created points of the mesh in a numbered list form. After the points, the joins necessary to recreate the object are stored. The joins reference three points by number and thus structure is preserved in the file. This is the basic structure of the GRASP .msh file. With correct formatting, the files could be read into GRASP as before.

### 6.8.2 New Mesh File Formatting

The Nastran Bulk Data File format is arranged differently than the python definition files. There is no header section at the start. The file is a list split into two parts: points and triangles. The points have the preface “GRID”, are numbered and contain an  $xyz$  Cartesian point. The triangles have the preface “CTRIA3” which denotes them as a three-point triangle. These entries have three constituent points which become the vertices of the triangle. Figure 6.120 shows the file layout:

```

19343 GRID,19342,0,844.1750,2191.589,3671.310CRLE
19344 GRID,19343,0,1169.852,2104.325,4090.822CRLE
19345 GRID,19344,0,1243.238,2084.661,2342.128CRLE
19346 GRID,19345,0,1348.492,2056.458,2217.769CRLE
19347 GRID,19346,0,1094.062,2124.633,3220.824CRLE
19348 GRID,19347,0,1175.933,2102.695,3512.256CRLE
19349 GRID,19348,0,988.8340,2152.828,3514.109CRLE
19350 GRID,19349,0,1332.650,2060.703,2768.357CRLE
19351 GRID,19350,0,1242.871,2084.759,2558.165CRLE
19352 GRID,19351,0,1383.523,2047.072,2428.573CRLE
19353 CTRIA3,1,0,2707,3783,3437CRLE
19354 CTRIA3,2,0,4752,4966,5144CRLE
19355 CTRIA3,3,0,2463,2221,3078CRLE
19356 CTRIA3,4,0,7892,8328,8584CRLE
19357 CTRIA3,5,0,7459,7460,8215CRLE
19358 CTRIA3,6,0,2661,1811,2662CRLE
19359 CTRIA3,7,0,6280,6490,7087CRLE
19360 CTRIA3,8,0,2196,185,2195CRLE
19361 CTRIA3,9,0,1380,6459,6243CRLE
19362 CTRIA3,10,0,4310,4750,4899CRLE

```

Figure 6.120: Section of a Nastran BDF file.

The “Free Field” format was used for the component meshes as, under this format, commas are used as the character separator. This makes the subsequent reformatting that bit easier. This format was chosen by opening a mesh file from FreeCAD in an open source meshing program known as “Gmsh”. The editor window can be seen in Figure 6.121. The mesh files are simply opened and saved again in the chosen format.

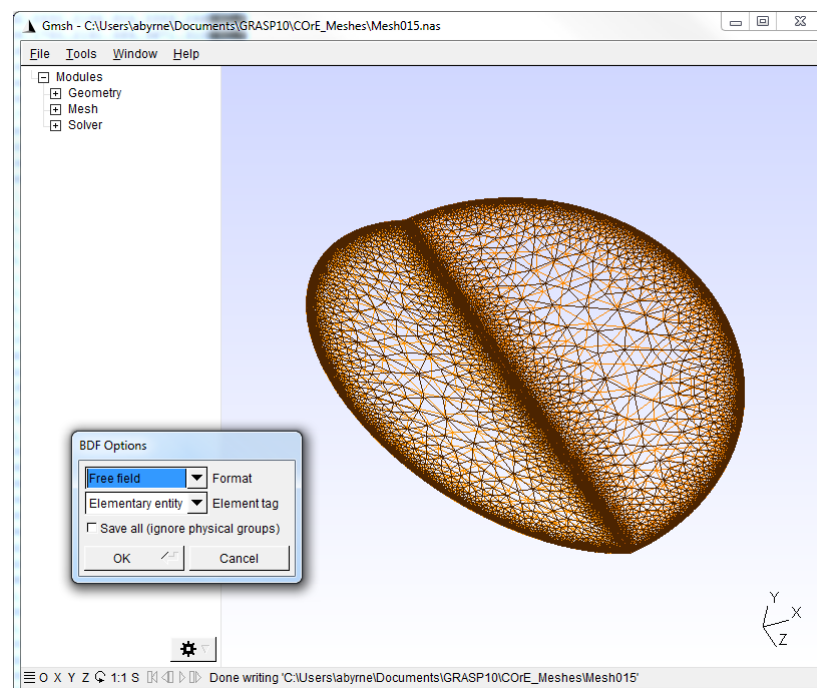


Figure 6.121: Gmsh editor window showing the format selector for the .bdf file.

The exact procedure for formatting a .bdf file to a grasp-accepted .msh file:

- Find “,0,” replace with “\r\n”
- Find “,” replace with “\s\s”
- Find “GRID”, replace with “[node]”
- Find “CTRIA3”, replace with “[patch]”
- Set text editor search mode to regular expression
- Find “^(\[[a-z]5,\]\s+\d+)”, replace with “\1\r\n3\s\s\s\s0\s\s\s\s0\s\s0\s0”
- Add the following lines at the beginning of the file
- Line 1: [version]
- Line 2: TICRA Mesh File, Version 1.0
- Line 3: [title]
- Line 4: *Title of mesh file goes here. User discretion.*
- Line 5: [region] 0
- Line 6: 0.10000000E+01 0.10000000E+01 0.00000000E+00^D

Please note that “\s” is the stand in for a space character. GRASP is very particular about file parsing, so it is advised that the above steps are followed to the letter to avoid problems. The newly reformatted file should now be ready for use with multi-face scatterer objects.

### 6.8.3 GRASP Multi-Face Scatterers

With the newly formatted and grouped mesh files ready for use, the construction of the objects in GRASP could now begin. A “Tabulated Mesh” object is used to represent the meshed components. These objects function similarly to the “Irregular Triangulation, XY Grid” objects. The major difference between these two objects, however, is that the “Tabulated Mesh” object requires no rim object. The component is taken in as is.

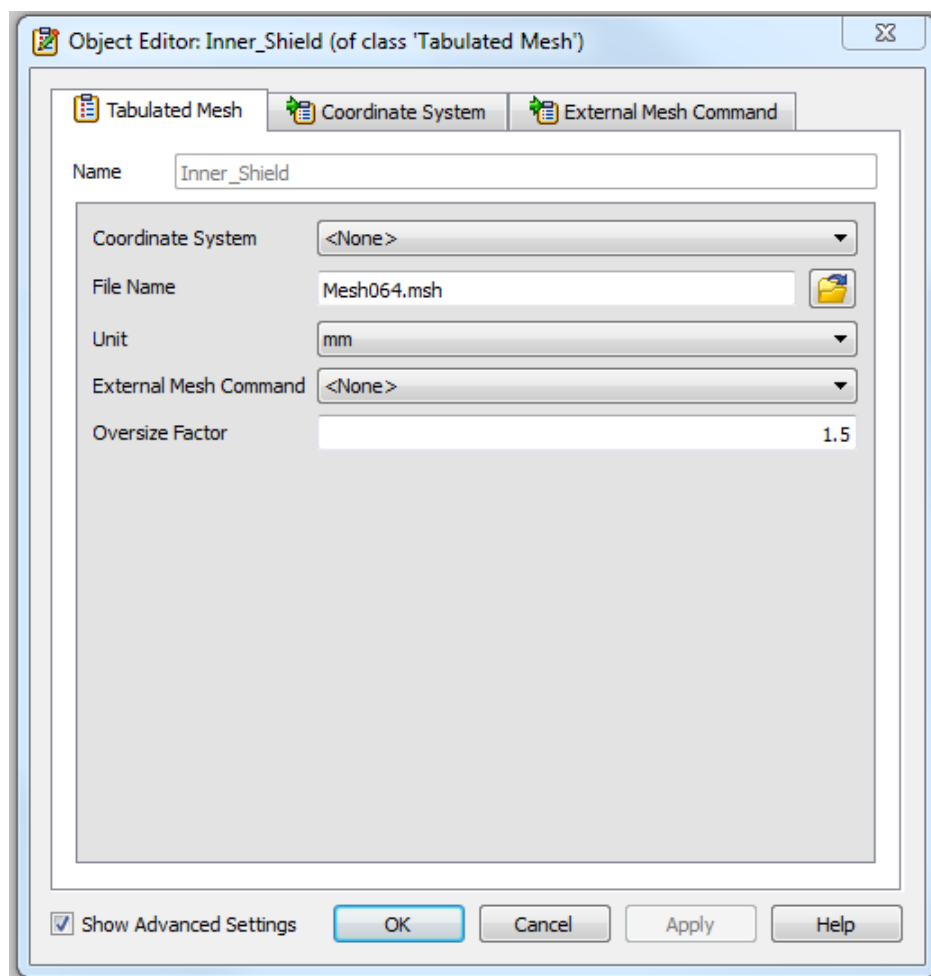


Figure 6.122: Tabulated Mesh editor window.

The coordinate system drop down list refers to the base coordinate system of the object. Note that the <None> attribute shown in Figure 6.122 is essentially using the GRASP global coordinate system. The mesh file is selected from the

file path command line. The unit option informs GRASP as to the units of data in the file. The External Mesh Command option specifies a plugin which can update the Tabulated Mesh object whenever a change is made to the mesh file itself. The Oversize Factor is used in refining the mesh itself should it be too sparsely populated.

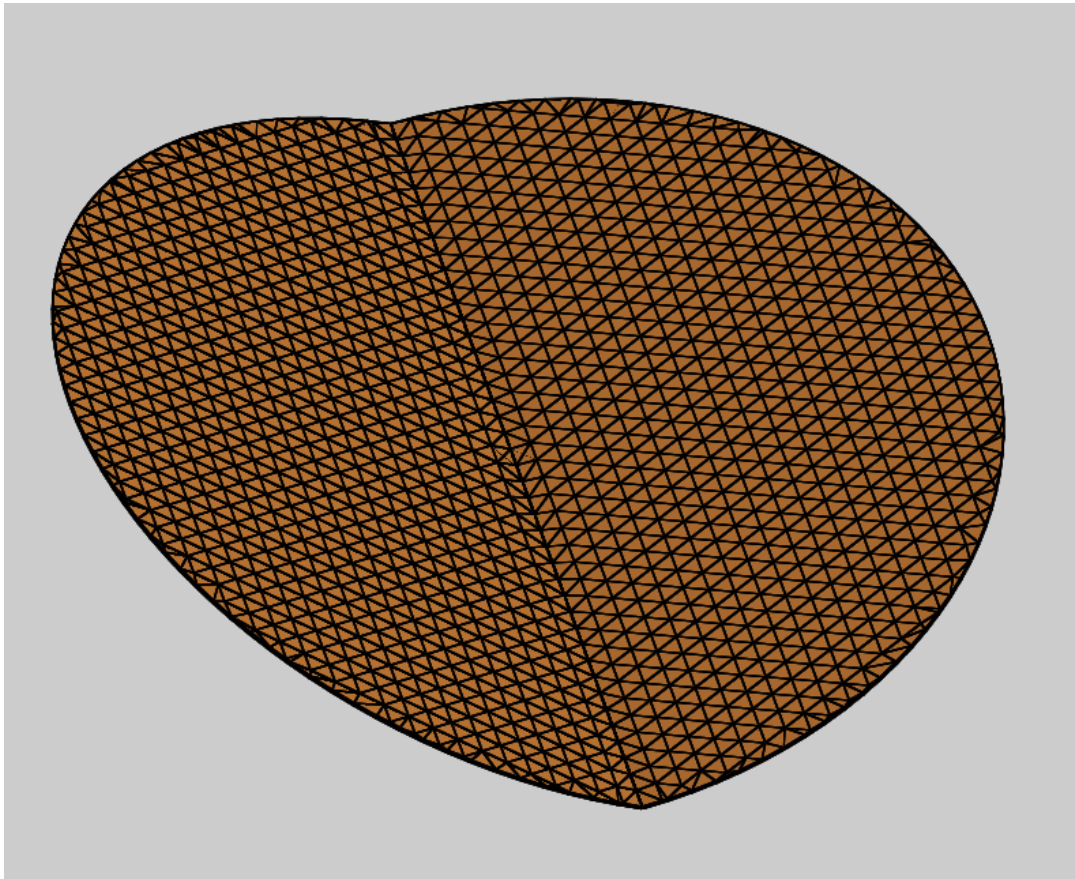


Figure 6.123: The inner thermal shield of *CORE*, meshed and present in GRASP.

Tabulated Mesh objects were used to represent all of the meshed telescope components. The inner shield can be seen in Figure 6.123. Once the object for each is created, a corresponding PO object must be created, as before. Single-Face PO objects cannot be used with Multi-Face Objects.

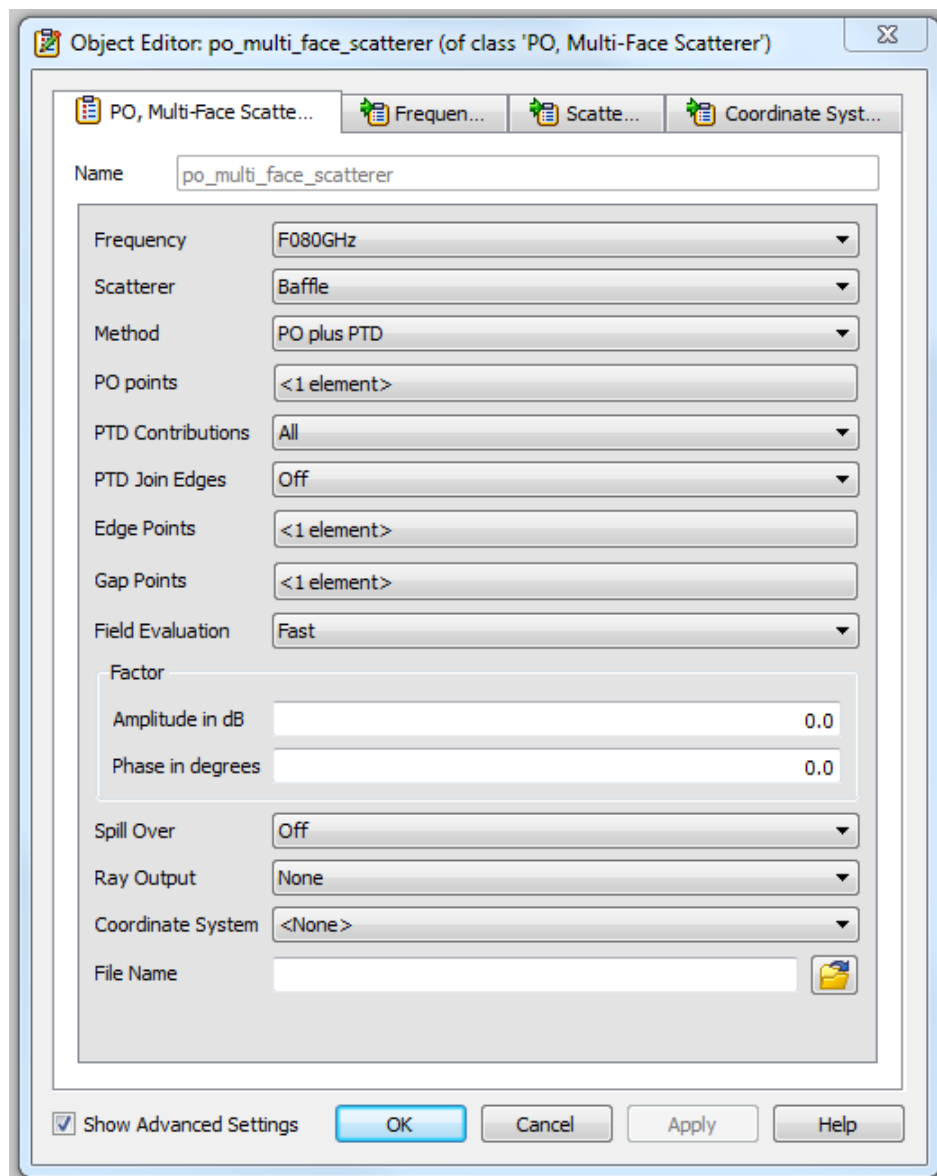


Figure 6.124: PO, Multi-Face Scatterer object editor window.

The editor window for a Multi-Face PO object is shown in Figure 6.124. This class of PO object shares much of its functionality with its single-face counterpart. PO calculations are established in the same manner, choosing the frequency and scattering object as before. PO and PTD contributions are calculated in the same manner as before, the only difference being that currents are calculated at each triangular segment rather than across the whole mirror face. The currents can also be stored for future use by providing a file path and file name.

### 6.8.4 New Coordinate System Integration

The final issue was the integration of the existing mirror global coordinate system with the new coordinate systems of the full model. All of the components shared the global coordinate system present in the CAD file as their reference coordinate system (see Figure 6.125). As a result, no repositioning or reorienting was needed after each component was imported, neatly sidestepping any potential errors that might arise. However, there was a disconnect between the coordinate systems of the new components and the existing coordinate systems of the mirrors, feeds and PO objects. This would need to be resolved.

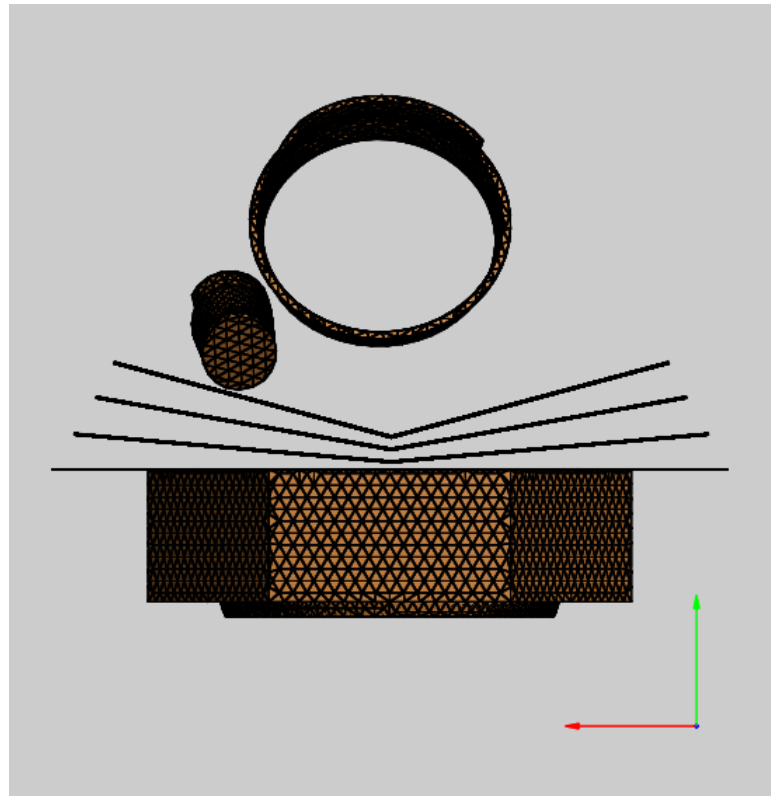


Figure 6.125: *CORE* components in GRASP. The new global coordinate system can be seen in the lower right.

The mirrors share a common coordinate system named “Mirror Global”. Any changes to the base coordinate system of “Mirror Global” would reorient the mirrors as a whole while keeping their relative positions and orientations intact.

A correct adjustment to “Mirror Global” would therefore allow the mirrors, feeds and output grids to be slotted into place among the new components. Luckily, the necessary transformations are all stored in the *CORE* .stp file and can be viewed with FreeCAD. FreeCAD orients objects using Euler  $XY'Z''$  rotations, also known as **yaw**, **pitch** and **roll**. The FreeCAD placement window is presented in Figure 6.126. These are familiar terms to those in aviation, but that system does not translate fully into GRASP. Recall that GRASP’s rotations are  $ZY'Z''$ . Therefore, a single coordinate system cannot be used to perform the orientation using the angles provided. Two linked coordinate systems must be used to imitate the **yaw**, **pitch** and **roll** convention.

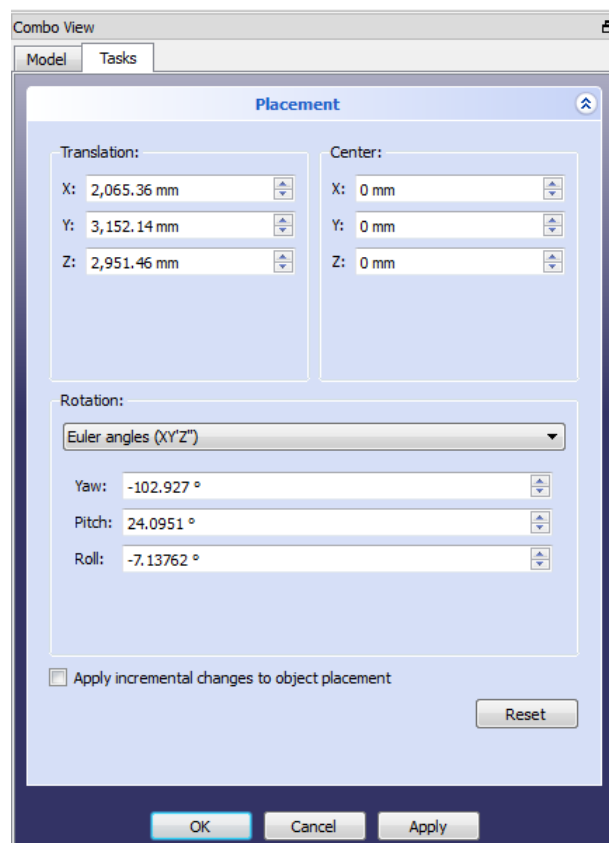


Figure 6.126: The placement window in FreeCAD for the *CORE* primary mirror.

The first coordinate system is created and is given the global coordinate system as its base. It is positioned 2065.36 mm along  $x$ , 3152.14 mm along  $y$  and 2951.46 mm along  $z$ . This is the correct point where “Mirror Global” should be located

according to the CAD model. Next, using the Euler angle tab, angle  $\alpha$  is set to  $-102.927^\circ$ . This corresponds to a rotation about the  $z$ -axis, which will be known as the **yaw** axis. Angle  $\beta$  will take a value of  $24.0951^\circ$ . This corresponds to rotation about the  $y$ -axis, which will be known as the **pitch** axis. This is as far as one coordinate system can be taken, as  $\gamma$  will rotate around the new  $z$ -axis. What is required is a rotation about the  $x$ -axis, which can be achieved with a second, fresh coordinate system which takes in the first one as its base. This new coordinate system must be set up to perform a rotation about the  $x$ -axis, which is denoted the **roll** axis. This can be done by setting  $\alpha$  to  $-90^\circ$  and  $\gamma$  to the opposite value,  $90^\circ$ . Any change of this coordinate systems  $\beta$  angle will cause a rotation about the  $x$ -axis, as is required.  $\beta$  will then be given a value of  $-7.13762^\circ$ . This completes the proxy Euler  $XY'Z''$  rotation. Note that if the values of  $\alpha$  and  $\gamma$  are reversed, then  $\beta$  must be a positive value ( $7.13762^\circ$ ). The direction of a rotation is determined by the sign of the angles, so this is just simply a reversal to reflect the change in  $\alpha$  and  $\gamma$ . The magnitude of  $\beta$  will not and must not change.

The last step of the integration process is to set the second coordinate system as the base of “Mirror Global”. Everything tied to this coordinate system will be slotted into place among the tabulated mesh components. The proxy rotation was easily verified as any incorrect step would lead to noticeable clipping of objects into one another. Distances between mesh vertices in both FreeCAD and GRASP were also used as verification; any incorrect orientation would lead to distance discrepancies between the CAD model and the GRASP one. The new nested structure of coordinate systems carried its own benefit. Ancillary objects like representations of the telescopes spin axis and optical axis could now be introduced into the model very easily. Having the GRASP model match the CAD model more closely would render it easier to send off the GRASP model to collaborators; there would now be recognisable elements, like distances, known angles

or coordinate systems, present. Finally, the two step rotation can be replaced with a single Euler  $ZY'Z''$  rotation with the *Redefine to Other Base* feature. Redefining the “Mirror Global” coordinate system to the model global will express the rotation in  $ZY'Z''$  form. The parameters are listed in Table 6.17:

Mirror Global Values	
X (mm)	2065.36
Y (mm)	3152.14
Z (mm)	2951.46
$\alpha$ (°)	-85.8747
$\beta$ (°)	25.0695
$\gamma$ (°)	-15.5271

Table 6.17: Values for the  $ZY'Z''$  rotation of Mirror Global.

The full model of the *CORE* telescope can be seen in Figure 6.127:

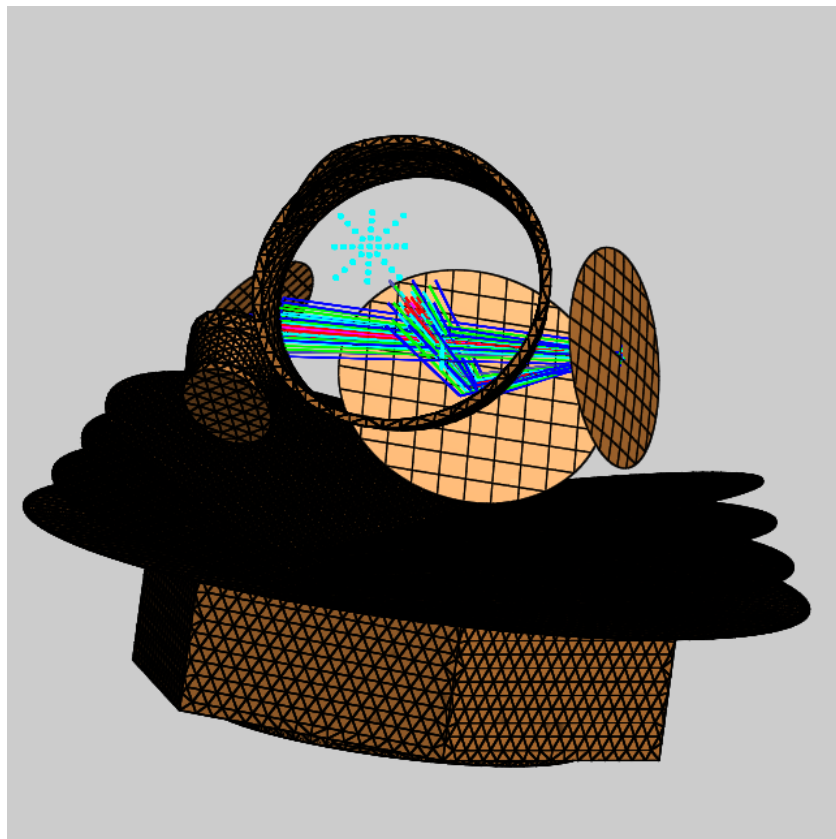


Figure 6.127: The full *CORE* model in GRASP.

The PO analysis of *CORE* ended at this point due to limited computational resources. No viable beams could be retrieved from the few successful calculations.

# Chapter 7

## Future Work

This final chapter will provide an outline as to how the work presented in this thesis could be advanced in the future.

### 7.1 *CORE*

Though *CORE* is no longer in the running for M5 assessment due to budgetary concerns, the work will be relevant to a future CMB B-mode mission. Topics to continue would be the analysis of the thermal shielding and baffling that have been imported into the model already to predict far out sidelobes and detailed beam predictions. Not only would this allow the effects of these components on the beams produced by the telescope to be quantified and allow stray light analysis to be feasible, it would continue to strengthen the analysis tools and techniques used in Maynooth and hopefully allow similar telescope systems to be routinely analysed in the future.

Optimisation of detector/feed locations in the focal plane area could be performed. Preliminary analysis has been presented here but a much more comprehensive programme of analysis is required to optimise the different channels in terms of the best locations to minimise the overall aberration over the focal plane.

Finally, there was a potential solution to attempt to flatten the focal plane area of the Offset Gregorian *CORE* design. This analysis would be accomplished by using a silicon lens combination known as a field flattener. This combination is made up of a convex-plano lens coupled to a plano-concave lens. This would

take place using Zemax OpticStudio and utilise the optimiser to converge on an optimal lens spacing, thickness and shape. This lens would also need to be larger than traditional lens designs (equivalent in size to the focal plane). This is challenging optically to integrate this successfully over a frequency range from 60 - 600 GHz. The new refractive tools in GRASP could also be applied to the problem.

## 7.2 LLAMA

Though the preliminary work has been carried out for three of LLAMA's potentially eleven bands, there remains a lot of potential work to follow on from the author's contribution. First of all the remaining bands need to be tested in the same manner to verify that the receiver design works well for those bands as well, thereby satisfying the stated goal.

Next, the current model in GRASP is very basic. There are a host of optical elements missing from the design that would need to be accounted for in more stringent analysis, like folding mirrors and apertures. There are many more smaller folding mirrors that will form the full receiver which will need to be implemented and verify that they are having no impact on the optical performance of the receiver. There are also polarising grids envisioned in the design whose impact will need to be analysed and potentially optimised with respect to orientation of grids to decrease noise. An elevation tube is present which will, by design or not, act as a kind of field stop and manipulate the structure of the beam between M3 and M4. This will be top of the list in terms of future additions to the Maynooth LLAMA model. Elements of the cryostat unit could also be included.

Lastly, a full analysis could be performed on the entire optical train including the main dish and subreflector. LLAMA is a 12 m Cassegrain type telescope. One

focus point of the receiver is the Cassegrain focus with the associated mirrors to eliminate the well-known aberrations that are part and parcel of the Cassegrain design. The full primary and secondary mirrors of LLAMA could easily be inserted into the existing model. This would allow for full propagation from the instrument plane through the optical train and onto the sky. This would represent a full optical model for LLAMA, given that it would be the most complete representation possible.

### 7.3 Meshing

The techniques to import and export optical components between different software packages is extremely important. To keep the integrity and definition of the mirrors, a deep understanding of meshing is required. The work presented in this thesis sets out the main requirements for meshing and is the basis of important work in going from ray analysis and design to physical optics analysis to exportation of surfaces for manufacture.

# Bibliography

Ade, P., Aikin, R., Barkats, D., Benton, S., Bischoff, C., Bock, J., Brevik, J., Buder, I., Bullock, E., Dowell, C., and Duband, L. (2014a). Detection of B-mode polarization at degree angular scales by BICEP2. *Physical Review Letters*, 112(24):4–22.

Ade, P. A. R., Aikin, R. W., Amiri, M., Barkats, D., Benton, S. J., Bischoff, C. A., Bock, J. J., Brevik, J. A., Buder, I., Bullock, E., Davis, G., Day, P. K., Dowell, C. D., Duband, L., Filippini, J. P., Fliescher, S., Golwala, S. R., Halpern, M., Hasselfield, M., Hildebrandt, S. R., Hilton, G. C., Irwin, K. D., Karkare, K. S., Kaufman, J. P., Keating, B. G., Kernasovskiy, S. A., Kovac, J. M., Kuo, C. L., Leitch, E. M., Llombart, N., Lueker, M., Netterfield, C. B., Nguyen, H. T., O’Brient, R., IV, R. W. O., Orlando, A., Pryke, C., Reintsema, C. D., Richter, S., Schwarz, R., Sheehy, C. D., Staniszewsk, Z. K., Story, K. T., Sudiwala, R. V., Teply, G. P., Tolan, J. E., Turner, A. D., Vieregg, A. G., Wilson, P., Wong, C. L., and Yoon, K. W. (2014b). BICEP2 II: Experiment and Three-Year Data Set. *The Astrophysical Journal*, 792(1):62.

Ade, P. A. R. and the *Planck* collaboration (2015). Planck 2015 results XIII. Cosmological parameters. *Astronomy and Astrophysics*, 594:32.

Arnone, D., Ciesla, C., Corchia, A., Egusa, S., Pepper, M., Chamberlain, J., Bezant, C., Linfield, E., Clothier, R., and Khammo, N. (1999). Applications of Terahertz (THz) Technology to Medical Imaging. *In Proc. SPIE*, 3828(1):209–220.

Baryshev, A., Baselmans, J. J. A., Freni, A., Gerini, G., Hoevers, H., Iacono, A., and Neto, A. (2011). Progress in Antenna Coupled Kinetic Inductance Detectors. *IEEE Transactions on Terahertz Science and Technology*, 1(1):113.

- Baumann, D., Cooray, A., Dodelson, S., Dunkley, J., Fraisse, A., Jackson, M., Kogut, A., L.M., K., Smith, K., and Zaldarriaga, M. (2009). A Mission to Map our Origins. *AIP Conference Proceedings*, 1141(1):3–9, 2.
- Byrd, J. (2010). THz Detectors - USPAS. [Online] <http://uspas.fnal.gov/materials/10MIT/4.THzDetectors.pdf> [Accessed: August 2017].
- Candotti, M. (2007). *Design, Analysis and Optimisation of Quasi-Optical Systems for Sub-MM Astronomy Instrumentation*. PhD thesis, NUI Maynooth.
- Carroll, B. W. and Ostlie, D. A. (2014). *An Introduction to Modern Astrophysics*. Pearson Education Limited. ISBN: 978-1-292-02293-2.
- Chang, S. and Prata, A. (2004). The Design of Classical Offset Dragonian Reflector Antennas With Circular Apertures. *IEEE TRANSACTIONS ON ANTENNAS AND PROPAGATION*, 52(1):12–19.
- Cowen, R. (2015). Gravitational waves discovery now officially dead. *Nature*, (1). [Online] <https://www.nature.com/news/gravitational-waves-discovery-now-officially-dead-1.16830> [Accessed: September 2017].
- Dassault Systèmes (2012). CST Studio Suite 2012, Platform: Windows.
- de Bernardis, P., Ade, P., Baselmans, J., Battistelli, E., Benoit, A., Bersanelli, M., Bideaud, A., Calvo, M., Casas, F., Castellano, G., et al. (2017). Exploring Cosmic Origins with CORE: The Instrument. *arXiv preprint arXiv:1705.02170*, pages 2, 6, 11–12. [Online] <https://arxiv.org/abs/1705.02170> [Accessed: October 2017].
- Drabowitch, S., Papiernik, A., Griffiths, H., Encinas, J., and Smith, B. L. (1998). *Modern Antennas*. IEEE Press.

- ESA (2015). PLANCK: GRAVITATIONAL WAVES REMAIN ELUSIVE. [Online] [http://m.esa.int/Our\\_Activities/Space\\_Science/Planck/Planck\\_gravitational\\_waves\\_remain\\_elusive](http://m.esa.int/Our_Activities/Space_Science/Planck/Planck_gravitational_waves_remain_elusive) [Accessed: August 2017].
- Federici, J., Schulkin, B., Huang, F., Gary, D., Barat, R., Oliveira, F., and Zimdars, D. (2005). THz imaging and sensing for security applications—explosives, weapons and drugs. *Semiconductor Science and Technology*, 20(7):S266–S280.
- Fitzgerald, A., Berry, E., Zinovev, N., Walker, G., Smith, M., and Chamberlain, J. M. (2002). An introduction to medical imaging with coherent terahertz frequency radiation. *Physics in Medicine and Biology*, 47(7):R67–R84.
- Fixsen, D. J. (2009). The temperature of the cosmic microwave background. *The Astrophysical Journal*, 707(2).
- Flauger, R., Hill, J., and Spergel, D. (2014). Toward an understanding of foreground emission in the BICEP2 region. *Journal of Cosmology and Astroparticle Physics*, 2014(08):2–10.
- Giovannini, M. (2004). Theoretical tools for CMB physics. *International Journal of Modern Physics D*, 14(03n04):7.
- Goldsmith, P. (1998). *Quasioptical Systems*. IEEE Press. ISBN: 0-7803-3439-6.
- Guth, A. H. (1981). Inflationary universe: A possible solution to the horizon and flatness problems. *American Physical Society Physical Review D*, 23(2):347.
- Hu, W. and White, M. (1997). A CMB polarization primer. *New Astronomy*, 2(4):3–7.
- Johansen, P. (1996). Uniform physical theory of diffraction equivalent edge currents for truncated wedge strips. *IEEE Transactions on Antennas and Propagation*, 44(7):989–995.

- Johansson, J. F. (1995). A Comparison of Some Feed Types. *Astronomical Society of the Pacific Conference Series*, 75:82.
- Kooi, J. (2016). LLAMA: First Light Unfolded Optics. Technical report.
- Kuo, C. L., Bock, J. J., Bonetti, J. A., Brevik, J., Chattopadhyay, G., Day, P. K., Golwala, S., Kenyon, M., Lange, A. E., LeDuc, H. G., Nguyen, H., Ogburn, R. W., Orlando, A., Transgrud, A., Turner, A., Wang, G., and Zmuidzinas, J. (2008). Antenna-coupled TES bolometer arrays for CMB polarimetry. 7020:70201I.
- Lee, Y.-S. (2009). *Principles of Terahertz Science and Technology*. Springer Science and Business Media.
- Lemaître, G. (1931). Expansion of the universe, a homogeneous universe of constant mass and increasing radius accounting for the radial velocity of extragalactic nebulae. *Monthly Notices of the Royal Astronomical Society*, 91:483–490.
- Linde, A. D. (1984). The inflationary universe. *Reports on Progress in Physics*, 47(8):925–986.
- Liu, S. and Long, D. (1978). Pyroelectric detectors and materials. *Proceedings of the IEEE*, 66(1):14 – 26.
- LLAMA (2016). Large Latin American Array: Project. [Online] <http://www.iar.unlp.edu.ar/llama-web/project.htm> [Accessed: August 2017].
- NASA (2010). WMAP Technical Specs. [Online] [https://map.gsfc.nasa.gov/mission/observatory\\_spec.html](https://map.gsfc.nasa.gov/mission/observatory_spec.html) [Accessed: August 2017].
- Page, L., Hinshaw, G., Komatsu, E., Nolta, M. R., Spergel, D. N., Bennett, C. L., Barnes, C., Bean, R., Doré, O., Dunkley, J., Halpern, M., Hill, R. S., Jarosik, N., Kogut, A., Limon, M., Meyer, S. S., Odegard, N., Peiris, H. V.,

- Tucker, G. S., Verde, L., Weiland, J. L., Wollack, E., and Wright, E. L. (2007). Three Year Wilkinson Microwave Anisotropy Probe (WMAP) Observations: Polarization Analysis. *Astrophysical Journal*, pages 335, 350.
- paultownsend.co.uk (2013). THz imaging of a tooth. [Online] <http://www.paultownsend.co.uk/research/fundamentals/terahertz-radiation/> [Accessed: August 2017].
- Pontoppidan, K., editor (2015). *GRASP Technical Description*. TICRA Engineering Consultants, Copenhagen.
- Samtleben, D., Staggs, S., and Winstein, B. (2007). The Cosmic Microwave Background for Pedestrians: A Review for Particle and Nuclear Physicists. *Annual Review of Nuclear and Particle Science*, 57:245–283.
- Sciencetech-inc.com (2017). Terahertz Gap image. [Online] <http://www.sciencetech-inc.com/application/thz-research.html> [Accessed: June 2017].
- Smoot, G. F., Bennett, C. L., Kogut, A., Wright, E. L., Aymon, J., Boggess, N. W., Cheng, E. S., de Amici, G., Gulkis, S., Hauser, M. G., Hinshaw, G., Jackson, P. D., Janssen, M., Kaita, E., Kelsall, T., Keegstra, P., Lineweaver, C., Loewenstein, K., Lubin, P., Mather, J., Meyer, S. S., Moseley, S. H., Murdock, T., Rokke, L., Silverberg, R. F., Tenorio, L., Weiss, R., and Wilkinson, D. T. (1992). Structure in the COBE differential microwave radiometer first-year maps. *The Astrophysical Journal*, 396(1):L1–L5.
- sron.nl (2017). Transition Edge Sensors. [Online] <https://www.sron.nl/technology-tes-ir-bolometers> [Accessed: August 2017].
- TICRA (1976). Version 9, Platform: Windows.
- Walker, C. K. (2016). *Terahertz Astronomy*. CRC Press.

- 
- Whale, M. (2010). *Optical Characterisation of Astronomical Submillimetre Receivers including ALMA Bands 5 and 9*. PhD thesis, NUI Maynooth.
- Yang, Y., Shutler, A., and D.Grischkowsky (2011). Measurement of the transmission of the atmosphere from 0.2 to 2 THz. *Optics Express*, 19(9):8830–8838.
- Zemax (1990). Version 16, Platform: Windows.